CHARACTERIZATION OF DEFORMATION DURING SYN-CONVERGENT EXTENSION: INSIGHTS FROM THE BRITTLE-DUCTILE-TRANSITION IN THE CORDILLERA BLANCA, PERU

A Dissertation Presented for the

Doctor of Philosophy

Degree

The University of Tennessee, Knoxville

Cameron Hughes

December 2019

DEDICATION

To Mary, Steve, Melanie, and Hayden, whom have supported me through all my endeavors.

ACKNOWLEDGEMENTS

I thank Micah Jessup and Colin Shaw for their guidance and support throughout this research. I thank my committee members: Robert D. Hatcher, Jr., Harry McSween, and Dayakar Penumadu for their time and for sharing their expertise in discussions to help this project progress. I also thank Dennis Newell for his contributions to field work and helping to strengthen my research and writing. Hannah Tefeteller, Aaron Stubblefield, and Tami Banks are thanked for their contributions to this project as undergraduate researchers at the University of Tennessee. I thank Russell Godkin for his industrious work helping with sample preparation as an undergraduate assistant at the University of Tennessee. Adam Weist and Carly Mueller are thanked for their assistance in sample preparation for X-Ray Fluorescence analysis as undergraduate assistants at the University of Wisconsin-Eau Claire. Allan Patchen is thanked for his invaluable assistance with EPMA analysis at the University of Tennessee. Discussions with Hannah Teffeteller, Alex Lusk, and Tyler Grambling progressed various ideas in this work forward. I appreciate the support of Linda Kah, Chris Fedo, and J. Brian Mahoney for instrument usage and sample preparation.

This project would not have come to fruition without the numerous people who provided support for this work, either by scientific discussion or by improvement of well-being. Tim Diedesch was instrumental in both regards. I thank my family—Mary, Steve, Hayden, Mel (Winters), Rebbecca, and Brian Winters, and the Diedesch family—Tim Jon, Barb, Jessica, and Josh, Courtney, and David Aresca for always being pillars of support. Sam Gwizd, Mike Lucas, Diego Sanchez, Audrey Martin, Jason Muhlbauer, Megan Mouser, Zach Stooksbury, Richie Ness, Jen Bauer, Sarah Sheffield, Jesse Ende, Ashley Manning-Berg, Ariana Boyd, Chad Melton, Cameron McCarty, Brandon Bagley, Brendan Donnely, Blake Roberts, Arya Udry, Miles Henderson, and Latisha Brengman are thanked for their support at various times during the last six years. Dr. Rebecca Morgan at UTK, Jason Bloom, Stacey Hyde, and Jeanne Zucker were critical for recovering after a brain injury that occurred in my first month as a graduate student and managing long-term wellness. I also want to thank the students I had the privilege of teaching while at the University of Tennessee, who helped motivate me to keep going on a daily basis.

ABSTRACT

The Andes Mountains are a culmination of smaller mountain ranges that form the longest mountain chain in the world, accommodating convergence and the subduction of the Nazca Plate under the South American Plate since the Late Jurassic. Subduction along the Andean margin varies from normal-dipping to flat-slab subduction, with flat-slab segments commonly characterized by crustal thicknesses upwards of ~70 km. The Peruvian segment is of particular interest, as magmatic arcs in this region show an eastward younging trend and active extension along the western margin of the youngest plutonic feature, the Cordillera Blanca batholith. Extension along this margin is limited to high elevations and occurs along an active low-angle normal detachment fault striking parallel to the trend of the ~200-km-long Cordillera Blanca mountain range, which hosts numerous peaks > 6000 m. The detachment exhumes a mylonitic shear zone of deformed batholith rocks. Tectonic fabrics suggest that 1) extension along the fault is parallel to the direction of plate convergence and regional crustal shortening, and 2) the shear zone crossed the brittle-ductile transition while it was actively deforming during exhumation. These conditions make for a unique setting in which to study the mid-crustal brittle-ductile-transition, and strain localization in a syn-convergent extensional setting where the regional principal stresses are known. This project characterizes deformation of the exhumed shear zone using detailed kinematic analyses, deformation temperature analyses, paleopiezometry, and geochemistry. From this work, a crustal strength profiles for the Cordillera Blanca has been constructed, providing a model for the rheologic evolution of this particular region and contributing to the structural community's understanding of the rheologic conditions that allow for convergence-parallel extension in the mid-crust.

TABLE OF CONTENTS

LIST OF FIGURES

LIST OF TABLES

INTRODUCTION

The Cordillera Blanca in central Peru is a batholith-cored mountain range bounded by a ~200-km-long low angle normal detachment fault. Slip along the fault began at ~5 Ma and is still ongoing (Giovanni et al., 2010), actively exhuming the batholith along a mylonitic shear zone that transitions from undeformed granodiorite through ultramylonite and cataclasite approaching the detachment (Petford and Atherton, 1992). The Cordillera Blanca detachment system is an important feature to study due to its unique tectonic setting: a flat slab segment of the subducting Nazca plate underlies the CB region (Jordan et al., 1983; Gutscher, Olivet, et al., 1999), and movement along the extensional detachment is directed parallel to the convergence direction of the Nazca and South American plates (Dalmayrac and Molnar, 1981; Schwartz, 1988b; McNulty and Farber, 2002).

In the transitional zone between the batholith and the detachment, ductile deformation occurs and is increasingly overprinted by brittle deformation nearer to the detachment, making the zone an area of great interest for understanding mechanisms that facilitate strain localization at the brittle-ductile-transition (BDT). Crustal strength is highest at the BDT, where Byerlee's law (Byerlee, 1978), which describes the differential stress required for brittle deformation with increasing crustal depth, and quartz flow laws (e.g. Brace and Kohlstedt, 1980; Paterson and Luan, 1990; Hirth et al., 2001; Tokle et al., 2019) intersect, typically at 10-15 km depth (Sibson, 1977). A significant body of work over the last several decades describes processes that occur in shear zones at and near the BDT, including mineralogical evolution, (LaTour and Barnett, 1987; Glazner and Bartley, 1991a; Yund and Tullis, 1991; Bialek, 1999; Goncalves et al., 2012), microstructural evolution (Lister and Snoke, 1984; Simpson, 1985; Paterson et al., 1989; Pryer, 1993; Passchier and Trouw, 2005), recrystallization mechanisms (Urai et al., 1986; Behrmann and Mainprice, 1987; Drury and Urai, 1990; Hirth and Tullis, 1992; Lloyd and Freeman, 1994; Stipp et al., 2002b, 2002a), and flow properties (Carter and Tsenn, 1987; Janecke and Evans, 1988; Tullis and Yund, 1991; Hirth and Tullis, 1992; Platt and Behr, 2011a).

Many researchers have utilized such advancements to investigate metamorphic core complexes (Hacker et al., 1990; Behr and Platt, 2011; Gottardi and Teyssier, 2013; Cooper et al., 2017), orogenic thrust belts (Whitmeyer and Wintsch, 2005), strike-slip shear zones (Stipp et al., 2002b, 2002a; Faleiros et al., 2010), and extensional shear zones (Wells et al., 2005; Langille et al., 2010). Although an increasing amount of research into extensional shear zones has focused on low-angle normal faults and syn-convergent extensional shear zones (e.g. Wells et al., 2005) similar in structure to the Cordillera Blanca Shear Zone (CBSZ), less work has been done on young, still active shear zones or on shear zones with a movement direction parallel to the overall regional convergence direction (Bessiere et al., 2018). The CB, where movement is parallel and opposing to the direction of overall regional convergence is thus an excellent location for advancing the understanding of syn-convergent extensional shear zones. Studying strain localization in this unique tectonic setting also allows for the application of relatively new methods in thermometry and paleopiezometry to a young shear zone to further constrain the strength of the mid-crust above a subducting flat slab.

Geologic Background

The Andean orogeny began in at least the late Jurassic (Megard, 1984), accommodating subduction of the Nazca plate beneath the South American plate (James, 1971). Subduction is segmented, with a normal slab dip of 30-35° beneath Colombia, the Central Andes and south-central Chile, that shallows to subhorizontal below the Peruvian, Bucaramanga, and Pampeanan segments (Gutscher, Malavieille, et al., 1999; Gutscher, Olivet, et al., 1999; Ramos, 1999;

Gutscher, 2002). Shortening above the Peruvian segment was accommodated by the Marañon fold and thrust belt to the east of the Cordillera Blanca from 20-12.5 Ma (Megard, 1984) and is presently accommodated further to the east by the Sub-Andean fold and thrust belt (Dalmayrac and Molnar, 1981). Magmatism occurred ~300 km west of the Cordillera Blanca from 105-34 Ma (Cobbing et al., 1981), migrated eastward from 50-20 Ma, (Cobbing, 1999), and ended with the latest magmatism in the Cordillera Blanca batholith and associated Yungay ignimbrites (Petford and Atherton, 1992).

The granodiorite-leucogranodiorite Cordillera Blanca batholith was emplaced at ~8 Ma and ~90 to ~300 MPa pressures (Petford and Atherton, 1996; McNulty et al., 1998; McNulty and Farber, 2002; Margirier et al., 2016), intruding the Jurassic Chicama Shale (Cobbing, 1981). It is separated from the volcanic rocks of the Cordillera Negra to the west by the Callejon de Hualyas sedimentary basin and the range-bounding Cordillera Blanca detachment fault, which dips ~30° WSW and exhumes a 100-500 m thick zone of mylonitized CBB footwall rocks. Active since ~5 Ma, the detachment has accommodated 12-15 km of crustal extension (Giovanni et al., 2010), localized to high elevations (Dalmayrac and Molnar, 1981). Previous research has focused on the geochemistry, emplacement mechanisms, and crustal source of the Cordillera Blanca batholith (Petford and Atherton 1992; Petford et al., 1996; McNulty et al., 1998; McNulty and Farber 2002), microseismicity associated with the CBD (Schwartz, 1988), and on the adjacent Callejón de Hualyas basin (Giovanni et al., 2010). Though these studies provide important context for understanding the CBSZ, minimal work has been done to characterize the CBSZ and the rheologic evolution of the detachment system in detail.

Purpose

The purpose of this research is to characterize strain localization at the brittle-ductile-transition in an active syn-convergent extensional fault system. Objectives fall into two categories, (1) overall targets of the NSF grant awarded to M. Jessup and C. Shaw (2012-2015), and (2) additional targets developed independently from preliminary work towards category 1 goals. The main objectives of the first category are to determine (a) temperature, (b) differential stress, (c) kinematics, and (d), microstructural evolution of progressive deformation from undeformed granodiorite to mylonite, ultramylonite, and cataclasite. Additional objectives stemming from preliminary work are to document the spatial changes of these conditions, particularly as they apply to the transition from magmatic to solid-state fabrics, and to evaluate the role of fluids in deformation by quantifying mass transfer across the shear zone.

Ultimately, the goal of attaining these data is to determine the deformation mechanisms acting to allow strain localization at the brittle-ductile-transition (BDT), to construct a crustal strength profile for the Cordillera Blanca, and to gain insight into fluid flow along the ductile to brittle transition in an extensional shear zone. Results from this research can aid studies by other researchers working in more complex shear zones and at the BDT.

BDT and Strain Localization

The BDT between the upper and lower crust is the strongest part of the continental crust and forms the base of the seismogenic zone (Sibson, 1977; Scholz, 1988; Behr and Platt, 2014). The BDT is an important target of study for understanding how tectonic stresses transfer from the mantle and lower crust to the upper crust and, on a large scale, how the mid-crust accommodates plate tectonics (Gueydan et al., 2014). Frictional, brittle processes dictate behavior of the upper crust (Byerlee, 1978; Carter and Tsenn, 1987; Kirby, 1980), crystal-plastic processes dictate the rheologic behavior of the lower crust (Carter and Tsenn, 1987), and in the mid-crust along the BDT zone the two processes compete with one another (Kirby, 1980; Scholz, 1988; Wintsch and Yeh, 2013; Oliot et al., 2014). The BDT typically occurs at 10-15 km depth (Sibson, 1977), but can vary in depth depending on a multitude of variables, including strain rate, temperature, presence and activity of water (Kirby, 1980; Tullis and Yund, 1980), degree of interconnectedness of minerals (Wintsch and Yeh, 2013), differential stress, mineralogy, texture, deformation mechanism, and preferred mineral orientations (Behr and Platt, 2011; Carter and Tsenn, 1987; Cooper et al., 2017; Platt and Behr, 2011b; Rutter, 1986). Over the last half century, experimental work has constrained many variables affecting the rheology of the BDT, providing a framework for studying ‘natural laboratories’ with experimentally derived parameters and material properties to improve our understanding of mid-crustal deformation.

Mechanisms that accommodate deformation within shear zones can change with mineralogy, but also with pressure, temperature, grain size, and strain-rate (Handy, 1989). Within monomineerallic systems, rheologic behavior can be described by flow laws for a specific mineral; i.e. quartz in the mid-upper crust or olivine in the mantle, (Hirth and Tullis, 1992; Gleason and Tullis, 1993; Hirth et al., 2001). Experimental studies have defined constitutive flow laws for quartz dislocation creep (Brace and Kohlstedt, 1980; Tullis and Yund, 1980; Hirth and Tullis, 1992; Gleason and Tullis, 1993; Hirth et al., 2001; Rutter and Brodie, 2004; Gratier et al., 2009; Fukuda and Shimizu, 2017) and diffusion creep (i.e. grain-size sensitive creep) in quartz (Kilian et al., 2011b) and feldspar dislocation creep (Rybacki and Dresen, 2000) and diffusion creep (Tullis and Yund, 1991; Stünitz and Tullis, 2001).

Strain localization within polyphase systems relies on the interplay of deformation mechanisms such as diffusion creep, dislocation creep, and dislocation glide as they change with varying strain rate, differential stress, temperature, and water fugacity (Rosenberg and Stünitz, 2003; Platt, 2015). Polymineralic systems depend upon the behavior of each phase independently as well as which phase forms the load-bearing framework, the degree of interconnectedness of the weakest phase, and metamorphic reactions (Holyoke and Tullis, 2006). This study investigates the relative role of both mono- and poly-phase domains in strain localization within granodiorite along the BDT in a syn-convergent extensional shear zone.

Methods Overview

Rock samples collected from the Cordillera Blanca, Peru during 2011, 2013, and 2015 are the basis for this research. All methods except whole-rock geochemistry use thin sections from hand samples cut perpendicular to foliation and parallel to stretching lineation (X-Z sections).

Kinematic Analysis

Field and petrographic methods were used to determine the kinematics of the CBSZ. Mesoscale structural features observed in the field were further investigated at microscales through petrographic analysis using transmitted light microscopy on oriented thin sections. Shear-sense indicators are documented with respect to sample orientation and large-scale motion on the CB detachment. Microstructural kinematic indicators used in this study include mica fish, porphyroclast tails, S-C fabrics (Lister and Snoke, 1984), shear bands, asymmetric myrmekite (Simpson and Wintsch, 1989), and quartz oblique grain-shape fabrics. Petrographic descriptions, including texturally evident stable mineral assemblages and shear-sense information, are documented for thin sections of samples representative of different deformation intensities and structural positions in the CBSZ from multiple transects across strike of the shear zone. This allows for potential spatial and temporal trends regarding mineralogy and kinematic indicators to be evaluated.

Deformation Temperatures

Quartz Recrystallization Microstructures

Construction of a crustal strength profile requires knowledge of the depth at which differential stresses are acting during deformation. Determining deformation temperatures allows crustal depths of deformation to be inferred, thus contributing fundamentally to an evaluation of crustal strength. In the middle crust, quartz accommodates differential stress though ductile deformation, and more specifically through internal deformation of grains that induces dynamic recrystallization (Urai et al., 1986). Studies of experimental and natural settings have defined three distinct recrystallization mechanisms that accommodate differential stress from temperatures of 280 °C to over 650 °C (Stipp et al., 2002b). Dynamic recrystallization occurs through competing grain boundary bulging and sub-grain rotation processes (Urai et al., 1986; Hirth and Tullis, 1992; Lloyd and Freeman, 1994; Stipp et al., 2002b; Platt and Behr, 2011a), and deformation is in most cases dominated by either bulging (BLG, low temperature grain-boundary bulging), sub-grain rotation (SGR), or grain-boundary migration (GBM, high temperature grain-boundary bulging) recrystallization (Stipp et al., 2002a, 2002b). At strain rates of ~ 10^{-12} s^{-1}, bulging recrystallization occurs at 280-400 °C and typically high differential stress, SGR at 400-500 °C and moderate differential stress, GBM at T > 500 °C and low differential stress, and chessboard extinction at T > 630 °C (Hirth and Tullis, 1992; Kruhl, 1996; Stipp et al., 2002a, 2002b). Grain and sub-grain orientations, grain boundary characteristics, and recrystallized grain size were observed to differentiate between BLG, SGR, GBM, and chessboard extinction, providing a preliminary semi-quantitative estimate of deformation temperatures for CB samples.

Feldspar textures were also documented to provide additional constraints on deformation processes and temperatures. While feldspar recrystallization mechanisms do not transition between recrystallization regimes as consistently as quartz mechanisms (Allison et al., 1979; Svava Olsen and Kohlstedt, 1985; Tullis and Yund, 1991; Pryer and Robin, 1996; Shigematsu, 1999; McLaren and Pryer, 2001; Stünitz et al., 2003), the transition of brittle to ductile deformation in feldspar and microstructural features such as flame perthite, kinking, bulging recrystallization, and microcracking provide important, though qualitative, information regarding deformation temperatures and mechanisms.

Two-feldspar Thermometry

Although textural observations alone only provide qualitative temperature data, when combined with compositional data they can provide quantitative deformation temperature estimates, for example through coupling textural analysis of asymmetric myrmekite (Simpson and Wintsch, 1989) with two-feldspar thermometry (Whitney and Stormer, 1977; i.e. Langille et al., 2010). Asymmetric albite-oligoclase myrmekite preferentially develops at high-strain sites of K-feldspar porphyroclasts when Na^+ is available to react (Simpson and Wintsch, 1989). Assuming a closed system at the grain-scale, the composite microstructure of a K-feldspar porphyroclast, impinging Na-rich myrmekite lobes distributed asymmetrically around the porphyroclast, and recrystallized K-feldspar tails records the temperature at which the deformation-induced reaction occurred. Only samples containing this set of features were used for two-feldspar thermometry, and multiple microstructures, when available, were analyzed from each sample to account for local variations.

Compositional data for use in two-feldspar thermometry was obtained using the CAMECA SX 100 Electron Microprobe Analyzer (EMPA) at the University of Tennessee Knoxville. Representative minerals throughout the sample were analyzed to fully characterize the sample composition. Detailed compositional analysis of myrmekite lobes, host porphyroclasts, and recrystallized tails within each sampled microstructure were collected to ensure minerals are in equilibrium without zonation. From these compositional data, activities of feldspars used in the thermometer were calculated using the AX program of Holland and Powell (2000) following the procedure of Langille et al. (2010), and concentrations of feldspars were normalized on the orthoclase-albite-anorthite ternary (to obtain $\alpha_{ab,PL}$ and $X_{ab,AF}$, respectively). Temperatures were calculated using equation 1 (Langille et al., 2010, modified from Whitney and Stormer 1977):

$$T\ (\mathrm{K}) = \frac{\left\{7973.1-16910.6X_{ab,AF}+9901.9X_{ab,AF}^2+\left(0.11-0.22X_{ab,AF}+0.11X_{ab,AF}^2\right)(10P)\right\}}{\left\{-19872ln\left(\frac{X_{ab,AF}}{\alpha_{ab,PL}}\right)+6.48-21.58X_{ab,AF}+23.72X_{ab,AF}^2-8.62X_{ab,AF}^3\right\}}$$

(1)

where $X_{ab,\,AF}$ is normalized molar concentration of albite in alkali feldspar, P is pressure (MPa), and $\alpha_{ab,\,PL}$ is the activity of albite in plagioclase. The maximum pressure was assumed to be 300 MPa based on thermobarometry of the undeformed batholith and of the contact aureole metamorphic assemblage (Petford and Atherton, 1992; Margirier et al., 2016). Temperatures obtained from this equation must be interpreted with caution as the thermometer records the last temperature at which the deformation-induced reaction occurred, and not necessarily the first or last temperature at which the rock deformed.

Titanium-in-Quartz Thermometry

Many observed samples do not contain either deformation-induced myrmekite or myrmekite that meets all textural requirements to provide reliable temperature estimates. As most of these samples are granitic, rather than pelitic, alternative methods that do not rely on traditional metamorphic mineral assemblages for exchange thermometry must be used. Wark and Watson (2006) developed a thermometer based on the substitution of Ti for Si in quartz, which utilizes the positive linear relationship of increasing Ti concentration with increasing temperature. TitaniQ is established as a reliable thermometer in igneous and volcanic systems when pressure and Ti activity are constrained (Thomas et al., 2010), and has been increasingly used in greenschist facies shear zones to determine deformation temperatures (Kidder et al., 2013; Xia and Platt, 2018).

Cathodoluminescence (CL) imaging is commonly used to assess relative Ti concentrations in quartz, and thus can aid in evaluating mineral zonation or multiple generations of quartz growth (e.g. Spear and Wark, 2009; Nachlas et al., 2014). Quartz luminescence over a broad spectrum occurs due to a range of impurities, such as lattice defects or incorporation of trace elements. Titanium in quartz luminesces at 330-340 nm wavelengths and up to 400 nm wavelengths (blue-violet), with greater amounts of Ti producing a stronger signal. Thus, filtering CL images to specific wavelengths can allow for evaluation of Ti zoning or overgrowths prior to conducting spot analyses for TitaniQ thermometry (Spear and Wark, 2009; Götze, 2012). This is important in distinguishing between multiple generations of quartz, as even minor variations in Ti concentration must be evaluated texturally to determine which concentrations represent different deformation stages. For instance, larger grains may record a higher concentration of Ti in the core, and thus a higher temperature, than that of the texturally preserved deformation stage. To account for this variation, CL imaging was conducted on samples prior to performing quartz compositional analyses using the CITL CL8200 Mk5-2 Optical Cathodoluminescence System, mounted on a Nikon Eclipse E400 microscope and attached to an Optronics camera, at University of Tennessee-Knoxville.

Some debate occurs regarding the reliability of TitaniQ in different dynamic recrystallization regimes though there is general agreement that TitaniQ is reliable under conditions required for GBM or chessboard recrystallization (Thomas et al., 2010; Grujic et al., 2011; Thomas and Watson, 2012; Wilson et al., 2012; Kidder et al., 2013; Nachlas et al., 2014, 2018). As these conditions tend towards preserving relatively high (on the order of 10-100 ppm) Ti in quartz as well as relatively large grain sizes, concentrations can be determined on an electron microprobe (Grujic et al., 2011; Nachlas et al., 2014). Thus, TitaniQ thermometry will also be conducted using data obtained from the EPMA at UTK. Preliminary EPMa analyses utilized rutile as a standard. However, to improve on the accuracy and validity of the analyses, subsequent data were collected using the synthetically Ti-doped quartz standard with known Ti concentration from the Structure, Tectonics, and Metamorphic Petrology research group at the University of Minnesota (Nachlas et al., 2014). Temperatures were calculated using the thermobarometers of Thomas et al. (2010):

$$T\ (°C) = \frac{60952\ +1741(P/100)}{1.520 - R\times lnX_{TiO_2}^{Qtz} + R\times ln\alpha_{TiO_2}} - 273.15 \quad (2)$$

where P is pressure (MPa), R is the gas constant, $X_{TiO_2}^{Qtz}$ is the concentration of Ti in quartz (ppm) and a_{TiO_2} is the TiO_2 activity, and of Huang and Audétat, (2012):

$$logTi(ppm) = -0.27943 \times \frac{10^4}{T} - 660.53 \times \left(\frac{(P/100)^{0.35}}{T}\right) + 5.6459, \quad (3)$$

where T is temperature (Kelvin) and P is pressure (MPa).

Crystallographic Preferred Orientations

Quartz crystallographic preferred orientations (CPO) can lend further insight into deformation temperature and mechanisms accommodating stress in the rock, which in turn may have implications for differential stress and strain rate during deformation. Quartz accommodates differential stress during ductile deformation through intra- and inter-granular processes. Intra-granular deformation results in dislocation tangles and features such as kinking, subgrains, and undulose extinction. Inter-granular deformation can be described by characteristic recrystallization microstructures, which include GBM, SGR, and BLG microstructures and rely on grain boundary descriptions to define. Intra-granular deformation can be described by slip systems activated along specific crystallographic planes of quartz crystals, which are defined by the orientation of quartz grain c- and a- axes. These slip systems are generally sensitive to temperature and compete with one another. Multiple slip systems are often active at any stage of deformation, but one slip system tends to be dominant. In non-coaxially deformed quartz-rich rocks, the slip systems of interest are basal <a>, rhomb <a>, prism <a>, and prism <c> slip, which generally progress from low-temperature to high-temperature, respectively (Lister and Hobbs, 1980; Schmid and Casey, 1986; Law, 2014).

Crystallographic preferred orientations of quartz c-, a-, and prism-normal-axes were measured using Oxford Instruments Channel 5 Flamenco acquisition software for electron backscatter diffraction (EBSD) at the Imaging and Chemical Analysis Laboratory at Montana State University. Preferred orientations are presented on lower hemisphere stereographic projection plots, with one point representing the mean orientation of an entire grain to avoid biases from large grains making up large portions of the sample area. Grain boundary maps and grain boundary misorientations were used to distinguish between recrystallized grains, relict grains, and sub-grains. From these categories, separate CPO pole figures were constructed to evaluate the slip systems operating in each deformation regime. Pole figures were constructed using the MTEX toolbox for Matlab (Mainprice et al., 2014).

Paleopiezometry

In quartz-dominated lithologies, differential stress can be quantified using the quartz recrystallized grain size piezometric relationship, in which smaller recrystallized grain sizes correspond to higher differential stresses (Twiss, 1977). Recrystallized grain sizes were determined for samples representing 1) increasing amounts of finite strain and 2) multiple transects through the shear zone across strike. Recrystallized grain size was determined through grain mapping of representative samples analyzed with Oxford Instruments Channel 5 Flamenco acquisition software on the EBSD-equipped field emission gun-scanning electron microscope (FEG-SEM) at Montana State University. Grain sizes were determined by fitting measured grains with an equivalent-area circle. Grain sizes and related differential stresses in Chapter I were determined using Oxford Instruments Channel 5 (version 5) Tango software. Grain sizes and related differential stresses in Chapter II were determined using both Channel 5 software and the MTEX toolbox for Matlab (Bachmann et al., 2011; Appendix II.III). The root mean square grain size equivalent diameter for a given sample was used for paleopiezometry calculations. Recrystallized grains were defined by a critical misorientation of 10 degrees, following the procedures outlined in Halfpenny et al. (2012).

Whole-rock Geochemistry

Fluid-rock interactions can be assessed by obtaining 'whole-rock' geochemistry, or the concentration of different elements representative of an entire rock sample. Fluid interaction with rocks can facilitate mineral reactions and chemical changes (McCaig, 1984, 1997; Wintsch et al., 1995). Chemical changes can be resolved by calculations relating the mass and concentrations of elements in each sample and comparing them to elements where no change is observed via the equation (Gresens, 1967):

$$X_i = \left[f_v\left(\frac{\rho^A}{\rho^O}\right)C_i^A - C_i^O\right] \times M^O \tag{4}$$

where X_i is the amount of component *i* lost or gained, f_v is the volume factor, ρ is specific gravity, *O* and *A* denote the original and altered rock, respectively, *C* is the concentration (weight fraction) of element *i*, and M^O is the initial mass of the unaltered rock. Graphical representation of mass and volume changes are derived from Gresens' equation (Eq. X) as reconfigured by Grant (1986):

$$C_i^A = \frac{M^O}{M^A}\left(C_i^O - \Delta C_i\right) \tag{5}$$

where M^A is the mass of the altered sample and ΔC_i is the change in concentration relative to the initial reference concentration of *i*, such that a line of constant concentration (isocon) is derived at which $\Delta C_i = 0$.

Whole-rock geochemistry for undeformed through highly deformed rock samples have been obtained. Interaction of fluids in disequilibrium with rocks during deformation is expected to result in deformed rock samples with different whole-rock chemistry relative to undeformed samples. Depending on the nature of the fluids and starting composition, differences between undeformed and deformed rocks may include, but not be limited to, depletion or increase in alkaline elements such as Ca, Na, and K, and/or mobile trace and rare earth elements, such as As, Zn, and La (McCaig, 1984; McCaig et al., 1990; Rolland et al., 2003a; Rolland and Rossi, 2016).

Whole-rock geochemical analysis was conducted for 39 rock samples, collected from Peru in 2013 and 2015, representing different stages of deformation across the width and length of the CBSZ and that have already been evaluated for temperature and stress, where applicable. After weathering rinds were removed, samples were crushed individually into fine powders and analyzed using the X-ray Fluorescence (XRF) spectrometer at the University of Wisconsin Eau-Claire to determine concentrations of select major elements (concentrations > 1 % by weight), minor elements (0.1-1.0 % by weight), and trace elements (0.001-0.1 % by weight) in each rock sample. Mass balance and volume change were calculated using results from XRF analysis using the Geochemical Data Toolkit (*GCDKit)* package for R (Janousek et al., 2003; Janoušek et al., 2006) to detect deviation in deformed samples from the undeformed whole-rock chemistry.

References

Allison, I., Barnett, R. . L., & Kerrich, R. (1979). Superplastic flow and changes in crystal chemistry of feldspar. *Tectonophysics*, *53*(1–2), 41–46. https://doi.org/10.1016/0040-1951(79)90351-2

Bachmann, F., Hielscher, R., & Schaeben, H. (2011). Grain detection from 2d and 3d EBSD data-Specification of the MTEX algorithm. *Ultramicroscopy*, *111*(12), 1720–1733. https://doi.org/10.1016/j.ultramic.2011.08.002

Behr, W. M., & Platt, J. P. (2011). A naturally constrained stress profile through the middle crust in an extensional terrane. *Earth and Planetary Science Letters*, *303*(3–4), 181–192. https://doi.org/10.1016/j.epsl.2010.11.044

Behr, W. M., & Platt, J. P. (2014). Brittle faults are weak, yet the ductile middle crust is strong: Implications for lithospheric mechanics. *Geophysical Research Letters*, *41*, 8067–8075. https://doi.org/10.1002/2014GL061349

Behrmann, J. H. H., & Mainprice, D. H. (1987). Deformation mechanisms in a high-temperature quartz-feldspar mylonite: evidence for superplastic flow in the lower continental crust.

Tectonophysics, *140*(2–4), 297–305. https://doi.org/10.1016/0040-1951(87)90236-8

Bessiere, E., Rabillard, A., Précigout, J., Arbaret, L., Jolivet, L., Augier, R., et al. (2018). Strain Localization Within a Syntectonic Intrusion in a Back-Arc Extensional Context: The Naxos Monzogranite (Greece). *Tectonics*, *37*, 558–587. https://doi.org/10.1002/2017TC004801

Bialek, D. (1999). Chemical changes associated with deformation of granites under greenschist facies conditions: The example of the Zawidow Granodiorite (SE Lusatian Granodiorite Complex, Poland). *Tectonophysics*, *303*(1–4), 251–261. https://doi.org/10.1016/S0040-1951(98)00248-0

Brace, W. F., & Kohlstedt, D. L. (1980). Limits on lithospheric stress imposed by laboratory experiments. *Journal of Geophysical Research: Solid Earth*, *85*(B11), 6248–6252. https://doi.org/10.1029/JB085iB11p06248

Byerlee, J. D. (1978). Friction of rocks. *Pure and Applied Geophysics*, *116*(4–5), 615–626. https://doi.org/10.1007/BF00876528

Carter, N. L., & Tsenn, M. C. M. C. (1987). Flow properties of continental lithosphere. *Tectonophysics*, *136*(1–2), 27–63. https://doi.org/10.1016/0040-1951(87)90333-7

Cobbing, E. J. (1999). The Coastal Batholith and other aspects of Andean magmatism in Peru. *Geological Society, London, Special Publications*, *168*, 111–122.

Cobbing, E. J., Pitcher, W. S., Wilson, J. J., Baldock, J. W., Taylor, W. P., McCourt, W., & Snelling, N. J. (1981). *The geology of the Western Cordillera of northern Peru*. *Overseas Memoir 5* (Overseas M). London, England: Institute of Geological Services.

Cooper, F. J., Platt, J. P., & Behr, W. M. (2017). Rheological transitions in the middle crust: insights from Cordilleran metamorphic core complexes. *Solid Earth*, *8*, 199–215.

https://doi.org/10.5194/se-8-199-2017

Dalmayrac, B., & Molnar, P. (1981). Parallel thrust and normal faulting in Peru and constraints on the state of stress. *Earth and Planetary Science Letters*, *55*(3), 473–481. https://doi.org/10.1016/0012-821X(81)90174-6

Drury, M. R., & Urai, J. L. (1990). Deformation-related recrystallization processes. *Tectonophysics*, *172*(3–4), 235–253. https://doi.org/10.1016/0040-1951(90)90033-5

Faleiros, F. M., Campanha, G. A. da C., Bello, R. M. da S., & Fuzikawa, K. (2010). Quartz recrystallization regimes, c-axis texture transitions and fluid inclusion reequilibration in a prograde greenschist to amphibolite facies mylonite zone (Ribeira Shear Zone, SE Brazil). *Tectonophysics*, *485*(1–4), 193–214. https://doi.org/10.1016/j.tecto.2009.12.014

Fukuda, J., & Shimizu, I. (2017). Theoretical derivation of flow laws for quartz dislocation creep: Comparisons with experimental creep data and extrapolation to natural conditions using water fugacity corrections. *Journal of Geophysical Research: Solid Earth*, *122*(8), 5956–5971. https://doi.org/10.1002/2016JB013798

Giovanni, M. K., Horton, B. K., Garzione, C. N., McNulty, B. a., & Grove, M. (2010). Extensional basin evolution in the Cordillera Blanca, Peru: Stratigraphic and isotopic records of detachment faulting and orogenic collapse in the Andean hinterland. *Tectonics*, *29*(6), 1–21. https://doi.org/10.1029/2010TC002666

Glazner, A. F., & Bartley, J. M. (1991). Volume loss, fluid flow and state of strain in extensional mylonites from the central Mojave Desert, California. *Journal of Structural Geology*, *13*(5), 587–594. https://doi.org/10.1016/0191-8141(91)90045-K

Gleason, G. C., & Tullis, J. (1993). Improving Flow Laws and Piezometers for Quartz and Feldspar Aggregates. *Geophysical Resarch Letters, 20*(8), 2111–2114.

Goncalves, P., Oliot, E., Marquer, D., & Connolly, J. a D. (2012). Role of chemical processes on shear zone formation: An example from the grimsel metagranodiorite (Aar massif, Central Alps). *Journal of Metamorphic Geology*, *30*(7), 703–722. https://doi.org/10.1111/j.1525-1314.2012.00991.x

Gottardi, R., & Teyssier, C. (2013). Thermomechanics of an extensional shear zone, Raft River metamorphic core complex, NW Utah. *Journal of Structural Geology*, *53*, 54–69. https://doi.org/10.1016/j.jsg.2013.05.012

Götze, J. (2012). Application of cathodoluminescence microscopy and spectroscopy in geosciences. *Microscopy and Microanalysis*, *18*(6), 1270–1284. https://doi.org/10.1017/S1431927612001122

Grant, J. A. (1986). The Isocon Diagram - A Simple Solution to Gresens' Equation for Metasomatic Alteration. *Economic Geology*, *81*(8), 1976–1982. https://doi.org/10.2113/gsecongeo.81.8.1976

Gratier, J.-P., Guiguet, R., Renard, F., Jenatton, L., & Bernard, D. (2009). A pressure solution creep law for quartz from indentation experiments. *Journal of Geophysical Research*, *114*(B3), 1–16. https://doi.org/10.1029/2008JB005652

Gresens, R. L. (1967). Composition-volume relationships of metasomatism. *Chemical Geology*, *2*(C), 47–65. https://doi.org/10.1016/0009-2541(67)90004-6

Grujic, D., Stipp, M., & Wooden, J. L. (2011). Thermometry of quartz mylonites: Importance of dynamic recrystallization on Ti-in-quartz reequilibration. *Geochemistry, Geophysics, Geosystems*, *12*(6), 1–19. https://doi.org/10.1029/2010GC003368

Gueydan, F., Precigout, J., & Montesi, L. G. J. (2014). Strain weakening enables continental plate tectonics. *Tectonophysics* , *631*(189–196).

Gutscher, M. A. (2002). Andean subduction styles and their effect on thermal structure and interplate coupling. *Journal of South American Earth Sciences*, *15*(1), 3–10. https://doi.org/10.1016/S0895-9811(02)00002-0

Gutscher, M. A., Malavieille, J., Lallemand, S., & Collot, J. Y. (1999). Tectonic segmentation of the North Andean margin: Impact of the Carnegie Ridge collision. *Earth and Planetary Science Letters*, *168*(3–4), 255–270. https://doi.org/10.1016/S0012-821X(99)00060-6

Gutscher, M. A., Olivet, J. L., Aslanian, D., Eissen, J. P., & Maury, R. (1999). The "lost Inca Plateau": Cause of flat subduction beneath Peru? *Earth and Planetary Science Letters*, *171*(3), 335–341. https://doi.org/10.1016/S0012-821X(99)00153-3

Hacker, B. R., Yin, A., Christie, J. M., & Snoke, A. W. (1990). Differential Stress, Strain Rate, and Temperatures of Mylonitization in the Ruby Mountains, Nevada: Implications for the Rate and Duration of Uplift. *Journal of Geophysical Research*, *95*(10), 8569–8580. https://doi.org/10.1029/JB095iB06p08569

Halfpenny, A., Prior, D. J., & Wheeler, J. (2012). Electron backscatter diffraction analysis to determine the mechanisms that operated during dynamic recrystallisation of quartz-rich rocks. *Journal of Structural Geology*, *36*, 2–15. https://doi.org/10.1016/j.jsg.2012.01.001

Handy, M. R. (1989). Deformation regimes and the rheological evolution of fault zones in the lithosphere: the effects of pressure, temperature, grainsize and time. *Tectonophysics*, *163*(1–2), 119–152. https://doi.org/10.1016/0040-1951(89)90122-4

Hippertt, J. F. M. (1998). Breakdown of feldspar, volume gain and lateral mass transfer during mylonitization of granitoid in a low metamorphic grade shear zone. *Journal of Structural Geology*, *20*(2–3), 175–193. https://doi.org/10.1016/S0191-8141(97)00083-7

Hirth, G., & Tullis, J. (1992). Dislocation creep regimes in quartz aggregates. *Journal of*

Structural Geology, *14*(2), 145–159. https://doi.org/10.1016/0191-8141(92)90053-Y

Hirth, G., Teyssier, C., Dunlap, J., Dunlap, W. J., & Dunlap, J. (2001). An evaluation of quartzite flow laws based on comparisons between experimentally and naturally deformed rocks. *International Journal of Earth Sciences*, *90*(1), 77–87. https://doi.org/10.1007/s005310000152

Holyoke, C. W., & Tullis, J. (2006). The interaction between reaction and deformation: An experimental study using a biotite + plagioclase + quartz gneiss. *Journal of Metamorphic Geology*, *24*(8), 743–762. https://doi.org/10.1111/j.1525-1314.2006.00666.x

Huang, R., & Audétat, A. (2012). The titanium-in-quartz (TitaniQ) thermobarometer: A critical examination and re-calibration. *Geochimica et Cosmochimica Acta*, *84*, 75–89. https://doi.org/10.1016/j.gca.2012.01.009

James, D. E. (1971). Plate Tectonic Model for the Evolution of the Central Andes. *Geological Society of America Bulletin*, *84*(4), 1497–1500. https://doi.org/10.1130/0016-7606(1973)84<1497:PTMFTE>2.0.CO;2

Janecke, S. U., & Evans, J. P. (1988). Feldspar-influenced rock rheologies. *Geology*, *16*(12), 1064–1067. https://doi.org/10.1130/0091-7613(1988)016<1064:FIRR>2.3.CO;2

Janousek, V., Farrow, C. M., Erban, V., Smid, J., & Survey, C. G. (2003). Geochemical Data Toolkit for Windows written in R language © 2000-2003. *Names*, 1–11.

Janoušek, V., Farrow, C. M., & Erban, V. (2006). Interpretation of whole-rock geochemical data in igneous geochemistry: Introducing Geochemical Data Toolkit (GCDkit). *Journal of Petrology*, *47*(6), 1255–1259. https://doi.org/10.1093/petrology/egl013

Jordan, T. E., Isacks, B. L., Allmendinger, R. W., Brewer, J. a., Ramos, V. A., & Ando, C. J. (1983). Andean tectonics related to geometry of subducted Nazca plate. *Geological*

Society of America Bulletin, *94*(3), 341–361. https://doi.org/10.1130/0016-7606(1983)94<341:ATRTGO>2.0.CO;2

Kidder, S. B., Avouac, J. P., & Chan, Y. C. (2013). Application of titanium-in-quartz thermobarometry to greenschist facies veins and recrystallized quartzites in the Hsüehshan range, Taiwan. *Solid Earth*, *4*(1), 1–21. https://doi.org/10.5194/se-4-1-2013

Kilian, R., Heilbronner, R. P., & Stünitz, H. (2011). Quartz microstructures and crystallographic preferred orientation: Which shear sense do they indicate? *Journal of Structural Geology*, *33*(10), 1446–1466. https://doi.org/10.1016/j.jsg.2011.08.005

Kirby, S. H. (1980). Tectonic stresses in the lithosphere: Constraints provided by the experimental deformation of rocks. *Journal of Geophysical Research: Solid Earth*, *85*(B11), 6353–6363. https://doi.org/10.1029/JB085iB11p06353

Kruhl, J. H. (1996). Prism- and basal-plane parallel subgrain boundaries in quartz: a microstructural geothermobaromether. *Journal of Metamorphic Geology*, *14*, 581–589. https://doi.org/10.1046/j.1525-1314.1996.00413.x

Langille, J. M., Jessup, M. J., Cottle, J. M., Newell, D. L., & Seward, G. (2010). Kinematic evolution of the Ama Drime detachment: Insights into orogen-parallel extension and exhumation of the Ama Drime Massif, Tibet-Nepal. *Journal of Structural Geology*, *32*(7), 900–919. https://doi.org/10.1016/j.jsg.2010.04.005

LaTour, T. E., & Barnett, R. L. (1987). Mineralogical changes accompanying mylonization in the Bitterrot dome of the Idaho batholith: Implications for timing of deformation. *Geological Society of America Bulletin*, *98*(March), 356–363.

Law, R. D. (2014). Deformation thermometry based on quartz c-axis fabrics and recrystallization microstructures: A review. *Journal of Structural Geology*, *66*, 129–161.

https://doi.org/10.1016/j.jsg.2014.05.023

Lister, G. S., & Hobbs, B. . E. (1980). The simulation of fabric development during plastic deformation and its application to quartzite: the influence of deformation history. *Journal of Structural Geology*, *2*(3), 355–370. https://doi.org/10.1016/0191-8141(80)90023-1

Lister, G. S., & Snoke, A. W. (1984). S-C Mylonites. *Journal of Structural Geology*, *6*(6), 617–638. https://doi.org/10.1016/0191-8141(84)90001-4

Lloyd, G. E., & Freeman, B. (1994). Dynamic recrystallization of quartz under greenschist conditions. *Journal of Structural Geology*, *16*(6), 867–881. https://doi.org/10.1016/0191-8141(94)90151-1

Mainprice, D. H., Bachmann, F., Heilscher, R., & Schaeben, H. (2014). Descriptive tools for the analysis of texture projects with large datasets using MTEX : strength, symmetry and components. *Geological Society, London, Special Publications*, *409*. https://doi.org/10.1144/SP409.8

Margirier, A., Audin, L., Robert, X., Herman, F., Ganne, J., & Schwartz, S. (2016). Time and mode of exhumation of the Cordillera Blanca batholith (Peruvian Andes). *Journal of Geophysical Research: Solid Earth*, *121*(8), 6235–6249. https://doi.org/10.1002/2016JB013055

McCaig, A. M. (1984). Fluid-rock interaction in some shear zones from the Pyrenees. *Journal of Metamorphic Geology*, *2*(2), 129–141. https://doi.org/10.1111/j.1525-1314.1984.tb00292.x

McCaig, A. M. (1997). The geochemistry of volatile fluid flow in shear zones. In M. B. Holness (Ed.), *Deformation-enhanced fluid transport in the Earth's crust and mantle* (pp. 227–266). London, England: Chapman & Hall.

McCaig, A. M., Wickham, S. M., & Taylor, H. P. (1990). Deep fluid circulation in alpine shear zones, Pyrenees, France: field and oxygen isotope studies. *Contributions to Mineralogy and Petrology*, *106*(1), 41–60. https://doi.org/10.1007/BF00306407

McLaren, A. C., & Pryer, L. L. (2001). Microstructural investigation of the interaction and interdependence of cataclastic and plastic mechanisms in Feldspar crystals deformed in the semi-brittle field. *Tectonophysics*, *335*(1–2), 1–15. https://doi.org/10.1016/S0040-1951(01)00042-7

McNulty, B. a., & Farber, D. (2002). Active detachment faulting above the Peruvian flat slab. *Geology*, *30*(6), 567–570. https://doi.org/10.1130/0091-7613(2002)030<0567:ADFATP>2.0.CO;2

McNulty, B. a., Farber, D. L., Wallace, G. S., Lopez, R., & Palacios, O. (1998). Role of plate kinematics and plate-slip-vector partitioning in continental magmatic arcs: Evidence from the Cordillera Blanca, Peru. *Geology*, *26*(9), 827–830. https://doi.org/10.1130/0091-7613(1998)026<0827:ROPKAP>2.3.CO;2

Megard, F. (1984). The Andean orogenic period and its major structures in central and northern Peru. *Journal of the Geological Society*, *141*(5), 893–900. https://doi.org/10.1144/gsjgs.141.5.0893

Nachlas, W. O., Whitney, D. L., Teyssier, C., Bagley, B., & Mulch, A. (2014). Titanium concentration in quartz as a record of multiple deformation mechanisms in an extensional shear zone. *Geochemistry, Geophysics, Geosystems*, *15*(4), 4692–4711. https://doi.org/10.1002/2015GC005918.Received

Nachlas, W. O., Thomas, J. B., & Hirth, G. (2018). TitaniQ deformed: Experimental deformation of out-of-equilibrium quartz porphyroclasts. *Journal of Structural Geology, 116*(July), 207–222. https://doi.org/10.1016/j.jsg.2018.07.012

Oliot, E., Goncalves, P., Schulmann, K., Marquer, D., & Lexa, O. (2014). Mid-crustal shear zone formation in granitic rocks: Constraints from quantitative textural and crystallographic preferred orientations analyses. *Tectonophysics*, *612–613*, 63–80. https://doi.org/10.1016/j.tecto.2013.11.032

Passchier, C. W., & Trouw, R. a J. (2005). *Microtectonics*. https://doi.org/10.1007/3-540-29359-0

Paterson, M. S., & Luan, F. C. (1990). Quartzite rheology under geological conditions. *Geological Society Special Publications*, *54*(Deformation Mechanisms, Rheology and Tectonics), 299–307. Retrieved from http://citeseerx.ist.psu.edu/viewdoc/download?doi=10.1.1.826.9323&rep=rep1&type=pdf

Paterson, S. R., Vernon, R. H., & Tobisch, O. T. (1989). A review of criteria for the identification of magmatic and tectonic foliations in granitoids. *Journal of Structural Geology*, *11*(3), 349–363. https://doi.org/10.1016/0191-8141(89)90074-6

Petford, N., & Atherton, M. P. (1992). Granitoid emplacement and deformation along a major crustal lineament: The Cordillera Blanca, Peru. *Tectonophysics*, *205*(1–3), 171–185. https://doi.org/10.1016/0040-1951(92)90425-6

Petford, N., & Atherton, M. P. (1996). Na-rich Partial Melts from Newly Underplated Basaltic Crust: the Cordillera Blanca Batholith, Peru. *Journal of Petrology*, *37*(6), 1491–1521. https://doi.org/10.1093/petrology/37.6.1491

Platt, J. P. (2015). Rheology of two-phase systems: A microphysical and observational approach. *Journal of Structural Geology*, *77*, 213–227. https://doi.org/10.1016/j.jsg.2015.05.003

Platt, J. P., & Behr, W. M. (2011a). Grainsize evolution in ductile shear zones: Implications for strain localization and the strength of the lithosphere. *Journal of Structural Geology*, *33*(4), 537–550. https://doi.org/10.1016/j.jsg.2011.01.018

Platt, J. P., & Behr, W. M. (2011b). Lithospheric shear zones as constant stress experiments. *Geology*, *39*(2), 127–130. https://doi.org/10.1130/G31561.1

Pryer, L. L., & Robin, P. Y. F. (1996). Differential stress control on the growth and orientation of flame perthite: A palaeostress-direction indicator. *Journal of Structural Geology*, *18*(9), 1151–1166. https://doi.org/10.1016/0191-8141(96)00037-5

Pryer, Lynn L. (1993). Microstructures in feldspars from a major crustal thrust zone: The Grenville Front, Ontario, Canada. *Journal of Structural Geology*, *15*(1), 21–36. https://doi.org/10.1016/0191-8141(93)90076-M

Ramos, V. A. (1999). Plate tectonic setting of the Andean Cordillera. *Episodes*, *22*(3), 183–190.

Rolland, Y., & Rossi, M. (2016). Two-stage fluid flow and element transfers in shear zones during collision burial-exhumation cycle: Insights from the Mont Blanc Crystalline Massif (Western Alps). *Journal of Geodynamics, 101*, 88–108. https://doi.org/10.1016/j.jog.2016.03.016

Rolland, Y., Cox, S., Boullier, A.-M. M., Pennacchioni, G., & Mancktelow, N. S. (2003). Rare earth and trace element mobility in mid-crustal shear zones: insights from the Mont Blanc Massif (Western Alps). *Earth and Planetary Science Letters*, *214*(1–2), 203–219. https://doi.org/10.1016/S0012-821X(03)00372-8

Rosenberg, C. L., & Stünitz, H. (2003). Deformation and recrystallization of plagioclase along a temperature gradient: An example from the Bergell tonalite. *Journal of Structural Geology*, *25*(3), 389–408. https://doi.org/10.1016/S0191-8141(02)00036-6

Rutter, E. H. (1986). On the nomenclature of mode of failure transitions in rocks.

Tectonophysics, *122*(3–4), 381–387. https://doi.org/10.1016/0040-1951(86)90153-8

Rutter, E. H., & Brodie, K. H. (2004). Experimental intracrystalline plastic flow in hot-pressed synthetic quartzite prepared from Brazilian quartz crystals. *Journal of Structural Geology*, *26*(2), 259–270. https://doi.org/10.1016/S0191-8141(03)00096-8

Rybacki, E., & Dresen, G. (2000). Dislocation and diffusion creep of synthetic anorthite aggregates. *Journal of Geophysical Research: Solid Earth*, *105*(B11), 26017–26036. https://doi.org/10.1029/2000JB900223

Schmid, S. M., & Casey, M. (1986). Complete Fabric Analysis of some Commonly Observed Quartz C-axis Patterns. *Geophysical Monograph*, *36*, 263–286.

Scholz, C. H. (1988). The brittle-plastic transition and the depth of seismic faulting. *Geologische Rundschau*, *77*, 319–328. https://doi.org/10.1007/BF01848693

Schwartz, D. P. (1988). Paleoseismicty and Neotectonics of the Cordillera Blanca Fault Zone, Zorthern Peruvian Andes. *Journal of Geophysical Research*, *93*(B5), 4712–4730.

Shigematsu, N. (1999). Dynamic recrystallization in deformed plagioclase during progressive shear deformation. *Tectonophysics*, *305*(4), 437–452. https://doi.org/10.1016/S0040-1951(99)00039-6

Sibson, R. H. (1977). Fault rocks and fault mechanisms. *Journal of the Geological Society*, *133*(3), 191–213. https://doi.org/10.1144/gsjgs.133.3.0191

Simpson, C. (1985). Deformation of granitic rocks across the brittle-ductile transition. *Journal of Structural Geology*, *7*(5), 503–511.

Simpson, C., & Wintsch, R. P. (1989). Evidence for deformation-induced K-feldspar replacement by myrmekite. *Journal of Metamorphic Geology*, *7*(2), 261–275. https://doi.org/10.1111/j.1525-1314.1989.tb00588.x

Spear, F. S., & Wark, D. a. (2009). Cathodoluminescence imaging and titanium thermometry in metamorphic quartz. *Journal of Metamorphic Geology*, *27*(3), 187–205. https://doi.org/10.1111/j.1525-1314.2009.00813.x

Stipp, M., Stünitz, H., Heilbronner, R. P., & Schmid, S. M. (2002a). Dynamic recrystallization of quartz: correlation between natural and experimental conditions. *Geological Society, London, Special Publications*, *200*(1), 171–190. https://doi.org/10.1144/GSL.SP.2001.200.01.11

Stipp, M., Stünitz, H., Heilbronner, R. P., & Schmid, S. M. (2002b). The eastern Tonale fault zone: A “natural laboratory” for crystal plastic deformation of quartz over a temperature range from 250 to 700 °C. *Journal of Structural Geology*, *24*(12), 1861–1884. https://doi.org/10.1016/S0191-8141(02)00035-4

Stünitz, H., & Tullis, J. (2001). Weakening and strain localization produced by syn-deformational reaction of plagioclase. *International Journal of Earth Sciences*, *90*(1), 136–148. https://doi.org/10.1007/s005310000148

Stünitz, H., Fitz Gerald, J. D., & Tullis, J. (2003). Dislocation generation, slip systems, and dynamic recrystallization in experimentally deformed plagioclase single crystals. *Tectonophysics*, *372*(3–4), 215–233. https://doi.org/10.1016/S0040-1951(03)00241-5

Svava Olsen, T., & Kohlstedt, D. L. (1985). Natural deformation and recrystallization of some intermediate plagioclase feldspars. *Tectonophysics*, *111*(1–2), 107–131. https://doi.org/10.1016/0040-1951(85)90067-8

Thomas, J. B., & Watson, E. B. (2012). Application of the Ti-in-quartz thermobarometer to rutile-free systems. Reply to: A comment on: “TitaniQ under pressure: The effect of pressure and temperature on the solubility of Ti in quartz” by Thomas et al. *Contributions* *to Mineralogy and Petrology*, *164*(2), 369–374. https://doi.org/10.1007/s00410-012-0761-5

Thomas, J. B., Watson, E. B., Spear, F. S., Shemella, P. T., Nayak, S. K., & Lanzirotti, A. (2010). TitaniQ under pressure: The effect of pressure and temperature on the solubility of Ti in quartz. *Contributions to Mineralogy and Petrology*, *160*(5), 743–759. https://doi.org/10.1007/s00410-010-0505-3

Tokle, L., Hirth, G., & Behr, W. M. (2019). Flow laws and fabric transitions in wet quartzite. *Earth and Planetary Science Letters*, *505*, 152–161. https://doi.org/10.1016/j.epsl.2018.10.017

Tullis, J., & Yund, R. a. (1980). Hydrolytic weakening of experimentally deformed Westerly granite and Hale albite rock. *Journal of Structural Geology*, *2*(4), 439–451. https://doi.org/10.1016/0191-8141(80)90005-X

Tullis, J., & Yund, R. A. (1991). Diffusion creep in feldspar aggregates: experimental evidence. *Journal of Structural Geology*, *13*(9), 987–1000. https://doi.org/10.1016/0191-8141(91)90051-J

Twiss, R. J. (1977). Theory And Applicability Of A Recrystallized Grain-Size Paleopiezometer. *Pure And Applied Geophysics*, *115*(1–2), 227–244.

Urai, J. L., Means, W. D., & Lister, G. S. (1986). Dynamic Recrystallization of Minerals. *Geophysical Monograph*, *36*, 161–199.

Wark, D. a., & Watson, E. B. (2006). TitaniQ: A titanium-in-quartz geothermometer. *Contributions to Mineralogy and Petrology*, *152*(6), 743–754. https://doi.org/10.1007/s00410-006-0132-1

Wells, M. L., Beyene, M. a., Spell, T. L., Kula, J. L., Miller, D. M., & Zanetti, K. a. (2005). The

Pinto shear zone; a Laramide synconvergent extensional shear zone in the Mojave Desert region of the southwestern United States. *Journal of Structural Geology*, *27*(9), 1697–1720. https://doi.org/10.1016/j.jsg.2005.03.005

Whitmeyer, S. J., & Wintsch, R. P. (2005). Reaction localization and softening of texturally hardened mylonites in a reactivated fault zone, central Argentina. *Journal of Metamorphic Geology*, *23*(6), 411–424. https://doi.org/10.1111/j.1525-1314.2005.00588.x

Whitney, J. A., & Stormer, J. C. J. (1977). The distribution of NaAlSi3O8 between coexisting microcline and plagioclase and its effect on geothermometric calculations. *American Mineralogist*, *62*, 687–691.

Wilson, C. J. N., Seward, T. M., Allan, A. S. R., Charlier, B. L. a, & Bello, L. (2012). A comment on: "TitaniQ under pressure: The effect of pressure and temperature on the solubility of Ti in quartz", by Jay B. Thomas, E. Bruce Watson, Frank S. Spear, Philip T. Shemella, Saroj K. Nayak and Antonio Lanzirotti. *Contributions to Mineralogy and Petrology*, *164*(2), 359–368. https://doi.org/10.1007/s00410-012-0757-1

Wintsch, R. P., & Yeh, M. W. (2013). Oscillating brittle and viscous behavior through the earthquake cycle in the Red River Shear Zone: Monitoring flips between reaction and textural softening and hardening. *Tectonophysics*, *587*, 46–62. https://doi.org/10.1016/j.tecto.2012.09.019

Wintsch, R. P., Christoffersen, R., & Kronenberg, a. K. (1995). Fluid-rock reaction weakening of fault zones. *Journal of Geophysical Research*, *100*(B7), 13021. https://doi.org/10.1029/94JB02622

Xia, H., & Platt, J. P. (2018). Is the Vincent fault in southern California the Laramide subduction zone megathrust ?, (Xx), 1–17. https://doi.org/10.1130/B31870.1/4301894/b31870.pdf

Yund, R. a., & Tullis, J. (1991). Compositional changes of minerals associated with dynamic recrystallizatin. *Contributions to Mineralogy and Petrology*, *108*(3), 346–355. https://doi.org/10.1007/BF00285942

CHAPTER I

DEFORMATION CONDITIONS DURING SYN-CONVERGENT EXTENSION ALONG THE CORDILLERA BLANCA SHEAR ZONE, PERU

A version of this chapter by Cameron A. Hughes, Micah J. Jessup, Colin A. Shaw, and Dennis L. Newell has been published in *Geosphere*:

Cameron A. Hughes, Micah J. Jessup, Colin A. Shaw, Dennis L. Newell: "Deformation conditions during syn-convergent extension along the Cordillera Blanca Shear Zone (CBSZ), Peru." *Geosphere, 2019.*

My major contributions to this manuscript include: 1) field work to collect samples, 2) preparing and cutting rocks for thin sections, 3) writing and receiving Sigma Xi Grants-in-Aid of Research funding for Titanium-in-Quartz analysis 4) conducting petrographic, electron microprobe, and electron backscatter diffraction analysis; 5) calculating deformation temperature, differential stress, and strain rate; 6) writing the manuscript, 7) creating most of the figures for this manuscript, 8) submitting the manuscript for publication, and 9) revising the manuscript.

Abstract

Strain localization across the brittle-ductile transition is a fundamental process in accommodating tectonic movement in the mid-crust. The tectonically active Cordillera Blanca Shear Zone (CBSZ), a ~200-km-long normal-sense shear zone situated within the footwall of a discrete syn-convergent extensional fault in the Peruvian Andes, is an excellent field laboratory to explore this transition. Field and microscopic observations indicate consistent top-down-to-the-southwest sense of shear and a sequence of tectonites ranging from undeformed granodiorite through mylonite and ultimately fault breccia along the detachment.

Using microstructural analysis, two-feldspar and Ti-in-quartz thermometry (TitaniQ), recrystallized quartz paleopiezometry, and analysis of quartz crystallographic preferred orientations (CPOs), we evaluate the deformation conditions and mechanisms in quartz and feldspar across the CBSZ. Deformation temperatures derived from asymmetric strain-induced myrmekite in a subset of tectonite samples are 410 ± 30° to 470 ± 36 °C, consistent with TitaniQ temperatures of 450 ± 60° to 490 ± 33 °C and temperatures above 400 °C estimated from microstructural criteria. Brittle fabrics overprint ductile fabrics within ~150 m of the detachment that indicate that deformation continued to lower temperature (~280 - 400 °C) and/or higher strain-rate conditions prior to the onset of pervasive brittle deformation. Initial deformation occurred via high-temperature fracturing and dissolution-precipitation in feldspar. Continued subsolidus deformation resulted in either layering of mylonites into monophase quartz and fine-grained polyphase domains or the interconnection of recrystallized quartz networks oriented obliquely to macroscopic foliation. The transition to quartz-controlled rheology occurred at temperatures near ~500 °C and at a differential stress of ~16.5 MPa. Deformation within the

CBSZ occurred predominantly above ~400 °C and at stresses up to ~71.4 MPa prior to the onset of brittle deformation.

Introduction

One of the most important long-standing problems in tectonics is the localization of strain during the transition from ductile to brittle deformation in the lithosphere (Kirby, 1983; Carter and Tsenn, 1987; Rutter et al., 2001b; Platt and Behr, 2011a; Sullivan et al., 2013; Spruzeniece and Piazolo, 2015). Deformation mechanisms and relative roles of temperature, strain rate, and fluids in localizing strain can vary widely along the brittle-ductile-transition (BDT). Crustal-scale shear zones are ideal settings for quantifying deformation conditions and discerning the mechanisms facilitating strain localization along the (BDT). However, many such examples have protracted and complicated histories making it difficult to discriminate the relative timing of ductile and brittle behavior (Singleton and Mosher, 2012; Cooper et al., 2017). As crustal strength along the BDT is contingent upon lithology and tectonic regime (Sibson, 1983; Carter and Tsenn, 1987), it is important to describe naturally occurring deformation in a range of geologic environments. Although previous work on crustal-scale shear zones near the BDT in granitoids is extensive (Simpson, 1985; Fitz Gerald and Stünitz, 1993; Stünitz and Fitz Gerald, 1993; Tsurumi et al., 2002; Ree et al., 2005; Pennacchioni et al., 2006; Behr and Platt, 2011; Zibra et al., 2012; Singleton and Mosher, 2012; Wintsch and Yeh, 2013; Sullivan et al., 2013; Columbu et al., 2015; Spruzeniece and Piazolo, 2015; Wehrens et al., 2016a), studies of young and/or currently active extensional shear zones are less common (Bessiere et al., 2018).

Rock strength along the BDT can be affected by variables that influence brittle deformation, including fluid pressure, strain rate, effective pressure, and mineralization along failure surfaces (Byerlee, 1978; Brace and Kohlstedt, 1980; Carter and Tsenn, 1987), and those that influence ductile deformation, such as temperature, activity of water (Kirby, 1980; Tullis and Yund, 1980; Yund and Tullis, 1980), interconnectedness of minerals (Wintsch and Yeh, 2013), differential stress, lithology, deformation mechanism, and preferred mineral orientations (Rutter, 1986; Carter and Tsenn, 1987; Behr and Platt, 2011; Platt and Behr, 2011b; Cooper et al., 2017). Experimental studies have delimited many of these factors (Tullis and Yund, 1991, 1987, 1980a; Hirth and Tullis, 1992, 1994; Heilbronner and Tullis, 2006; Stünitz and Tullis, 2001; Holyoke and Tullis, 2006; Holyoke and Kronenberg, 2010; Stipp, 2003), providing a framework for studying "natural laboratories" (e.g. Lloyd et al., 1992; Hirth et al., 2001a; Stipp et al., 2002a, 2002b; Wells et al., 2005; Behr and Platt, 2011, 2014; Gottardi fand Teyssier, 2013; Sullivan et al., 2013; Spruzeniece and Piazolo, 2015; Viegas et al., 2016; Rahl and Skemer, 2016).

The tectonically active Cordillera Blanca shear zone (CBSZ), a ~200-km-long normal-sense shear zone in the Peruvian Andes, occurs almost entirely in the granodioritic Cordillera Blanca Batholith (Atherton and Sanderson, 1987; Petford and Atherton, 1992; McNulty et al., 1998), which was emplaced at 14-5 Ma (U-Pb zircon, Mukasa, 1984; McNulty et al., 1998; Giovanni, 2007). This granodiorite is the predominant lithology in the exhumed footwall of the Cordillera Blanca detachment normal fault, which is the expression of the upper, brittle portion of the CBSZ and has been active since ~5 Ma (Bonnot, 1984; Giovanni, 2007). Tectonic fabrics progress from undeformed granodiorite in the core of the batholith in the east, through mylonites and ultramylonites towards the west, culminating in cataclasite and breccia along the detachment surface. The CBSZ is an excellent case study of the BDT, as the relatively simple deformation history and consistent lithology facilitate comparison of fabrics, deformation mechanisms, and deformation conditions at different structural levels across the BDT.

We present new data characterizing mid-crustal deformation within the CBSZ including deformation temperatures of quartz and feldspar, quartz crystallographic preferred orientations (CPOs), flow stress, and microstructural relationships relating to changing deformation mechanisms. Previous work describes the transition from magmatic to subsolidus tectonic fabrics in the CBSZ (Petford and Atherton, 1992), but no constraints on ductile deformation conditions are presently available. An additional motivation for this study is to offer the first quantitative constraints on ductile to brittle deformation conditions within the CBSZ and evaluate the deformation mechanisms that facilitate the fabric transition described by Petford and Atherton (1992). In this study, we present data supporting early deformation by high-temperature fracturing in a feldspar-controlled framework followed by predominantly quartz-controlled rheology, with at least local polyphase-controlled rheology within layered mylonites. Our results indicate that deformation during exhumation produced overprinting fabrics reflecting changes in deformation mechanism and an increase in strain rate. Strain localized from a ~450 m thick plastic shear zone to a ~150 m thick brittle fault zone along a discrete detachment fault.

Geologic Background and Sample Descriptions

Subduction along the Andean margin of South America began by at least the Jurassic and cycled between steep- and shallow-to-flat-slab subduction until its present configuration (James, 1971; Jordan et al., 1983; Ramos, 1999). The Cordillera Blanca range is situated above the Peruvian flat-slab segment of the present margin (Gutscher, Olivet, et al., 1999; McNulty and Farber, 2002), within the central-eastern Cordillera Occidental along the western margin of the Marañón fold and thrust belt (Fig. 1.1). West of the Cordillera Blanca lies the Cordillera Negra, a 54-15 Ma volcanic arc related to normal subduction along the Peru-Chile trench (Petford and Atherton, 1992; Scherrenberg et al., 2014, 2016). Beginning at ~15 Ma, magmatism migrated eastward, culminating in the intrusion and crystallization of the Cordillera Blanca batholith from 13.7 ± 0.3 Ma to 5.3 Ma ± 0.3 Ma (U-Pb zircon, Mukasa, 1984; Giovanni, 2007) and eruption of the associated Yungay and Fosrtaleza ignimbrites between 8.7 ± 1.6 and 4.5 ± 0.2 Ma (40Ar/39Ar biotite, Bonnot, 1984; Giovanni et al., 2010) and 6.2 ± 0.2 and 4.9 ± 0.2 Ma, respectively (K-Ar biotite, Wilson, 1975; Cobbing et al., 1981). These events mark the last episode of arc magmatism in this region (Cobbing et al., 1981; Bonnot, 1984; Mukasa, 1984; Petford and Atherton, 1996; McNulty et al., 1998; McNulty and Farber, 2002; Giovanni, 2007; Giovanni et al., 2010). Crustal shortening associated with convergence of the South American and Nazca plates also migrated inboard, east of the Marañon massif, to the present Subandean fold and thrust belt (Fig. 1.1).

The Cordillera Blanca range is cored by the granodiorite-leucogranodiorite Cordillera Blanca batholith (Atherton and Sanderson, 1987; Petford and Atherton, 1992). Batholith

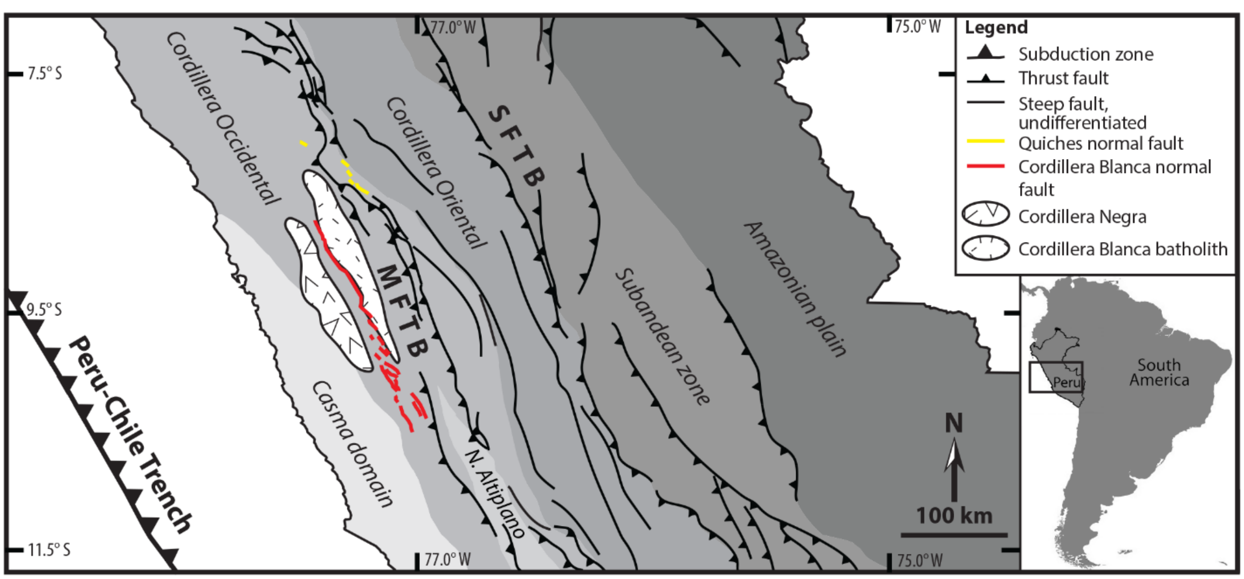

Fig. 1.1. Tectono-physiographic map of Central Peru, after Pfiffner and Gonzalez (2013). MFTB: Marañon fold and thrust belt; SFTB: Subandean fold and thrust belt. Inset shows location of tectono-physiographic map with respect to South America.

emplacement is estimated at ~300 MPa (McNulty and Farber, 2002) and >200 MPa (Petford and Atherton, 1992) from mineral assemblages in the pelitic contact aureole, and at 90 ± 10 MPa to 260 ± 30 MPa at 720-800 °C from recent amphibole thermobarometry of batholith rocks (Margirier et al., 2016). The batholith cooled rapidly at 200 °C/m.y. until ~4 Ma and subsequently cooled at 25 °C/m.y. from 4-0 Ma (Margirier et al., 2015). Extension along the CBD fault initiated at ~5 Ma (Bonnot, 1984; Giovanni, 2007), accommodating 12-15 km of normal-sense displacement (Giovanni et al., 2010). A series of glacially and fluvially incised ravines (quebradas) cut across the Cordillera Blanca nearly orthogonal to strike of the range (Wise and Noble, 2003), providing exposure of the full ductile- to brittle-fabric gradient developed in the CBSZ (Fig. 1.2). Fault scarps along the detachment truncate glacial moraines, offsetting moraine crests by ~2 to 70 m (Bonnot et al., 1988; Schwartz, 1988a; Siame et al., 2006). The most recent faulting is bracketed by detrital charcoal in colluvium between 2440 ± 1060 and 750 ± 80 ^{14}C years B.P, and by positioning of pre-Incan structures relative to fault scarps at 1500-2000 years B.P. (Schwartz, 1988a). The hanging wall comprises Jurassic to Cretaceous sediments, Eocene-Pliocene volcanics, and Miocene-Pliocene sediments of the Lloclla Formation (Cobbing et al., 1981; Petford and Atherton, 1992; Giovanni et al., 2010; Margirier et al., 2015). Hot springs issue along the main detachment system and along steeply dipping faults and inferred synthetic faults proximal to the shear zone (Newell et al., 2015).

We present data from samples collected in Quebrada Gatay (Fig. 1.2) and describe CBSZ deformation relative to structural depths below the exposed detachment surface. Q. Gatay samples (Appendix I, Table S1) were collected across the ductile to brittle fabric transition and are mostly leucogranodiorite, with a small number from quartz veins oriented parallel to foliation and phyllites from a lens of the Jurassic Chicama Formation host rock. Supplemental information

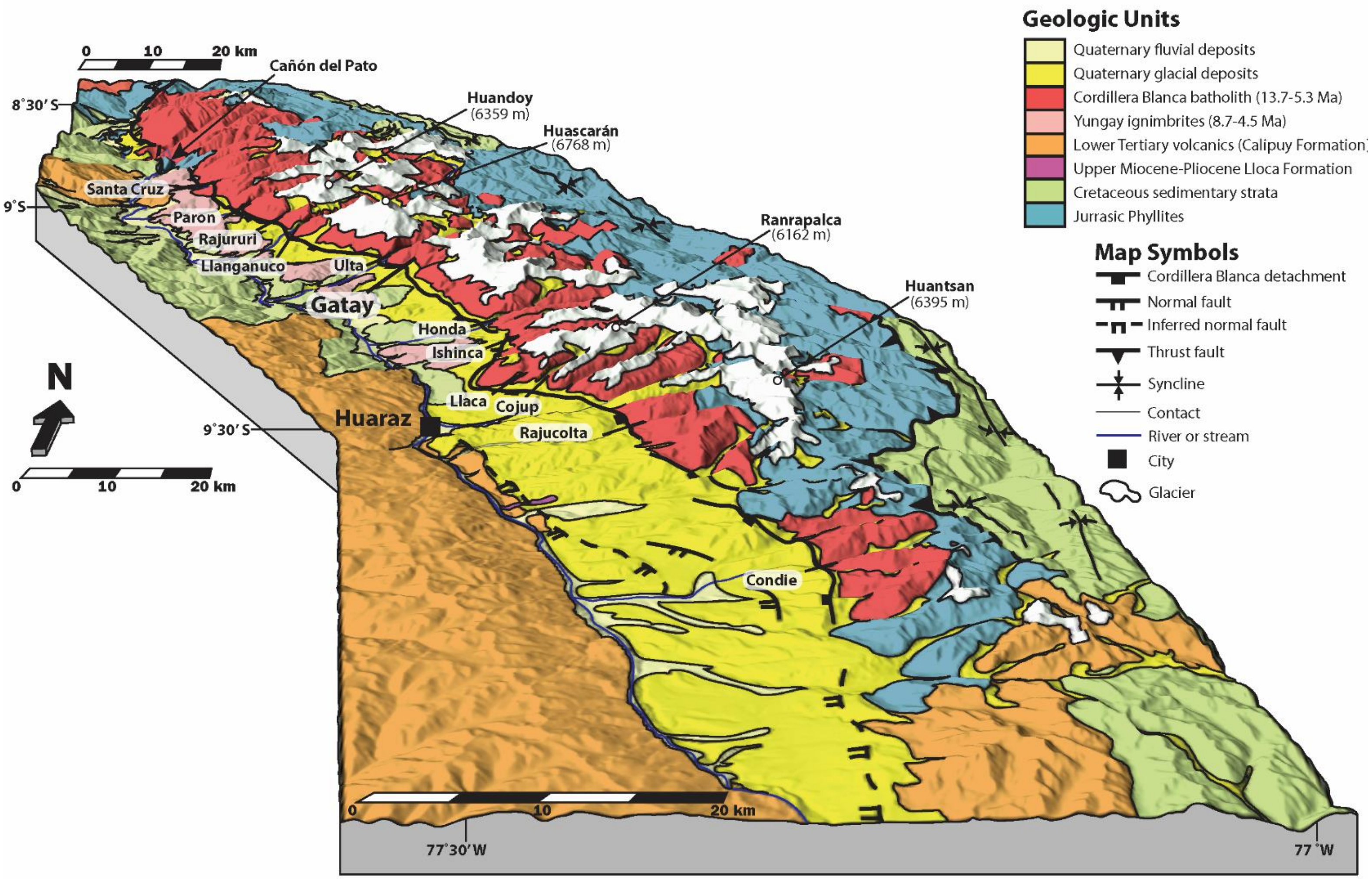

Fig. 1.2. 3D digital elevation model, derived from 90m Shuttle Radar Topography Mission data obtained from http://www.viewfinderpanoramas.org/dem3.html, with overlain geologic map (Giovanni, et al., 2010) of the Cordillera Blanca. Quebradas (ravines) labeled along west side of range. The ~200-km-long CBD forms the upper boundary of the Cordillera Blanca Shear Zone.

is available in Tables S1-S2, Figs. S1-S2, and Text S1-S3 at https://doi.org /10.1130 /GES02040.S1 and in Appendix I.

Methods

Thirty-two samples were collected from Quebrada Gatay in July 2013 and were cut into thin sections perpendicular to foliation and parallel to lineation (X-Z sections). We used optical petrography, electron backscatter diffraction (EBSD) analysis, and electron probe microanalyzer (EPMA) analysis to evaluate microstructures, quartz crystallographic preferred orientations, deformation temperature, and flow stress across the fabric progression from undeformed granite to ultramylonite and cataclasite.

Deformation Temperatures

Two-feldspar Geothermometry

Deformation temperatures were estimated for samples with asymmetric strain-induced myrmekite (ASIM) using two-feldspar thermometry of co-existing feldspars within the symplectite (Simpson and Wintsch, 1989; Langille et al., 2010). ASIM develops when aqueous Na^+ is concentrated at high-stress sites along K-feldspar grain boundaries (Fig. 1.3A; Simpson and Wintsch, 1989). High strain facilitates the reaction (Simpson and Wintsch, 1989; Tsurumi et al., 2002; Menegon et al., 2008):

K-feldspar + Na^+ → Na-feldspar + quartz + K^+. (1)

The resulting ASIM microstructure comprises a K-feldspar porphyroclast impinged by asymmetrically distributed albite-oligoclase lobes that grow parallel to the maximum incremental shortening axis and contain vermicular quartz. K-feldspar recrystallizes as tails in low-strain sites (Fig. 1.3A; Simpson and Wintsch, 1989).

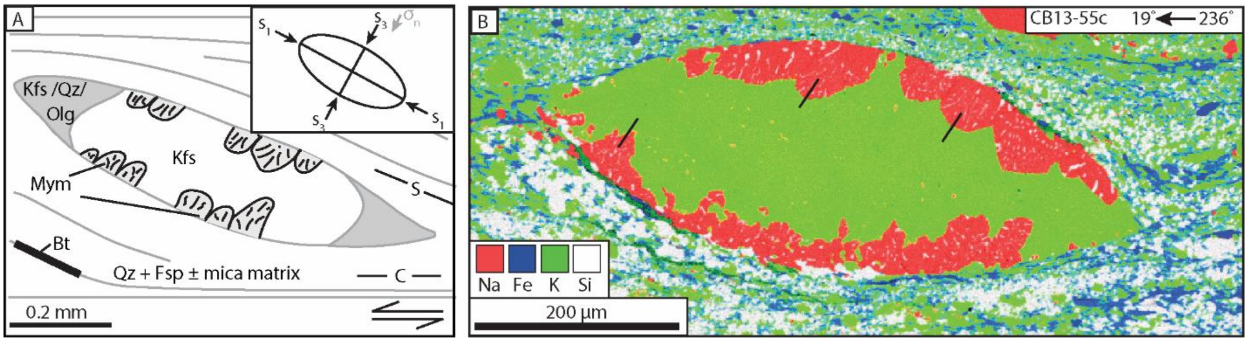

Fig. 1.3. Asymmetric strain-induced myrmekite. A) Schematic diagram of strain-induced myrmekite (after Simpson & Wintsch, 1989). Inset shows the principal strain ellipse. Orientation of normal stress (σn) relative to myrmekite from Simpson and Wintsch (1989). Bt—biotite Kfs—potassium feldspar, Mym—myrmekite, Olg—oligoclase, Qtz—quartz. Albite-oligoclase myrmekite lobes grow towards center of host porphyroclast. Lobes are concentrated at high-strain sites, shown relative to S-C mylonitic fabric. B) X-ray compositional map of major element compositions of asymmetric strain-induced myrmekite microstructure. Surrounding matrix is recrystallized quartz (white), biotite (blue) and K-feldspar (green). Black lines denote locations of spot analysis transects for use in thermometry calculations. Arrow notation indicates trend and plunge of lineation, with arrow pointing down-plunge.

We derive ASIM deformation temperatures using chemical compositions from along the interface of the K-feldspar porphyroclast and the Na-feldspar myrmekitic lobe (Fig. 1.3B; Langille et al., 2010). Mineral compositions were obtained using the Cameca SX-100 EPMA at the University of Tennessee-Knoxville (UTK; Knoxville, Tennessee, USA) by spot analysis at 15 keV, 10 nA, 5 µm spot size, and 30 s counting time). X-ray maps (Na, K, Si, and Fe) were made at 15 keV, 20 nA, 50 ms dwell time, and 1 µm spot size to evaluate compositional zoning in porphyroclasts and myrmekite lobes and to characterize matrix phases. Multiple lobes from individual ASIM-bearing porphyroclasts were analyzed to determine the average deformation temperature. Temperatures were calculated using the 2-feldspar thermometer (Stormer, 1975; Whitney and Stormer, 1977)

$$T\ (K) = \frac{\{7973.1-16910.6X_{ab,AF}+9901.9X_{ab,AF}^2+\left(0.11-0.22X_{ab,AF}+0.11X_{ab,AF}^2\right)(10P)\}}{\left\{-19872ln\left(\frac{X_{ab,AF}}{\alpha_{ab,PL}}\right)+6.48-21.58X_{ab,AF}+23.72X_{ab,AF}^2-8.62X_{ab,AF}^3\right\}}, (2)$$

where $X_{ab,\,AF}$ is normalized molar concentration of albite in alkali feldspar, P is pressure (MPa), and $\alpha_{ab, PL}$ is the activity of albite in plagioclase. Because shear sense from ASIM is consistent with shear sense from other indicators, temperatures derived from ASIM are assumed to be deformation temperatures (Simpson and Wintsch, 1989; Langille et al., 2010). Temperatures were calculated at 100 MPa and 300 MPa pressures and are presented here calculated at 300 MPa with errors of the 2σ standard deviation of feldspar compositions propagated through the thermometer. Reported temperatures and errors do not include the ± 50 °C error from the thermometer. Mineral compositions used for thermometry calculations are reported in Table S2.

Titanium-in-Quartz (TitaniQ) Geothermometry

TitaniQ thermometry utilizes the log-linear relationship between increasing Ti concentration in quartz with increasing temperature (Wark and Watson, 2006). Established as a reliable thermometer in igneous and volcanic systems when pressure and Ti activity (α_{TiO_2}) are constrained, TitaniQ has also been increasingly used in greenschist facies shear zones to determine deformation conditions (e.g. Kidder et al., 2013). Some debate occurs regarding the reliability of TitaniQ in different dynamic recrystallization regimes though there is general agreement that TitaniQ is reliable under conditions required for grain-boundary migration (GBM) recrystallization (Thomas et al., 2010; Behr et al., 2011; Grujic et al., 2011; Thomas and Watson, 2012; Kidder et al., 2013; Nachlas et al., 2014; Cross et al., 2015) Recent experimental evidence suggests that Ti concentrations are efficiently re-equilibrated during recrystallization by grain boundary formation and migration (Nachlas et al., 2018). Because high temperature and/or low-strain rate conditions tend towards preserving Ti concentrations on the order of 10-100 ppm, concentrations can be determined on an electron microprobe for quartz exhibiting GBM (high temperature and/or low-strain rate) recrystallization microstructures (Behr et al., 2011; Grujic et al., 2011; Nachlas et al., 2014, 2018). Samples without GBM recrystallization microstructures were not considered for analysis in this study due to the likelihood that Ti concentrations would be below the detection limit of the EPMA at UTK, or otherwise may be preserving inherited Ti concentrations from higher temperature deformation (i.e. Grujic et al., 2011). Although Nachlas et al. (2018) suggest that Ti should be re-equilibrated for recrystallized quartz even at low temperatures, resolving possible inherited concentrations vs. recrystallized Ti concentrations would require higher precision instrumentation.

Cathodoluminescence (CL) imaging was conducted prior to EPMA analyses. CL imaging details and EPMA conditions for TitaniQ analyses are provided in Text S1 (Appendix I). Temperatures were calculated using the thermobarometer of Thomas et al. (2010).

$$T\ (°C) = \frac{60952\ +1741(P/100)}{1.520 - R \times lnX_{TiO_2}^{Qtz} + R \times ln\alpha_{TiO_2}} - 273.15 \quad (3)$$

where P is pressure (MPa), R is the gas constant, $X_{TiO_2}^{Qtz}$ is the concentration of Ti in quartz (ppm) and a_{TiO_2} is the TiO_2 activity, and the thermobarometer of Huang and Audétat, (2012)

$$logTi(ppm) = -0.27943 \times \frac{10^4}{T} - 660.53 \times \left(\frac{(P/100)^{0.35}}{T}\right) + 5.6459, \quad (4)$$

where T is temperature (Kelvin) and P is pressure (MPa). TiO_2 activity for silicic igneous rocks can be difficult to constrain (Huang and Audétat, 2012), although for most igneous and metamorphic rocks α_{TiO_2} is above ~0.5, and in silicic melts is typically above ~0.6 (Hayden and Watson, 2007). Activity can by further constrained by presence of ilmenite or titanite (α_{TiO2} 0.7-0.8) (Ghent and Stout, 1984; Peterman and Grove, 2010; Cross et al., 2015)

Quartz Crystallographic Preferred Orientations

Quartz crystallographic preferred orientations (CPOs) were obtained using EBSD on the field emission gun-scanning electron microscope at the Imaging and Chemical Analysis Laboratory (ICAL) at Montana State University (Bozeman, Montana, USA). Analyses were conducted at 20 Pa and 20-30 kV, and Kikuchi band diffraction patterns were collected for quartz for 75 reflectors using Oxford Instruments HKL Channel 5 Flamenco software (ver. 5.5). Step sizes ranged from 1.5 to 5 μm depending on minimum grain size observed under petrographic microscope. Pole figures of quartz c- and a-axes orientations were constructed using the MTEX toolbox (Bachmann et al., 2010) for MATLAB. Details on raw EBSD data processing are provided in supplemental Text S2 (Appendix I). EBSD was applied to 8 representative samples in interconnected quartz-rich domains as far away from other phases as possible to minimize potential affects from pinning. CPO pole figures are lower hemisphere projections of c- and a-axes using one point per grain, where grains are defined using at least 8 pixels and a critical misorientation of 10°, contoured at 7.5° half-width (see Text S2, Appendix I). Fabric strength was evaluated using the M-index of Skemer et al., (2005) and the J-index of (Bunge, 1982).

Flow Stress

Differential stresses were estimated using recrystallized grain size piezometry, where differential stress and recrystallized grain size are inversely related by the following expression (Twiss, 1977; Stipp and Tullis, 2003)

$d = \beta\sigma^m$. (5)

Differential stresses were calculated using the piezometer calibration of Stipp and Tullis (2003), modified after Holyoke and Kronenberg (2010), where d is the root mean square (RMS) of the grain size distribution, β is an empirically derived constant (3640 μm/MPa^m), m is an experimentally derived stress exponent (-1.26), and σ is differential stress. These values were compared to the recent "sliding-resolution" piezometer calibration for EBSD-derived grain sizes, where β and m are $10^{4.22 \pm 0.51}$ and -1.59 ± 0.26, respectively (Cross et al., 2017). Grain size distributions (Fig. S1, Appendix I) were derived from EBSD analysis on representative quartz-rich domains from mylonitic granodiorite and mylonitic quartz veins, where grain size was defined as the diameter of an equivalent area circle. Errors on differential stress estimates are the standard deviation relative to RMS for the grain size distribution propagated through the piezometer.

Results

Mesoscale Observations

Mean foliation from Quebrada Gatay strikes 167°± 5° and dips 23° ± 5°, and mean stretching lineation trends toward 239° ± 6°, plunging 24° ± 6° (Fig. 1.4A). The detachment surface exposed at Q. Gatay (Fig. 1.4A) strikes approximately 150° and dips ~26° based on a series of three-point problems solved using Google Earth. Data from structural positions between 150 and 300 m below the detachment are sparse due to steep terrain and vegetative cover. An injection complex of leucogranodiorite veins intrudes into a host rock (shale) lens 130-150 m below the detachment surface (Fig. 1.4B). Localized zones of mylonite to ultramylonite from 5 to 50 cm thick occur at structural positions as deep as 385 m below the detachment within otherwise undeformed to protomylonitic granite (Fig. 1.4C). Quartz veins 10 to 60 cm thick occur parallel and subparallel to foliation throughout the shear zone (Fig. 1.4D). A progression in fabric from undeformed granodiorite to ultramylonite with consistent SSW-dipping foliation is observed (Fig. 1.4E) and is the basis for interpretations of deformation mechanisms and conditions during shear zone evolution.

Microstructural Observations

Observed microstructures can be divided based on interconnected phases into feldspar,

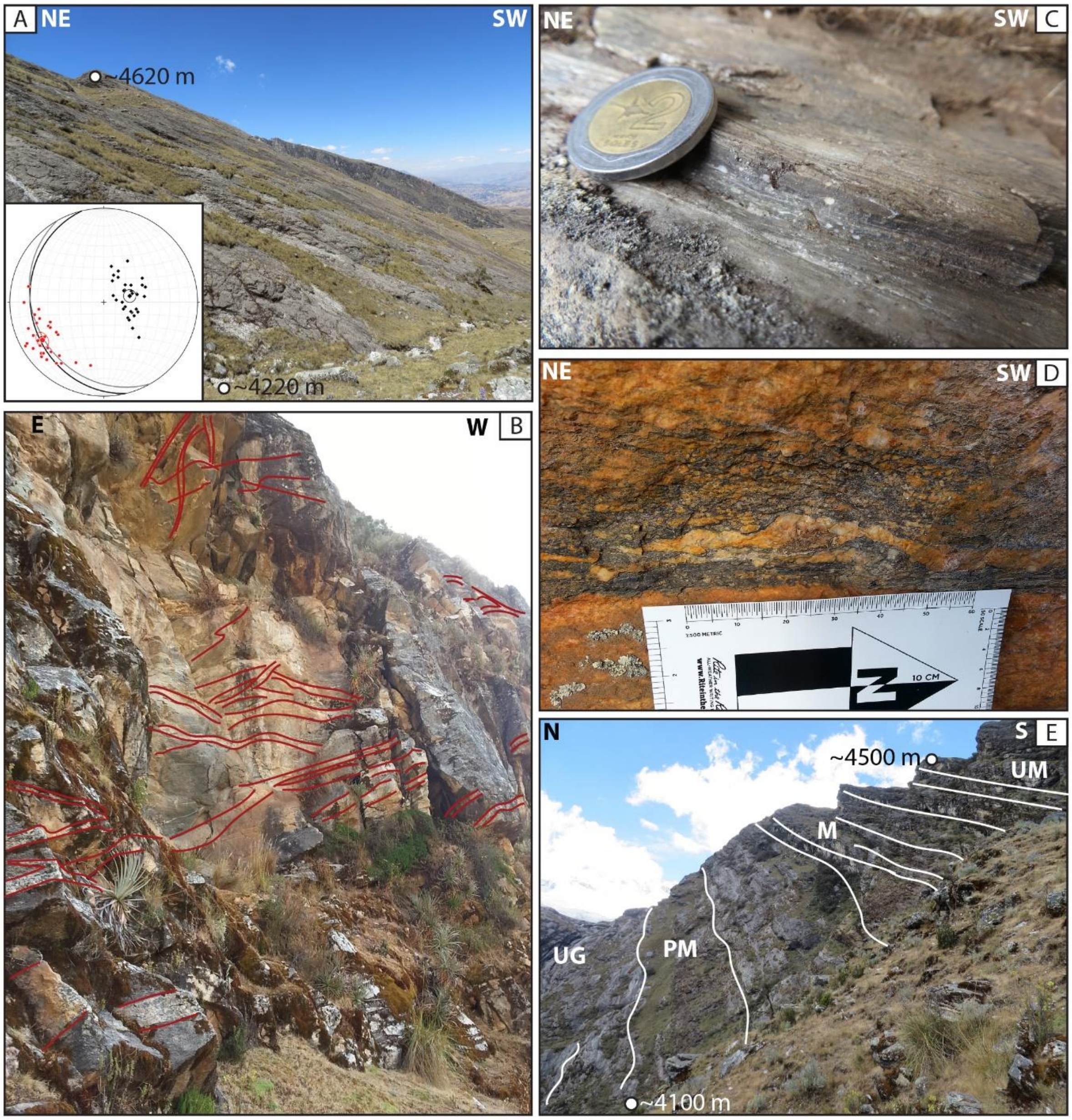

Fig. 1.4. Field photos from the south side of Quebrada Gatay. A) Detachment surface on the south side of Quebrada Gatay, looking to the southeast. Inset: stereonet of poles to foliation (black diamonds, N=33), mean foliation plane (black great circle) stretching lineations (red circles, N = 33), and mean detachment surface derived from Google Earth (grey great circle). Large symbols are Fisher mean vectors with 95% confidence intervals. B) Injection complex of leucogranodioritic veins into lens of Jurrasic Chicama Formation shale. Outcrop view is ~8 m tall. C) Ultramylonitic foliation with feldspar sigma clasts indicating dextral (top-to-SW) shear and asymmetric folding. Peruvian two-sol piece (appx. 2.4 cm diameter) for scale. D) Biotite-rich domain above a foliation-parallel quartz vein. E) Pervasive SW-dipping foliation across the Cordillera Blanca shear zone. White circles mark elevation. UG: undeformed granite; PM: protomylonite; M: mylonite; UM: ultramylonite.

quartz, mica, and polyphase domains. These domains are spatially variable such that rheological framework may be controlled by either quartz, feldspar, mica, or a combination thereof.

Feldspar

Within ~150 m of the detachment, through-going features such as fractures, microfaults, and cataclasite cut across feldspar and adjacent phases (Fig. 1.5A, Table 1.1). At structurally high positions, feldspar porphyroclasts are commonly fractured and filled with quartz and/or K-feldspar. These fractures tend to be isolated to feldspar porphyroclasts and do not extend into surrounding phases. Some feldspar fragments are rotated with respect to the other fragment(s) within the original porphyroclast, forming V-shaped pull apart structures (Fig. 1.5B; i.e. Fukuda et al., 2012; Hippertt, 1993; Samanta et al., 2002). Undulose extinction and deformation lamellae are common within plagioclase porphyroclasts.

Fine-grained feldspar aggregates occur in layered mylonitic to ultramylonitic samples at structural depths from 430 to 111 m. Finely recrystallized grains mantle porphyroclasts and form tails on σ- and δ- type feldspar porphyroclasts that deflect into quartz + feldspar shear bands (Fig. 1.5C). Within these samples, myrmekite commonly has formed along high-strain sites of K-feldspar porphyroclasts as well as within fine-grained plagioclase-K-feldspar aggregates (Fig. 1.5D).

Interconnected networks of feldpsar porphyroclasts or phenocrysts occur below 350 m. At 350 m, mylonitic samples contain interconnected plagioclase phenocrysts that exhibit bulging recrystallization at feldspar-feldspar grain boundaries (Fig. 1.5E) and contain biotite at triple junctions (Fig. 1.5F). Biotite also occurs in low-strain sites of boudinaged plagioclase where interconnected quartz and interconnected feldspar coincide. Plagioclase boudins are relatively symmetrical, tapered yet connected, and have concave-faced boundaries (Fig. 1.5G). Weakly

Fig. 1.5. Representative images of feldspar microstructures. Images are cross-polarized light (XPL) photomicrographs unless otherwise noted. Labels denote trend and plunge of lineation, with arrow pointing down-plunge, and structural depth below the Cordillera Blanca detachment (in meters); arrowhead indicators specified below as (color). Pl: plagioclase, Bt— biotite, Qz—Quartz, Fsp— feldspar (undifferentiated), Kfs— K-feldspar, Mym—myrmekite Wm: white mica. A) Cataclasite including internally deformed plagioclase clasts (white) and dynamically recrystallized quartz (red) in biotite-rich (left) and biotite-poor (right) quartz-feldspar matrix. B) Fractured plagioclase phenocrysts with small offset (red) and V-pull apart structure with quartz infill (yellow). Patchy extinction is present near offset fracture (white). C) Dynamically recrystallized plagioclase (red), creating a core-mantle structure. Recrystallized feldspar tail deflects into quartz-rich shear band; grain size of quartz and plagioclase decreases with deflection into shear band (yellow). Subgrain rotation (SGR) and grain-boundary migration (GBM) recrystallization microstructures are present in adjacent quartz domain. D) Interconnected domain of recrystallized plagioclase and K-feldspar (white) adjacent to quartz domain exhibiting GBM recrystallization microstructure. K-feldspar porphyroclasts contain recrystallized tails and asymmetric strain-induced myrmekite (red). Myrmekite also present in recrystallized plagioclase + K-feldspar matrix (yellow). E) New grains formed by bulging recrystallization (BLG) in plagioclase (red) F) BSE Image of interconnected plagioclase domain, biotite and quartz along triple junctions (red). Biotite occupies grain boundaries between plagioclase phenocrysts (yellow). K-feldspar hosted as inclusions within phenocrysts and as fracture fill (white). G) BSE image of boudinaged plagioclase within quartz matrix (red). Biotite and quartz occupy dilatant sites in pinch-and-swell structure (yellow). H) Wedge-shaped K-feldspar fracture filled with quartz exhibiting chessboard extinction (CB) that is continuous crystallographically with quartz within plagioclase fracture (yellow). Image rotated 90 degrees counter-clockwise from X-Z orientation. I) Recrystallized plagioclase along K-feldspar grain boundaries and fractures (red). GBM is present in interstitial quartz. J) Myrmekite growth into K-feldspar, with white mica along initial Kfs grain boundary

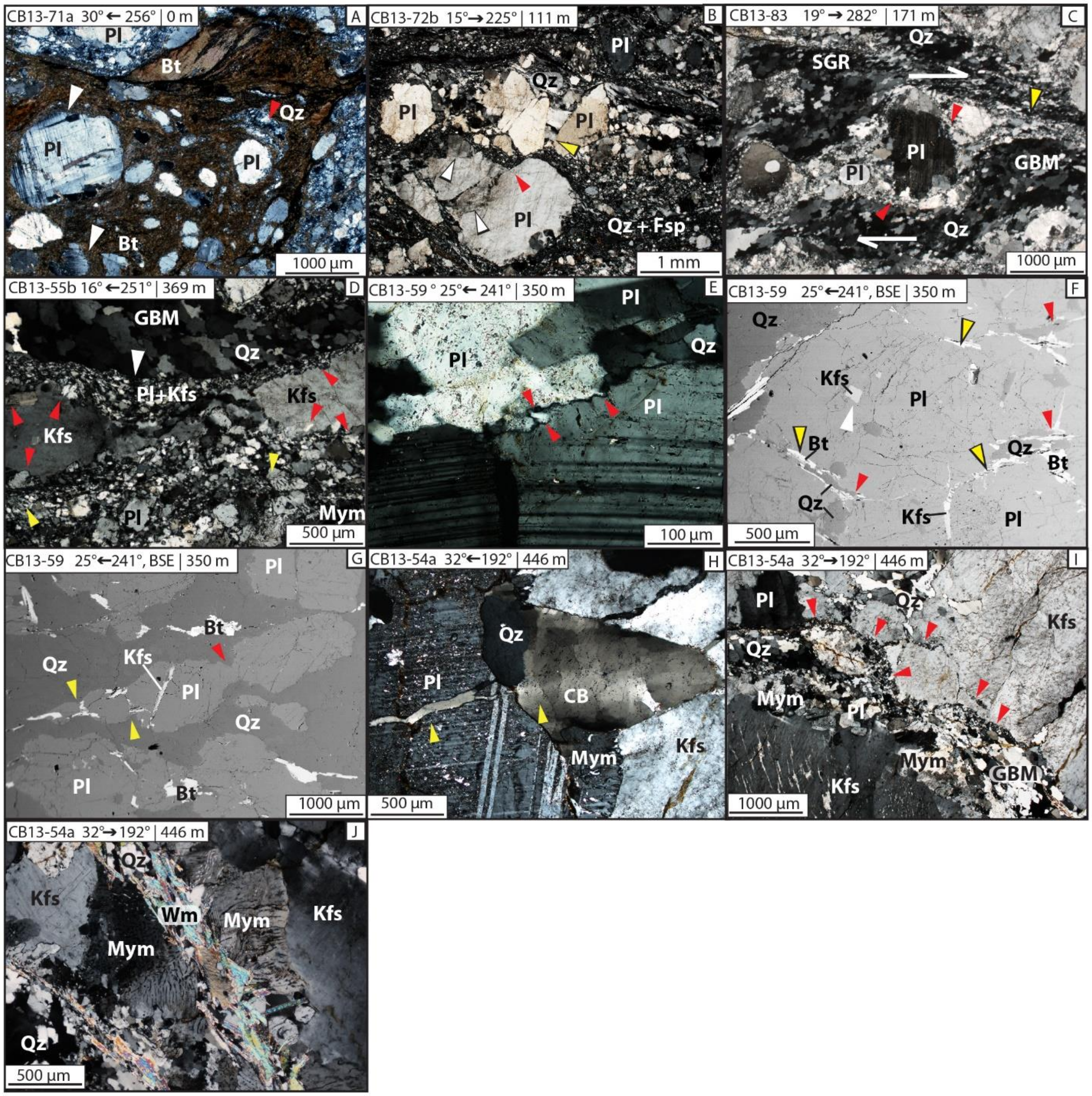
CB13-71a 30° ← 256° | 0 m
A
Pl
Bt
Qz
Pl
Pl
Bt
1000 µm
CB13-72b 15° → 225° | 111 m
B
Pl
Qz
Pl
Pl
Pl
Qz + Fsp
1 mm
CB13-83 19° → 282° | 171 m
C
Qz
SGR
Pl
Pl
GBM
Qz
1000 µm
CB13-55b 16° ← 251° | 369 m
D
GBM
Qz
Pl+Kfs
Kfs
Kfs
Pl
Mym
500 µm
CB13-59 ° 25° ← 241° | 350 m
E
Pl
Pl
Qz
Pl
100 µm
CB13-59 25° ← 241°, BSE | 350 m
F
Qz
Kfs
Pl
Bt
Qz
Bt
Qz
Kfs
Pl
500 µm
CB13-59 25° ← 241°, BSE | 350 m
G
Pl
Bt
Qz
Kfs
Pl
Qz
Pl
Bt
1000 µm
CB13-54a 32° ← 192° | 446 m
H
Qz
Pl
CB
Mym
Kfs
500 µm
CB13-54a 32° → 192° | 446 m
I
Pl
Qz
Kfs
Qz
Mym
Pl
Mym
GBM
Kfs
1000 µm
CB13-54a 32° → 192° | 446 m
J
Qz
Kfs
Wm
Mym
Mym
Kfs
Qz
500 µm

TABLE 1.1. MICROSTRUCTURAL OBSERVATIONS WITH RESPECT TO STRUCTURAL DEPTH FOR ALL QUEBRADA GATAY SAMPLES, CORDILLERA BLANCA SHEAR ZONE

Sample	Rock type*	Fabric†	Structural depth (m)	Microstructures§		Rheological domain#
				Quartz	Feldspar	
CB13-71a	gd	cat	0	BLG, SGR	P, FR, D	d^X
CB13-71b	gd	cat	0	BLG, SGR	P, D, FR	d^X
CB13-77a	gd	myl	92	BLG, SGR	D, B, FR	c, d
CB13-77b	p	sch	93	BLG, SGR, U	T, DRX	-**
CB13-77c	qv	umyl	94	SGR	P, FR, T	d^X
CB13-72a	gd	myl	111	SGR ,BLG	M, ASIM, E, FR, D, U	c, d, e, f
CB13-72b	gd	myl	111	BLG, SGR	P, T, PA, FR, F	c, d, f
CB13-73a	gd	cat	126	BLG, SGR	T	d^X
CB13-73b	gd	cat	126	BLG. SGR, PT	PT	d, e^X
CB13-74a	gd	cat	131	SGR, BLG	D, P	d^X
CB13-74b	p	sch	131	GBM, SGR	D, P, T, BD, K	-
CB13-81	p	sch	131	GBM	T, DRX	-
CB13-82	gd	myl	131	SGR, GBM	ASIM, P, T, DRX, PA, D, K	d, e, f
CB13-79	gd	pmyl	134	GBM, SGR	DRX, ASIM	c, d, f
CB13-80a	gd	umyl	134	SGR	N.A.††	e
CB13-80b	p	sch	134	GBM, SGR	N.A.	-
CB13-75	gd	myl, br	146	BLG, SGR	ASIM, D, U, B, K, PA, FR	d, f^X
CB13-76	gd	myl	149	SGR, BLG	D, T, PA	d^X
CB13-78	gd	myl	152	BLG, SGR	ASIM, D, P, T, PA, FR	c, d, f
CB13-83	gd	myl	171	SGR, GBM	ASIM, D, U, DRX, T, FR	c, f
CB13-84	gd	myl	232	GBM	ASIM, F, U, DRX, FR	c, e, f
CB13-53	gd	myl	304	GBM	M,DRX, ASIM, F	f
CB13-85	gd	myl	312	SGR	ASIM, D, DRX, M, F, FR	c, f
CB13-59	gd	myl	350	GBM	BD, BLG	b
CB13-58	gd	myl	354	SGR, GBM	M	f
CB13-55b	gd	pmyl	369	GBM	M, ASIM, U, BLG	c, f, e
CB13-55c	gd	umyl	369	SGR	ASIM, U, DRX, PA, T	c, g
CB13-57a	gd	myl	384	BLG, SGR	DRX, T, PA	d, e, f, g

Table 1.1, continued.

Sample	Rock type*	Fabric†	Structural depth	Quartz	Feldspar	Rheological domain#
CB13-57b	qv	umyl	385	BLG	N.A.	d
CB13-57c	qv	umyl	386	SGR,BLG	N.A.	d
CB13-56	p	sch	390	GBM	T	-
CB13-55a	gd	pmyl	430	GBM, SGR	BLG, M, FR, ASIM, U	a, f
CB13-54	gd	wd	446	CB, GBM	BLG, M, BLG, FR	a

Notes:

*gd—granodiorite; p—pelite; qv— quartz vein

†cat— cataclasite, br— breccia, umyl— ultramylonite, myl— mylonite, pmyl— protomylonite; wd— weakly deformedt

§ASIM— asymmetric strain-induced myrmekite; B— bookshelf feldspar; BD— boudinage; BLG— bulging recrystallization; CB— chessboard extinction; D— deformation lamellae; DRX— dynamic recrystallization; E— exsolution; F— flame perthite; FR— fractured; GBM— grain boundary migration recrystallization; K— kinked; M— myrmekite (non-strain-induced); P—patchy extinction; PA— pull-aparts; PT— pseudotachylyte; SGR— subgrain rotation recrystallization; T— feldspar tails; U— undulose extinction

#Rheological domains A-F from Figure 11 for granodiorite and quartz veins prior to throughgoing brittle overprinting, which is denoted by X.

**- not applicable

††N.A.: not applicable (no feldspar present)

deformed samples at deepest structural positions are characterized by interconnected networks of K-feldspar and plagioclase phenocrysts that exhibit intragranular fractures (Figs. 1.5H, 1.5I). Recrystallization has occurred along plagioclase grain boundaries and along intragranular fractures within plagioclase and K-feldspar phenocrysts (Fig. 1.5I). Large (~500 µm) myrmekite lobes have grown into K-feldspar phenocrysts (Fig. 1.5J).

Quartz

Quartz domains occur primarily as either interconnected networks surrounding other phases or as monophase aggregates in layered mylonites. Quartz commonly displays grain shape fabrics that define S-planes and exhibits dynamic recrystallization microstructures spanning the range of characteristic grain boundary microstructures described by Stipp et al. (2002a, 2002b; Fig. 1.6). Distribution with respect to structural depth of quartz recrystallization microstructures along with that of feldspar microstructures discussed above and microfabrics including interconnected phase, inferred quartz crystallographic slip systems, and deformation temperatures discussed in the following sections are summarized in Fig. 1.7.

In the upper ~150 m of the shear zone, ductile fabrics including bulging recrystallization (BLG) and subgrain rotation recrystallization (SGR) microstructures in quartz are overprinted by brittle fabrics. (Fig. 1.6A-1.6D; Table 1.1). Serrated grain boundaries and fine recrystallized grains characteristic of BLG recrystallization (Stipp et al., 2002b) occur in samples that also contain polygonal subgrains and new rotated grains within quartz porphyroclasts, characteristic of SGR recrystallization (Stipp et al., 2002a; 1.6E). Samples within the upper ~150 m of the shear zone that exhibit only ductile fabrics contain microstructures indicative of SGR recrystallization or a combination of BLG and SGR.

Fig. 1.6. Cross-polarized light photomicrographs of quartz microstructures. Labels denote trend and plunge of lineation, with arrow pointing down-plunge, and structural depth below the Cordillera Blanca detachment (in meters); arrowhead indicators specified below as (color). Bt—biotite; Chl—chlorite; Fsp—feldspar (undifferentiated); Kfs—K-feldspar; Pl—plagioclase; Qz—quartz; Wm—white mica. Quartz recrystallization microstructures: BLG—bulging; SGR—subgrain rotation; GBM—grain-boundary migration. A) Micro-faults truncating mylonitic foliation at high angles. Mylonitic fabric records SGR and BLG in quartz. B) Quartz SGR overprinted by fluid inclusion planes (red) oriented subparallel to shear bands (yellow). C) Pseudotachylite injection vein (yellow) and pseudotachylyte layer oriented parallel to mylonitic foliation (white), containing deformed mylonitic clasts and plagioclase feldspar grains (red). Relative orientation of mylonitic S-C fabric shown at upper left. D) Quartz SGR with grain shape fabric (GSF), truncated by cataclasite with biotite-rich matrix (yellow) and mylonitic clasts (red). E) BLG and SGR recrystallization in quartz and SGR in quartz affected by nearby feldspar porphyroclasts (lower part of image). Biotite-rich shear band is present (red). F) GBM in quartz domains adjacent to recrystallized feldspar. Some quartz grains are pinned at feldspar-quartz grain boundaries (red). G) SGR in quartz. H) GSF in quartz exhibiting GBM recrystallization microstructure. I) BLG (red) and SGR in quartz. White mica forms fish and shear bands (yellow) J) Quartz exhibiting GBM, deflecting into fine-grained quartz-feldspar-mica shear bands (yellow). Myrmekite (red) grows into K-feldspar porphyroclasts and within matrix. Recrystallized feldspar occurs along plagioclase and K-feldspar porphyroclast edges (white). K) Orthogonal subgrain boundaries forming chessboard extinction (CB) in quartz.

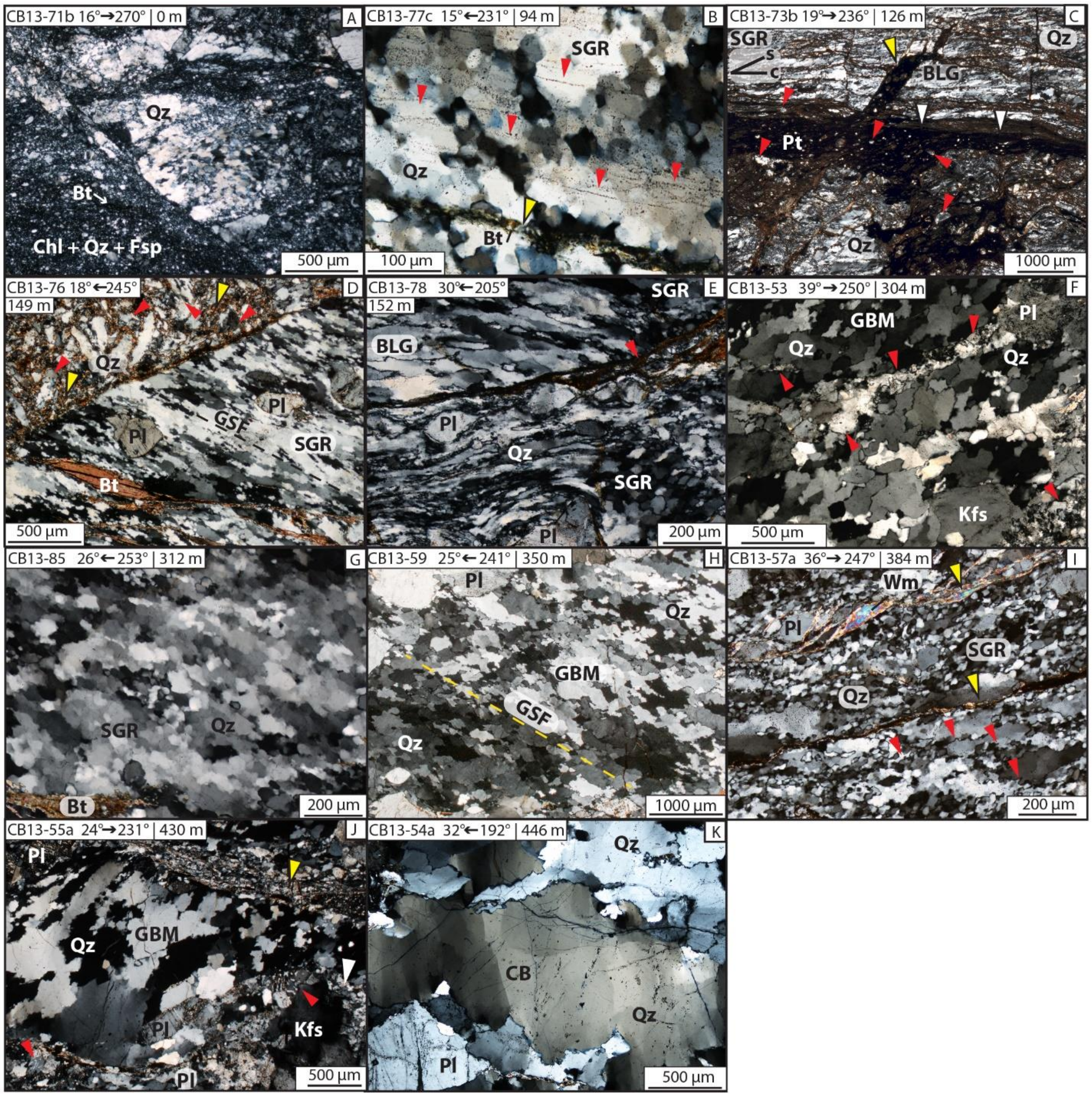

CB13-71b 16°→270° | 0 m
A
Qz
Bt
Chl + Qz + Fsp
500 µm
CB13-77c 15°←231° | 94 m
B
SGR
Qz
Bt
100 µm
CB13-73b 19°→236° | 126 m
C
SGR
s
c
BLG
Qz
Pt
Qz
1000 µm
CB13-76 18°←245°
149 m
D
Qz
Pl
GSF
Pl
SGR
Bt
500 µm
CB13-78 30°←205°
152 m
E
SGR
BLG
Pl
Qz
SGR
Pl
200 µm
CB13-53 39°→250° | 304 m
F
GBM
Pl
Qz
Qz
Kfs
500 µm
CB13-85 26°←253° | 312 m
G
SGR
Qz
Bt
200 µm
CB13-59 25°←241° | 350 m
H
Pl
Qz
GBM
GSF
Qz
1000 µm
CB13-57a 36°→247° | 384 m
I
Wm
Pl
SGR
Qz
200 µm
CB13-55a 24°→231° | 430 m
J
Pl
Qz
GBM
Pl
Kfs
Pl
500 µm
CB13-54a 32°←192° | 446 m
K
Qz
CB
Qz
Pl
500 µm

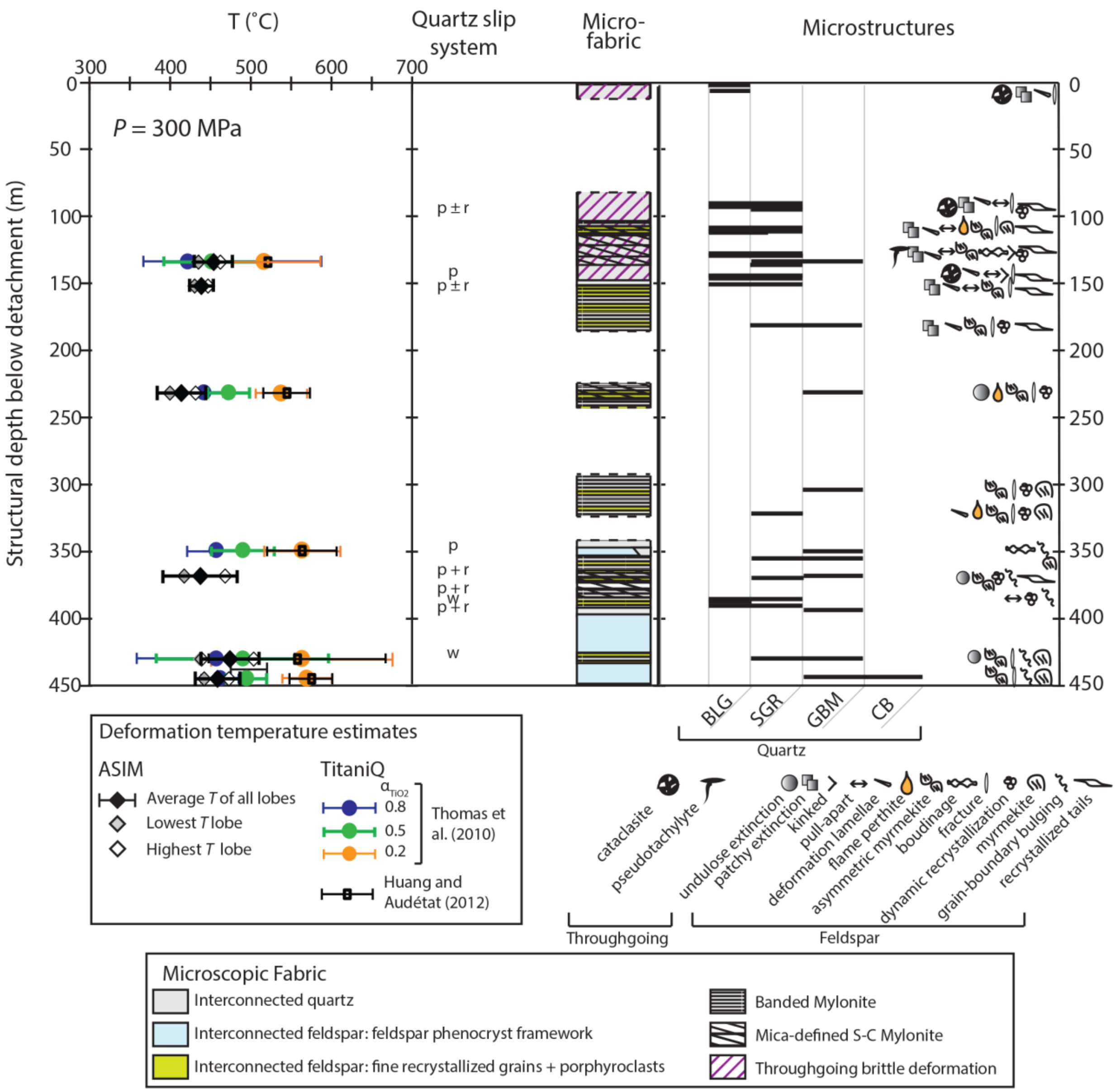

Fig. 1.7. Summary figure of microstructural analysis, geothermometry, and quartz CPO results at increasing structural depths below the Cordillera Blanca detachment. Quartz slip systems: p: prism <a>, r: rhomb <a>, w: weak. Deformation temperature (T) errors as reported in Table 1.2. Error bars for average ASIM temperatures do not include the ± 50 °C error on the thermometer. P—pressure; TitaniQ—Ti-in-quartz thermometer; αTiO2—Ti activity; BLG—bulging recrystallization; SGR—subgrain rotation recrystallization; GBM—grain-boundary migration recrystallization; CB—chessboard extinction.

TABLE 1.2. DEFORMATION TEMPERATURES

Sample	Structural depth (m)	Ti (ppm)[†]	N[§]	Temperature (°C)							
				TitaniQ*				ASIM			
				Thomas et al., 2010			Huang and Audetat (2012)				
				Activity 0.2	Activity 0.5	Activity 0.8		Average[#]	Highest T Lobe	Lowest T Lobe	N**
CB13-79	134	8 ± 6	34	516 ± 71	451 ± 60	421 ± 55	520 ± 66	450 ± 24	461	434	4
CB13-78	152	-[††]	-	-	-	-	-	440 ± 15	446	429	3
CB13-84	232	11 ± 4	11	542 ± 32	472 ± 26	441 ± 24	544 ± 29	410 ± 30	429	399	3
CB13-59	350	14 ± 7	59	563 ± 47	489 ± 39	456 ± 36	563 ± 43	-	-	-	-
CB13-55c	369	-	-	-	-	-	-	440 ± 46	467	416	4
CB13-55a	430	13 ± 12	12	556 ± 118	484 ± 99	452 ± 92	557 ± 110	470 ± 36	502	435	14
CB13-54	446	14 ± 6	53	563 ± 40	489 ± 33	456 ± 30	574 ± 30	460 ± 28	474	441	4

Notes: TitaniQ—Ti-in-quartz; ASIM—ssymmetric strain-induced myrmekite; *T*—temperature; activity—Ti activity.

* Error shown is Ti concentration uncertainty propagated through thermometer.

[†] 2σ standard deviation.

[§] Number of points analyzed.

[#] Error is 2σ standard deviation of temperatures from all measured lobes.

** Number of myrmkite lobes analyzed. Number of points analyzed per lobe varies between samples (see Table S2).

[††]–, not determined.

Samples from deeper than ~150 m below the detachment preserve ductile deformation in quartz and lack evidence for through-going brittle deformation. Quartz in most samples at these positions exhibits dominant SGR recrystallization microstructures, large grains with amoeboidal grain boundaries and commonly undulose extinction indicative of grain-boundary migration (GBM) recrystallization (GBM; Stipp et al., 2002a), or both SGR and GBM recrystallization microstructures (Fig. 1.6F-1.6J). Two samples from 384-386 m below the detachment record a combination of BLG and SGR recrystallization in quartz (Fig. 1.6I). At structurally deep positions, quartz forms discontinuous lenses and/or fills fractures in feldspar phenocrysts (Figs. 1.5H, 1.6J, 1.6K). Structurally deepest positions preserve large amoeboid quartz grains characteristic of GBM recrystallization microstructures within isolated quartz pockets at the interstices between feldspar phenocrysts (430 m; Fig. 1.5H). Planar, orthogonal subgrain boundaries indicative of chessboard extinction in quartz occurs at deepest structural positions (446 m; Figs. 1.5H, 1.6K).

Microfabrics

Microfabrics described here refer to the interconnected phase(s) present as well as which phases define S- C-, and C'- surfaces and which of these surfaces is prominent within the foliation.

S-C Mylonites

S-C mylonites are broadly characterized by prominent interconnected quartz domains with S-planes defined primarily by quartz grain shape fabrics and mica. Type I S-C fabrics as described by Berthé et al. (1979) and Lister and Snoke (1984), where S-surfaces anastomose into and out of C-surfaces and C'-surfaces are relatively well-developed (Fig. 1.8A, 1.8B) and type II

S-C fabrics, which contain prominent C-surfaces defined by tails of sheared mica fish and S-surfaces defined by quartz grain shape fabrics (Fig. 1.8C), are observed in the CBSZ. Quartz in S-C mylonites surrounds isolated feldspar porphyroclasts that contain ASIM or are fractured with quartz infill (Fig. 1.8C). Biotite or white mica shear bands in some cases have become interconnected, enveloping feldspar porphyroclasts and dynamically recrystallized quartz clasts (Fig. 1.8D).

Banded Mylonites

Banded mylonites comprising interlayered monophase aggregates of quartz or feldspar and polyphase aggregates of feldspar + quartz ± mica up to ~1500 μm thick (Fig. 1.8E-I) are observed between 111 and 430 m structural depth. (Fig. 1.7, Table 1.1). Boundaries between layers tend to align with mesoscopic foliation, which are typically the most prominent foliation surfaces (Fig. 1.8E). Fine-grained feldspar ± mica bands alternate with monomineralic quartz layers containing microstructures characteristic of SGR and/or GBM recrystallization (Figs. 1.8F, 1.5D). Quartz + feldspar domains exhibit relatively equant grain shapes and grain sizes smaller than those of either feldspar or quartz monophase domains and occur as continuous bands up to ~500 μm thick (Fig. 1.8G). Domains of finely recrystallized quartz + feldspar + mica appear to originate at plagioclase or K-feldspar porphyroclasts and extend into bands up to ~1.5 mm thick that are continuous at the thin-section to hand-sample scale (Fig. 1.8H). Fine-grained aggregates contain plagioclase with more albitic composition than porphyroclasts intermixed with K-feldspar, quartz, and biotite (Fig. 1.8I). K-feldspar occupies dilatant sites and triple junctions within quartz aggregates and between plagioclase grains (Fig. 1.8I).

Fig. 1.8. Photomicrographs of microfabrics. Images are cross-polarized light (XPL) unless otherwise noted. Labels denote trend and plunge of lineation, with arrow pointing down-plunge, and structural depth below the Cordillera Blanca detachment (in meters); arrowhead indicators specified below as (color). Bt—biotite; Fsp—feldspar (undifferentiated); Kfs—K-feldspar; Pl—plagioclase, Qz—quartz, Wm—white mica, (undifferentiated). A) Plane polarized light (PPL) image of type I S-C mylonite. S-surfaces anastamose in and out of C-surfaces. C' bands are defined by biotite and finely recrystallized quartz and feldspar. B) Type I S-C mylonite. S-surfaces defined by mica fish and quartz anastamose into C-surfaces. C) Type II S-C mylonite. S-surfaces are defined by biotite fish and quartz grain shape fabric (GSF). Biotite tails define C-surfaces. D) White mica + biotite shear bands deflecting around recrystallized quartz and plagioclase porphyroclasts. GSF in quartz porphyroclast aligned with S- plane defined by micas. E) PPL image of banded mylonite with biotite-rich and biotite-poor, quartz-rich layers. F) Compositionally banded mylonite with discontinuous mono- and polyphase layers. Monophase layers consist of quartz (white) or white mica (yellow); polyphase layers consist of quartz + plagioclase + K-feldspar (blue), K-feldspar + plagioclase (red), or white mica + quartz + plagioclase + K-feldspar (green). G) Banded mylonite with continuous quartz layers and feldspar + quartz ± biotite (white) layers deflecting around fractured (red) and partially recrystallized (yellow) plagioclase porphyroclasts. Quartz exhibits oblique GSF (yellow dashed line). H) Recrystallization along rim of K-feldspar and plagioclase grains and within tails. Tails disaggregate into fine-grained biotite + quartz + plagioclase + K-feldspar matrix (red). I) Backscattered electron (BSE) image of intermixed fine-rained polyphase matrix. K-feldspar occupies dilatant sites between plagioclase and quartz grains (red). Biotite and K-feldspar occupy grain boundaries and triple junctions (yellow). Black is result of holes and/or poor polish.

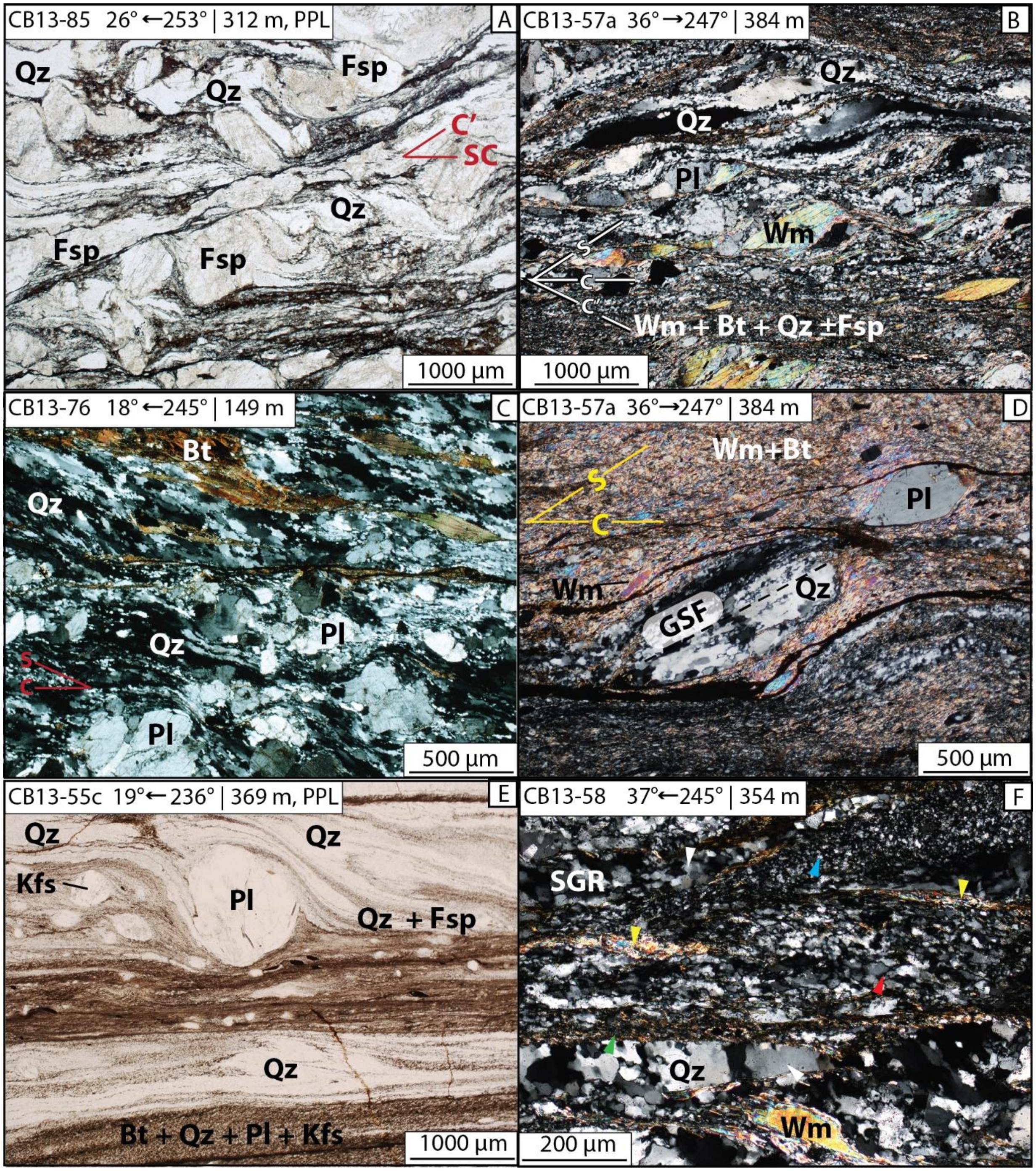

Fig. 1.8, continued.

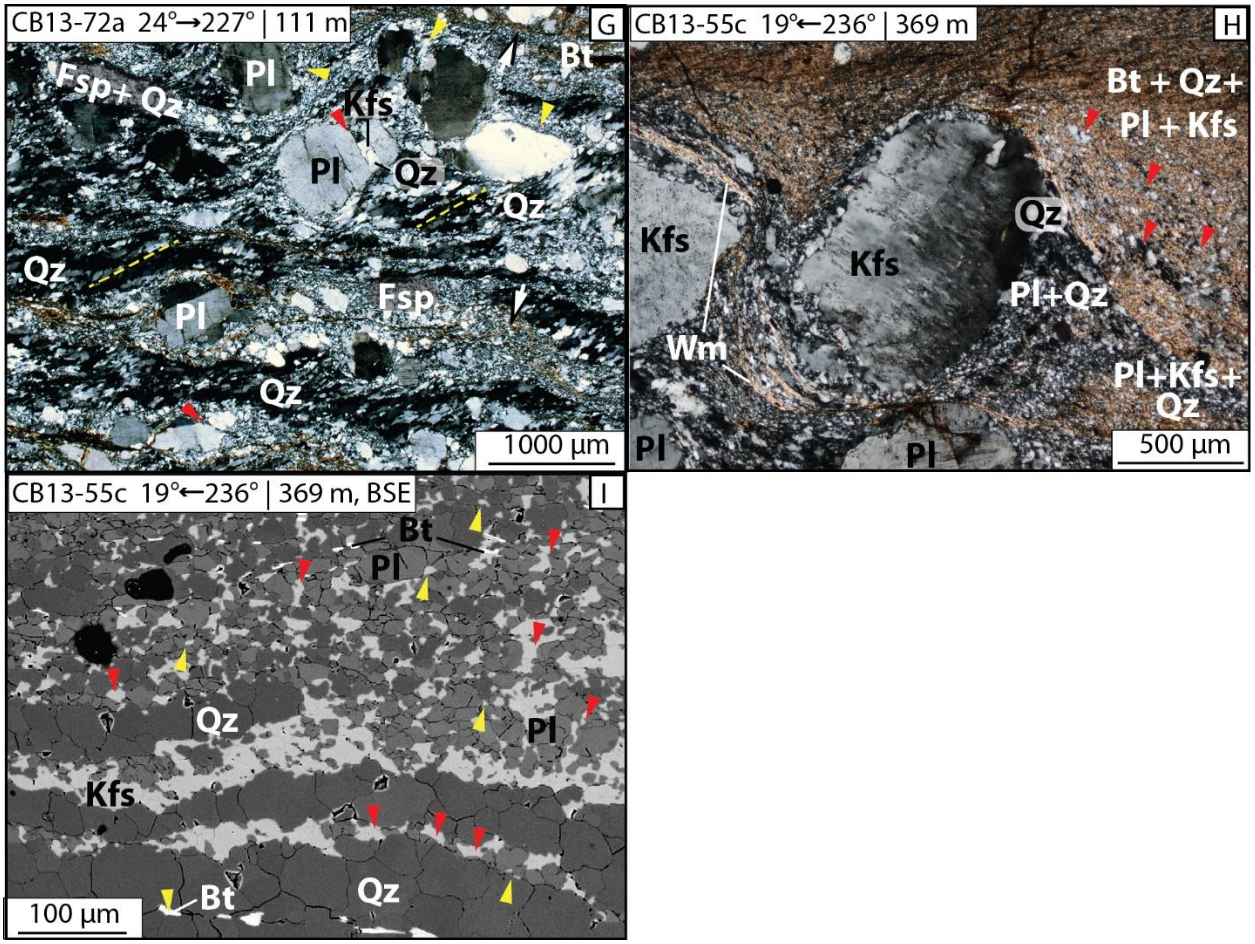

Fig. 1.8, continued.

Deformation Temperatures

Two-feldspar Geothermometry

Deformation temperatures derived from asymmetric strain-induced myrmekite (ASIM) for six samples from structural depths of 134 m to 446 m below the detachment range from 410 ± 30 °C to 470 ± 36° C (Table 1.2, Fig. 1.7). Temperatures do not vary systematically with structural depth and instead overlap within the 50 °C error of the thermometer.

TitaniQ Geothermometry

Deformation temperatures at structural depths from 134 to 446 m are between 451 ± 60 and 489 ± 33 °C, using the Thomas et al. (2010) TitaniQ geothermometer, assuming α_{TiO_2} of 0.5 and 300 MPa pressure. This assumption is made based on the absence in samples of a Ti-bearing phase other than biotite that is in clear equilibrium with quartz. Ti-bearing phases such as rutile and/or ilmenite are only present in three analyzed samples and were either along cleavage planes in biotite or within fractures that cut across recrystallized grain boundaries. The assumed activity of 0.5 is in line with Ti activities determined by geochemical modeling for granitoids of similar composition at similar pressures to those of the CBSZ (Huang and Audétat, 2012) as well as experimentally grown quartzites where rutile is present but sparse (>200 µm between grains; Nachlas and Hirth, 2015). Ti activities as low as 0.2 have been reported in some plutons as well as volcanic rocks with similar compositions to the Cordillera Blanca Batholith (Huang and Audétat, 2012; Kularatne and Audétat, 2014). Temperatures are ~70 °C hotter for α_{TiO_2} of 0.2 and ~30 °C cooler for an activity of 0.8 (Table 1.2). Temperatures estimated from the Huang and Audetat (2012) TitaniQ calibration ranging from 520 ± 66 °C to 574 ± 30 °C. These values are within 10 °C of temperatures estimated using the Thomas et al. (2010) calibration for α_{TiO_2} of

0.2 (Fig. 1.7, Table 1.2). TitaniQ thermobarometry demonstrates a slight decrease in temperature at decreasing structural depths (Fig. 1.7). However, this systematic variation is not readily observed with ASIM thermometry (Fig. 1.7, Table 1.2). Conservatively, deformation temperatures from TitaniQ thermobarometry are between 451 ± 60 °C and 574 ± 30 °C. TitaniQ temperatures for the CBSZ should be received with caution because, in addition to the uncertainty regarding α_{TiO_2}, the measured Ti concentrations are at or near the detection limit of ~11 ppm for all samples (see supplemental Text S3, Appendix I, for additional details).

Quartz CPOs

Quartz CPO patterns indicate predominant prism <a> and rhomb <a> slip (Fig. 1.9). Most samples from 94 m to 380 m from the detachment show slightly elongated y-maxima characteristic of dominant prism <a> slip with subsidiary rhomb <a> slip. Samples at 384 m and 430 m below the detachment had weak CPOs with M-indices ≤ 0.07. CPO strength otherwise appears uncorrelated with structural depth or slip system. At 152 m and 369 m, a- and prism-normal- axes do not form the six maxima expected for <a> slip and are instead smeared into three dispersed maxima.

Flow Stress

Differential stress, hereafter referred to as “stress,” estimates (Table 1.3) range from 16.5 ± 13 MPa to 71.5 ± 36 MPa using the Holyoke and Kronenberg (2010) piezometer, measured at 350 m (sample CB13-59) and 149 m (sample CB13-76), respectively (Fig. 1.10). The structurally highest sample, CB13-77c (94 m), yields 40.0 ± 22 MPa. The highest stress of 71.5 ± 36 MPa is from the deepest sample that contains throughgoing brittle overprinting of ductile fabrics (CB13-76, 149 m). An intermediately positioned sample CB13-78 (152 m) records the

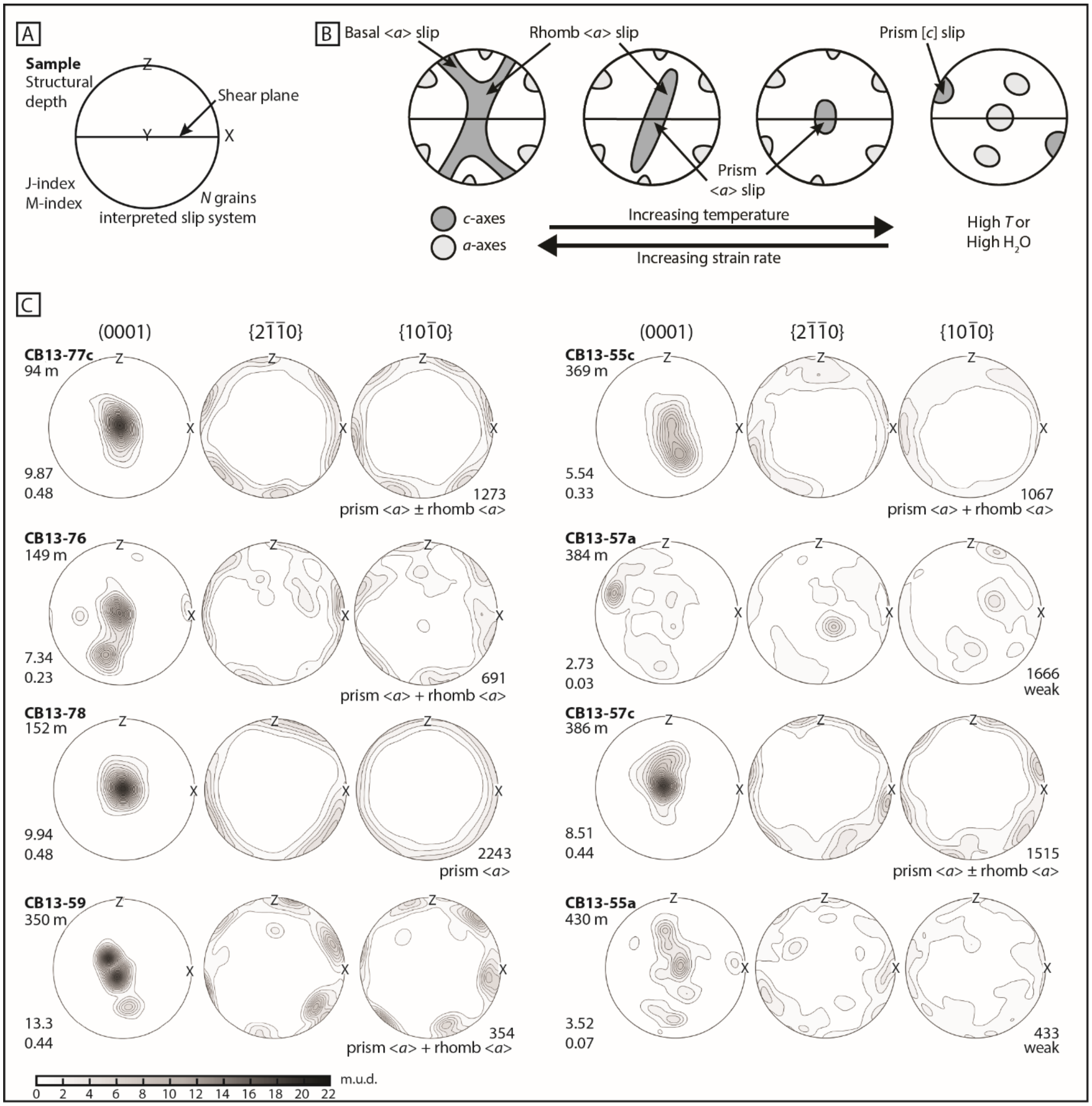

Fig. 1.9. Quartz crystallographic preferred orientations. A) Orientation of quartz CPO pole figures relative to shear plane and X-Z thin section, with key to labels for panel C. J-index (Bunge, 1982) and M-index (Skemer et al., 2005) indicate fabric strength. N—number of grains. B) Schematic c- and a-axes pole figures of quartz CPOs for different quartz slip systems with changing temperature (T), strain rate, and H2O conditions (after Passchier and Trouw, 2005). C) Equal-area lower-hemisphere pole figures of quartz c- (0001), a- $\{2\bar{1}\bar{1}0\}$, and prism-normal- $\{10\bar{1}0\}$ axes. All plots are 1 point per grain, contoured at 1 m.u.d. (multiples of uniform distribution) intervals, using a 7.5° half-width. Orientation of figures relative to X-Z plane, as well as labels, are as in A).

TABLE 1.3. PALEOPIEZOMETRIC AND STRAIN RATE ESTIMATES, CORDILLERA BLANCA SHEAR ZONE

Sample	Structural depth (m)	Grain Size: RMS* (μm)	Grain Size: 1σ s.d.† (μm)	Grain Size: Std. err.§ (μm)	N#	Differential Stress**: HK10†† (MPa)	Differential Stress**: ST03§§ (MPa)	Differential Stress**: C17## (MPa)	Temperature: TitaniQ*** (°C)	Temperature: ASIM (°C)
CB13-77c	94	23.5	12.3	0.47	687	40.0 ± 22	54.6 ± 35	61.9 ± 25	-###	-
CB13-76****	149	11.3	5.7	0.26	482	71.5 ± 36	97.6 ± 59	98.1 ± 38	451 ± 60	450 ± 24
CB13-78	152	12.9	5.4	0.14	1586	64.3 ± 26	87.9 ± 43	90.2 ± 27	-	440 ± 15
CB13-59	350	71.7	44.9	3.3	185	16.5 ± 13	22.5 ± 19	30.7 ± 17	489 ± 39	-
CB13-55c	369	18.6	9.0	0.3	907	48.2 ± 23	65.8 ± 38	71.7 ± 26	-	440 ± 46
CB13-57a	384	15.3	7.2	0.2	1269	56.3 ± 26	76.9 ± 43	81.2 ± 29	-	-
CB13-57c	386	14.3	6.7	0.22	977	59.3 ± 27	81.0 ± 45	84.6 ± 30	-	-
CB13-55a	430	30.9	14.1	0.72	380	32.1 ± 14	43.9 ± 24	52.0 ± 18	484 ± 99	470 ± 36

Notes: TitaniQ —Ti-in-quartz; ASIM—asymmetric strain-induced myrmekite.

*Root mean square of grain size distribution

†1σ standard deviation of grain size distribution

§Standard error of grain size distribution

#Number of grains within population used for paleopiezometry

**Errors are 1σ standard deviation of grain size propagated through piezometer. Average of stress error above and below RMS (from low and high grain size errors, respectively) is reported.

††Stress calculated using Stipp and Tullis (2003) piezometer modified by Holyoke and Kronenberg (2010).

§§Stress calculated using Stipp and Tullis (2003) piezometer.

##Stress calculated using Cross et al. (2017b) sliding piezometer calibration.

††† Calculated using wet quartz flow law of Hirth et al. (2001): $\dot{\varepsilon} = A f_{H_2O}^{m} \sigma^{n} \times 10^{(-Q/RT)}$, where log(A)= -11.2 ± 0.6 MPa -n/s (n is the stress exponent =4), ; Q=135 ± 15 kJ/mol; m=1; n=4; R = 8.314 x 10^{-3} kJ/mol·K, f_{H2O} is water fugacity, assuming water pressure = lithostatic at pressure = 300 MPa, calculated using fugacity calculator: https://www.esci.umn.edu/people/researchers/withe012/fugacity.htm (Sterner and Pitzer, 1994).

§§§ Calculated using prism <a> flow law of Tokle et al. (2019), using the same equation as Hirth et al. (2001), but where A = 1.75 x 10^{-12} MPa $^{-n}$/s, Q=125 ± 15 kJ/mol; m = 1; n = 4; with R, T, and f_{H2O} as in the Hirth et al. (2001) flow law.

-: not determined

****Temperatures derived from nearby CB13-79 (134 m)

Table 1.3, continued.

Sample	Strain Rate TitaniQ††† (s^{-1})	ASIM††† (s^{-1})	TitaniQ§§§ (s^{-1})	ASIM §§§ (s^{-1})
CB13-77c	2.5×10^{-12}	2.6×10^{-12}	3.6×10^{-12}	3.5×10^{-12}
CB13-76****	-	1.0×10^{-12}	-	1.6×10^{-12}
CB13-78	2.6×10^{-14}	-	3.5×10^{-14}	-
CB13-59	-	3.0×10^{-13}	-	5.1×10^{-13}
CB13-55c	-	-	-	-
CB13-57a	-	-	-	-
CB13-57c	3.7×10^{-13}	1.4×10^{-13}	4.3×10^{-13}	2.8×10^{-13}
CB13-55a				

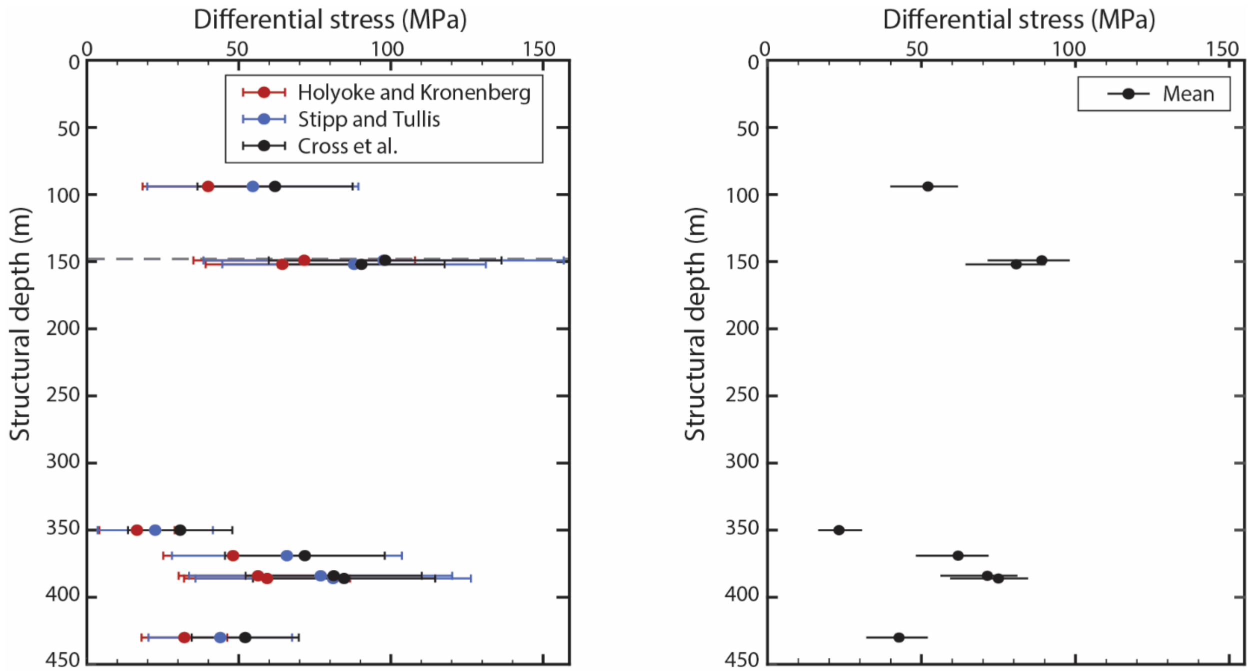

Fig. 1.10. Differential stress estimates with increasing depth below the Cordillera Blanca detachment. A) Differential stress estimates for Stipp and Tullis (2003), (Holyoke and Kronenberg, 2010), and (Cross et al., 2017b) piezometers, shown relative to structurally deepest observed sample containing throughgoing brittle overprint (grey dashed line). Error bars are standard deviation on root mean square grain size propagated through each piezometer. B. Mean differential stress of the three piezometers. Error bars are maximum range of stress estimates from the three calibrations.

next highest stress of 64.3 ± 26 MPa. CB13-59 (350 m) yielded the lowest stress estimate of observed samples, 16.5 ± 13 MPa. Further below the detachment, CB13-55c (369 m) yields a stress of 48.2 ± 23 MPa. Stresses calculated at lower structural positions are 56.3 ± 26 MPa and 59.3 ± 27 MPa, from CB13-57a (384 m) and CB13-57c (386 m), respectively. The lowest structural position analyzed (CB13-55a, 430 m) yields a stress of 32.1 ± 14 MPa. Stress estimates using the Stipp and Tullis (2003) and Cross et al. (2017b) calibrations range from 22.5 ± 19 to 97.6 ± 59 MPa and 30.7 ± 17 to 98.1 ± 38 MPa, respectively and are within error of those calculated using the Holyoke and Kronenberg (2010) calibration (Fig. 1.10, Table 1.3). In summary, a consistent gradient in stress as a function of structural depth is not observed, rather, the highest stresses are observed at intermediate structural positions near 150 m where the deepest through-going brittle overprinting is observed.

Discussion

Quartz CPOs

It is important to note that CPOs may be inherited from earlier deformation. Strong pre-existing growth CPOs in quartz veins have been shown to influence CPOs of quartz veins deformed at lower temperatures, where quartz initially grew in an orientation favorable for easy slip at high temperatures (e.g. prism <a> slip at T > 500 °C) (Pennacchioni et al., 2010). Grains were oriented unfavorably for basal <a> slip when temperatures decreased during deformation such that even at relatively low temperatures, strong CPOs indicative of prism <a> ± rhomb <a> slip were preserved (Toy et al., 2008; Pennacchioni et al., 2010). Previous work also suggests that oriented grain growth during submagmatic flow may influence later CPO development during sub-solidus deformation (Zibra et al., 2012). We thus consider the possibility that strong CPOs at positions nearer to the detachment may be inherited from early deformation at relatively high temperatures where prism <a> slip was initially favored, or from oriented grain growth during submagmatic flow. The weak fabric in the deepest sample analyzed for EBSD (CB13-55a, 430 m) resembles an elongate y-axis maximum expected for prism <a> ± rhomb <a> slip that is seen in stronger CPOs at structurally higher positions (Fig. 1.9). Although this could suggest some degree of inheritance from a pre-existing CPO in the weakly deformed granodiorite, ASIM and TitaniQ estimates suggest that deformation for most of the CBSZ occurred at temperatures above ~400 °C, which is consistent with temperatures where prism <a> and rhomb <a> slip are expected to occur more readily than basal <a> slip (Law et al., 1990; Toy et al., 2008). CPO inheritance is a possibility in the CBSZ but is not required to explain our data.

Deformation Mechanisms

Feldspar

Fracturing. Feldspar exhibits fracturing throughout most of the CBSZ (Fig. 1.7). At structurally higher positions fractures occur predominantly in plagioclase porphyroclasts that are surrounded by quartz and/or fine-grained feldspar + quartz ± mica domains At structurally deep positions, K-feldspar and plagioclase phenocrysts form an interconnected framework that features inter- and intra- granular fractures. Previous studies have documented fracturing at sub-magmatic to subsolidus conditions in networks of load-bearing interconnected feldspar (Rosenberg, 2001; Zibra et al., 2012; Bessiere et al., 2018). Syn-magmatic fractures in granitoids are characterized by K-feldspar and plagioclase films along grain boundaries at high-angles to foliation planes and by fractures filled with at least one phase that would crystallize from a residual melt (Rosenberg, 2001). These characteristics are consistent with those describedby Bouchez et al. (1992) for submagmatic fractures at melt fractions between 0.10 and 0.30. Submagmatic fractures are described as those 1) that transectsingle grains, 2) that are filled with a phase that is crystallographically and compositionally continuous inside and outside of the fracture, and 3) whose filling phase is expected to crystallize from the residual melt (Bouchez et al., 1992). Within the CBSZ, fractures satisfying these criteria occur at structurally deep positions, where quartz exhibiting the same orientation extends from a wedge-shaped pocket into an adjacent narrow fracture (Fig. 1.5H, 446 m). The amount of melt required to produce submagmatic fractures has been debated. Melt fractions of 0.3 to 0.5 had been argued to be required for the formation of through-going melt-filled fractures (Arzi, 1978; Paterson et al., 1989), though further investigation into the experimental work from whence these values were derived suggest that melt-filled fractures could be produced at lower melt fractions, potentially as low as 0.07 (Rosenberg and Handy, 2005).

Although quartz crystallization would be consistent with the third criterion above as set forth by Bouchez et al. (1992), other evidence for magmatic deformation or submagmatic deformation, such as imbricated feldspar phenocrysts, are not observed in the CBSZ. The wedge-shaped nature of the quartz exhibiting chessboard extinction is consistent with some degree of rotation of the fractured K-feldspar (Hippertt, 1993), which must have occurred at or above the temperature required for chessboard extinction in quartz (~630 °C Kruhl, 1996), placing it in the field of high-temperature subsolidus deformation. Alternatively, the quartz exhibiting chessboard extinction may have been late-stage melt filling a pocket between plagioclase and K-feldspar porphyroclasts, with submagmatic fracturing occurring at the melt-porphyrolcast interface of the melt pocket at a low melt fraction, still near the boundary between submagmatic and subsolidus conditions (Paterson et al., 1989). In either scenario, evidence for the role of fracturing in feldspar deformation at high temperatures is observed at deepest structural positions within the CBSZ.

Dislocation creep versus Cataclastic Flow. Deformation experiments on plagioclase single crystals with no initial microstructure other than growth twins suggests that feldspar experiences complex semi-brittle cataclastic flow, where brittle processes (i.e. micro-fracturing) and plastic processes (i.e. deformation twinning via dislocation climb) are interdependent (McLaren and Pryer, 2001). The coincidence of deformation lamellae with fractured feldspar porphyroclasts and undulose extinction within the upper ~180 m of the CBSZ may suggest the activity of this type of semi-brittle flow. These microstructures are also consistent with those described for cataclastic flow by Tullis and Yund (1987). In their albite aggregate deformation experiments, Tullis and Yund (1987) described characteristic microstructures of cataclastic flow that include undulatory and/or patchy extinction and flattening, grain-scale faults with small offset, and microcracks. The authors note that patchy undulose extinction, which has also been interpreted to represent dislocation creep (Tullis and Yund, 1977) is typically caused by microcrack arrays and crushed zones visible at the sub-micron scale.

Evidence for the activity of dislocation creep in feldspar is also observed within the CBSZ. Dynamic recrystallization in feldspar can produce relatively small, rounded, and undeformed feldspar porphyroclasts (Tullis and Yund, 1985). During dislocation creep in feldspar, recrystallization is primarily accommodated by migrating grain boundaries (Tullis and Yund, 1987), producing grain boundary bulges and small strain-free recrystallized grains (Stünitz et al., 2003) characteristic of BLG recrystallization microstructures. Additional related microstructures can include undulatory extinction in relatively equant grains and augen surrounded by a fine-grained matrix at relatively high strains. Undulose extinction primarily due to dislocation creep sweeps continuously across a grain, as opposed to the patchy undulose extinction that can result from dislocation entanglement (e.g. Hirth and Tullis, 1992) or cataclastic flow (Tullis and Yund, 1987). Fine, equant, relatively strain-free, recrystallized grains occur along the margins of porphyroclasts, grain-boundaries, and fractures, commonly extending out into tails under high strains (Tullis and Yund, 1985).

Within the CBSZ, fine recrystallized feldspar occurs at a wide range of structural depths (92 to 446 m, Table 1.1, Fig. 1.7). As these microstructures may be formed by either catalastic flow or dislocation creep, interpreting deformation mechanisms by singular microstructures alone is difficult. Here, interpretation of the activity of dislocation creep in feldspar is limited to samples where grain boundary bulges can be observed (i.e. Fig. 1.5E) and where undulatory extinction, if present, is continuous across grains rather than patchy. If patchy undulose extinction occurs, especially if coinciding with kinked or bent twins or cleavage planes, or pull-apart type fractures, the prominent deformation mechanism is interpreted to be cataclastic flow. Under these considerations, dislocation creep in feldspar likely occurred at relatively deep structural positions (350 m to 446 m) suggesting deformation temperatures above ~450 °C (Yund and Tullis, 1980), consistent with ASIM derived temperatures of 440 ± 46 to 470 ± 36 °C and TitaniQ temperatures of 484 ± 99 to 489 ± 39 °C (Thomas et al. (2010) calibration; α_{TiO2} =0.5) for the same structural positions (Fig. 1.10). Alternatively, cataclastic flow likely occurred at structural positions above ~350 m. This relationship may be oversimplified, as a cataclastic overprint (in feldspar) could reduce evidence for dislocation creep, but also more simply because of the similarity of microstructures between cataclastic flow and dislocation creep (i.e. Tullis and Yund, 1987).

Quartz

Dislocation creep. Recrystallization microstructures and crystallographic preferred orientations can be used to distinguish between prominent deformation mechanisms (Hirth and Tullis, 1992; Stipp et al., 2002b). Recrystallized quartz CPOs mainly show patterns indicative of dominant prism <a> slip with variable lesser contributions of rhomb <a> slip, which is consistent with quartz dislocation creep at 94 – 386 m below the detachment surface (Fig. 1.9). Previous studies suggest that temperature is the primary contributing factor to activating different slip systems in quartz aggregates, with the transition from basal slip to prism slip occurring at high temperatures (Tullis et al., 1973; Mainprice et al., 1986; Morales et al., 2011). Above ~500 °C, prism <a> occurs as the dominant slip system, and at increasingly high temperatures of ~600 °C slip in the <a> direction gives way to dominant prism [c] slip (Mainprice et al., 1986; Schmid and Casey, 1986; Kruhl, 1996; Passchier and Trouw, 2005). However, transitions between dominant slip mechanisms inferred from quartz CPOs may also be affected by changes of strain rate and/or the activity of water within the shear zone (Fig. 1.9; Mainprice and Paterson, 1984; Stipp et al., 2002b; Mancktelow and Pennacchioni, 2004; Law, 2014; Morales et al., 2014). Excluding the weak fabrics of CB13-57a and CB13-55a (384 and 430 m, respectively), quartz CPOs indicate predominant activity of prism <a> slip and rhomb <a> slip, which are consistent with dislocation creep in quartz at $T > 400$ °C (Schmid and Casey, 1986; Stipp et al., 2002a, 2002b; Stünitz et al., 2003).

Grain boundary sliding. Weak CPOs at 384 and 430 m depth, as well as dispersed a-axes maxima at 152 m and 369 m depth may suggest the activity of other deformation mechanisms, such as diffusion creep and/or grain boundary sliding (GBS) (Bestmann and Prior, 2003; Wightman et al., 2006; Cross et al., 2017a) or relatively low amounts of accumulated strain (Lister and Hobbs, 1980; Toy et al., 2008). Diffusion creep is unlikely in coarse-grained quartz aggregates (Rutter and Brodie, 2004), such as those in CB13-55a (430 m). The weak CPO in CB13-55a more plausibly reflects relatively low strain, which is within reason for its deep structural position (430 m) relative to the detachment fault. This relationship is consistent with weak CPOs at positions structurally removed from the main detachment and/or shear zone in other natural settings (Haertel et al., 2013; Haertel and Herwegh, 2014) or in low finite strains in numerical models (Keller and Stipp, 2011; Lister and Hobbs, 1980).

The weak CPO at 384 m (CB13-57a) and the dispersed a-axes patterns at 152 and 369 m depth (CB13-78 and CB13-55c, respectively) may reflect grain boundary sliding (GBS). Dispersed CPO patterns are often attributed to grain boundary sliding (GBS) (Jiang et al., 2000; Bestmann and Prior, 2003; Storey and Prior, 2005; Warren and Hirth, 2006; Cross et al., 2017a).

Microstructures such as four-grain junctions, square or rectangular grain shapes, alignment of multiple grain boundaries parallel to foliation, and recrystallized grains smaller than subgrains are thought to be indicative of grain boundary sliding (Halfpenny et al., 2012; Miranda et al., 2016; Rahl and Skemer, 2016). CPOs of sub-populations at 384 m (CB13-57a) shows that the weak c-axis maxima derive mainly from relict grains and that recrystallized grains have dispersed orientations (Fig. S2, Appendix I). In this sample, four-grain junctions associated with square grain shapes and alignment of edges across multiple grains also occur within the finer recrystallized population (Fig. S2, Appendix I). These observations, in addition to the dispersion of the CPO in the fine-grained recrystallized quartz population are consistent with the activity of GBS in quartz (Bestmann and Prior, 2003; Halfpenny et al., 2006; Wightman et al., 2006; Gan et al., 2007; Kilian et al., 2011; Cross et al., 2017a).

Polyphase Domains

Microstructural observations suggest that polyphase quartz + feldspar ± mica domains may be promoted by phase mixing via grain boundary sliding, dynamic recrystallization, and pressure-solution creep. Precipitation of soluble phases such as K-feldspar or quartz in dilatant openings, such as in recrystallized porphyroclast tails or pull-apart zones in fine-grained aggregates, has previously been interpreted to represent GBS (Behrmann and Mainprice, 1987; Kilian et al., 2011a; Platt, 2015). At least local GBS is supported by K-feldspar in dilatant sites and at triple junctions within quartz aggregates and between plagioclase grains (Fig. 1.8I; Stünitz and Tullis, 2001; Fusseis et al., 2009; Oliot et al., 2014; Menegon et al., 2015; Spruzeniece and Piazolo, 2015; Czaplińska et al., 2015; Viegas et al., 2016). Disaggregation of dynamically recrystallized feldspar porphyroclast tails into polyphase quartz + plagioclase + K-feldspar ± biotite domains (Fig. 1.8H) is consistent with microstructures inferred to form from precipitation in dilatant openings following dynamic recrystallization in porphyroclast tails, where rotation of grains opens up pore space that is subsequently filled by K-feldspar (Kilian et al., 2011a; Platt, 2015).

Strain Rates

Strain rates derived from the wet quartz flow law of Hirth et al. (2001) are 2.6 x10^{-14} to 2.6 x 10^{-12} s^{-1} using the Holyoke and Kronenberg (2010) piezometer and temperatures from TitaniQ (α_{TiO_2}=0.5) and ASIM thermometry. Strain rates increase to 3.1 x 10^{-13} to 9.4 x 10^{-12} using the Cross et al. (2017b) piezometer. Highest calculated strain rates (2 to 9 x 10^{-12} s^{-1}) are from ~150 m below the detachment, near the position of the deepest throughgoing brittle overprint. Displacement of 12-15 km along the detachment since ~5 Ma (Bonnot, 1984; Giovanni, 2007; Giovanni et al., 2010) yields a time-averaged slip rate of 2.4-3 mm/yr. If it is assumed that the width of the shear zone between a given sample and the detachment was active during shear zone evolution, shear zone widths prior to onset of brittle deformation were between ~450 m and ~150 m. These widths correspond to time-averaged strain rates from 1.7 to 6.3 x 10^{-13} s^{-1} for 450 and 150 m widths, respectively, under the assumption that strain rate = velocity/width (Platt and Behr, 2011b). Despite uncertainties in temperature and stress values, strain rates estimated from individual samples generally agree with time-averaged strain rate for the CBSZ.

Use of ASIM temperatures in the quartz flow law requires a simplified assumption that myrmekite formation and quartz deformation are coeval. TitaniQ temperatures at α_{TiO_2}=0.5 overlap with ASIM temperatures within error (Fig. 1.7, Table 1.2), supporting the use of ASIM temperatures as an approximation of deformation temperatures in quartz for strain rate calculations when quartz-based temperature data are unavailable. ASIM temperatures are broadly consistent with temperatures > 400 °C inferred from quartz CPOs as well as temperatures expected for SGR recrystallization (400-500 °C; Stipp et al., 2002a), and are within error of the transition to GBM recrystallization at strain rates of ~10^{-12} s^{-1} (480-530 °C Stipp et al., 2002a). TitaniQ analyses were selectively conducted on samples with GBM recrystallization microstructures, which at strain rates of ~10^{-12} s^{-1} occur at temperatures above 500 °C (Stipp et al., 2002a). ASIM temperatures and TitaniQ temperatures for these samples, while in agreement with each other at α_{TiO_2}=0.5, are below the expected range from Stipp et al. (2002a). Deformation experiments suggests that one order of magnitude variation in strain rate has a similar effect on recrystallization microstructure to a 200 °C shift in temperature and that an increase in water content changes recrystallization microstructures in a similar matter to an increase in temperature (Stipp et al., 2006).

Shear Zone Evolution

Based on overprinting relationships and structural position relative to the detachment fault, we propose a conceptual model for the evolution of the Cordillera Blanca Shear Zone during post-magmatic cooling. In this model, initial deformation in the CBSZ was accommodated by high-temperature feldspar fracturing. Continuing subsolidus deformation occurred at temperatures above ~400 °C through varying contributions of dislocation creep in feldspar, dislocation creep in quartz, cataclasis in feldspar, and at least locally by GBS in polyphase aggregates composed of quartz + feldspar ± mica. The evolution of these mechanisms in the CBSZ does not follow a single progression. Rather, our data support a conceptual model where banded mylonites and/or interconnected quartz domains formed as a result of multiple deformation mechanisms that likely reflect changes in temperature, strain rate and presence of fluids prior to the onset of throughgoing brittle deformation (Fig. 1.11).

Fig. 1.11. Schematic line drawings summarizing evolution of deformation mechanisms and related microstructures in the CBSZ. Arrows denote possible microstructural progressions, labelled with processes facilitating change in microstructure. Gray arrows denote transitional microstructures and processes. Abbreviations: F—feldspar, Q—quartz; htf—high-temperature fracturing; ssf—subsolidus fracturing; disc: dislocation creep; rx: reaction to Na-rich plagioclase; ff—fracture fill; cc—cataclasis; rot—rotation; Mrxn—myrmekite-forming reaction; CB—chessboard extinction; GBM—grain-boundary migration recrystallization; BLG—bulging recrystallization; SGR—subgrain rotation recrystallization; ASIM—asymmetric strain-induced myrmekite; GSF—grain shape fabric; GBS—grain boundary sliding; Dil—dilation. Scale bars are approximate. For clarity, grain sizes of quartz in 11D depicted as slightly larger than actual. See text for details.

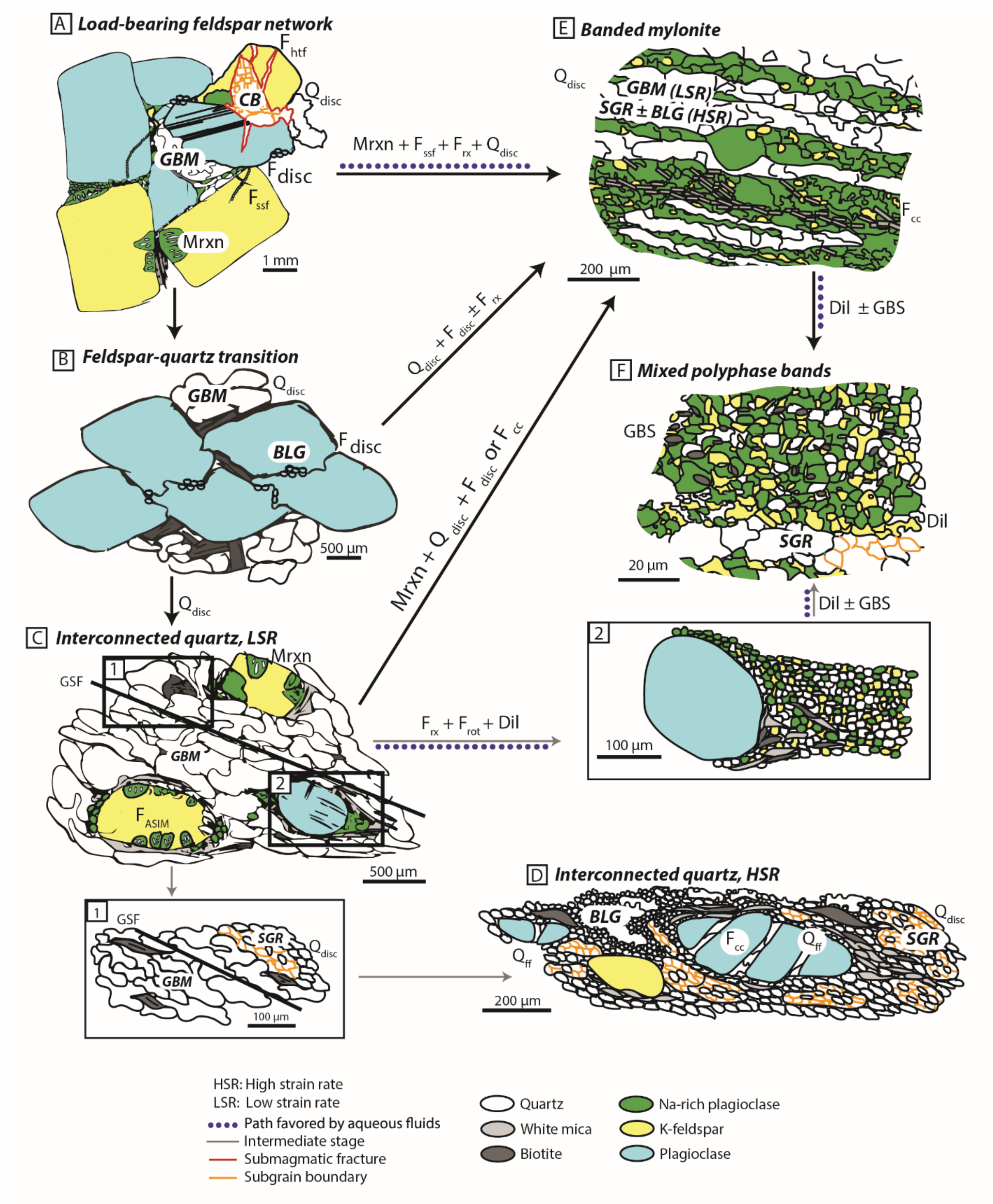

A Load-bearing feldspar network
F htf
Q disc
CB
GBM
F disc
F ssf
Mrxn
1 mm
B Feldspar-quartz transition
GBM
Q disc
BLG
F disc
500 µm
Q disc
C Interconnected quartz, LSR
Mrxn
GSF
GBM
F ASIM
500 µm
1
GSF
SGR
Q disc
GBM
100 µm
2
E Banded mylonite
Q disc
GBM (LSR)
SGR ± BLG (HSR)
F cc
200 µm
Mrxn + F ssf + F rx + Q disc
Q disc + F disc ± F rx
Mrxn + Q disc + F disc or F cc
Dil ± GBS
F Mixed polyphase bands
GBS
Dil
SGR
20 µm
Dil ± GBS
F rx + F rot + Dil
100 µm
D Interconnected quartz, HSR
BLG
Q disc
Q ff
F cc
SGR
200 µm
HSR: High strain rate
LSR: Low strain rate
Path favored by aqueous fluids
Intermediate stage
Submagmatic fracture
Subgrain boundary
Quartz
White mica
Biotite
Na-rich plagioclase
K-feldspar
Plagioclase

Initial Deformation

Earliest deformation occurred via fracturing and neocrystallization of K-feldspar and plagioclase and dislocation creep in quartz (Fig. 1.11A). Chessboard extinction in quartz within submagmatic, intragranular K-feldspar fractures (Figs. 1.5H, 1.11A) represents the onset of subsolidus deformation at T> 630 °C (Kruhl, 1996). Quartz with chessboard extinction and large grains with amoeboid grain boundaries and undulose extinction indicative of GBM recrystallization are common within isolated pockets at the interstices between feldspar phenocrysts. As such, these quartz domains are interpreted to be passive markers of deformation conditions and rheology is inferred to be controlled by the interconnected network of feldspar phenocrysts.

Grain Size Reduction

Grain size reduction of the feldspar network occurred by dislocation creep in plagioclase, recrystallization to fine-grained feldspar or feldspar + quartz along intragranular fractures in K-feldspar phenocrysts, and myrmekite growth (Figs. 1.5I, 1.5J, 1.11A). BLG recrystallization occurs along fractures and the rims of magmatic plagioclase and K-feldspar grains (Fig. 1.5E, 1.5I), suggesting that deformation was partially accommodated by dislocation creep in feldspar during early stages of shear zone evolution. Dissolution along plagioclase and K-feldspar fractures facilitated by aqueous fluids is inferred from the crystallization of finer-grained, more sodic feldspar grains along these sites (Fitz Gerald and Stunitz, 1993; Fusseis and Handy, 2008; Viegas et al., 2016).

At structurally deep positions within the CBSZ, prominent myrmekite growth along K-feldspar boundaries that is associated with white mica and quartz (Figs. 1.5J, 1.11A) also supports the role of fluids in early grain size reduction of the load-bearing feldspar network

(Menegon et al., 2006; Ree et al., 2005; Tsurumi et al., 2002). The presence of white mica and quartz along the inferred original K-feldspar edge supports myrmekite growth facilitated by a local addition of water, where excess K+ is released and myrmekite and muscovite are formed at the expense of K-feldspar following the reaction (Phillips et al., 1972):

$$\underset{\substack{\text{alkali}\\\text{feldspar}}}{\left\{\begin{matrix}3KAlSi_3O_8\\NaAlSi_3O_8\end{matrix}\right\}}+\underset{\substack{\text{calcic}\\\text{plagioclase}}}{\left\{\begin{matrix}CaAl_2Si_2O_8\\NaAlSi_3O_8\end{matrix}\right\}}+\underset{\text{water}}{H_2O}\rightarrow\underset{\substack{\text{more sodic}\\\text{plagioclase}}}{\left\{\begin{matrix}CaAl_2Si_2O_8\\2NaAlSi_3O_8\end{matrix}\right\}}+\underset{\text{quartz}}{6SiO_2}+\underset{\text{muscovite}}{KAl_2(Al,Si_3)O_{10}(OH)_2}+K_2O \quad (6).$$

Collectively, these observations suggest a role of fluids in promoting grain size reduction via fracturing, recrystallization, and myrmekite formation within an initially interconnected network of feldspar phenocrysts at > 400 °C within the CBSZ.

Interconnection of Quartz Domains

Quartz deformed by dislocation creep in interconnected networks around other isolated phases at a wide range of structural depths in the CBSZ (Fig. 1.7). The transition from a coarse-grained feldspar network to interconnected quartz network (Fig. 1.11B) is preserved at 350 m structural depth (i.e. CB13-59, Figs. 1.5E-1.5G, 1.6H), where quartz exhibits GBM recrystallization microstructures and plagioclase is boudinaged. The tapered, relatively symmetric nature of plagioclase boudins suggests that quartz was less competent than feldspar, and flowed into boudin necks (Goscombe et al., 2004). As plagioclase within this sample also exhibits BLG recrystallization (Fig. 1.5E), deformation at the transition from a coarse-feldspar network to a quartz network is consistent with the model for a two-phase system in which both rheological phases deform viscously (i.e. Fig. 1b of Handy et al., 1999). In the CBSZ, this transition occured under relatively low stress (16.5 ± 13 MPa in quartz) near ~500 °C, at the lowest strain rate estimated for individual samples, ~3 x 10^{-14} s^{-1}. Similar differential stresses are reported for extensional mylonitic granitoids exhibiting microstructures indicative of GBM recrystallization in quartz and plastic deformation in feldspar in the core (10-16 MPa) and mylonitic front (~16 MPa) of the Whipple Mountains metamorphic core complex (California, USA) in the North American Cordillera (Behr and Platt, 2011; Cooper et al., 2017).

Deformation within interconnected quartz domains proceeds predominantly by dislocation creep. GBM, SGR, or SGR + GBM recrystallization microstructures in quartz occur at structural positions deeper than ~150 m below the detachment (Fig. 1.11C), whereas SGR ± BLG recrystallization microstructures primarily occur at structural positions shallower than ~150 m (Fig. 1.11D), with the exception of a relatively narrow zone at ~385 m depth (Fig. 1.7). These microstructures are accompanied by quartz CPOs that mainly show strong fabrics indicative of prism <a> slip and subsidiary rhomb <a> slip, consistent with quartz dislocation creep at > 400 °C. The shift in GBM to BLG recrystallization microstructures in addition to SGR microstructures at ~150 is likely due to increasing strain rate. This microstructural transition is often attributed to decreasing temperature, where GBM recrystallization occurs above ~500 °C, and BLG recrystallization occurs below ~400 °C (Stipp et al., 2002b). However, estimated deformation temperatures in the CBSZ are consistently above 400 °C and within ~70 °C of each other, suggesting that temperature is likely not the main contributing factor in microstructural evolution. Furthermore, a change in temperature alone would not explain the narrow zone of BLG recrystallization microstructures near ~385 m depth, as temperature changes would be expected to be relatively large-scale due to pluton cooling and/or exhumation of the shear zone along the detachment. Although strain rate could only be derived for a limited number of samples, strain rates estimated for samples near the ~150 m microstructural transition with differential stresses of ~70 MPa (3×10^{-12} s^{-1}; CB13-76, CB13-78) are an order of magnitude higher than those estimated in deeper positions, supporting the role of strain rate in shear zone evolution. Strain rate estimates near ~150 m in the CBSZ are similar to the upper range of those calculated for the Ruby Mountains core complex (Nevada, USA; 10^{-11} to 10^{-13} s^{-1}) at similar differential stresses (~64 MPa) (Hacker et al., 1990).

Layering of Banded Mylonites

Layering of banded mylonites (Fig. 1.11E) occurs at depths ranging from 430 m to 111 m (Fig. 1.7). Formation of layered mylonites in granitoids has previously been attributed to reaction weakening associated with myrmekite formation and recrystallization of myrmekite (Ishii et al., 2007; Menegon et al., 2008) or to cataclastic deformation in feldspar (Pryer, 1993; Hippertt, 1998; Viegas et al., 2016b). Unlike with myrmekite formation, development of banded mylonites by cataclastic deformation can occur solely through brittle breakdown of feldspar with no reaction products (Viegas et al., 2016a). The deepest banded mylonite (CB13-55a, 430 m) records a transition from a coarse-grained feldspar network (Figs. 1.11A, 1.11B) to banded mylonite (Fig. 1.11E) at ~470 °C and moderately low stress (32.1 ± 14 MPa), corresponding to a strain rate of ~1 x 10^{-13} s^{-1}. In this sample, K-feldspar porphyroclasts with asymmetric strain-induced myrmekite have recrystallized tails that deflect into feldspar-rich layers. This transition, in addition to the abundance of myrmekite within the the CBSZ along K-feldspar porphyroclasts and also within feldspar C-bands (Figs. 1.7, 1.8D) suggests that myrmekite reaction, rather than cataclastic deformation, is the main process contributing to layering of banded mylonites within the CBSZ.

Development of polyphase domains within banded mylonites (Fig. 1.11F, i.e. CB13-55C, 369 m) may be promoted by dilation and precipitation accompanied by grain boundary sliding. Dissolution and precipitation in polyphase domains within this sample is inferred from K-feldspar filling dilatant sites between fine recrystallized quartz as well as from biotite and K-feldspar at quartz and plagioclase triple junctions. K-feldspar dissolution is reasonable in this scenario considering the abundance of myrmekite within the CBSZ (Fig. 1.7) and the excess K_2O produced in the myrmekite forming reaction (Eq. 6; Ishii et al., 2007). This type of behavior and microstructure is consistent with disaggregation of monophase domains by dynamic recrystallization, dissolution and precipitation in dilatant sites opened by rotation, and grain boundary sliding (Kilian et al., 2011a; Platt, 2015). Quartz domains also support a possible role of grain boundary sliding, as the CPOs show smeared a-axes with three dispersed maxima, consistent with the activity of GBS (Cross et al., 2017). Polygonal subgrains consistent with SGR recrystallization in quartz with a strong Y-maximum c-axis orientation indicate that dislocation creep with preferential prism <a> slip was also active, perhaps suggesting that quartz deformation at least locally was accommodated by a combination of grain boundary sliding and dislocation creep, or DisGBS (i.e. Miranda et al., 2016).

Conclusions

1. The CBSZ preserves an ~450-m-thick extensional shear zone characterized by undeformed granite in the core of the Cordillera Blanca batholith and increasingly mylonitized fabrics towards the western margin of the batholith. Brittle deformation occurs in the uppermost ~150 m, as evidenced by pseudotachylite, fault breccia, and cataclasite, and culminates in a moderate- to low- angle normal detachment fault.
2. Deformation along the CBSZ was initiated at near-solidus conditions above ~630 °C in weakly deformed granodiorite at the structurally lowest position relative to the discrete detachment fault and continued to subsolidus conditions by fracturing of feldspar phenocrysts, dislocation creep, and neocrystallization of fine-grained feldspar along with growth of

myrmekite. Initial interconnection of quartz domains occurred at temperatures near 500 °C under low stress (16.5 ± 13 MPa). Layering of mylonites at structurally deep positions occurred at 470 ± 50 °C where quartz recrystallized via grain-boundary migration and subgrain rotation processes during deformation by dislocation creep. Myrmekite growth contributed to the formation of banded mylonites with quartz monophase and quartz + feldspar ± mica polyphase domains. Dissolution and precipitation in dilatant sites may also have played a role in formation of layered mylonites and at least locally contributed, along with grain boundary sliding, to formation of fine-grained, mixed quartz + K-feldspar + Na-feldspar + biotite domains.

3. Quartz deformed predominantly by dislocation creep between 400 and 500 °C, producing strong CPOs indicative of prism <a> slip and rhomb <a> slip. Variations in differential stress estimates despite similar deformation temperatures across the shear zone suggest that strain rate, rather than temperature, may have been more important in shear zone evolution for the CBSZ. Through-going brittle fabrics overprint ductile quartz-rich fabrics within the upper ~150 m.

4. Differential stresses from the CBSZ are consistent with estimates from granitoids in other extensional settings such as the Ruby Mountains, and Whipple Mountains core complexes in the North American Cordillera. The highest differential stress in the CBSZ was recorded by the deepest sample within the shear zone to preserve a through-going brittle overprint of ductile fabrics, indicating that within the CBSZ, rocks have a strength of at least 71.5 ± 36 MPa at the ductile to brittle transition.

Acknowledgements

We thank Andrew Cross and John Platt for thorough and constructive reviews. Quartz reference materials were graciously provided by W. Nachlas. We thank J. Mauch for sampling support in the field, along with L. Kellerman at the Montana State University Imaging and

Chemical Analysis Laboratory for technical assistance in acquiring EBSD data, and A. Patchen at the University of Tennessee for assistance in acquiring EPMA data. We thank J. Langille for assistance in drafting of the map modified from Giovanni et al. (2010). A. Cafferata of Caraz, Peru and J. Olaza of Huaraz, Peru aided in field expeditions. This work would not have been possible without funding support from the National Science Foundation through grants EAR #1220237 to M. Jessup and EAR #1220216 to C. Shaw. TitaniQ geothermometry was funded by the Sigma Xi Grant-in-Aid of Research program, awarded to C. Hughes.

References

Arzi, A.A., 1978, Critical phenomena in the rheology of partially melted rocks: Tectonophysics, v. 44, p. 173–184, doi: 10.1016/0040-1951(78)90069-0.

Atherton, M.P., and Sanderson, L. M., 1987, The Cordillera Blanca Batholith: a study of granite intrusion and the relation of crustal thickening to peraluminosity: Geologisch Rundschau, v. 76, p. 213–232.

Bachmann, F., Hielscher, R., and Schaeben, H., 2010, Texture Analysis with MTEX – Free and Open Source Software Toolbox: Solid State Phenomena, v. 160, p. 63–68, doi: 10.4028/www.scientific.net/SSP.160.63.

Behr, W.M., and Platt, J.P., 2011, A naturally constrained stress profile through the middle crust in an extensional terrane: Earth and Planetary Science Letters, v. 303, p. 181–192, doi: 10.1016/j.epsl.2010.11.044.

Behr, W.M., and Platt, J.P., 2014, Brittle faults are weak, yet the ductile middle crust is strong: Implications for lithospheric mechanics: Geophysical Research Letters, v. 41, p. 8067–8075, doi: 10.1002/2014GL061349.

Behr, W.M., Thomas, J.B., and Hervig, R.L., 2011, Calibrating Ti concentrations in quartz for

SIMS determinations using NIST silicate glasses and application to the TitaniQ geothermobarometer: American Mineralogist, v. 96, p. 1100–1106, doi: 10.2138/am.2011.3702.

Behrmann, J.H., and Mainprice, D.H., 1987, Deformation mechanisms in a high-temperature quartz-feldspar mylonite: evidence for superplastic flow in the lower continental crust: Tectonophysics, v. 140, p. 297–305, doi: 10.1016/0040-1951(87)90236-8.

Berthé, D., Choukroune, P., and Jegouzo, P., 1979, Orthogneiss, mylonite and non coaxial deformation of granites: the example of the South Armorican Shear Zone: Journal of Structural Geology, v. 1, p. 31–42, doi: 10.1016/0191-8141(79)90019-1.

Bessiere, E., Rabillard, A., Précigout, J., Arbaret, L., Jolivet, L., Augier, R., Menant, A., and Mansard, N., 2018, Strain Localization Within a Syntectonic Intrusion in a Back-Arc Extensional Context: The Naxos Monzogranite (Greece): Tectonics, v. 37, p. 558–587, doi: 10.1002/2017TC004801.

Bestmann, M., and Prior, D.J., 2003, Intragranular dynamic recrystallization in naturally deformed calcite marble: diffusion accommodated grain boundary sliding as a result of subgrain rotation recrystallization: Journal of Structural Geology, v. 25, p. 1597–1613, doi: 10.1016/S0191-8141(03)00006-3.

Bonnot, D., 1984, Neotectonique et tectonique active de la Cordillere Blanche et du Callejon de Huaylans (Andes nord-Peruviennes) [Ph.D. thesis]: University de Paris-Sud, 123 p.

Bonnot, D., Sébrier, M., and Mercier, J., 1988, Évolution géodynamique plio-quaternaire du bassin intra-cordillérain du Callejon de Huaylas et de la Cordillère Blanche, Pérou: Géodynamique, v. 3, p. 57–83.

Bouchez, J.-L., Delas, C., Gleizes, G., and Nédélec, A., and Cuney, M., 1992, Submagmatic microfractures in granites: Geology, v. 20, p. 35–38.

Brace, W.F., and Kohlstedt, D.L., 1980, Limits on lithospheric stress imposed by laboratory experiments: Journal of Geophysical Research: Solid Earth, v. 85, p. 6248–6252, doi: 10.1029/JB085iB11p06248.

Bunge, H.J., 1982, Texture Analysis in Materials Science: Mathematical Methods (English [second] edition): London, Butterworths, 593 p.

Byerlee, J., 1978, Friction of rocks: Pure and Applied Geophysics, v. 116, p. 615–626, doi: 10.1007/BF00876528.

Carter, N.L., and Tsenn, M.C., 1987, Flow properties of continental lithosphere: Tectonophysics, v. 136, p. 27–63, https://doi.org/10.1016/0040-1951(87)90333-7.

Cobbing, E.J., Pitcher, W.S., Wilson, J.J., Baldock, J.W., Taylor, W.P., McCourt, W., and Snelling, N.J., 1981, The geology of the Western Cordillera of northern Peru: London, England, Institute of Geological Services, 144 p.

Columbu, S., Cruciani, G., Fancello, D., Franceschelli, M., and Musumeci, G., 2015, Petrophysical properties of a granite-protomylonite-ultramylonite sequence: insight from the Monte Grighini shear zone, central Sardinia, Italy: European Journal of Mineralogy, v. 27, p. 471–486, doi: 10.1127/ejm/2015/0027-2447.

Cooper, F.J., Platt, J.P., and Behr, W.M., 2017, Rheological transitions in the middle crust: insights from Cordilleran metamorphic core complexes: Solid Earth, v. 8, p. 199–215, doi: 10.5194/se-8-199-2017.

Cross, A.J., Kidder, S., and Prior, D.J., 2015, Using microstructures and TitaniQ thermobarometry of quartz sheared around garnet porphyroclasts to evaluate microstructural evolution and constrain an Alpine Fault Zone geotherm: v. 75, p. 17–31.

Cross, A.J., Hirth, G., and Prior, D.J., 2017a, Effects of secondary phases on crystallographic preferred orientations in mylonites: Geology, v. 45, p. 955–958, doi: 10.1130/G38936.1.

Cross, A.J., Prior, D.J., Stipp, M., and Kidder, S., 2017b, The recrystallized grain size piezometer for quartz: An EBSD-based calibration: Geophysical Research Letters, v. 44, p. 6667–6674, doi: 10.1002/2017GL073836.

Czaplińska, D., Piazolo, S., and Zibra, I., 2015, The influence of phase and grain size distribution on the dynamics of strain localization in polymineralic rocks: Journal of Structural Geology, v. 72, p. 15–32, doi: 10.1016/j.jsg.2015.01.001.

Fitz Gerald, J.D., and Stünitz, H., 1993, Deformation of granitoids at low metamorphic grade. I: Reactions and grain size reduction: Tectonophysics, v. 221, p. 269–297, doi: 10.1016/0040-1951(93)90164-F.

Fukuda, J.I., Okudaira, T., Satsukawa, T., and Michibayashi, K., 2012, Solution-precipitation of K-feldspar in deformed granitoids and its relationship to the distribution of water: Tectonophysics, v. 532–535, p. 175–185, doi: 10.1016/j.tecto.2012.01.033.

Fusseis, F., and Handy, M.R., 2008, Micromechanisms of shear zone propagation at the brittle-viscous transition: Journal of Structural Geology, v. 30, p. 1242–1253, doi: 10.1016/j.jsg.2008.06.005.

Fusseis, F., Regenauer-Lieb, K., Liu, J., Hough, R.M., and De Carlo, F., 2009, Creep cavitation can establish a dynamic granular fluid pump in ductile shear zones.: Nature, v. 459, p. 974–977, doi: 10.1038/nature08051.

Gan, W., Zhang, P., Shen, Z.K., Niu, Z., Wang, M., Wan, Y., Zhou, D., and Cheng, J., 2007, Present-day crustal motion within the Tibetan Plateau inferred from GPS measurements: Journal of Geophysical Research: Solid Earth, v. 112, B08416, doi:

10.1029/2005JB004120.

Ghent, E.D., and Stout, M.Z., 1984, TiO2 activity in metamorphosed pelitic and basic rocks: principles and applications to metamorphism in southeastern Canadian Cordillera: Contributions to Mineralogy and Petrology, v. 86, p. 248–255, doi: 10.1007/BF00373670.

Giovanni, M.K., 2007, Tectonic and Thermal Evolution of the Cordillera Blanca Detachment System, Peruvian Andes: Implications for Normal Faulting in a Contractional Orogen [Ph.D. thesis]: University of California Los Angeles, 237 p.

Giovanni, M.K., Horton, B.K., Garzione, C.N., McNulty, B. a., and Grove, M., 2010, Extensional basin evolution in the Cordillera Blanca, Peru: Stratigraphic and isotopic records of detachment faulting and orogenic collapse in the Andean hinterland: Tectonics, v. 29, TC6007, doi: 10.1029/2010TC002666.

Goscombe, B.D., Passchier, C.W., and Hand, M., 2004, Boudinage classification: End-member boudin types and modified boudin structures: Journal of Structural Geology, v. 26, p. 739–763, doi: 10.1016/j.jsg.2003.08.015.

Gottardi, R., and Teyssier, C., 2013, Thermomechanics of an extensional shear zone, Raft River metamorphic core complex, NW Utah: Journal of Structural Geology, v. 53, p. 54–69, doi: 10.1016/j.jsg.2013.05.012.

Grujic, D., Stipp, M., and Wooden, J.L., 2011, Thermometry of quartz mylonites: Importance of dynamic recrystallization on Ti-in-quartz reequilibration: Geochemistry, Geophysics, Geosystems, v. 12, Q06012, doi: 10.1029/2010GC003368.

Gutscher, M.A., Olivet, J.L., Aslanian, D., Eissen, J.P., and Maury, R., 1999, The “lost Inca Plateau”: Cause of flat subduction beneath Peru? Earth and Planetary Science Letters, v.

171, p. 335–341, doi: 10.1016/S0012-821X(99)00153-3.

Hacker, B.R., Yin, A., Christie, J.M., and Snoke, A.W., 1990, Differential Stress, Strain Rate, and Temperatures of Mylonitization in the Ruby Mountains, Nevada: Implications for the Rate and Duration of Uplift: Journal of Geophysical Research, v. 95, p. 8569–8580, doi: 10.1029/JB095iB06p08569.

Haertel, M., and Herwegh, M., 2014, Microfabric memory of vein quartz for strain localization in detachment faults: A case study on the Simplon fault zone: Journal of Structural Geology, v. 68, p. 16–32, doi: 10.1016/j.jsg.2014.08.001.

Haertel, M., Herwegh, M., and Pettke, T., 2013, Titanium-in-quartz thermometry on synkinematic quartz veins in a retrograde crustal-scale normal fault zone: Tectonophysics, v. 608, p. 468–481, doi: 10.1016/j.tecto.2013.08.042.

Halfpenny, A., Prior, D.J., and Wheeler, J., 2006, Analysis of dynamic recrystallization and nucleation in a quartzite mylonite: Tectonophysics, v. 427, p. 3–14, doi: 10.1016/j.tecto.2006.05.016.

Halfpenny, A., Prior, D.J., and Wheeler, J., 2012, Electron backscatter diffraction analysis to determine the mechanisms that operated during dynamic recrystallisation of quartz-rich rocks: Journal of Structural Geology, v. 36, p. 2–15, doi: 10.1016/j.jsg.2012.01.001.

Handy, M.R., Wissing, S.B., and Streit, L.E., 1999, Frictional-viscous flow in mylonite with varied bimineralic composition and its effect on lithospheric strength: Tectonophysics, v. 303, p. 175–191, doi: 10.1016/S0040-1951(98)00251-0.

Hayden, L.A., and Watson, E.B., 2007, Rutile saturation in hydrous siliceous melts and its bearing on Ti-thermometry of quartz and zircon: Earth and Planetary Science Letters, v. 258, p. 561–568, doi: 10.1016/j.epsl.2007.04.020.

Heilbronner, R.P., and Tullis, J., 2006, Evolution of c axis pole figures and grain size during dynamic recrystallization: Results from experimentally sheared quartzite: Journal of Geophysical Research: Solid Earth, v. 111, B10202, doi: 10.1029/2005JB004194.

Hippertt, J.F.M., 1993, ’V’-pull-apart microstructures: a new shear-sense indicator: Journal of Structural Geology, v. 15, p. 1393–1403, doi: 10.1016/0191-8141(93)90001-Q.

Hippertt, J.F.M., 1998, Breakdown of feldspar, volume gain and lateral mass transfer during mylonitization of granitoid in a low metamorphic grade shear zone: Journal of Structural Geology, v. 20, p. 175–193, doi: 10.1016/S0191-8141(97)00083-7.

Hirth, G., Teyssier, C., and Dunlap, W.J., 2001, An evaluation of quartzite flow laws based on comparisons between experimentally and naturally deformed rocks: International Journal of Earth Sciences, v. 90, p. 77–87, doi: 10.1007/s005310000152.

Hirth, G., and Tullis, J., 1992, Dislocation creep regimes in quartz aggregates: Journal of Structural Geology, v. 14, p. 145–159, doi: 10.1016/0191-8141(92)90053-Y.

Hirth, G., and Tullis, J., 1994, The brittle-plastic transition in experimentally deformed quartz aggregates: Journal of Geophysical Research, v. 99, p. 11731–11747, doi: 10.1029/93JB02873.

Holyoke, C.W., III, and Kronenberg, A.K., 2010, Accurate differential stress measurement using the molten salt cell and solid salt assemblies in the Griggs apparatus with applications to strength, piezometers and rheology: Tectonophysics, v. 494, p. 17–31, doi: 10.1016/j.tecto.2010.08.001.

Holyoke, C.W., III, and Tullis, J., 2006, The interaction between reaction and deformation: An experimental study using a biotite + plagioclase + quartz gneiss: Journal of Metamorphic Geology, v. 24, p. 743–762, doi: 10.1111/j.1525-1314.2006.00666.x.

Huang, R., and Audétat, A., 2012, The titanium-in-quartz (TitaniQ) thermobarometer: A critical examination and re-calibration: Geochimica et Cosmochimica Acta, v. 84, p. 75–89, doi: 10.1016/j.gca.2012.01.009.

Ishii, K., Kanagawa, K., Shigematsu, N., and Okudaira, T., 2007, High ductility of K-feldspar and development of granitic banded ultramylonite in the Ryoke metamorphic belt, SW Japan: Journal of Structural Geology, v. 29, p. 1083–1098, doi: 10.1016/j.jsg.2007.02.008.

James, D.E., 1971, Plate Tectonic Model for the Evolution of the Central Andes: Geological Society of America Bulletin, v. 82, p. 3325-3346, doi: https://doi.org/10.1130/0016-7606(1971)82[3325:PTMFTE]2.0.CO;2

Jiang, Z., Prior, D.J., and Wheeler, J., 2000, Albite crystallographic preferred orientation and grain misorientation distribution in a low-grade mylonite: implications for granular flow: Journal of Structural Geology, v. 22, p. 1663–1674.

Jordan, T.E., Isacks, B.L., Allmendinger, R.W., Brewer, J. a., Ramos, V.A., and Ando, C.J., 1983, Andean tectonics related to geometry of subducted Nazca plate.: Geological Society of America Bulletin, v. 94, p. 341–361, doi: 10.1130/0016-7606(1983)94<341:ATRTGO>2.0.CO;2.

Keller, L.M., and Stipp, M., 2011, The single-slip hypothesis revisited: Crystal-preferred orientations of sheared quartz aggregates with increasing strain in nature and numerical simulation: Journal of Structural Geology, v. 33, p. 1491–1500, doi: 10.1016/j.jsg.2011.07.008.

Kidder, S., Avouac, J.P., and Chan, Y.C., 2013, Application of titanium-in-quartz thermobarometry to greenschist facies veins and recrystallized quartzites in the

Hsüehshan range, Taiwan: Solid Earth, v. 4, p. 1–21, doi: 10.5194/se-4-1-2013.

Kilian, R., Heilbronner, R.P., and Stünitz, H., 2011, Quartz grain size reduction in a granitoid rock and the transition from dislocation to diffusion creep: Journal of Structural Geology, v. 33, p. 1265–1284, doi: 10.1016/j.jsg.2011.05.004.

Kirby, S.H., 1983, Rheology of the Lithosphere: Reviews of Geophysics and Space Physics, v. 21, p. 1458–1487.

Kirby, S.H., 1980, Tectonic stresses in the lithosphere: Constraints provided by the experimental deformation of rocks: Journal of Geophysical Research: Solid Earth, v. 85, p. 6353–6363, doi: 10.1029/JB085iB11p06353.

Kruhl, J.H., 1996, Prism- and basal-plane parallel subgrain boundaries in quartz: a microstructural geothermobaromether: Journal of Metamorphic Geology, v. 14, p. 581–589, doi: 10.1046/j.1525-1314.1996.00413.x.

Kularatne, K., and Audétat, A., 2014, Rutile solubility in hydrous rhyolite melts at 750-900°C and 2kbar, with application to titanium-in-quartz (TitaniQ) thermobarometry: Geochimica et Cosmochimica Acta, v. 125, p. 196–209, doi: 10.1016/j.gca.2013.10.020.

Langille, J.M., Jessup, M.J., Cottle, J.M., Newell, D.L., and Seward, G., 2010, Kinematic evolution of the Ama Drime detachment: Insights into orogen-parallel extension and exhumation of the Ama Drime Massif, Tibet-Nepal: Journal of Structural Geology, v. 32, p. 900–919, doi: 10.1016/j.jsg.2010.04.005.

Law, R.D., 2014, Deformation thermometry based on quartz c-axis fabrics and recrystallization microstructures: A review: Journal of Structural Geology, v. 66, p. 129–161, doi: 10.1016/j.jsg.2014.05.023.

Law, R.D., Schmid, S.M., and Wheeler, J., 1990, Simple shear deformation and quartz crystallographic fabrics: a possible natural example from the Torridon area of NW Scotland: Journal of Structural Geology, v. 12, p. 29–45, doi: 10.1016/0191-8141(90)90046-2.

Lister, G.S., and Hobbs, B.E., 1980, The simulation of fabric development during plastic deformation and its application to quartzite: the influence of deformation history: Journal of Structural Geology, v. 2, p. 355–370, doi: 10.1016/0191-8141(80)90023-1.

Lister, G.S., and Snoke, A.W., 1984, S-C Mylonites: Journal of Structural Geology, v. 6, p. 617–638, doi: 10.1016/0191-8141(84)90001-4.

Lloyd, G.E., Law, R.D., Mainprice, D.H., and Wheeler, J., 1992, Microstructural and crystal fabric evolution during shear zone formation: Journal of Structural Geology, v. 14, p. 1079–1100, doi: 10.1016/0191-8141(92)90037-W.

Mainprice, D.H., Bouchez, J.-L., Blumenfeld, P., and Tubia, J.M., 1986, Dominant c slip in naturally deformed quartz: Implications for dramatic plastic softening at high temperature: Geology, v. 14, p. 819–822, doi: 10.1130/0091-7613(1986)14.

Mainprice, D.H., and Paterson, M.S., 1984, Experimental studies of the role of water in the plasticity of quartzites: Journal of Geophysical Research, v. 89, p. 4257–4269.

Mancktelow, N.S., and Pennacchioni, G., 2004, The influence of grain boundary fluids on the microstructure of quartz-feldspar mylonites: Journal of Structural Geology, v. 26, p. 47–69, doi: 10.1016/S0191-8141(03)00081-6.

Margirier, A., Audin, L., Robert, X., Herman, F., Ganne, J., and Schwartz, S., 2016, Time and mode of exhumation of the Cordillera Blanca batholith (Peruvian Andes): Journal of Geophysical Research: Solid Earth, v. 121, p. 6235–6249, doi: 10.1002/2016JB013055.

Margirier, A., Robert, X., Audin, L., Gautheron, C., Bernet, M., Hall, S., and Simon-Labric, T., 2015, Slab flattening, magmatism, and surface uplift in the Cordillera Occidental (Northern Peru): Geology, v. 43, p. 1031–1034, doi: 10.1130/G37061.1.

McLaren, A.C., and Pryer, L.L., 2001, Microstructural investigation of the interaction and interdependence of cataclastic and plastic mechanisms in Feldspar crystals deformed in the semi-brittle field: Tectonophysics, v. 335, p. 1–15, doi: 10.1016/S0040-1951(01)00042-7.

McNulty, B. a., and Farber, D., 2002, Active detachment faulting above the Peruvian flat slab: Geology, v. 30, p. 567–570, doi: 10.1130/0091-7613(2002)030<0567:ADFATP>2.0.CO;2.

McNulty, B. a., Farber, D.L., Wallace, G.S., Lopez, R., and Palacios, O., 1998, Role of plate kinematics and plate-slip-vector partitioning in continental magmatic arcs: Evidence from the Cordillera Blanca, Peru: Geology, v. 26, p. 827–830, doi: 10.1130/0091-7613(1998)026<0827:ROPKAP>2.3.CO;2.

Menegon, L., Fusseis, F., Stünitz, H., and Xiao, X., 2015, Creep cavitation bands control porosity and fluid flow in lower crustal shear zones: Geology, v. 43, p. 227-230, doi: 10.1130/G36307.1.

Menegon, L., Pennacchioni, G., and Spiess, R., 2008, Dissolution-precipitation creep of K-feldspar in mid-crustal granite mylonites: Journal of Structural Geology, v. 30, p. 565–579, doi: 10.1016/j.jsg.2008.02.001.

Menegon, L., Pennacchioni, G., and Stünitz, H., 2006, Nucleation and growth of myrmekite during ductile shear deformation in metagranites: Journal of Metamorphic Geology, v. 24, p. 553–568, doi: 10.1111/j.1525-1314.2006.00654.x.

Miranda, E.A., Hirth, G., and John, B.E., 2016, Microstructural evidence for the transition from dislocation creep to dislocation-accommodated grain boundary sliding in naturally deformed plagioclase: Journal of Structural Geology, v. 92, p. 30-45, doi: 10.1016/j.jsg.2016.09.002.

Morales, L.F.G., Lloyd, G.E., and Mainprice, D.H., 2014, Fabric transitions in quartz via viscoplastic self-consistent modeling part I: Axial compression and simple shear under constant strain: Tectonophysics, v. 636, p. 52–69, doi: 10.1016/j.tecto.2014.08.011.

Morales, L.F.G., Mainprice, D.H., Lloyd, G.E., and Law, R.D., 2011, Crystal fabric development and slip systems in a quartz mylonite: an approach via transmission electron microscopy and viscoplastic self-consistent modelling, *in* Prior, D.J., Rutter, E.H., and Tatham, D.J., eds., Deformation Mechanisms, Rheology and Tectonics: Microstructures, Mechanics and Anisotropy: Geological Society, London, Special Publications, v. 360, p. 151–174, doi: 10.1144/SP360.9.

Mukasa, S.B., 1984, Comparative Pb isotope systematics and zircon U-Pb geochronology for the Coastal, San Nicolas, and Cordillera Blanca Batholiths, Peru [Ph.D. thesis]: Santa Barbara, University of California, Santa Barbara, 148 p.

Nachlas, W.O., and Hirth, G., 2015, Experimental constraints on the role of dynamic recrystallization on resetting the Ti-in-quartz thermobarometer: Journal of Geophysical Research: Solid Earth, v. 120, p. 8120–8137, doi: 10.1002/2015JB012274.

Nachlas, W.O., Thomas, J.B., and Hirth, G., 2018, TitaniQ deformed: Experimental deformation of out-of-equilibrium quartz porphyroclasts: Journal of Structural Geology, v. 116, p. 207–222, doi: 10.1016/j.jsg.2018.07.012.

Nachlas, W.O., Whitney, D.L., Teyssier, C., Bagley, B., and Mulch, A., 2014, Titanium concentration in quartz as a record of multiple deformation mechanisms in an extensional shear zone: Geochemistry, Geophysics, Geosystems, v. 15, p. 1374–1397, doi:

10.1002/2013GC005200.

Newell, D.L., Jessup, M.J., Hilton, D.R., Shaw, C., and Hughes, C., 2015, Mantle-Derived Helium in Hot Springs of the Cordillera Blanca, Peru: Implications for Mantle-to- Crust Fluid Transfer in a Flat-Slab Subduction Setting: Chemical Geology Chemical Geology Chemical Geology, v. 417, p. 200–209, doi: 10.1016/j.chemgeo.2015.10.003.

Oliot, E., Goncalves, P., Schulmann, K., Marquer, D., and Lexa, O., 2014, Mid-crustal shear zone formation in granitic rocks: Constraints from quantitative textural and crystallographic preferred orientations analyses: Tectonophysics, v. 612–613, p. 63–80, doi: 10.1016/j.tecto.2013.11.032.

Passchier, C.W., and Trouw, R. a J., 2005, Microtectonics: Berlin, Heidelberg, Springer-Verlag, 366 p., doi: 10.1007/3-540-29359-0.

Paterson, S.R., Vernon, R.H., and Tobisch, O.T., 1989, A review of criteria for the identification of magmatic and tectonic foliations in granitoids: Journal of Structural Geology, v. 11, p. 349–363, doi: 10.1016/0191-8141(89)90074-6.

Pennacchioni, G., Menegon, L., Leiss, B., Nestola, F., and Bromiley, G., 2010, Development of crystallographic preferred orientation and microstructure during plastic deformation of natural coarse-grained quartz veins: Journal of Geophysical Research: Solid Earth, v. 115, B12405, doi: 10.1029/2010JB007674.

Pennacchioni, G., Di Toro, G., Brack, P., Menegon, L., and Villa, I.M., 2006, Brittle-ductile-brittle deformation during cooling of tonalite (Adamello, Southern Italian Alps): Tectonophysics, v. 427, p. 171–197, doi: 10.1016/j.tecto.2006.05.019.

Peterman, E.M., and Grove, M., 2010, Growth conditions of symplectic muscovite + quartz: Implications for quantifying retrograde metamorphism in exhumed magmatic arcs:

Geology, v. 38, p. 1071–1074, doi: 10.1130/G31449.1.

Petford, N., and Atherton, M.P., 1992, Granitoid emplacement and deformation along a major crustal lineament: The Cordillera Blanca, Peru: Tectonophysics, v. 205, p. 171–185, doi: 10.1016/0040-1951(92)90425-6.

Petford, N., and Atherton, M.P., 1996, Na-rich Partial Melts from Newly Underplated Basaltic Crust: the Cordillera Blanca Batholith, Peru: Journal of Petrology, v. 37, p. 1491–1521, doi: 10.1093/petrology/37.6.1491.

Pfiffner, O. A., and Gonzalez, L., 2013., Mesozoic–Cenozoic Evolution of the Western Margin of South America: Case Study of the Peruvian Andes: Geosciences, v. 3, p. 262-310.

Phillips, E.R., Ransom, D.M., and Vernon, R.H., 1972, Myrmekite and muscovite developed by retrograde metamorphism at Broken Hill, New South Wales: Mineralogical Magazine, v. 38, p. 570–78.

Platt, J.P., 2015, Rheology of two-phase systems: A microphysical and observational approach: Journal of Structural Geology, v. 77, p. 213–227, doi: 10.1016/j.jsg.2015.05.003.

Platt, J.P., and Behr, W.M., 2011a, Grainsize evolution in ductile shear zones: Implications for strain localization and the strength of the lithosphere: Journal of Structural Geology, v. 33, p. 537–550, doi: 10.1016/j.jsg.2011.01.018.

Platt, J.P., and Behr, W.M., 2011b, Lithospheric shear zones as constant stress experiments: Geology, v. 39, p. 127–130, doi: 10.1130/G31561.1.

Pryer, L.L., 1993, Microstructures in feldspars from a major crustal thrust zone: The Grenville Front, Ontario, Canada: Journal of Structural Geology, v. 15, p. 21–36, doi: 10.1016/0191-8141(93)90076-M.

Rahl, J.M., and Skemer, P., 2016, Microstructural evolution and rheology of quartz in a mid-crustal shear zone: Tectonophysics, v, 680, p. 129-139, doi: 10.1016/j.tecto.2016.05.022.

Ramos, V.A., 1999, Plate tectonic setting of the Andean Cordillera: Episodes, v. 22, p. 183–190.

Ree, J.H., Kim, H.S., Han, R., and Jung, H., 2005, Grain-size reduction of feldspars by fracturing and neocrystallization in a low-grade granitic mylonite and its rheological effect: Tectonophysics, v. 407, p. 227–237, doi: 10.1016/j.tecto.2005.07.010.

Rosenberg, C.L., 2001, Deformation of partially molten granite: a review and comparison of experimental and natural case studies: International Journal of Earth Sciences, v. 90, p. 60–76, doi: 10.1007/s005310000164.

Rosenberg, C.L., and Handy, M.R., 2005, Experimental deformation of partially melted granite revisited: Implications for the continental crust: Journal of Metamorphic Geology, v. 23, p. 19–28, doi: 10.1111/j.1525-1314.2005.00555.x.

Rutter, E.H., 1986, On the nomenclature of mode of failure transitions in rocks: Tectonophysics, v. 122, p. 381–387, doi: 10.1016/0040-1951(86)90153-8.

Rutter, E.H., and Brodie, K.H., 2004, Experimental intracrystalline plastic flow in hot-pressed synthetic quartzite prepared from Brazilian quartz crystals: Journal of Structural Geology, v. 26, p. 259–270, doi: 10.1016/S0191-8141(03)00096-8.

Rutter, E.H., Holdsworth, R.E., and Knipe, R.J., 2001. The nature and tectonic significance of fault-zone weakening: an introduction, *in* Holdsworth, R.E., Strachan, R.A., Magloughlin, J.F. & Knipe, RJ. (eds). The Nature and Tectonic Significance of Fault Zone Weakening. Geological Society, London, Special Publications, 186.

Samanta, S.K., Mandal, N., and Chakraborty, C., 2002, Development of different types of pull-apart microstructures in mylonites: An experimental investigation: Journal of Structural Geology, v. 24, p. 1345–1355, doi: 10.1016/S0191-8141(01)00139-0.

Scherrenberg, A.F., Holcombe, R.J., and Rosenbaum, G., 2014, The persistence and role of basin structures on the 3D architecture of the Marañón Fold-Thrust Belt, Peru: Journal of South American Earth Sciences, v. 51, p. 45–58, doi: 10.1016/j.jsames.2013.12.007.

Scherrenberg, A.F., Kohn, B.P., Holcombe, R.J., and Rosenbaum, G., 2016, Thermotectonic history of the Marañón Fold–Thrust Belt, Peru: Insights into mineralisation in an evolving orogen: Tectonophysics, v. 667, p. 16–36, doi: 10.1016/j.tecto.2015.11.007.

Schmid, S.M., and Casey, M., 1986, Complete Fabric Analysis of some Commonly Observed Quartz C-axis Patterns, *in* Hobbs, B.E., and Heard, H.C., eds., Mineral and Rock 1149 Deformation: Laboratory Studies: American Geophysical Union Geophysical Monograph, v. 36, p. 263–286, https://doi.org/10.1029/GM036p0263.

Schwartz, D.P., 1988, Paleoseismicity and Neotectonics of the Cordillera Blanca Fault Zone, Northern Peruvian Andes: Journal of Geophysical Research, v. 93, p. 4712–4730.

Siame, L.L., Sébrier, M., Bellier, O., and Bourles, D., 2006, Can cosmic ray exposure dating reveal the normal faulting activity of the Cordillera Blanca Fault, Peru? Revista de la Asociacion Geologica Argentina, v. 61, p. 536–544.

Sibson, R.H., 1983, Continental fault structure and the shallow earthquake source: Journal of the Geological Society, v. 140, p. 741–767, doi: 10.1144/gsjgs.140.5.0741.

Simpson, C., 1985, Deformation of granitic rocks across the brittle-ductile transition: Journal of Structural Geology, v. 7, p. 503–511.

Simpson, C., and Wintsch, R.P., 1989, Evidence for deformation-induced K-feldspar replacement by myrmekite: Journal of Metamorphic Geology, v. 7, p. 261–275, doi: 10.1111/j.1525-1314.1989.tb00588.x.

Singleton, J.S., and Mosher, S., 2012, Mylonitization in the lower plate of the Buckskin-Rawhide detachment fault, west-central Arizona: Implications for the geometric evolution of metamorphic core complexes: Journal of Structural Geology, v. 39, p. 180–198, doi: 10.1016/j.jsg.2012.02.013.

Skemer, P., Katayama, I., Jiang, Z., and Karato, S., 2005, The misorientation index: Development of a new method for calculating the strength of lattice-preferred orientation: Tectonophysics, v. 411, p. 157–167, doi: 10.1016/j.tecto.2005.08.023.

Spruzeniece, L., and Piazolo, S., 2015, Strain localization in brittle–ductile shear zones: fluid-abundant vs. fluid-limited conditions (an example from Wyangala area, Australia): Solid Earth, v. 6, p. 881–901, doi: 10.5194/se-6-881-2015.

Sterner, S.M., and Pitzer, K.S., 1994, An equation of state for carbon dioxide valid from zero to extreme pressures: Contributions to Mineralogy and Petrology, v. 117, p. 362–374, doi: 10.1007/BF00307271.

Stipp, M., Stünitz, H., Heilbronner, R.P., and Schmid, S.M., 2002a, Dynamic recrystallization of quartz: correlation between natural and experimental conditions, *in* De Meer, S., Drury, M.R., De Bresser, J.H.P., and Pennock, G.M., eds., Deformation Mechanisms, Rheology and Tectonics: Status and Future Perspectives: Geological Society, London, Special Publications, v. 200, p. 171–190, doi: 10.1144/GSL.SP.2001.200.01.11.

Stipp, M., Stünitz, H., Heilbronner, R.P., and Schmid, S.M., 2002b, The eastern Tonale fault zone: A “natural laboratory” for crystal plastic deformation of quartz over a temperature range from 250 to 700 °C: Journal of Structural Geology, v. 24, p. 1861–1884, doi: 10.1016/S0191-8141(02)00035-4.

Stipp, M., and Tullis, J., 2003, The recrystallized grain size piezometer for quartz: Geophysical Research Letters, v. 30, p. 1–5, doi: 10.1029/2003GL018444.

Stipp, M., Tullis, J., and Behrens, H., 2006, Effect of water on the dislocation creep microstructure and flow stress of quartz and implications for the recrystallized grain size piezometer: Journal of Geophysical Research: Solid Earth, v. 111, B04201, doi: 10.1029/2005JB003852.

Storey, C.D., and Prior, D.J., 2005, Plastic Deformation and Recrystallization of Garnet: A Mechanism to Facilitate Diffusion Creep: Journal of Petrology, v. 46, p. 2593–2613, doi: 10.1093/petrology/egi067.

Stormer, J.C. Jr., 1975, A Practical Two-feldspar Geothermometer: American Mineralogist, v. 60, p. 667-674.

Stünitz, H., and Fitz Gerald, J.D., 1993, Deformation of granitoids at low metamorphic grade. II: Granular flow in albite-rich mylonites: Tectonophysics, v. 221, p. 299–324, doi: 10.1016/0040-1951(93)90164-F.

Stünitz, H., Fitz Gerald, J.D., and Tullis, J., 2003, Dislocation generation, slip systems, and dynamic recrystallization in experimentally deformed plagioclase single crystals: Tectonophysics, v. 372, p. 215–233, doi: 10.1016/S0040-1951(03)00241-5.

Stünitz, H., and Tullis, J., 2001, Weakening and strain localization produced by syn-deformational reaction of plagioclase: International Journal of Earth Sciences, v. 90, p. 136–148, doi: 10.1007/s005310000148.

Sullivan, W. a., Boyd, a. S., and Monz, M.E., 2013, Strain localization in homogeneous granite near the brittle-ductile transition: A case study of the Kellyland fault zone, Maine, USA: Journal of Structural Geology, v. 56, p. 1–19, doi: 10.1016/j.jsg.2013.09.003.

Thomas, J.B., and Watson, E.B., 2012, Application of the Ti-in-quartz thermobarometer to rutile-free systems. Reply to: A comment on: “TitaniQ under pressure: The effect of pressure and temperature on the solubility of Ti in quartz” by Thomas et al: Contributions to Mineralogy and Petrology, v. 164, p. 369–374, doi: 10.1007/s00410-012-0761-5.

Thomas, J.B., Watson, E.B., Spear, F.S., Shemella, P.T., Nayak, S.K., and Lanzirotti, A., 2010, TitaniQ under pressure: The effect of pressure and temperature on the solubility of Ti in quartz: Contributions to Mineralogy and Petrology, v. 160, p. 743–759, doi: 10.1007/s00410-010-0505-3.

Tokle, L., Hirth, G., and Behr, W.M., 2019, Flow laws and fabric transitions in wet quartzite: Earth and Planetary Science Letters, v. 505, p. 152-161, https://doi.org/10.1016/j.epsl.2018.10.01.

Toy, V.G., Prior, D.J., and Norris, R.J., 2008, Quartz fabrics in the Alpine Fault mylonites: Influence of pre-existing preferred orientations on fabric development during progressive uplift: Journal of Structural Geology, v. 30, p. 602–621, doi: 10.1016/j.jsg.2008.01.001.

Tsurumi, J., Hosonuma, H., and Kanagawa, K., 2002, Strain localization due to a positive feedback of deformation and myrmekite-forming reaction in granite and aplite mylonites along the Hatagawa Shear Zone of NE Japan: Journal of Structural Geology, v. 25, p. 557–574, doi: 10.1016/S0191-8141(02)00048-2.

Tullis, J., Christie, J.M., and Griggs, D.T., 1973, Microstructures and preferred orientations of experimentally deformed quartzites: Bulletin of the Geological Society of America, v. 84, p. 297–314, doi: 10.1130/0016-7606(1973)84<297:MAPOOE>2.0.CO;2.

Tullis, J., and Yund, R. a, 1991, Diffusion creep in feldspar aggregates: experimental evidence: Journal of Structural Geology, v. 13, p. 987–1000, doi: 10.1016/0191-8141(91)90051-J.

Tullis, J., and Yund, R.A., 1985, Dynamic recrystallization of feldspar: A mechanism for ductile shear zone formation: Geology, v. 13, p. 238, doi: 10.1130/0091-

7613(1985)13<238:DROFAM>2.0.CO;2.

Tullis, J., and Yund, R. a., 1977, Experimental deformation of dry Westerly granite: Journal of Geophysical Research, v. 82, p. 5705–5718.

Tullis, J., and Yund, R. a., 1980, Hydrolytic weakening of experimentally deformed Westerly granite and Hale albite rock: Journal of Structural Geology, v. 2, p. 439–451, doi: 10.1016/0191-8141(80)90005-X.

Tullis, J., and Yund, R.A., 1987, Transition from cataclastic flow to dislocation creep of feldspar: mechanisms and microstructures.: Geology, v. 15, p. 606–609, doi: 10.1130/0091-7613(1987)15<606:TFCFTD>2.0.CO.

Twiss, R.J., 1977, Theory And Applicability Of A Recrystallized Grain-Size Paleopiezometer: Pure And Applied Geophysics, v. 115, p. 227–244.

Viegas, G., Menegon, L., and Archanjo, C., 2016, Brittle grain-size reduction of feldspar, phase mixing and strain localization in granitoids at mid-crustal conditions (Pernambuco shear zone, NE Brazil): Solid Earth, v. 7, p. 375–396, doi: 10.5194/se-7-375-2016.

Wark, D. a., and Watson, E.B., 2006, TitaniQ: A titanium-in-quartz geothermometer: Contributions to Mineralogy and Petrology, v. 152, p. 743–754, doi: 10.1007/s00410-006-0132-1.

Warren, J.M., and Hirth, G., 2006, Grain size sensitive deformation mechanisms in naturally deformed peridotites: Earth and Planetary Science Letters, v. 248, p. 438–450, doi: 10.1016/j.epsl.2006.06.006.

Wehrens, P., Berger, A., Peters, M., Spillmann, T., and Herwegh, M., 2016, Deformation at the frictional-viscous transition: Evidence for cycles of fluid-assisted embrittlement and ductile deformation in the granitoid crust: Tectonophysics, v. 693, p. 66–84.

Wells, M.L., Beyene, M. a., Spell, T.L., Kula, J.L., Miller, D.M., and Zanetti, K. a., 2005, The Pinto shear zone; a Laramide synconvergent extensional shear zone in the Mojave Desert region of the southwestern United States: Journal of Structural Geology, v. 27, p. 1697–1720, doi: 10.1016/j.jsg.2005.03.005.

Whitney, J.A., Stormer, J. C. Jr., 1977, The distribution of $NaAlSi_3O_8$ between coexisting microcline and plagioclase and its effect on geothermometric calculations: American Mineralogist, v. 62, p. 687-691.

Wightman, R.H., Prior, D.J., and Little, T.A., 2006, Quartz veins deformed by diffusion creep-accommodated grain boundary sliding during a transient, high strain-rate event in the Southern Alps, New Zealand:, doi: 10.1016/j.jsg.2006.02.008.

Wilson, P.A., 1975, Potassium-argon age studies in peru with particular reference to the chronology of emplacement of the coastal batholith [Ph.D. thesis]: Liverpool, UK, The University of Liverpool (United Kingdom), 299 p.

Wintsch, R.P., and Yeh, M.W., 2013, Oscillating brittle and viscous behavior through the earthquake cycle in the Red River Shear Zone: Monitoring flips between reaction and textural softening and hardening: Tectonophysics, v. 587, p. 46–62, doi: 10.1016/j.tecto.2012.09.019.

Wise, J.M., and Noble, D.C., 2003, Geomorphic Evolution of the Cordillera Blanca, Northern Peru: Boletín de la Sociedad Geológica del Perú v. 96, p. 65–85.

Yund, R.A., and Tullis, J., 1980, Contributions to Mineralogy and Petrology The Effect of Water, Pressure, and Strain on Ai/Si Order-Disorder Kinetics in Feldspar: Contrib. Mineral. Petrol, v. 72.

Zibra, I., Kruhl, J.H., Montanini, a., and Tribuzio, R., 2012, Shearing of magma along a high-grade shear zone: Evolution of microstructures during the transition from magmatic to solid-state flow: Journal of Structural Geology, v. 37, p. 150–160, doi: 10.1016/j.jsg.2012.01.011.

Appendix I.I. Supplemental Tables

TABLE S1. SAMPLE LOCATIONS AND FIELD MEASUREMENTS

Sample	Location Latitude	Location Longitude	Elevation (m) Field*	Elevation (m) Google Earth†	Foliation Strike	Foliation Dip	Lineation Plunge	Lineation Trend
	(Decimal Degrees)							
CB13-53	-9.2043	-77.5746	3810	3821	160	39	39	250
CB13-54a	-9.2029	-77.5709	3916	3878	102	32	32	192
CB13-55a	-9.2033	-77.5712	3902	3870	141	24	24	231
CB13-55b	-9.2031	-77.5679	4030	4096	110	25	16	251
CB13-55c	-9.2031	-77.5679	4030	4096	120	25	19	236
CB13-56	-9.2039	-77.5718	3889	3872	192	29	19	218
CB13-57a	-9.2039	-77.5719	3878	3871	172	36	36	247
CB13-57b	-9.2039	-77.5719	3878	3871	165	30	27	220
CB13-57c	-9.2039	-77.5719	3878	3871	150	21	21	240
CB13-58	-9.2039	-77.5719	3877	3886	156	37	37	245
CB13-59	-9.2042	-77.5721	3867	3891	148	28	25	241
CB13-71a	-9.2099	-77.5698	4226	4223	166	30	30	256
CB13-71b	-9.2099	-77.5698	4226	4223	180	16	16	270
CB13-72a	-9.2062	-77.5709	4184	4150	167	30	24	227
CB13-72b	-9.2062	-77.5709	4184	4150	120	42	40	235
CB13-73a	-9.2059	-77.5709	4170	4141	204	29	26	260
CB13-73b	-9.2059	-77.5709	4170	4141	213	25	19	236
CB13-74a	-9.2058	-77.5709	4164	4138	145	10	5	241
CB13-74b	-9.2058	-77.5709	4164	4138	215	27	11	237
CB13-75	-9.2057	-77.5712	4145	4110	150	20	20	240
CB13-76	-9.2057	-77.5715	4155	4092	199	18	18	245
CB13-77a	-9.2067	-77.5693	4237	4231	200	26	15	225
CB13-77b	-9.2067	-77.5693	4237	4231	199	25	13	229
CB13-77c	-9.2067	-77.5693	4237	4231	196	31	15	231
CB13-78	-9.2058	-77.5721	4099	4062	115	30	30	205
CB13-79	-9.2058	-77.5721	4094	4016	148	40	40	238
CB13-80a	-9.2060	-77.5733	4019	4016	222	34	28	240
CB13-80b	-9.2060	-77.5733	4019	4016	225	44	31	264
CB13-81	-9.2060	-77.5735	4002	4013	158	26	22	215
CB13-82	-9.2060	-77.5735	4000	4013	170	11	8	242
CB13-83	-9.2055	-77.5738	3968	3970	192	19	19	282
CB13-84	-9.2049	-77.5742	3911	3899	112	20	17	230
CB13-85	-9.2041	-77.5752	3868	3791	163	26	26	253

Notes:
*measured in field with Garmin eTrex
†elevation from sample coordinates in Google Earth

TABLE S2. MINERAL CHEMISTRY OF ASYMMETRIC STRAIN-INDUCED MYRMEKITE AND ASSOCIATED DEFORMATION TEMPERATURES

CB13-55a	Porphyroclast 1								Porphyroclast 2			
	Lobe 1		Lobe 2		Lobe 3		Lobe 4		Lobe 1		Lobe 2	
	Myrm	*Kfs*	*Myrm*	*Kfs*	*Myrm*	*Kfs*	*Mym*	*Kfs*	*Myrm*	*Kfs*	*Myrm*	*Kfs*
N*	*3*	*3*	*4*	*7*	*8*	*2*	*1*	*2*	*7*	*4*	*2*	*2*
Oxide												
SiO2	65.7	64.4	65.4	64.5	65.1	64.4	65.4	64.4	64.8	64.5	64.9	64.3
Al2O3	21.1	18.3	21.5	18.3	21.5	18.2	21.4	18.3	21.8	18.3	21.7	18.3
FeO	0.010	0.010	0.009	0.010	0.015	0.009	0.0	0.0	0.011	0.011	0.018	0.006
MgO	0.003	0.001	0.004	0.002	0.010	0.009	0.0	0.0	0.003	0.011	0.001	0.000
CaO	2.12	0.020	2.41	0.013	2.55	0.051	2.36	0.0	2.76	0.012	2.65	0.000
Na2O	10.2	1.01	10.1	1.13	10.1	1.26	10.1	1.13	9.82	1.11	9.91	1.07
K2O	0.097	15.5	0.189	15.3	0.172	15.0	0.153	15.2	0.214	15.5	0.225	15.5
Total	*99.3*	*99.3*	*99.6*	*99.4*	*99.5*	*99.0*	*99.5*	*99.2*	*99.5*	*99.5*	*99.4*	*99.3*
Ions												
Si	2.90	2.99	2.88	2.99	2.88	3.00	2.89	2.99	2.87	2.99	2.87	2.99
Al	1.10	1.00	1.12	1.00	1.12	1.00	1.11	1.00	1.14	1.00	1.13	1.01
Fe2	0.000	0.000	0.000	0.000	0.000	0.001	0.000	0.000	0.000	0.000	0.001	0.000
Mg	0.000	0.000	0.000	0.000	0.001	0.001	0.000	0.000	0.000	0.001	0.000	0.000
Ca	0.101	0.001	0.114	0.001	0.121	0.003	0.112	0.001	0.131	0.001	0.126	0.000
Na	0.875	0.091	0.866	0.102	0.864	0.114	0.868	0.102	0.842	0.100	0.850	0.097
K	0.006	0.920	0.011	0.905	0.010	0.888	0.009	0.905	0.012	0.916	0.013	0.919
Total	*4.99*	*5.01*	*4.99*	*5.01*	*5.00*	*5.00*	*4.99*	*5.01*	*4.99*	*5.01*	*4.99*	*5.01*
Aan†	0.200	-	0.230	-	0.240	-	0.190		0.260	-	0.250	-
stdev	0.019	-	0.020	-	0.021	-	0.019		0.021	-	0.021	-
Aab	0.890	0.931	0.880	-	0.870	-	0.880	0.620	0.860	0.994	0.860	0.972
stdev	0.022	0.023	0.022	-	0.022	-	0.022	0.016	0.021	0.025	0.022	0.024
Asan	-	0.920	-	0.910	-	0.900	-	0.910	-	0.910	-	0.920
stdev	-	0.023	-	0.023	-	0.023	-	0.023	-	0.023	-	0.023
Xan	0.103	0.001	0.115	0.001	0.121	0.003	0.113	0.001	0.133	0.001	0.127	0.000
Xab	0.892	0.090	0.874	0.101	0.869	0.113	0.878	0.101	0.855	0.098	0.860	0.095
Xor	0.006	0.909	0.011	0.898	0.010	0.884	0.009	0.897	0.012	0.901	0.013	0.905

	Porphyroclast 1				Porphyroclast 2	
3 kbar	Lobe 1	Lobe 2	Lobe 3	Lobe 4	Lobe 1	Lobe 2
T (°C)	460	478	496	478	478	473
Porphyroclast Average	478				475	
Sample Average	477					

Notes:
*Number of points analyzed
†Aan, Aab, Asan: Activity (anorthite), (albite),(sanidine), Activities calculated using AX software (Holland and Powell, 2014)

Table S2, continued.

CB13-55a	Porphyroclast 2							
	Lobe 3		Lobe 4		Lobe 5		Lobe 6	
	Myrm	*Kfs*	*Myrm*	*Kfs*	*Myrm*	*Kfs*	*Myrm*	*Kfs*
Oxides	*7*	*5*	*2*	*2*	*5*	*2*	*3*	*2*
SiO2	64.5	64.1	65.3	64.8	65.0	64.2	65.2	64.4
Al2O3	21.8	18.3	21.6	18.7	21.6	18.4	21.4	18.4
FeO	0.013	0.000	0.000	0.004	0.018	0.019	0.023	0.000
MgO	0.005	0.001	0.000	0.006	0.004	0.008	0.004	0.005
CaO	2.96	0.007	2.52	0.037	2.71	0.036	2.41	0.019
Na2O	9.63	1.04	9.90	1.15	9.82	0.890	9.96	1.10
K2O	0.196	15.5	0.227	15.2	0.190	15.7	0.215	15.5
Totals	*99.2*	*99.0*	99.6	100.0	99.4	99.3	99.2	99.5
Ions								
Si	2.86	2.99	2.88	2.99	2.88	2.99	2.89	2.99
Al	1.14	1.01	1.12	1.01	1.13	1.01	1.12	1.01
Fe2	0.000	0.000	0.000	0.000	0.001	0.001	0.001	0.000
Mg	0.000	0.000	0.000	0.000	0.000	0.001	0.000	0.001
Ca	0.141	0.000	0.116	0.002	0.129	0.002	0.115	0.001
Na	0.829	0.094	0.860	0.103	0.842	0.081	0.856	0.099
K	0.011	0.920	0.014	0.897	0.011	0.932	0.012	0.916
Sum	*4.99*	*5.01*	4.99	5.00	4.99	5.01	4.99	5.01
Aan	0.280	-	0.230	-	0.260	-	0.23	-
stdev	0.022	-	0.021	-	0.021	-	0.0204	-
Aab	0.850	0.920	0.870	-	0.860	0.849	0.87	0.986
stdev	0.021	0.023	0.022	-	0.022	0.021	0.0218	0.025
Asan	-	0.954	-	0.910	-	0.93	-	0.920
stdev	-	0.024	-	0.023	-	0.0232	-	0.023
Xan	0.144	0.000	0.117	0.002	0.131	0.001789	0.117	0.001
Xab	0.845	0.093	0.869	0.102	0.858	0.079285	0.871	0.097
Xor	0.011	0.907	0.014	0.896	0.011	0.918927	0.012	0.902

	Porphyroclast 2			
3kbar	Lobe 3	Lobe 4	Lobe 5	Lobe 6
T (°C)	496	481	449	474
Porphyroclast Average	475			
Sample Average	477			

Table S2, continued.

CB13-55a	Porphyroclast 3							
	Lobe 1		Lobe 2		Lobe 3		Lobe 4	
	Myrm	*Kfs*	*Myrm*	*Kfs*	*Myrm*	*Kfs*	*Myrm*	*Kfs*
Oxides	*6*	*2*	*5*	*3*	*3*	*4*	*3*	*3*
SiO2	65.3	64.6	65.1	64.6	65.2	64.6	65.4	64.8
Al2O3	21.5	18.3	21.5	18.1	21.5	18.1	21.4	18.3
FeO	0.012	0.013	0.000	0.021	0.013	0.007	0.010	0.000
MgO	0.007	0.004	0.001	0.003	0.001	0.009	0.005	0.000
CaO	2.66	0.019	2.91	0.015	2.74	0.02	2.68	0.021
Na2O	10.1	1.30	9.8	0.980	9.87	1.02	9.95	1.20
K2O	0.191	15.1	0.220	15.5	0.197	15.4	0.227	15.4
Totals	99.7	99.3	99.5	99.2	99.5	99.2	99.6	99.7
Ions								
Si	2.88	3.00	2.88	3.00	2.88	3.00	2.89	3.00
Al	1.12	1.00	1.12	0.99	1.12	0.993	1.11	0.996
Fe2	0.000	0	0	0.001	0.001	0.000	0.000	0.000
Mg	0.001	0.001	0.000	0.000	0.000	0.001	0.000	0.000
Ca	0.126	0.001	0.138	0.001	0.130	0.001	0.127	0.001
Na	0.860	0.117	0.841	0.088	0.846	0.092	0.851	0.108
K	0.011	0.894	0.012	0.922	0.011	0.912	0.013	0.911
Sum	5.00	5.01	4.99	5.01	4.99	5.00	4.99	5.01
Aan	0.25	-	0.27	-	0.26	-	0.25	-
stdev	0.021	-	0.022	-	0.021	-	0.021	-
Aab	0.87	-	0.85	0.913	0.86	0.942	0.86	-
stdev	0.022	-	0.021	0.023	0.022	0.023	0.022	-
Asan	-	0.90	-	0.92	-	0.92	-	0.91
stdev	-	0.023	-	0.023	-	0.023	-	0.023
Xan	0.126	0.001	0.139	0.001	0.132	0.001	0.128	0.001
Xab	0.863	0.115	0.848	0.087	0.857	0.091	0.859	0.106
Xor	0.011	0.884	0.013	0.912	0.011	0.908	0.013	0.893

	Porphyroclast 3			
3kbar	Lobe 1	Lobe 2	Lobe 3	Lobe 4
T (°C)	499	464	468	488
Porphyroclast Averaage	480			
Sample Average	477			

Table S2, continued.

CB13-55c	Porphyroclast 1 Lobe 1		Porphyroclast 2 Lobe		Lobe 2		Lobe 3	
	Myrm	*Kfs*	*Myrm*	*Kfs*	*Myrm*	*Kfs*	*Myrm*	*Kfs*
	3	*5*	*8*	*8*	*3*	*2*	*2*	*2*
Oxide								
SiO2	67.0	64.4	66.1	64.3	65.0	63.8	65.8	64.3
Al2O3	20.6	18.4	20.7	18.3	21.4	18.4	21.2	18.6
FeO	0.024	0.010	0.051	0.030	0.105	0.119	0.048	0.031
MgO	0.012	0.000	0.005	0.002	0.001	0.003	0.007	0.007
CaO	0.20	0.031	1.70	0.016	2.29	0.000	1.81	0.000
Na2O	10.5	1.08	10.7	0.745	10.4	0.690	10.6	0.849
K2O	0.087	15.1	0.150	15.7	0.164	15.9	0.166	15.5
Total	*98.4*	*99.0*	99.5	99.1	99.4	99.0	99.6	99.3
Ions								
Si	2.94	2.99	2.92	3.00	2.88	2.98	2.90	2.99
Al	1.06	1.01	1.08	1.00	1.12	1.02	1.10	1.02
Fe2	0.000	0.000	0.002	0.001	0.004	0.004	0.002	0.001
Mg	0.001	0.000	0.000	0.000	0.000	0.000	0.000	0.001
Ca	0.087	0.002	0.080	0.001	0.109	0.000	0.086	0.000
Na	0.893	0.097	0.917	0.067	0.895	0.063	0.905	0.076
K	0.005	0.897	0.008	0.932	0.009	0.946	0.009	0.921
Sum	*4.98*	*5.00*	5.00	5.00	5.01	5.01	5.00	5.00
Aan	0.18	-						
stdev	0.02	-	0.16	-	0.21	-	0.17	-
Aab	0.91	0.99	0.02	-	0.02	-	0.02	-
stdev	0.02	0.02	0.91	0.75	0.89	0.70	0.91	0.83
Asan	-	0.91	0.02	0.02	0.02	0.02	0.02	0.02
stdev	-	0.02	-	0.94	-	0.94	-	0.93
Xan	0.010	0.002	-	0.02	-	0.02	-	0.02
Xab	0.984	0.097	0.912	0.067	0.884	0.062	0.905	0.077
Xor	0.005	0.901	0.008	0.932	0.009	0.938	0.009	0.923

	Porphyroclast 1	Porphyroclast 2		
3 kbar	Lobe 1	Lobe 1	Lobe 2	Lobe 3
T (°C)	467	422	416	437
Porphyroclast Average	467	425		
Sample Average	436			

Table S2, continued

CB13-78	Porphyroclast 1 Lobe 1		Porphyroclast 2 Lobe 1		Porphyroclast 3 Lobe 1	
	Myrm	*Kfs*	*Myrm*	*Kfs*	*Myrm*	*Kfs*
	10	*3*	*2*	*7*	*4*	*3*
Oxides						
SiO2	64.4	64.1	65.4	64.6	64.1	64.4
Al2O3	22.5	18.4	21.3	18.4	22.3	18.4
FeO	0.029	0.008	0.000	0.011	0.024	0.012
MgO	0.005	0.002	0.018	0.003	0.001	0.012
CaO	3.35	0.026	2.87	0.033	3.35	0.017
Na2O	9.67	0.730	9.67	0.858	9.39	0.777
K2O	0.188	15.8	0.127	15.6	0.153	15.7
Totals	*100.2*	*99.1*	99.4	99.5	99.3	99.4
Ions						
Si	2.84	2.99	2.90	2.99	2.84	2.99
Al	1.17	1.01	1.12	1.01	1.17	1.01
Fe2	0.001	0.000	0.000	0.000	0.001	0.000
Mg	0.000	0.000	0.001	0.000	0.000	0.001
Ca	0.158	0.001	0.136	0.002	0.159	0.001
Na	0.826	0.066	0.833	0.077	0.807	0.070
K	0.011	0.941	0.007	0.922	0.009	0.930
Sum	*5.00*	*5.01*	5.00	5.00	4.98	5.00
Aan	0.31	-	0.27	-	0.32	-
stdev	0.02	-	0.02	-	0.02	-
Aab	0.83	-	0.86	0.83	0.83	0.77
stdev	0.02	-	0.02	0.02	0.02	0.02
Asan	-	0.99	-	0.93	-	0.94
stdev	-	0.02	-	0.02	-	0.02
		0.933				
Xan	0.159	0.001	0.140	0.002	0.001	0.163
Xab	0.830	0.065	0.853	0.077	0.070	0.828
Xor	0.011	0.933	0.007	0.921	0.929	0.009

	Porphyroclast 1	Porphyroclast 2	Porphyroclast 3
3 kbar	Lobe 1	Lobe 1	Lobe 1
T (°C)	431	446	439
Porphyroclast Average	431	446	439
Sample Average	439	439	

Table S2, continued

CB13-79	Porphyroclast 1 Lobe 1		Lobe 2		Lobe 3		Porphyroclast 2 Lobe 1	
	Myrm	*Kfs*	*Myrm*	*Kfs*	*Myrm*	*Kfs*	*Mym*	*Kfs*
	7	*6*	*4*	*6*	*6*	*6*	*2*	*2*
Oxides	65.2	64.6	64.8	64.8	65.4	64.7	67.9	64.8
SiO2	22.0	18.6	22.3	18.7	22.0	18.6	20.4	18.7
Al2O3	2.78	0.018	3.11	0.000	2.69	0.004	2.25	0.011
FeO	n.d.	n.d.	n.d.	n.d.	n.d.	n.d.	n.d.	n.d.
MgO	0.011	0.009	0.002	0.009	0.004	0.001	0.003	0.014
CaO	10.1	0.97	9.82	0.975	10.1	0.980	10.00	0.825
Na2O	0.14	15.9	0.17	15.9	0.15	15.9	0.122	16.1
K2O	100.2	100.0	100.2	100.4	100.3	100.1	100.7	100.5
Totals								
Ions	2.86	2.98	2.85	2.99	2.87	2.98	2.95	2.98
Si	1.14	1.01	1.15	1.01	1.14	1.01	1.04	1.01
Al	0.131	0.001	0.147	0.000	0.127	0.000	0.105	0.001
Fe2	n.d.	n.d.	n.d.	n.d.	n.d.	n.d.	n.d.	n.d.
Mg	0.000	0.001	0.000	0.000	0.001	0.000	0.000	0.001
Ca	0.856	0.087	0.837	0.087	0.857	0.088	0.843	0.074
Na	0.008	0.936	0.010	0.933	0.008	0.935	0.007	0.947
K								
	5.00	5.02	5.00	5.02	5.00	5.02	4.95	5.02
Sum								
	0.26	-	0.29	-	0.25	-	0.22	-
Aan	0.02	-	0.02	-	0.02	-	0.02	-
stdev	0.86	0.90	0.85	0.90	0.87	0.90	0.88	0.79
Aab	0.02	0.02	0.02	0.02	0.02	0.02	0.02	0.02
stdev	-	0.92	-	0.92	-	0.92	-	0.93
Asan	-	0.02	-	0.02	-	0.02	-	0.02
stdev								
	0.132	0.001	0.148	0.000	0.128	0.000	0.110	0.000
Xan	0.860	0.085	0.842	0.085	0.864	0.086	0.883	0.072
Xab	0.008	0.914	0.010	0.915	0.008	0.914	0.007	0.928
Xor	Porphyroclast 1						Porphyroclast 2	
	Lobe 1		Lobe 2		Lobe 3		Lobe 1	
3 kbar	459		461		457		434	
T (°C)	459						434	
Porphyroclast Average	450							
Sample Average								

Table S2, continued.

	CB13-84					
	Porphyroclast 1					
	Lobe 1		Lobe 2		Lobe 3	
	Myrm	*Kfs*	*Myrm*	*Kfs*	*Myrm*	*Kfs*
	13	*10*	*12*	*11*	*5*	*5*
Oxide						
SiO2	66.6	64.3	66.5	64.6	67.0	64.5
Al2O3	21.2	18.7	21.2	18.6	20.6	18.5
FeO	1.74	0.013	1.67	0.008	1.28	0.007
MgO	n.d.	n.d.	n.d.	n.d.	n.d.	n.d.
CaO	0.008	0.007	0.011	0.003	0.012	0.002
Na2O	10.3	0.682	10.3	0.806	10.3	0.631
K2O	0.19	16.0	0.14	15.9	0.15	16.2
Totals	100.0	99.7	99.8	99.9	99.4	99.9
Ions						
Si	2.92	2.98	2.92	2.99	2.95	2.99
Al	1.10	1.02	1.10	1.01	1.07	1.01
Fe2	0.081	0.001	0.079	0.000	0.060	0.000
Mg	n.d.	n.d.	n.d.	n.d.	n.d.	n.d.
Ca	0.000	0.000	0.000	0.000	0.000	0.000
Na	0.873	0.061	0.874	0.072	0.879	0.057
K	0.011	0.950	0.008	0.937	0.008	0.954
Sum	4.98	5.01	4.97	5.01	4.96	5.01
Aan	0.17	-	0.16	-	0.13	-
stdev	0.02	-	0.02	-	0.01	-
Aab	0.91	0.69	0.91	0.78	0.93	0.64
stdev	0.02	0.02	0.02	0.02	0.02	0.02
Asan	-	0.94	-	0.94	-	0.95
stdev	-	0.02	-	0.02	-	0.02
Xan	0.084	0.001	0.082	0.000	0.064	0.000
Xab	0.905	0.061	0.910	0.072	0.927	0.056
Xor	0.011	0.939	0.008	0.928	0.009	0.943

	Porphyroclast 1		
3 kbar	Lobe 1	Lobe 2	Lobe 3
T (°C)	411	429	400
Porphyroclast Average	414		
Sample Average	414		

Table S2, continued.

	CB13-54							
	Porphyroclast 1						Porphyroclast 2	
	Lobe 1		Lobe 2		Lobe 3		Lobe 1	
	Myrm	*Kfs*	*Myrm*	*Kfs*	*Myrm*	*Kfs*	*Mym*	*Kfs*
	15	*8*	*8*	*6*	*5*	*6*	*6*	
Oxide								
SiO2	66.1	64.7	65.2	64.6	65.5	64.4	65.8	64.8
Al2O3	21.5	18.6	21.9	18.6	21.8	18.6	21.7	18.6
FeO	2.09	0.023	2.63	0.014	2.47	0.022	2.45	0.009
MgO	n.d.	n.d.	n.d.	n.d.	n.d.	n.d.	n.d.	n.d.
CaO	0.018	0.004	0.016	0.012	0.008	0.009	0.005	0.008
Na2O	10.1	0.96	9.75	1.04	9.87	0.853	10.0	1.10
K2O	0.204	15.7	0.295	15.6	0.232	15.9	0.197	15.5
Totals	99.9	100.0	99.8	99.8	99.8	99.8	100.1	100.0
Ions								
Si	2.90	2.99	2.87	2.99	2.88	2.98	2.89	2.99
Al	1.11	1.01	1.14	1.01	1.13	1.02	1.12	1.01
Fe2	0.099	0.001	0.125	0.001	0.116	0.001	0.115	0.000
Mg	n.d.	n.d.	n.d	n.d	n.d	n.d	n.d.	n.d.
Ca	0.001	0.000	0.001	0.000	0.000	0.000	0.000	0.000
Na	0.857	0.086	0.833	0.094	0.842	0.077	0.853	0.098
K	0.011	0.926	0.017	0.917	0.013	0.939	0.011	0.915
Sum	4.98	5.01	4.98	5.01	4.98	5.02	4.99	5.01
Aan	0.20	-	0.25	-	0.24	-	0.23	-
stdev	0.02	-	0.02	-	0.02	-	0.02	-
Aab	0.89	0.90	0.86	0.95	0.87	0.82	0.87	0.98
stdev	0.02	0.02	0.02	0.02	0.02	0.02	0.02	0.02
Asan	-	0.92	-	0.92	-	0.93	-	0.92
stdev	-	0.02	-	0.02	-	0.02	-	0.02
Xan	0.102	0.001	0.128	0.001	0.120	0.001	0.118	0.000
Xab	0.886	0.085	0.855	0.092	0.867	0.075	0.871	0.097
Xor	0.012	0.914	0.017	0.907	0.013	0.924	0.011	0.903

	Porphyroclast 1			Porphyroclast 2
3 kbar	Lobe 1	Lobe 2	Lobe 3	Lobe 1
T (°C)	453	469	441	474
Porphyroclast Average	454			474
Sample Average	459			

Appendix I.II. Supplemental Text

Supplemental Text S1. Cathodoluminescence Imaging and TitaniQ Analyses

Titanium in quartz produces a detectable cathodoluminescence (CL) signal, which can aid in evaluating possible mineral zonation or multiple generations of quartz growth. Quartz luminescence over a broad spectrum can be due to a range of impurities, such as lattice defects or incorporation of trace elements. Titanium luminesces at 330-340 nm wavelengths and up to 400 nm wavelengths (blue-violet), with greater amounts of Ti producing a stronger signal. Filtering CL images to specific wavelengths can allow for evaluation of Ti zoning or overgrowths (Spear and Wark, 2009; Gotze et al., 2012). This is important in distinguishing between multiple potential generations of quartz, as even minor variations in Ti concentration must be evaluated texturally to determine which concentrations are representative of different deformation time stamps. CL images were captured using the CITL CL8200 Mk5-2 Optical Cathodoluminescence System, mounted on a Nikon Eclipse E400 microscope and attached to an Optronics camera, at University of Tennessee-Knoxville. Operating conditions were 256 µA current and 20 kV electron beam. Images were filtered for blue wavelength through manually variable exposures, where blue exposures were set to between 6 minutes, 49 seconds and 21 minutes, 59 seconds. Images were captured under Turbo mode via Magnafire software and CCD camera such that locations imaged with CL were not exposed for longer than ~8 minutes, thus minimizing effects of shifting emission spectra with time (Götze, 2002).

Spot analyses for Titanium-in-Quartz (TitaniQ) thermometry were conducted using the EPMA at UTK. Two to three spectrometers (PET, LLIF, LLIF or PET, LLIF) were used to count Ti Kα X-rays. Peak count times were 960 s (alternating between 192 s on peak, 96 s on high and low backgrounds), yielding a detection limit of 11 ppm. Accuracy of measurements was evaluated against synthetic quartz crystals containing known Ti concentrations and against Herkimer quartz as a blank.

Supplemental Text S2. Raw EBSD Processing

Raw data was processed in Channel 5 to remove wild spikes (individual pixels with orientations dissimilar to all 8 surrounding neighbors), to adjust misindexed pixel orientations to 5 nearest neighbors, and to remove systematic misindexing of grains at orientations 60° (±5°) to the {0001} (or c) axis to account for quartz pseudosymmetry. Subsequent data processing, pole figure construction, and calculations of fabric strength were completed using the MTEX toolbox for MATLAB (Hielscher and Schaeben, 2008; Mainprice et al., 2015).

Grain size is calculated as the diameter of an equivalent-area circular grain. The root mean square of grain size distributions generated from Channel 5 HKL Tango software is used in paleopiezometry calculations. Grains outside of the 95% threshold of grain size distributions were checked against grain size maps to evaluate if they were relict (outlier of largest grains) or false grains (outlier of smallest grains) and removed from the final distribution used for paleopiezometry.

Supplemental Text S3. Discussion of TitaniQ Results and Interpretations

Geochemical modeling may help to resolve the uncertainty in $\boldsymbol{a_{TiO_2}}$ in the system and application of instrumentation with significantly lower (i.e. ppb) detection limits, such as laser ablation-inductively coupled plasma- mass spectrometry (< 1 ppm detection limit, Haertel et al., 2013; Huang and Audétat, 2012) or secondary ion mass spectrometry (<100 ppb detection limit, (Cross et al., 2015; Xia and Platt, 2018) could aid in refining temperature estimates. However, these techniques are outside the scope of this paper.

Discussion of TitaniQ Reliability in the CBSZ

TitaniQ and ASIM deformation temperatures are in agreement within error, assuming α_{TiO_2} of 0.5-0.8 using the Thomas et al (2010) calibration. Limitations to the applications of TitaniQ to CBSZ rocks are discussed below, including thermometer calibration, activity constraints, and instrumental precision. The Huang and Audétat (2012) calibration is derived from a quartz bar grown synthetically by dissolution and reprecipitation. This calibration is dependent on growth rate, having only been calibrated for Ti concentrations in the slowest grown quartz samples (Huang and Audétat, 2012; Nachlas and Hirth, 2015b). Huang and Audétat (2012) tested their calibration against igneous quartz with independently estimated temperatures where Ti activities were between 0.15 and 0.6, and found their TitaniQ calibration to be in agreement with independent temperature estimates. Later experimental studies found Ti concentrations to be independent of growth rate, calling the applicability of the Huang and Audétat (2012) calibration into question and confirming the original Thomas et. al. (2010) calibration (Nachlas and Hirth, 2015b; Thomas et al., 2015).

Ti concentrations for analyzed samples from the CBSZ are relatively consistent within individual samples, where 2σ error is ≤ 7ppm with the exception of CB13-55a (430 m, discussed below). However, it is important to note that the detection limit on the EPMA is 11 ppm. Considering the instrumental detection limit along with the 2σ error on Ti concentrations, TitaniQ temperatures for all samples can be inferred to overlap within error. Furthermore, the assumption of a constant Ti activity across ~300 m of the shear zone width is likely oversimplified. We do not place much weight on the apparent variation of ~50 °C in TitaniQ temperatures from structurally high (446 m) to structurally low (134 m) positions. ASIM temperatures vary between samples beyond the error of the thermometer (50 °C). However, when considering error on the thermometer compounded with 2σ error on feldspar compositions, all ASIM temperatures also overlap.

Analysis on sample CB13-55a was conducted using a preliminary setup with three spectrometers (2 PET and 1 LLIF) with peak count times of 300 s on all three spectrometers or peak times of 300 s on PET and 600 s on LLIF spectrometers, yielding a detection limit between 13-22 ppm for individual analyses. Column conditions were 15 keV, 100 nA current, with a 20 μm beam size. Although this setup yields a less desirable detection limit and in turn introduces a greater uncertainty in Ti concentrations, the average temperature, assuming $\boldsymbol{\alpha_{TiO_2}}$ between 0.5 and 0.8, is within error of the ASIM-derived temperature, which is relatively well constrained with analysis of 14 myrmekite lobes.

A discrepancy exists between microstructurally vs. quantitatively derived temperatures for the deepest sample, CB13-54a (446 m). This sample preserves chessboard extinction within fractured feldspar (i.e. Fig. 1.5L) as well as grain-boundary migration. Chessboard (CB) extinction is commonly attributed to basal <a> and prism [c] slip associated with the α-β transition in quartz (Kruhl, 1996). Even at the low pressures expected for the CBSZ (1-3 kb; Margirier et al., 2016), temperatures required for chessboard extinction are at least ~ 630 °C (Kruhl, 1996). Ti concentration is consistent between GBM and CB domains. This could be explained by an initially low Ti activity (~0.1) when CB occurred and increased Ti activity during deformation, by decreased Ti concentrations due to volume diffusion at high temperatures, by 'resetting' the Ti concentration at lower GBM temperatures, or simply by instrumental accuracy.

One sample that contained both GBM and SGR quartz recrystallization microstructures was analyzed for TitaniQ thermometry (CB13-79; 134 m). Ti-concentration (8 ± 6 ppm) was below the detection limit (11 ppm) of the electron probe microanalyzer (EPMA) at the University of Tennessee. SGR microstructures could indicate higher-strain rather than lower temperature conditions than those occurring during GBM recrystallizaiton, such that the Ti concentration would still be consistent with concentrations expected at relatively high temperatures. However, our analysis of this sample suggests that TitaniQ analysis especially for samples with SGR recrystallization microstructures is not viable without more precise instrumentation.

Appendix I.III. Supplemental Figures

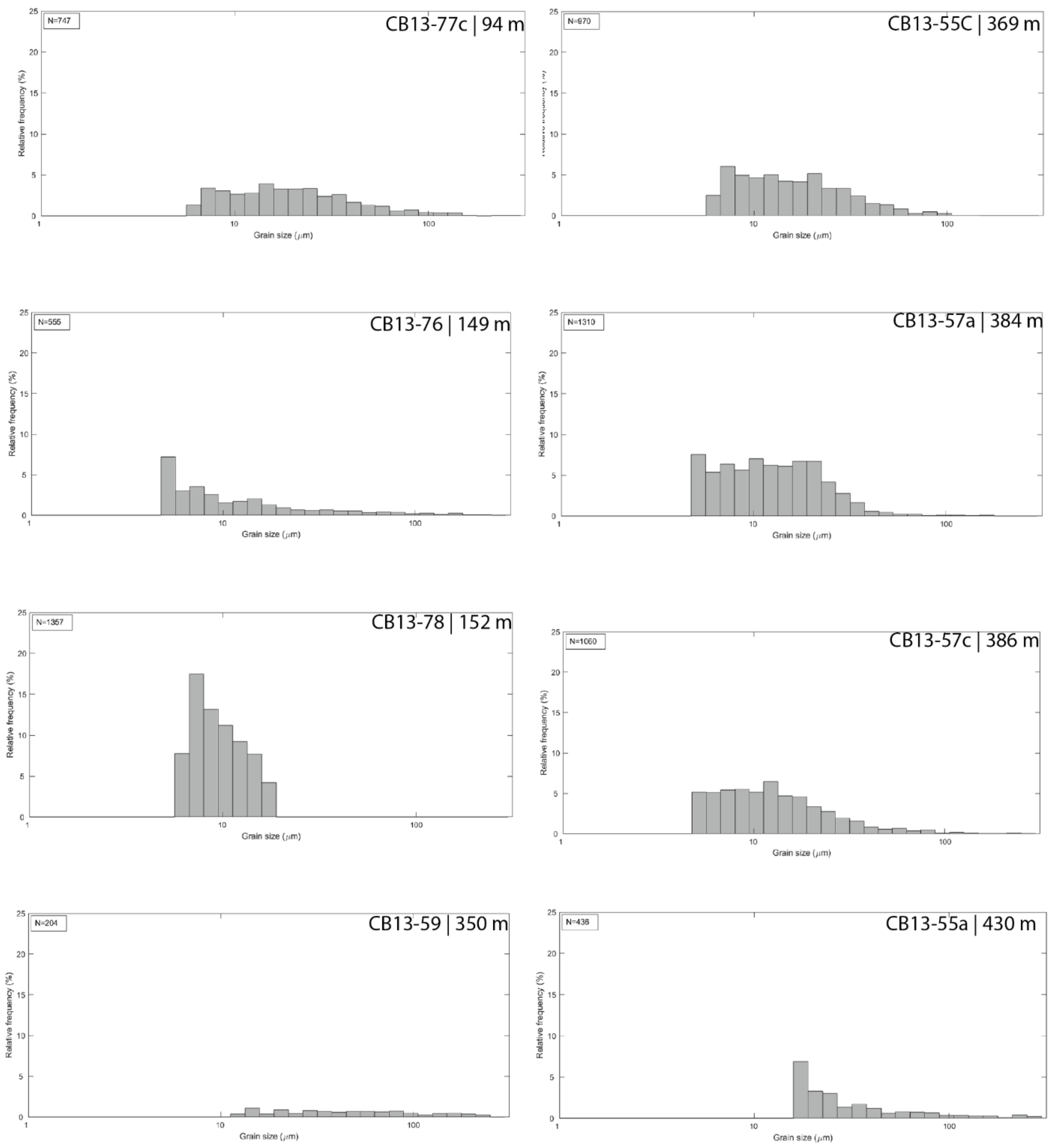

Fig. S1. Quartz recrystallized grain size distributions. Number of grains in each population (N) in upper left corner. Sample numbers listed with structrual depth below the detachment.

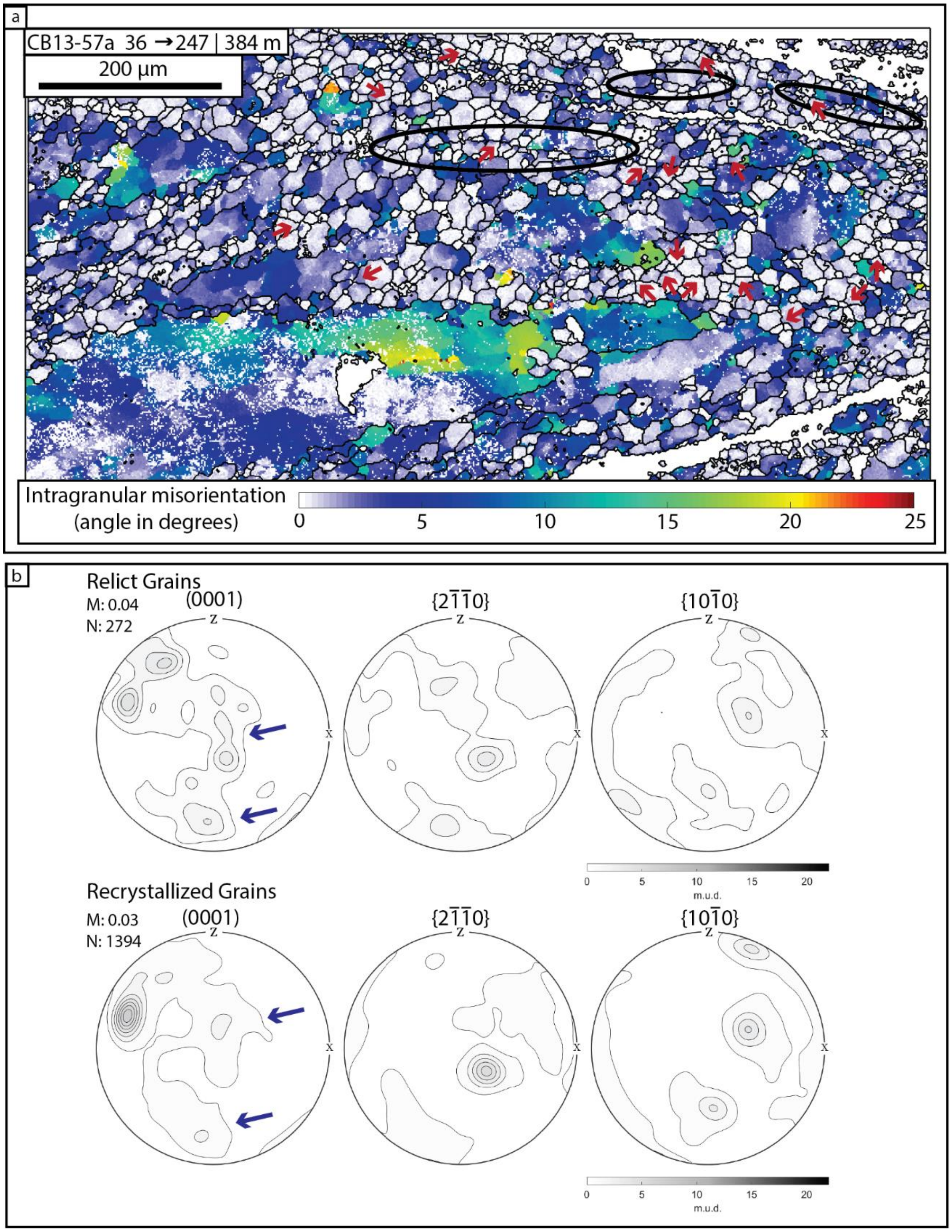

Fig. S2. EBSD-based evidence for grain boundary sliding in CB13-57a (384 m). a) map of intragranular misorientations (relative to mean orientation of grain) using 'mis2mean' property in MTEX toolbox for MATLAB. Grain boundaries shown in black, critical misorientation: 10 degrees. Thick black ellipses highlight aligned grain boundaries. Red arrows point to 4-grain junctions. b) 1 point per grain pole figures of crystallographic preferred orientations for relict quartz grains (upper) and recrystallized quartz grains (lower). Note the dispersion of weak maxima near the central (Y-direction) and lower perihphal areas in the recyrstallized pole figure relative to the relict pole figure (blue arrows).

CHAPTER II

EVIDENCE FOR STRAIN RATE VARIATION AND AN ELEVATED TRANSIENT GEOTHERMAL GRADIENT DURING SHEAR ZONE EVOLUTION IN THE CORDILLERA BLANCA, PERU

A version of this chapter by Cameron A. Hughes, Micah J. Jessup, Colin A. Shaw, and Dennis L. Newell is currently in preparation for submission:

Cameron A. Hughes, Micah J. Jessup, Colin A. Shaw, and Dennis L. Newell: "Evidence for strain rate variation and an elevated transient geothermal gradient during shear zone evolution in the Cordillera Blanca, Peru." *Tectonophysics, in preparation.*

My major contributions to this manuscript include: 1) field work to collect samples and collect structural measurements, 2) conducting petrographic, structural, electron microprobe, and electron backscatter diffraction analysis, 3) calculating deformation temperature, differential stress, and strain rate, 4) writing the manuscript, and 5) drafting most figures for this manuscript. As corresponding author, I will be submitting this manuscript and will be responsible for revising this manuscript.

Abstract

Recrystallized quartz paleopiezometry, two-feldspar thermometry on asymmetric strain-induced myrmekite, and structural analysis from the Cordillera Blanca shear zone (CBSZ), Peru provide evidence for shear zone evolution within a transient elevated geotherm during syn-convergent extension. The CBSZ occupies the footwall of the Cordillera Blanca detachment fault, an active low-moderate angle detachment fault extending for ~200 km along the western margin of the Cordillera Blanca mountain range in central Peru. Shear zone width varies by a factor of six along strike, with widths of up to ~400 m within the central segment of the shear zone. Comparison of differential stresses, temperatures, microstructures, and quartz crystallographic preferred orientations from three detailed transects across the shear zone suggest that the variation in width along strike likely results from variable exhumation rate, slip rates, and/or fault geometry along strike. Within the context of existing thermochronology, constraints on batholith emplacement, and previously determed offset along the Cordillera Blanca detachment, our data suggest that ductile deformation in the CBSZ occurred within a transient elevated geothermal gradient of ~50 °C/km, which deviated from the 30 °C/km gradient for an unspecified duration of time. Our results are consistent with existing regional models of enhanced exhumation along the central portion of the detachment system related to intrusion of the youngest magmas in the Cordillera Blanca batholith.

Introduction

The CBSZ offers a classic arena to investigate the role of magmatism and active syn-convergent extension where extension is directed nearly perpendicular to orogenic strike (Cobbing et al., 1981; Dalmayrac and Molnar, 1981; Suarez et al., 1983; Schwartz, 1988b; Deverchere et al., 1989). Indeed, the Cordillera Blanca was among the first areas where ongoing orogen-normal extension occurring in tandem with convergent orogeny was studied in detail.

Dalmayrac and Molnar (1981) first recognized the apparently paradoxical kinematics of the CBSZ and attributed opposing extension and convergence to gravitational body forces acting on high topography and the related crustal root (Dalmayrac and Molnar, 1981; Sebrier et al., 1985; Giovanni et al., 2010). Their analysis suggesed that syn-convergent extension in the highest parts of the orogen is driven by potential energy differences between high and low topography. Competing models for syn-convergent extension along the CBD have since been proposed. These include thermal weakening due to magmatism (Petford and Atherton, 1992; McNulty and Farber, 2002; Margirier et al., 2015) and interactions between the low-angle subducting Nazca plate and the overriding South American continent, (Sebrier et al., 1985; McNulty et al., 1998; McNulty and Farber, 2002; Margirier et al., 2015).

This study applies primary observations of processes and conditions within the CBSZ to elucidate the role that magmatic heating may have played in localizing strain along the CBSZ and promoting syn-convergent extension in the high Andes of central Peru. We do not directly address the source of the driving forces for syn-convergent extension – whether internal body forces or applied tectonic boundary forces – rather, we examine factors that may have controlled the spatial and temporal variations in crustal strength that could control regional localization of deformation. We evaluate spatial variation in strain localization along the CBSZ and thermal evolution of the shear zone informed by microstructural analysis, quartz crystallographic preferred orientations, two-feldspar thermometry on asymmetric strain-induced myrmekite, and recrystallized quartz paleopiezometry. Using these data, we construct a regional crustal strength profile and conceptual model of shear zone development that synthesizes our results.

Regional Geology

In central Peru, the Cordillera Blanca detachment (CBD) accomodates syn-convergent extension that is directed nearly perpendicular to orogenic strike (Cobbing et al., 1981; Dalmayrac and Molnar, 1981; Suarez et al., 1983; Schwartz, 1988b; Deverchere et al., 1989). Dipping WSW, the moderate- to low- angle CBD juxtaposes the dominantly granodioritic Cordillera Blanca batholith in the footwall with Mesozoic to Cenozoic sedimentary, metamorphic, and volcanic rocks in the hanging wall. The supradetachment Callejon de Huaylas basin formed largely during syn-convergent extension (Giovanni et al., 2010).

U-Pb zircon dates indicate that the Cordillera Blanca batholith (CBB) was emplaced from 14-5 Ma (Mukasa, 1984; McNulty et al., 1998; Giovanni, 2007; Margirier et al., 2016), with the youngest dates occurring in the central part of the range (Margirier et al., 2016). The Cordillera Blanca batholith consists of two geochemical facies; an older, more basic tonalite-trondjehmite facies (14-9 Ma), and a more alkalic leucogranodiorite facies that constitutes most of the batholith (6-5 Ma; Petford and Atherton, 1996). Oldest U-Pb zircon dates are 13.7 ± 0.3 Ma (Mukasa, 1984), located within the southern Carhuish stock (Fig. 2.1). The youngest zircon dates are 5.3 ± 0.3 Ma, located in the central part of the batholith (Giovanni, 2007). $^{40}Ar/^{39}Ar$ biotite dates from the relatively undeformed core in the central part of the batholith are 5.18 ± 0.05 Ma and young towards the fault (Petford and Atherton, 1992). Andalusite-bearing assemblages in the shale contact aureole indicate that the batholith was emplaced at 200-350 MPa (Petford and Atherton, 1992; Wise and Noble, 2003), corresponding to depths of emplacement between 7.6 km and 13.3 km, assuming an average density of 2670 kg/m^3 (Couch and Whitsett, 1981; Petford and Atherton, 1996). Amphibole thermobarometry suggests emplacement pressures of 90 to 260 MPa (Margirier et al., 2016), corresponding to depths of 3.4 to 9.9 km. Magmatic

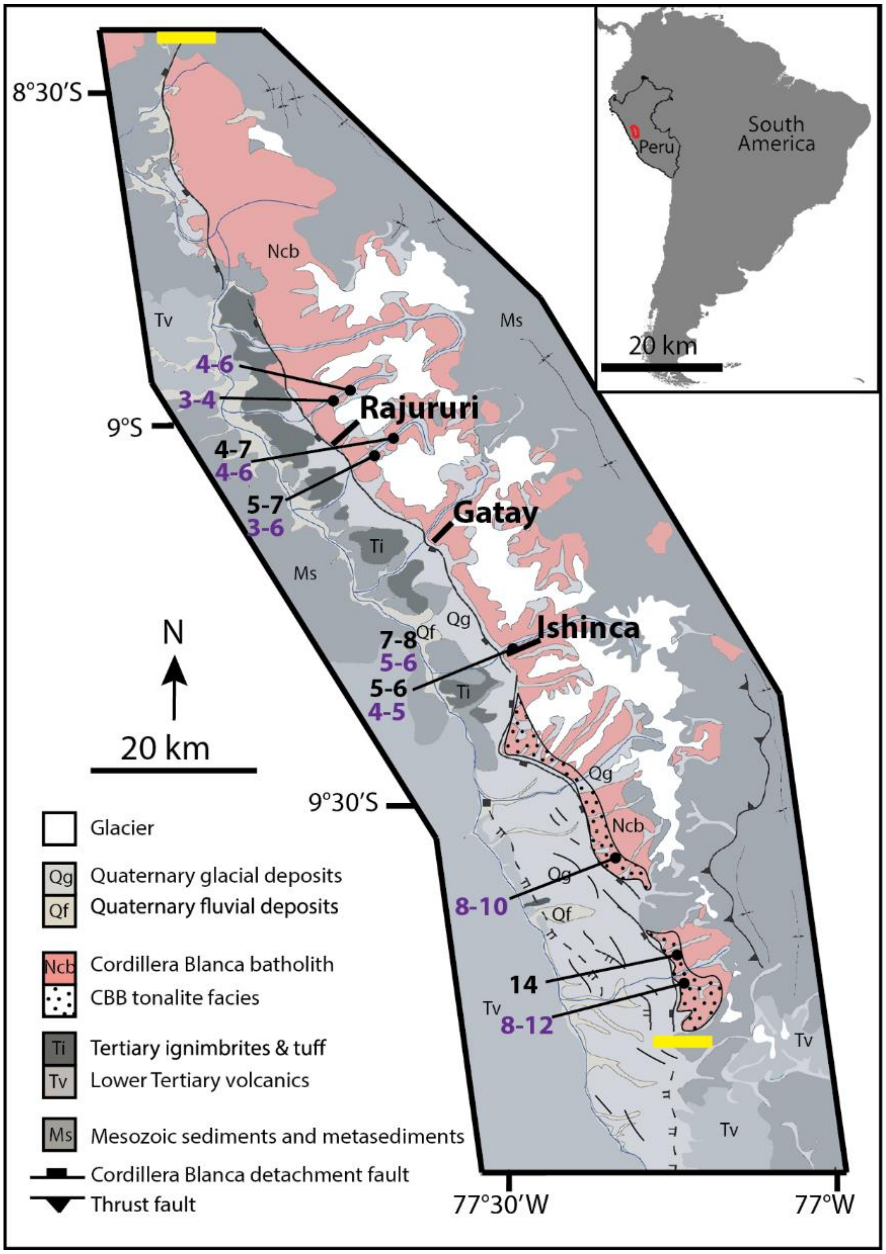

Fig. 2.1. Simplified geologic map of the Cordillera Blanca, Peru. Modified from Giovanni et al. (2010). Distribution of Cordillera Blanca batholith (CBB) tonalite facies after (Petford and Atherton, 1996) Inset shows position of map relative to South America. Transects that are the focus of quantitative analysis in this study are labelled in black. Ages to the left of the Cordillera Blanca detachment denote U-Pb zircon ages (black) and 40Ar/39Ar biotite ages (purple) (Mukasa, 1984; Petford and Atherton, 1992; McNulty et al., 1998; Giovanni, 2007; Giovanni et al., 2010). Yellow bars show location bounds of fault map shown in Fig. 2.2.

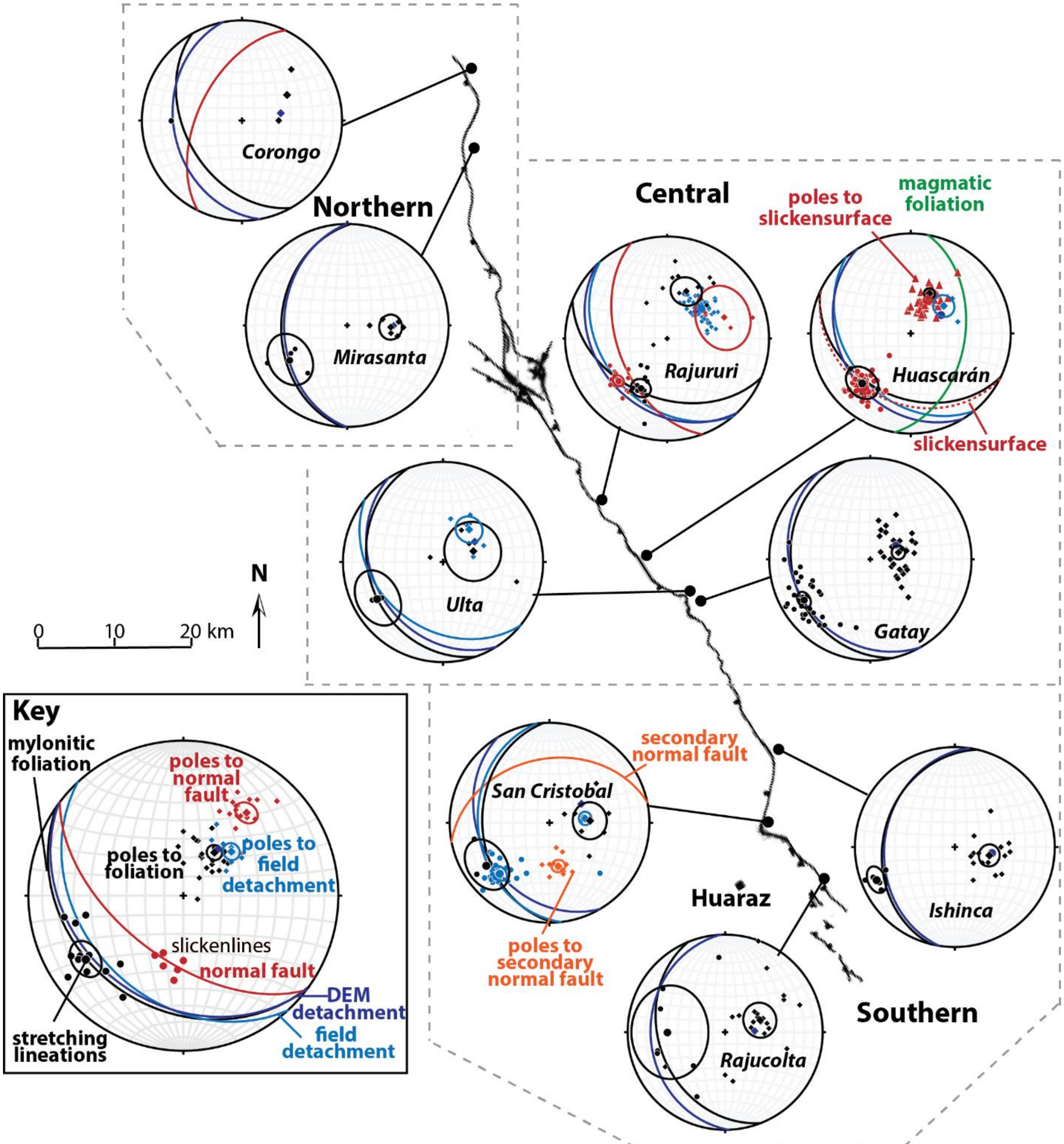

Fig. 2.2. Structural measurements for transects across the CBSZ from the northern, central, and southern groups along strike of the Cordillera Blanca detachment fault. Fisher mean vectors are plotted with 1σ standard deviation error and the same symbology as the related poles or lineations. Map of fault trace from (Schwartz, 1988). DEM detachment: detachment surface derived from digital elevation model, built with 30 m Shuttle Radar Topography Mission data (opentopo.com), using ArcMap 10.6. Hundreds to thousands of great circles for DEM-derived aspect and slope measurements of the detachment surface exist for each transect. For clarity, poles to these data are not plotted and only the fisher mean vector is plotted, where 1 sigma error on the is contained within the symbol. Additional details on structural measurements are provided in Table S3. Field detachment: detachment surface as measured in field.

structures present within the CB include biotite-layering and schlieren defined by biotite ± hornblende ± titanite up to ~0.5 m in width, which diminish into otherwise undeformed granite (Petford and Atherton, 1992).

The Cordillera Blanca fault zone is ~180 km long and consists of the Cordillera Blanca detachment (CBD) fault that generally trends N145-N156°, dips 22-39° WSW (Fig. 2.2) and is truncated by steeply dipping neotectonic fault scarps (Schwartz, 1988b; Petford and Atherton, 1992). For ~110 km along strike in the northern and central parts of the fault zone, the CBD is the upper boundary to the mylonitic Cordillera Blanca shear zone (CBSZ), which occurs in the granodiorite. A general fabric gradient occurs within the CBSZ, transitioning from undeformed-weakly deformed leucogranorite at structurally deep positions through mylonite, ultramylonite, cataclasite, and/or breccia with increasing proximity to the detachment (Petford and Atherton, 1992; Hughes et al., 2019). Structurally shallow positions near the CBD are typically characterized by ultramylonite, breccia, and cataclasite, where breccia and cataclasite develop parallel to pre-existing mylonitic fabrics (Hughes et al., 2019). Local meters-scale perturbations of this gradient occur, where narrow zones of ultramylonite are observed within otherwise undeformed-weakly deformed granodiorite (Hughes et al., 2019). A cataclastic zone was previously identified to be ~30 m thick (Mercier et al., 1992; Petford and Atherton, 1992), however data presented by Hughes et al. (2019) suggest that the cataclastic zone is up to at least ~120 m thick in the geographically central part of the shear zone and locally contains ultracataclasite and pseudotachylite injection veins that cut across mylonitic fabrics.

$^{40}Ar/^{39}Ar$ geochronology of the Lloclla tuff, a basal unit in the Callejon de Huaylas supradetachment basin, indicates displacement along the detachment fault began at ~5.4 Ma (Giovanni et al., 2010). Since fault initation, 12-15 km displacement has occurred along the

Detachment, as determined by restoration of a sedimentary contact (Giovanni et al., 2010). The extensional direction along the fault zone rotated from the pre-Pliocene orientation of N050-060°E, as indicated by mineral lineations along the main fault surface, to N105° (σ_3, with sub-vertical σ_1) in the Pliocene, as indicated by striations along brittle fault planes that coincide with striation orientations along synsedimentary Pliocene faults within the Callejon de Huayalas Basin (Mercier et al., 1992). Fault plane solutions and stress tensors from microseismicity collected within the Cordillera Blanca and supradetachment basin indicate modern extension directed towards N60°E with σ_1 (vertical) and σ_2 having similar magnitudes (Deverchere et al., 1989). A maximum ~50 MPa average differential stress has been calculated for the Cordillera Blanca region, constrained by the relief in the Cordillera Blanca and the juxtaposition of normal faulting at high elevations and thrust faulting at lower elevations (Dalmayrac and Molnar, 1981).

Exhumation rates for the Cordillera Blanca are 1.1 km/My since 2.8 Ma based on apatite fission track (AFT) data, (Montario, 2001). AFT data collected from 3450-3480 m elevation in Quebrada (Q.) Llanganuco show that the geographically central segment of the footwall was cooled to ~150 °C by ~3 Ma (Montario, 2001). Constrained by apatite helium (AHe) and zircon helium (ZHe) dating, exhumation rates from the northern boundary of the CBB are estimated at 0.60-0.88 km/Ma since 2.0 ± 0.2 Ma and 1.26-1.84 km/Ma since 2.7 ± 0.2 Ma, respectively (Michalak, 2013). Margirer et al. (2016) suggest exhumation rates of 0.2 km/Ma from 6-5 Ma, 0.3 km/Ma from 5-2 Ma, and ~1 km/Ma from 2-0 Ma and higher exhumation rates in the central CB relative to the northern and southern CB. Garver, Montario, et al., (2005) suggested that based on $^{40}Ar/^{39}Ar$, zircon fission track (ZFT), and AFT ages, the most rapid exhumation occurred from 4-2 Ma in the central part of the range, but did not report any resolved rates.

The modern Cordillera Blanca is an active hydrothermal area, with thermal springs as hot as 89 °C issuing from along the main detachment fault in the north and along mapped quaternary faults within the Callejon de Huaylas Basin (Newell et al., 2015). Assuming a modern geothermal gradient of 25 °C/km following sparse data suggesting low modern heat flow, hydrothermal fluids are interpreted to circulate to depths of 8-11 km; however, this could be shallower if the springs represent localized higher heat flow and a more elevated geothermal gradient (Newell et al., 2015). Previous work by Uyeda and Watanabe (1970) at the Raura mine to the south of the Cordillera Blanca near the Cordillera Huayhuash, Peru suggests the modern geothermal gradient in the region may be as high as 40-60 °C/km. However, the data they used to determine the gradient may potentially be unreliable due to substantial fluid circulation in the mine (Uyeda and Watanabe, 1970). In summary, both the modern geothermal gradient and the geothermal gradient upon initiation of the Cordillera Blanca detachment system may be elevated but are ultimately poorly constrained.

Kinematics and Structure

Tectonic Fabrics

In all transects including and north of Q. Ishinca, except the northernmost (Corongo, Fig. 2.2), the exposed detachment surface forms the uppermost limit of the mylonitic shear zone (Fig. 2.3a). Fabrics progress from weakly deformed granodiorite towards the core of the mountain range and become increasingly mylonitized towards shallower structural positions with increasing proximity to the detachment (Petford and Atherton, 1992; Hughes et al., 2019). S-C fabrics observed in the field consistently record top-down-to-the-southwest sense of shear (Fig. 2.3b). Microstructural indicators including mica fish, oblique grain-shape fabrics in recrystallized quartz, delta and sigma feldspar clasts, asymmetric strain-induced myrmekite, and

Fig. 2.3. Meso- and micro-structural observations of tectonic fabrics. a) Photo looking to north side of Q. Rajururi. Brittle detachment surface (dashed black line) forms upper boundary of ductile shear zone along the western margin of the Cordillera Blanca batholith. Dashed red line: approximate lower shear zone boundary. b) S-C mylonitic fabric from Q. Ulta indicating top-down-to-the-southwest shear. 2 sol piece (~2.4 cm) for scale. c) Cross-polarized light (XPL) photomicrograph of asymmetrically distributed strain induced myrmekite on K-feldspar porphyroclast (white arrows) and white mica fish (red arrow) indicating top-to-the-southwest shear. d) S-C mylonitic fabric and en echelon tension fractures truncated by pseudotachylite (red arrows) and small off-set steep faults (black half arrows) near entrance to Q. Ulta. Two-sol piece (~2.4 cm) at center of photo for scale. e) Ultramylonite and pseudotachylite within otherwise undeformed coarse-grained granodiorite within the central part of the Cordillera Blanca. Fine-grained fabric continues for at least 10-20 m to the NNE. f) XPL photomicrograph from southern segment, Q. Rajucolta. Breccia fine-grained micas and epidote surrounding larger clasts of feldspar (red arrows) truncating relatively undeformed granodiorite (lower).

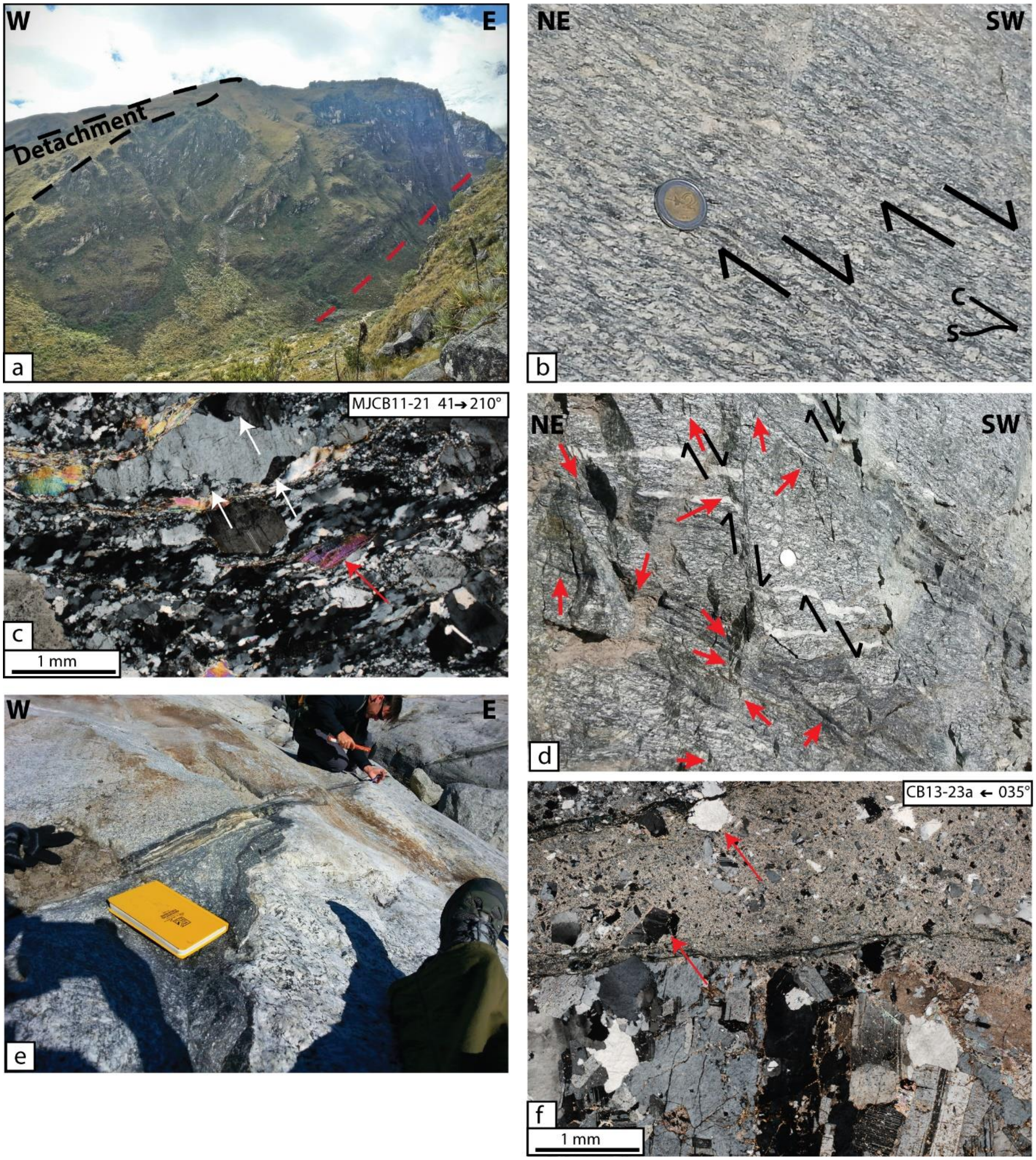
W
E
Detachment
a
NE
SW
C
S
b
MJCB11-21 41→210°
c
1 mm
NE
SW
d
W
E
e
CB13-23a ← 035°
f
1 mm

S-C fabrics also indicate top-down-to-the-southwest shear (Fig. 2.3c). Ultramylonites and cataclasites occur near the detachment, and within the upper ~150 m of the shear zone, pseudotachylite, as evidenced by the fault-vein, injection-vein geometry (i.e. Kirkpatrick et al., 2009; Kirkpatrick and Rowe, 2013), and sharp edges (i.e. Kirkpatrick et al., 2009) and brittle faulting truncates ductile fabrics in some areas (Fig. 2.3d). Within the central part of the Cordillera Blanca range, narrow zones of mylonite and ultramylonite are observed in otherwise undeformed granodiorite (Fig. 2.3e).

In transects south of Q. Llaca, mylonitic zones are either discontinuous, as in Q. Rajucolta, or not observed, as in Q. Condie. At Q. Rajucolta, the trace of the Cordillera Blanca fault is still continuous with the main fault segment at Q. Llaca (Fig. 2.4), and the detachment truncates undeformed-weakly deformed granodiorite. Here, although some isolated mylonitic fabrics are observed, the deformation zone is instead characterized by cataclastic fabrics overprinting relatively undeformed granodiorite (Fig. 2.3f). Further to the south, the trace of the Cordillera Blanca fault system splays and steps into the Callejon de Huaylas basin (Schwartz, 1988b; Margirier et al., 2017). Within Q. Condie (Fig. 2.4), where this type of fault geometry occurs, relatively undeformed granodiorite is cut by brittle faults near the western valley entrances along the range front. This is one of the examples that could be observed directly, but without systematic observations between Q. Condie and Rajucolta, it is difficult to know if these brittle fabrics were consentient along the strike of the fault zone.

Shear Zone Width

Shear zone widths for different transects are discussed in the context of relative geographic position along strike. Observed transects are subdivided into the following groups (Fig. 2.4); northern: Corongo, Mirasanta, and Canon da Pato; central: Paron, Rajururi,

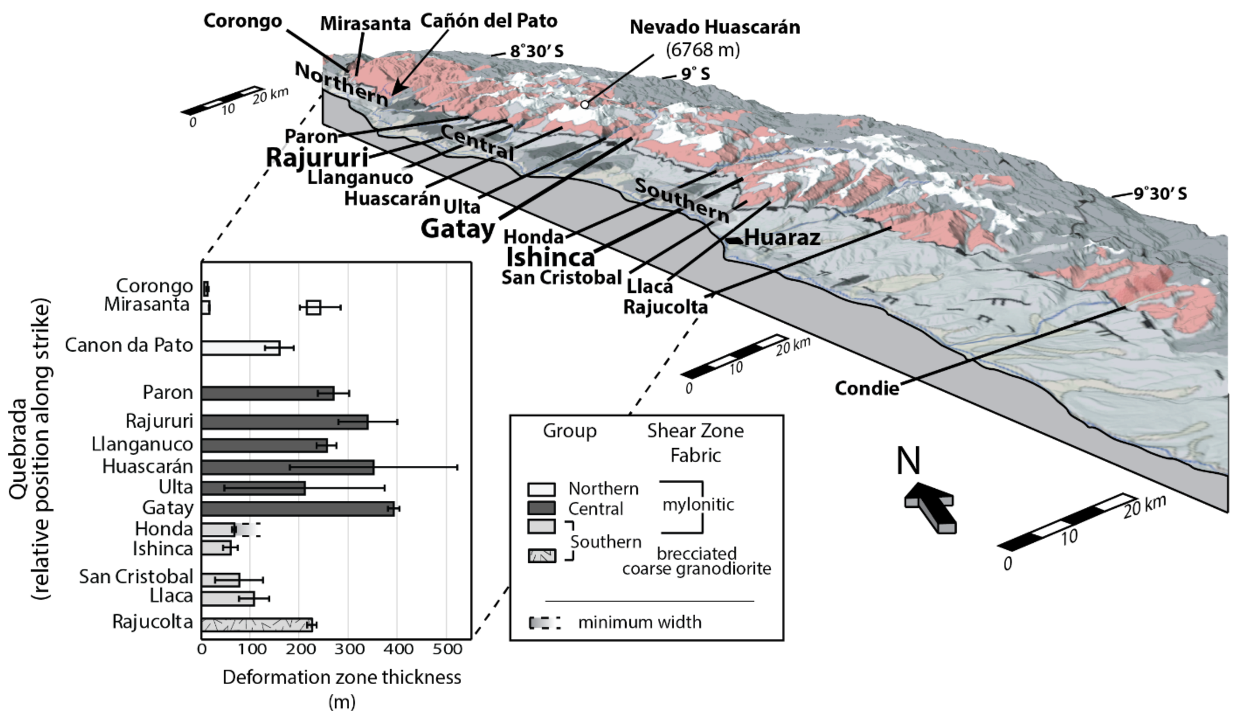

Fig. 2.4. Shear zone thicknesses relative to position along strike of the Cordillera Blanca detachment. Positions of transects depicted on a 3D digital elevation model derived from 90 m Shuttle Radar Topography Mission data (**http://www.viewfinderpanoramas.org/dem3.html**) overlain with simplified geologic map modified from Giovanni et al. (2010). Shear zones are subdivided into three groups based on geographic position: northern, central, and southern. Transects that are the focus of quantitative analysis in this study are shown in large, bold text

Llanganuco, Huascaran, Ulta, and Gatay; and southern: Honda, Ishinca, San Cristobal, Llaca and Rajucolta. Methods for calculating structural depth and shear zone widths are detailed in Supplementary Text S1. Some structural depths for samples near the detachment have 1σ standard deviations that are slightly greater than the calculated depth, which we attribute to corrugations along the detachment surface (Petford and Atherton, 1992), and simplification of the detachment at a given transect as a planar surface. This has a negligible effect on calculated shear zone widths.

Shear zone widths are greatest within the central Cordillera Blanca (Fig. 2.4, Table 2.1). Mylonitic thicknesses are lower in the north, diminishing northwards towards the tip of the mapped brittle fault structure to 6 ± 2 m near Corongo. Two relatively narrow shear zones are

TABLE 2.1. SHEAR ZONE WIDTH ALONG STRIKE

Quebrada	Average shear zone width (m)	Std. Dev.
Corongo	6	2
Mirasanta N	17	1
Mirasanta S	28	41
Canon del Pato	160	29
Paron	270	32
Rajururi	340	60
Llanganuco	256	20
Huascaran	352	171
Ulta	211	163
Gatay	393	12
Honda	67	4
Ishinca	60	15
San Cristobal	78	49
Llaca	108	31
Rajucolta*	226	10

Notes:
*No continuous mylonitic shear zone observed. Width describes width of zone where brittle deformation truncates relatively undeformed granodiorite.

observed along a transect along a road oblique to strike at Mirasanta. One shear zone is 17 ± 1 m and is capped by the detachment, whereas the other is ~30 m thick and occurs at a projected structural depth of 241-270 ± 41 m below the same detachment surface. At Canon del Pato the shear zone is up to 160 ± 29 m wide. Within central group the shear zone is between 256 ± 20 (Q. Llanganuco) and 393 ± 12 m (Q. Gatay) wide. Shear zone width is notably narrower in the southern group, where Q. Honda, Q. Ishinca, and San Cristobal are 67 ± 4 and 60 ± 15 m wide, and 78 ± 49 m respectively. A minimum shear zone width is reported for Q. Honda, as the deepest positions that have been sampled are protomylonitic, implying that the transition to undeformed granodiorite occurs at yet deeper positions. Shear zone width is slightly higher in Q.

Llaca (108 ± 31 m), which is the southernmost observed transect where the mylonitic shear zone is continuous and capped by the detachment fault. Generally, the central part of the CBSZ is up to 6 times wider than the southern part of the CBSZ. Q. Rajucolta, ~10 km southeast of Q. Llaca, contains discontinuous lenses of mylonite but does not have a mylonitic shear zone that is bounded by the detachment surface. Rather, a fault zone is observed where cataclasite primarily overprints relatively undeformed granodiorite and in some instances truncates the discontinuous mylonitic fabrics. This fault zone extends for 225 ± 9 m, where deeper than 225 m, undeformed granodiorite is observed without cataclastic overprint.

Quartz Recrystallization Microstructures and Deformation Temperatures

Deformation temperatures during shearing were estimated from quartz recrystallization microstructures (Stipp et al., 2002b) for all samples in central Q. Rajururi and Q. Gatay, and southern Q. Ishinca. Quartz crystallographic fabrics and two-feldspar thermometry on asymmetric strain-induced myrmekite (ASIM) provide additional quantitative temperature constraints for a subset of samples. These methods, along with deformation temperatures for Q. Gatay, were previously reported by Hughes et al. (2019). Temperature ranges for quartz recrystallization microstructures were originally reported for strain rates of 10^{-12} s^{-1}, with an error for transitions between characteristic microstructures of ± 30 °C (Stipp et al., 2002a). An increase in strain rate by one order of magnitude can have the same effect on microstructures as a ~200 °C decrease in temperature and an increase in water content can have the same effect as an increase in temperature (Stipp et al., 2006).

In Q. Gatay, temperatures estimated from quartz recrystallization microstructures decrease from over ~630 °C, constrained by the presence of chessboard extinction (CB) in quartz (Kruhl, 1996) at the structurally deepest position (393 ± 12 m, CB13-54a) to 280-500 °C at the structurally highest position along the detachment fault surface (Fig. 2.5). Temperatures from ASIM thermometry for structural positions between 110 ± 16 and 393 ± 12 m are between 410 ± 30 and 470 ± 36 °C. Titanium-in-quartz (TitaniQ) thermometry at depths between 124 ± 36 and 393 ± 12 m below the detachment yields similar temperatures, between 451 ± 60 and 489 ± 39 °C (Hughes et al., 2019). Quartz recrystallization microstructures, ASIM thermometry, and TitaniQ thermometry demonstrate a slight decrease in temperature with shallowing structural position towards the detachment in Q. Gatay (Fig. 2.5; Hughes et al, 2019).

New temperature data from Q. Rajururi to the north, and Q. Ishinca to the south, of Q. Gatay exhibit less distinctive trends with respect to structural depth (Fig. 2.5; Table 2.2). Temperatures above ~500 °C, estimated based on the presence of grain boundary migration (GBM) quartz recrystallization microstructures (Stipp et al., 2002b) without lower temperature and/or higher strain rate bulging (BLG) or subgrain rotation (SGR) microstructures, are found at deep structural positions (258 ± 96 to 340 ± 60 m) in Q. Rajururi. The deepest sample from Q. Rajururi (CB13-29, 340 ± 60 m) also contains prismatic subgrains characteristic of CB extinction in quartz, suggesting temperatures above ~630 °C (Kruhl, 1996). In Q. Ishinca, subgrains indicating chessboard extinction are preserved in a relatively deep sample (CB13-09b, 43 ± 22 m) that also contains GBM, SGR, and BLG microstructures. Otherwise, temperatures above ~400 °C, suggested by the presence of SGR and GBM recrystallization microstructures are found at the deepest positions in Q. Ishinca (46 ± 21 to 49 ± 11 m). SGR and GBM recrystallization microstructures are observed at shallow and moderate structural positions (0 to 32 ± 17 m and 65 ± 24 m) in Q. Rajururi, and moderate to deep structural positions (92 ± 18 to 141 ± 21 m, 277 ± 73 m, and 386 ± 8 m) in Q. Gatay. BLG microstructures are observed in samples that also preserve SGR ± GBM microstructures at shallower relative structural positions within each

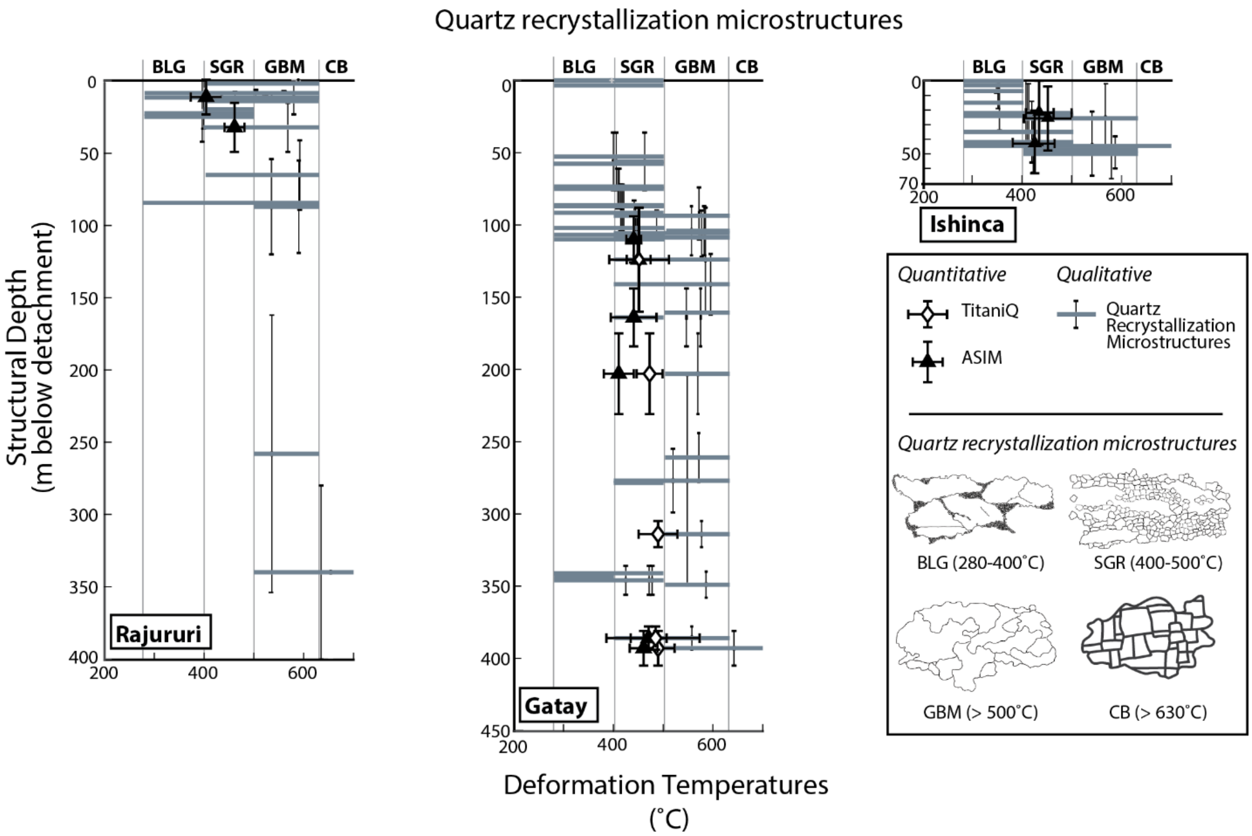

Fig. 2.5. Relationship between structural depth below the detachment and deformation temperatures from Rajururi (central), Gatay (central) and Ishinca (southern) transects. Gray bars denote temperature ranges estimated from quartz recrystallization microstructures. Bulging (BLG), subgrain rotation (SGR), and grain boundary migration (GBM) recrystallization microstructures occur at 280-400 °C, 400-500 °C , and > 500 °C, respectively (Stipp et al., 2002b). These temperatures were originally reported with errors of ± 30 °C and assumed a strain rate of 10^{-12} s^{-1} (Stipp et al., 2002b). Chessboard (CB) extinction in quartz indicates temperatures above 600-630 °C at pressures of 100-300 MPa (Kruhl, 1996). Schematic microstructures shown in right inset: BLG, SGR, and GBM from Stipp et al. (2002b). Although there is no upper limit to the temperatures at which GBM occurs (Stipp et al., 2002b) GBM recrystallization is shown at temperatures of 500-630 °C for clarity relative to the onset of CB extinction ~630 °C. Temperatures for Q. Gatay originally reported in Hughes et al. (2019). Vertical black bars denote errors on structural depth, offset along x-axis for clarity. Titanium-in-quartz (TitaniQ) errors are 1σ standard deviation, asymmetric strain-induced myrmekite (ASIM) errors are 2σ standard deviation (Table 2.2).

TABLE 2.2. DEFORMATION TEMPERATURES WITH RESPECT TO STRUCTURAL DEPTH, CORDILLERA BLANCA SHEAR ZONE

Sample	**Quebrada**	**Structural depth** (m)	**Quartz recrystallization microstructures** *T* (°C)[a]	BLG *280-400*	SGR *400-500*	GBM *> 500*	CB *> 630*[b]	**Brittle Overprint** CC	PT	**Quantitative temperature estimates** TitaniQ[c]	ASIM[d]
CB13-71a	Gatay	0 ± 0		x	x			x			
CB13-71b	Gatay	0 ± 0		x	x			x			
CB13-77a	Gatay	56 ± 20		x	x						
CB13-77b	Gatay	56 ± 20			x						
CB13-77c	Gatay	56 ± 20		x	x						
CB13-72a	Gatay	75 ± 14		x	x						
CB13-72b	Gatay	75 ± 14		x	x						
CB13-73a	Gatay	88 ± 16		x	x			x			
CB13-73b	Gatay	88 ± 16		x	x			x	x		
CB13-74a	Gatay	92 ± 18		x	x			x			
CB13-74b	Gatay	92 ± 18			x	x		x			
CB13-75	Gatay	102 ± 19		x	x						
CB13-81	Gatay	104 ± 17				x					
CB13-82	Gatay	104 ± 17			x	x					
CB13-76	Gatay	106 ± 19		x	x			x			
CB13-80a	Gatay	106 ± 16			x						
CB13-80b	Gatay	106 ± 16			x	x		x			
CB13-78	Gatay	110 ± 16		x	x						440 ± 15
CB13-79	Gatay	124 ± 36			x	x				451 ± 60	450 ± 24
CB13-83	Gatay	141 ± 21			x	x					
CB13-55b	Gatay	164 ± 20				x					
CB13-55c	Gatay	164 ± 20			x						440 ± 46
CB13-84	Gatay	203 ± 28				x				472 ± 26	410 ± 30
CB13-53	Gatay	261 ± 17				x					
CB13-58	Gatay	277 ± 73			x	x					

Table 2.2, continued.

Sample	Quebrada	Structural depth (m)	Quartz recrystallization microstructures					Brittle Overprint		Quantitative temperature estimates	
			T (°C)[a]	BLG *280-400*	SGR *400-500*	GBM *> 500*	CB *> 630*[b]	CC	PT	TitaniQ[c]	ASIM[d]
CB13-85	Gatay	277 ± 22			x						
CB13-59	Gatay	314 ± 9				x				489 ± 39	
CB13-57a	Gatay	346 ± 10		x	x						
CB13-57b	Gatay	346 ± 10		x							
CB13-57c	Gatay	346 ± 10		x	x						
CB13-56	Gatay	349 ± 9				x					
CB13-55a	Gatay	386 ± 8			x	x				484 ± 99	470 ± 36
CB13-54a	Gatay	393 ± 12				x	x			489 ± 33	460 ± 28
CB11-24	Rajururi	0 ± 0			x	x					
CB11-23	Rajururi	10 ± 3		x	x	x					
CB11-22	Rajururi	10 ± 4		x	x	x					
CB11-21	Rajururi	11 ± 12			x	x					404 ± 31
CB11-20	Rajururi	21 ± 14			x						
CB11-18	Rajururi	21 ± 21		x	x						
CB11-19	Rajururi	23 ± 10		x	x			x			
CB11-17	Rajururi	32 ± 17			x	x					461 ± 20
CB11-25	Rajururi	65 ± 24			x	x					
CB11-26	Rajururi	87 ± 33		x	x	x					
CB11-27	Rajururi	87 ± 32				x					
CB11-28	Rajururi	258 ± 96				x					
CB11-29	Rajururi	340 ± 60				x	sg				
CB13-01	Ishinca	0 ± 0		x				x			
CB13-02	Ishinca	3 ± 5		x				x			
CB13-03	Ishinca	7 ± 12		x				x			
CB13-04	Ishinca	15 ± 19		x				x			

Table 2.2, continued.

Sample	Quebrada	Structural depth (m)	Quartz recrystallization microstructures					Brittle Overprint		Quantitative temperature estimates	
				BLG	SGR	GBM	CB				
			T (°C)[a]	*280-400*	*400-500*	*> 500*	*> 630*[b]	CC	PT	TitaniQ[c]	ASIM[d]
CB13-05a	Ishinca	22 ± 22		x	x						426 ± 18
CB13-06a	Ishinca	24 ± 22		x	x						
CB13-06b	Ishinca	24 ± 22		x	x			x			
CB13-06d	Ishinca	24 ± 22			x	x					433 ± 27
CB13-07	Ishinca	35 ± 21		x	x						
CB13-09a	Ishinca	42 ± 21		x	x						
CB13-09b	Ishinca	43 ± 22		x	x	x	sg				
CB13-10	Ishinca	46 ± 21			x	x					419 ± 42
CB13-11	Ishinca	49 ± 11			x	x					

Notes: BLG —bulging; SGR — subgrain rotation; GBM — grain boundary migration (Stipp et al., 2002a); CB — chessboard extinction (Kruhl, 1996); CC— cataclasite; PT —pseudotachylyte. Data for Q. Gatay previously reported in Hughes et al (in press). x — contains microstructure. sg — contains prismatic subgrains characteristic of chessboard extinction occuring at high angle to thin section plane (Kruhl, 1996)

[a]Assuming strain rate is approximately 1 x 10^{-12} s^{-1}
(Stipp et al., 2002b)

[b]Temperature of CB extinction at ~300 MPa confining pressure
(Kruhl, 1996)

[c]Calculated using the Thomas et. al (2010) TitaniQ calibration assuming confining pressure = 300 MPa (Hughes et al., in press). Errors are 1σ standard deviation.

[d]Calculated using the Whitney and Stormer (1977) two-feldspar thermometer. Errors are 2σ standard deviation.

transect: within the upper ~90 m of Q. Rajururi, within the upper ~110 m of Q. Gatay, and from 22-43 ± 22 m structural depth within Q. Ishinca. Coinciding BLG ± SGR microstructures also occur in a narrow zone at 346 ± 10 m structural depth in Q. Gatay, suggesting locally moderate to high strain-rates and/or a wider range of temperatures (280-500 °C). In the shallowest ~15 m of Q. Ishinca, BLG occurs without SGR recrystallization microstructures, suggesting either high strain-rate and/or low temperature (280-400 °C) deformation (Stipp et al., 2002b).

New ASIM data for five samples from Q. Rajururi and Q. Ishinca yielded average deformation temperatures from 419 ± 42 to 461 ± 20 °C. Individual myrmekite lobes from Q. Rajururi yielded temperatures as low as 372 ± 50 °C (CB11-21; 11 ± 12 m structural depth) and as high as 504 ± 50 °C (CB11-17; 32 ± 17 m structural depth). Temperatures from individual myrmekite lobes in Ishinca were as low as 364 ± 50 °C (CB13-10; 46 ± 21 m structural depth) and as high as 471 ± 50 °C (CB13-06d; 24 ± 22 m structural depth). Temperatures derived from two-feldspar thermometry on ASIM are generally consistent with the lower ranges of temperatures estimated from recrystallized quartz microstructures.

Quartz Crystallographic Fabrics

Quartz crystallographic fabrics were analyzed by electron backscatter diffraction (EBSD) using the field emission gun scanning electron microscope (FEG-SEM) at the Imaging and Chemical Analysis Laboratory at Montana State University. Data were cleaned using Oxford Instruments Channel 5 software and subsequently processed using the MTEX toolbox for MatLab (Hielscher and Schaeben, 2008). Analytical conditions and raw data processing follow the methods described by Hughes et al. (2019) and can also be found in Supplementary Text S2. Pole figures for quartz c- and a-axes orientations in MTEX along with fabric strength estimates using the J-index (Bunge and Esling, 1982) and M-index (Skemer et al., 2005). As M-index is less affected by the number of orientations analyzed than the J-index for populations with n > 150 (Skemer et al., 2005), we favor the M-index as a representation of quartz crystallographic fabric strength.

Quartz c- and a-axes pole figures for most samples from Q. Rajurui, Q. Gatay, and Q. Ishinca show distributions characteristic of rhomb <a> + prism <a> slip, prism <a> with lesser contributions of rhomb <a> slip, or prominent prism <a> slip. Prominent rhomb <a> ± prism <a> slip is observed in one sample and prism [c] slip is observed in two samples (Fig. 2.6, Table 2.3). In Q. Rajururi, positions nearest the detachment indicate predominant prism <a> slip with varying contributions of rhomb <a> slip (MJCB11-23, MJCB11-21, MJCB11-20 at 10 ± 3 m, 11 ± 12, and 21 ± 14 m, respectively). Intermediate structural positions show prominent y-axis maxima indicative of prism <a> slip (MJCB11-17 and MJCB11-25; 32 ± 17 m and 65 ± 24 m, respectively). C-axes from the deepest sample analyzed in Q. Rajururi (MJCB11-29; 340 ± 60 m) are along the periphery and inclined towards the z-plane (foliation plane), indicating prominent prism [c] slip. Fabric strength appears to be independent of slip system or structural depth in Q. Rajururi. The observed shift from varying combinations of prism <a> + rhomb <a> slip, to prism <a> slip, and ultimately prism [c] slip suggests a general increase in temperature and/or decrease in strain rate towards deeper structural positions in Q. Rajururi.

Q. Gatay pole figures show quartz c- and a-axes distributions consistent with prominent prism <a> with subsidiary rhomb <a> slip at most structural positions (Hughes et al. 2019). Two samples from structurally deep positions (CB13-57c and CB13-55a, 346 ± 10 and 386 ± 8 m, respectively) yielded weak fabrics with M-indices <0.1 (Hughes et al., 2019). As in Q. Rajururi, fabric strength in Q. Gatay is independent of both structural position and prominent slip system.

Fig. 2.6. a) Quartz c-axis (0001) and a-axis (10$\bar{1}$0) pole figures from Qs. Rajururi, Gatay, and Ishinca. Each transect displayed in order of increasing structural depth towards bottom. Plots are equal-area lower hemisphere projections, 1 point per grain, of recrystallized quartz grains, contoured to multiples of uniform distribution (m.u.d.). Slip systems as follows: p: prism <a>, r: rhomb <a>, b: basal <a>, c: prism [c], w: weak fabric. Pole figures for Q. Gatay originally reported in Hughes et al (2019). b) Schematic diagram showing typical c-axes and a-axes distributions for different quartz slip systems (modified from (Toy et al., 2008), after (Schmid and Casey, 1986; Passchier and Trouw, 2005). Generally, at lower temperatures and/or higher strain rates, a combination of basal, rhomb, and prism <a> slip occurs. Increasing temperature or decreasing strain rate results in rhomb <a> + prism <a>, then prism <a> slip only at higher temperatures and/or lower strain rates (Schmid and Casey, 1986; Passchier and Trouw, 2005). c) Schematic diagram of pole figure showing relative position to XZ plane of thin section and shear plane. J-index and M-index are measures of strength (higher numbers are stronger fabrics). N: number of grains contoured on pole figure.

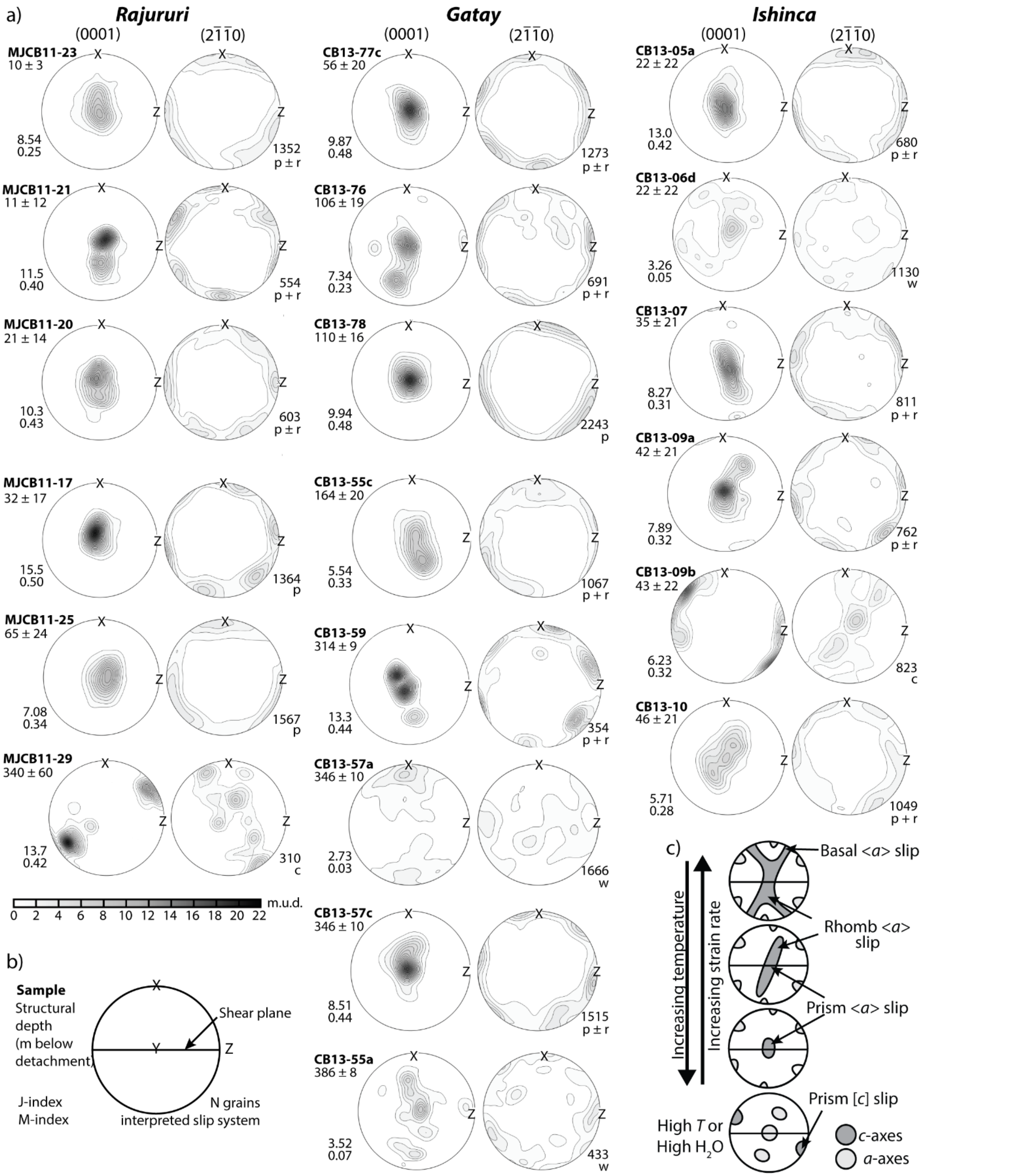

a)
Rajururi
Gatay
Ishinca
(0001)
(2$\bar{1}\bar{1}$0)
MJCB11-23
10 ± 3
8.54
0.25
1352
p ± r
MJCB11-21
11 ± 12
11.5
0.40
554
p + r
MJCB11-20
21 ± 14
10.3
0.43
603
p ± r
MJCB11-17
32 ± 17
15.5
0.50
1364
p
MJCB11-25
65 ± 24
7.08
0.34
1567
p
MJCB11-29
340 ± 60
13.7
0.42
310
c
CB13-77c
56 ± 20
9.87
0.48
1273
p ± r
CB13-76
106 ± 19
7.34
0.23
691
p + r
CB13-78
110 ± 16
9.94
0.48
2243
p
CB13-55c
164 ± 20
5.54
0.33
1067
p + r
CB13-59
314 ± 9
13.3
0.44
354
p + r
CB13-57a
346 ± 10
2.73
0.03
1666
w
CB13-57c
346 ± 10
8.51
0.44
1515
p ± r
CB13-55a
386 ± 8
3.52
0.07
433
w
CB13-05a
22 ± 22
13.0
0.42
680
p ± r
CB13-06d
22 ± 22
3.26
0.05
1130
w
CB13-07
35 ± 21
8.27
0.31
811
p + r
CB13-09a
42 ± 21
7.89
0.32
762
p ± r
CB13-09b
43 ± 22
6.23
0.32
823
c
CB13-10
46 ± 21
5.71
0.28
1049
p + r
X
Z
m.u.d.
0 2 4 6 8 10 12 14 16 18 20 22
b)
Sample
Structural depth (m below detachment)
J-index
M-index
Shear plane
Y
N grains
interpreted slip system
c)
Increasing temperature
Increasing strain rate
Basal <a> slip
Rhomb <a> slip
Prism <a> slip
Prism [c] slip
High T or High H_2O
c-axes
a-axes

TABLE 2.3. RECRYSTALLIZED GRAIN SIZE, DIFFERENTIAL STRESS, AND STRAIN RATE ESTIMATES FOR THE CORDILLERA BLANCA SHEAR ZONE, PERU.

Sample	**Quebrada**	**Structural Depth** (m)			**RMS Grain Size** (μm)			**Differential Stress** (MPa)														
								HK10					ST03					C17				
CB11-17	Rajururi	32	±	17	23.2	±	12.0	**40.4**	+	31.6	-	11.4	**55.2**	+	43.2	-	15.5	**63.8**	+	43.1	-	16.3
CB11-20	Rajururi	21	±	14	34.6	±	22.4	**29.4**	+	37.9	-	9.6	**40.2**	+	51.7	-	13.1	**48.0**	+	52.6	-	14.3
CB11-21	Rajururi	11	±	12	44.7	±	30.6	**24.0**	+	36.0	-	8.1	**32.8**	+	49.1	-	11.1	**40.1**	+	50.7	-	12.4
CB11-23	Rajururi	10	±	3	19.5	±	9.5	**46.4**	+	32.2	-	12.5	**63.3**	+	44.0	-	17.1	**72.1**	+	43.5	-	17.7
CB11-25	Rajururi	65	±	24	39.6	±	26.2	**26.4**	+	36.0	-	8.8	**36.1**	+	49.2	-	12.0	**43.6**	+	50.5	-	13.2
CB11-29	Rajururi	340	±	60	74.1	±	52.4	**16.1**	+	26.5	-	5.6	**21.9**	+	36.2	-	7.6	**28.0**	+	38.9	-	8.83
CB13-05a	Ishinca	22	±	22	19.4	±	13.3	**46.5**	+	70.0	-	15.8	**63.6**	+	95.7	-	21.6	**72.4**	+	92.1	-	22.4
CB13-06b	Ishinca	24	±	22	18.7	±	8.6	**47.9**	+	30.4	-	12.5	**65.5**	+	41.5	-	17.0	**74.3**	+	41.0	-	17.5
CB13-06d	Ishinca	24	±	22	16.3	±	10.2	**53.4**	+	63.2	-	17.1	**73.0**	+	86.3	-	23.4	**81.9**	+	82.6	-	23.9
CB13-07	Ishinca	35	±	21	26.5	±	17.1	**36.3**	+	46.4	-	11.9	**49.6**	+	63.4	-	16.2	**58.0**	+	63.0	-	17.3
CB13-09a	Ishinca	42	±	21	27.9	±	17.4	**34.9**	+	40.9	-	11.1	**47.7**	+	55.8	-	15.2	**55.9**	+	55.9	-	16.3
CB13-09b	Ishinca	43	±	22	36.6	±	23.9	**28.1**	+	37.0	-	9.3	**38.4**	+	50.6	-	12.6	**46.2**	+	51.6	-	13.8
CB13-10	Ishinca	46	±	21	24.9	±	13.5	**38.2**	+	32.8	-	11.1	**52.2**	+	44.8	-	15.2	**60.7**	+	44.9	-	16.0
CB13-55a	Gatay	386	±	8	49.7	±	32.6	**22.1**	+	29.4	-	7.3	**30.1**	+	40.1	-	9.9	**37.2**	+	42.0	-	11.2
CB13-55c	Gatay	164	±	20	18.2	±	9.0	**49.0**	+	35.1	-	13.4	**66.9**	+	48.0	-	18.2	**75.7**	+	47.0	-	18.8
CB13-57a	Gatay	346	±	10	13.7	±	6.6	**61.3**	+	41.4	-	16.4	**83.8**	+	56.6	-	22.3	**92.7**	+	54.3	-	22.4
CB13-57c	Gatay	346	±	10	12.9	±	6.4	**64.3**	+	46.0	-	17.5	**87.9**	+	62.8	-	23.9	**96.7**	+	59.8	-	23.9
CB13-59	Gatay	314	±	9	59.6	±	39.6	**19.1**	+	26.3	-	6.4	**26.1**	+	36.0	-	8.7	**32.7**	+	38.2	-	9.90
CB13-76*	Gatay	106	±	19	14.6	±	9.0	**58.3**	+	65.9	-	18.4	**79.7**	+	90.1	-	25.2	**88.6**	+	85.5	-	25.5
CB13-77c	Gatay	56	±	20	18.9	±	10.1	**47.5**	+	39.6	-	13.7	**64.9**	+	54.2	-	18.7	**73.7**	+	53.1	-	19.3
CB13-78	Gatay	110	±	16	14.8	±	7.1	**57.7**	+	39.5	-	15.5	**78.8**	+	54.0	-	21.1	**87.7**	+	52.1	-	21.3

Table 2.3, continued.

Sample	Differential Stress (MPa)			Temperature (°C)		Strain Rate (s^{-1})					
				TitaniQ	ASIM	**TitaniQ**			**ASIM**		
	Mean Stress					*HK10*	*C17*	*Mean Stress*	*HK10*	*C17*	*Mean Stress*
CB11-17	53.1	+ 10.7	- 12.7		461 ± 20				3.6×10^{-13}	2.2×10^{-12}	1.1×10^{-12}
CB11-20	39.2	+ 8.83	- 9.8								
CB11-21	32.3	+ 7.77	- 8.28		404 ± 31				4.9×10^{-15}	3.8×10^{-14}	1.6×10^{-14}
CB11-23	60.6	+ 11.5	- 14.2								
CB11-25	35.4	+ 8.26	- 8.96								
CB11-29	22.0	+ 5.98	- 5.93								
CB13-05a	60.8	+ 11.6	- 14.3		426 ± 18				1.7×10^{-13}	1.0×10^{-12}	5.0×10^{-13}
CB13-06b	62.6	+ 11.7	- 14.6								
CB13-06d	69.5	+ 12.5	- 16.0		433 ± 27				3.9×10^{-13}	2.7×10^{-12}	1.2×10^{-12}
CB13-07	48.0	+ 10.0	- 11.7								
CB13-09a	46.2	+ 9.79	- 11.3								
CB13-09b	37.6	+ 8.59	- 9.44								
CB13-10	50.3	+ 10.3	- 12.1		419 ± 42				5.9×10^{-14}	3.7×10^{-13}	1.8×10^{-13}
CB13-55a	29.8	+ 7.37	- 7.72	484 ± 99	470 ± 36	7.1×10^{-14}	5.7×10^{-13}	2.4×10^{-13}	4.4×10^{-14}	3.5×10^{-13}	1.5×10^{-13}
CB13-55c	63.9	+ 11.9	- 14.9		440 ± 46				3.6×10^{-13}	2.1×10^{-12}	2.2×10^{-12}
CB13-57a	79.3	+ 13.4	- 17.9								
CB13-57c	83.0	+ 13.7	- 18.6								
CB13-59	25.9	+ 6.71	- 6.85	489 ± 39		4.7×10^{-14}	4.0×10^{-13}	1.6×10^{-13}			
CB13-76*	75.5	+ 13.0	- 17.2	451 ± 60	450 ± 24	2.5×10^{-12}	5.8×10^{-12}	3.1×10^{-12}	1.1×10^{-12}	5.7×10^{-12}	3.0×10^{-12}
CB13-77c	62.1	+ 11.7	- 14.5								
CB13-78	74.7	+ 13.0	- 17.0		440 ± 15				7.0×10^{-13}	3.7×10^{-12}	2.0×10^{-12}

Note:
*Temperature obtained from nearby sample CB13-79 (Hughes et al., 2019).

Table 2.3, continued.

Sample	Quartz CPO	
	Dominant	Subsidiary
CB11-17	p	na
CB11-20	p	r
CB11-21	p,r	na
CB11-23	p	r
CB11-25	p	na
CB11-29	c	na
CB13-05a	p	r
CB13-06b	r	p
CB13-06d	w	na
CB13-07	p, r	na
CB13-09a	p	r
CB13-09b	c	na
CB13-10	p, r	na
CB13-55a	w	na
CB13-55c	p,r	na
CB13-57a	w	na
CB13-57c	p	r
CB13-59	p,r	na
CB13-76*	p,r	na
CB13-77c	p	r
CB13-78	p	na

Pole figures from most samples in Q. Ishinca show y-axis maxima with central girdles, indicating predominantly prism <a> slip with varying contributions of rhomb <a> slip. The pole figure for CB13-06b (22 ± 22 m) shows two c-axes maxima inclined along the x-axis relative to the y-axis, suggesting prominent rhomb <a> slip with a lesser contribution of prism<a> slip. C-axes from CB13-06d (22 ± 22 m) cluster around a slight y-maxima but have an overall weak fabric with a fabric strength of <0.1. CB13-09b (43 ± 22 m) shows c-axes inclined toward the shear plane along the periphery indicative of prism [c] slip. Observing only the samples exhibiting prism <a> and/or rhomb <a> slip in Q. Ishinca, fabric strength decreases slightly away from the detachment surface.

The prominence of rhomb <a> and prism <a> slip across all three transects suggests that deformation across the CBSZ occurred predominantly by dislocation creep in quartz (Lister and Hobbs, 1980; Stipp et al., 2002b, 2002a). Prism [c] slip, observed in quebradas Rajururi and Ishinca, typically occurs at high temperatures and can be facilitated by the presence of H_2O (Blacic, 1975; Blumenfeld et al., 1986). Although Blacic (1975) showed that prism [c] slip can be facilitated by water at high temperatures (~ 700 °C), Kruhl (1998, 1996) has shown that hydrolytic weakening from H_2O diffusion in the c-direction is not required to activate prism [c] slip and occurs at slightly lower temperatures (600-630 °C) at pressures expected for the Cordillera Blanca (i.e. 100-300 MPa, Margirier et al., 2016). C-axes clustered near the extensional direction have also been attributed to preferential grain growth under submagmatic conditions rather than to prism [c] slip (Gapais and Barbarin, 1986; Zibra et al., 2012). Gapais and Barbarin (1986) argued that because the associated a-axis CPO pattern was complex and quartz grains were not notably elongated, prism [c] slip was not responsible for CPO development. For the two Cordillera Blanca samples with C-axes inclined toward the extensional direction, distinct a-axes single girdle patterns comprising three sub-maxima (Fig. 2.6), along with quartz shape preferred orientations (Fig. S3) and the observation of chessboard extinction in quartz, suggest that the pattern is indeed a result of prism [c] slip. The relative roles of elevated temperatures and water in facilitating prism [c] slip are less certain.

Flow Stress Estimates

Recrystallized quartz grain size decreases with increased differential stress (Twiss, 1977; Stipp and Tullis, 2003). This relationship has been experimentally calibrated as a paleopiezometer (Stipp and Tullis, 2003; Holyoke and Kronenberg, 2010), and has recently been calibrated for quartz grain sizes determined using EBSD (Cross et al., 2017). Cross et al. (2017) systematically separated relict grains from recrystallized grains using the grain orientation spread, a measure of internal lattice distortion, of quartz grains. Separating grain populations in this manner is an objective way to select only recrystallized grains for paleopiezometry based on lattice strain rather than grain size, as recrystallized and relict grain sizes often overlap (Cross et al., 2017; Supplementary Fig. S4).

Differential stresses were calculated using the recent 1μm calibration recrystallized quartz piezometer for EBSD-acquired data of Cross et al. (2017). EBSD data were cleaned using Oxford Instruments Channel5 software by removing wild spikes and filling non-indexed grains by interpolation of orientations from 5-nearest neighbors. Subsequent processing and grains size distributions were made using MTEX (Bachmann et al., 2011) following the procedure outlined in the supplementary information of Cross et al (2017) with a critical misorientation of 10°. Minimum grain size was 8 pixels, corresponding to grain sizes of 4.8-12.8 μm for step sizes of 1.5-5 μm, respectively. Grains were subdivided into relict and recrystallized subsets using a threshold value for grain orientation spread (GOS), a measure of lattice distortion within a single grain, that was determined using a trade-off curve (Cross et al., 2017). Paleo-stress estimates reported here are for the recrystallized subset, which contains grains with a GOS below the threshold value. The grain size used for the piezometer is the root mean square (RMS) of equivalent circle diameters for the grain population (Stipp and Tullis, 2003; Cross et al., 2017).

Stresses reported here are derived from the Cross et al. (2017) 1 µm paleopiezometer calibration (Fig. 2.7). Stresses calculated using the Stipp and Tullis (2003) and Holyoke and Kronenberg (2010) calibrations are 3-9 MPa lower and 15-25 MPa lower than those calculated using the Cross et al. (2017) piezometer, respectively (Table 2.3, Supplementary Fig. S5). Lowest stresses of 28.0 +39/-8.9 MPa (340 ± 60 m; Q. Rajururi) to 37.2 +42/-11 MPa (386 ± 8 m; Q. Gatay) occur at the structurally deepest positions in samples where GBM recrystallization microstructures and/or CB extinction are observed. Relatively low stresses (40.1 +50/-12 MPa

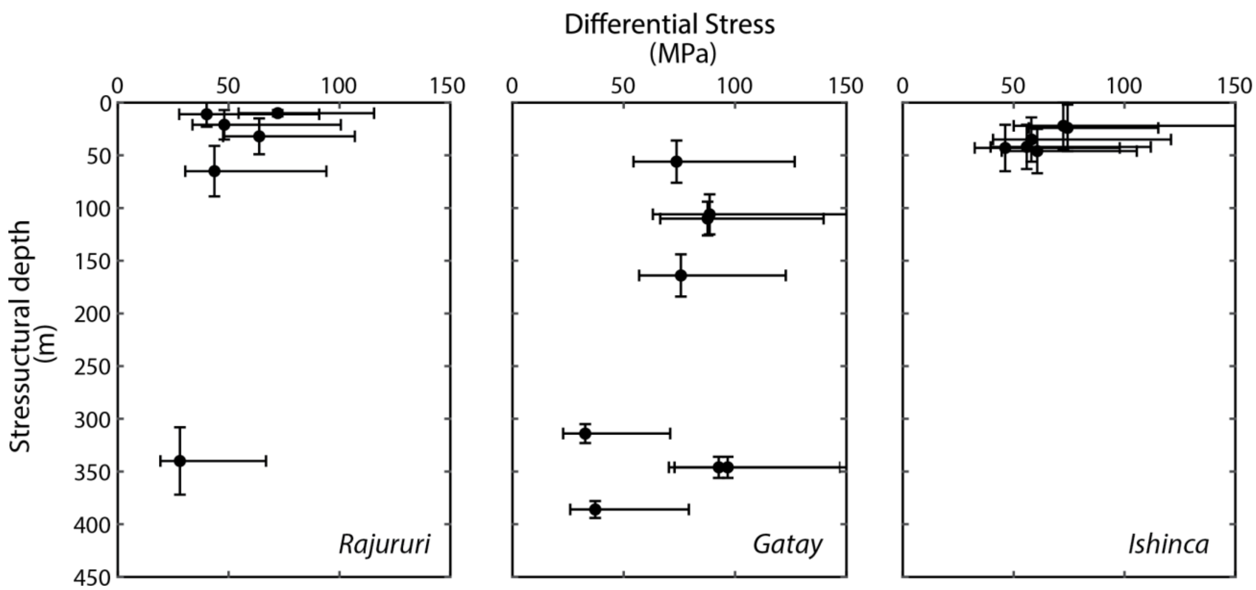

Fig. 2.7. Relationship between differential stress and structural depth below detachment for Qs. Rajururi, Gatay, and Ishinca. Stresses calculated using the 1 µm calibration of Cross et al. (2017) (C17). Errors are 1σ standard deviation of root mean square grain size, propagated through the piezometer. Stresses for Q. Gatay originally reported in Hughes et al. (2019).

(11 ± 12 m) to 58.0 +63/-17 MPa (35 ± 21 m) are observed in the upper 65 m of the shear zone in Q. Rajururi and from 35-46 m structural depth Ishinca. Moderate stresses of 63.8 +43/-16 MPa (32 ± 17 m; Q. Rajururi) to 75.7 + 47/-19 MPa (164 ± 20 m; Q. Gatay) occur at relatively shallow positions (~32 m) in Q. Rajururi, at shallow-intermediate positions in Q.Gatay (56-164 m), and relatively shallow positions (22-24 m) in Q. Ishinca. Two zones of relatively high differential stress are observed within Q. Gatay and one within Q. Ishinca. At structural positions 106 ± 19 m and 110 ± 16 m below the detachment in Q. Gatay, the deepest throughgoing brittle overprint on ductile fabrics occurs (Hughes et al., 2019) and stresses are 88.6 +86/-26 and 87.7 +85/-21 MPa. Along a relatively narrow mylonitic zone at 346 ± 10 m also in Q. Gatay, stresses are 92.7 + 54/-22 and 96.7 +60/-24 MPa. The highest stress recorded in Q. Ishinca is 81.9 +83/-24 MPa (24 ± 22 m). Considering all transects together, the lowest calculated stresses are limited to structural positions deeper than ~340 m. However, as relatively low stresses (40-64 MPa) are also observed within 50 m of the detachment, and as highest stresses (88-97 MPa) occur at structural positions ~110 m and ~346 m below the detachment, no clear trend between differential stress with structural depth occurs.

Discussion

Some have argued that thermal weakening from batholith magmatism did not play a significant role in governing extension along the CBD (e.g. Giovanni et al., 2010). Within the context of existing constraints, our data demonstrate that the shear zone along the CBD likely developed in an elevated geothermal gradient, supporting at least indirectly the role of magmatism in CBSZ evolution (i.e. Petford and Atherton, 1992; McNulty and Farber, 2002; Margirier et al., 2015a).

Strain Rate

Calculated strain rates derived from paired recrystallized quartz paleopiezometry using the Cross et al. (2017) paleopiezometer and ASIM two-feldspar thermometry from individual samples (hereafter referred to as "microstructurally-derived strain rates" are between 3.8 x 10^{-14} s^{-1} (CB11-21; 11 ± 12 m) and 3.7 x 10^{-12} s^{-1} (CB13-78; 110 ± 16 m) using the wet quartzite flow law of Hirth et al. (2001) (Table 2.3; Fig. 2.8). Strain rates decrease to between 4.9 x 10^{-15} s^{-1} and 7.0 x 10^{-13} s^{-1} using the Holyoke and Kronenberg (2010). These estimates rely on the simplified assumption that quartz dynamic recrystallization and ASIM formation are coeval (Langille et al., 2010; Hughes et al., 2019). General agreement between temperature estimates derived from quartz microstructures, TitaniQ thermometry, and ASIM thermometry, along with kinematically consistent oblique grain shape fabrics in quartz and distribution of ASIM along K-feldspar porphyroclasts, support this assumption. A higher strain rate (5.6 x 10^{-12} s^{-1}; 106 ± 19 m) was calculated for CB13-76 using ASIM thermometry from nearby CB13-79 (124 ± 36 m). The slowest calculated strain rate, 3.8 x 10^{-14} s^{-1}, is from a structurally shallow position in Q. Rajururi (11 ± 12 m) and is an order of magnitude lower than the slowest strain rate calculated for either Q. Ishinca (3.7 x 10^{-13} s^{-1}; 46 ± 21 m) or Q. Gatay (3.5 x 10^{-13} s^{-1}; 386 ± 8 m). In general, strain rates from Q. Ishinca and Q. Gatay appear to increase towards the detachment (Fig. 2.8). Q. Rajururi differs from Q. Gatay and Q. Ishinca in that the slowest strain rate is nearest the detachment.

Microstructurally-derived strain rates for Q. Rajururi and Q. Ishinca are broadly consistent with strain rates derived from overall shear zone width and estimated slip rates along the detachment fault (hereafter referred to as "macrostructurally-derived strain rates" at 6 Ma of

Fig. 2.8. Cross-sections of the CBSZ and bounding detachment fault (thick black line) for Qs. Rajururi, Gatay, and Ishinca, shown relative to simplified map from Fig. 2.1. Reference map modified from Giovanni et al. (2010). Cross sections denote quartz recrystallization mechanisms (gray line and dot patterns), interpolated from microstructures observed in thin sections from known locations. BLG: bulging recrystallization, SGR: subgrain rotation recrystallization, GBM: grain boundary migration recrystallization, CB: chessboard extinction. Quartz slip systems are denoted by symbols that are filled based on the differential stress calculated for a given sample using the Cross et al. (2017) 1 μm recrystallized quartz paleopiezometer. Quantitative deformation temperatures are denoted with crosses color-coded to temperatures. Black crosses denote errors in geographic position: horizontal error is 1σ standard deviation of the average map distance from sample to detachment, vertical error is 1σ standard deviation of average elevation (see Supplemental Text S1 for additional details). Black circles indicate samples with qualitative data only. Calculated strain rates (s^{-1}) for samples where both stress and temperature have been quantified are labelled in white rounded rectangles. Strain rates derived from shear zone thickness and previously determined exhumation rate (0.2 km/Ma) ((Margirier et al., 2015)) in italics beneath transect name. Structural depth contours denoted in purple on cross sections. Approximate location of lower shear zone boundary denoted by thick dashed black line. All cross sections are shown with no vertical exaggeration. Elevations given in meters above sea level. Note that cross-section for Ishinca is scaled 2:1 relative to Rajururi and Gatay for clarity.

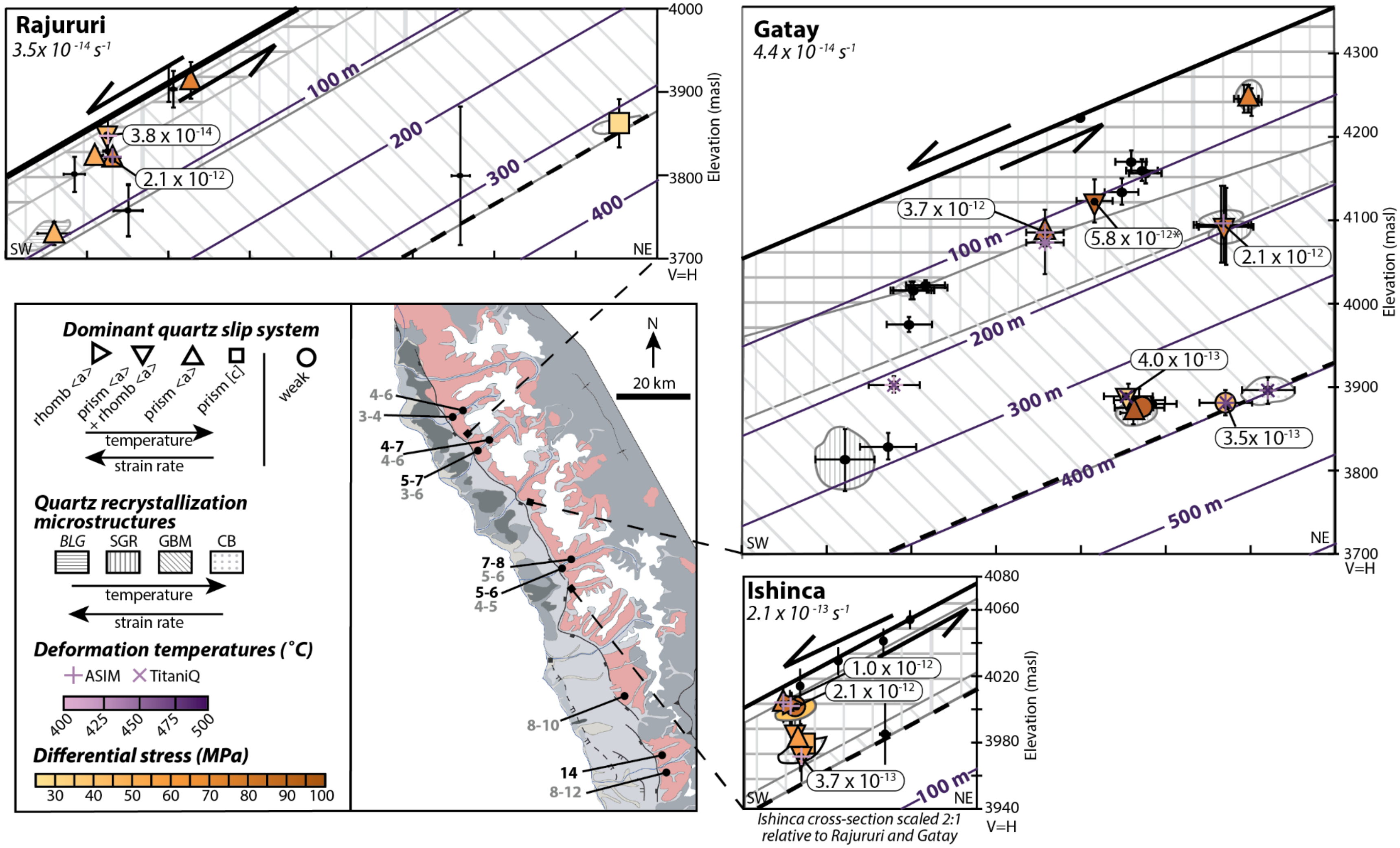
Rajururi
3.5x 10 -14 s-1
3.8 x 10-14
2.1 x 10-12
100 m
200
300
400
SW
NE
4000
3900
3800
3700
V=H
Elevation (masl)
Gatay
4.4 x 10 -14 s-1
3.7 x 10-12
5.8 x 10-12*
2.1 x 10-12
4.0 x 10-13
3.5x 10-13
100 m
200 m
300 m
400 m
500 m
4300
4200
4100
4000
3900
3800
3700
Ishinca
2.1 x 10 -13 s-1
1.0 x 10-12
2.1 x 10-12
3.7 x 10-13
4080
4060
4020
3980
3940
Ishinca cross-section scaled 2:1 relative to Rajururi and Gatay
Dominant quartz slip system
rhomb <a>
prism <a> + rhomb <a>
prism <a>
prism [c]
weak
temperature
strain rate
Quartz recrystallization microstructures
BLG
SGR
GBM
CB
Deformation temperatures (˚C)
ASIM
TitaniQ
400
425
450
475
500
Differential stress (MPa)
30
40
50
60
70
80
90
100
N
20 km
4-6
3-4
4-7
4-6
5-7
3-6
7-8
5-6
5-6
4-5
8-10
14
8-12

3.5 x 10^{-14} s^{-1} and 2.1 x 10^{-13} s^{-1}, respectively. Microstructurally-derived strain rates for Q. Gatay are up to two orders of magnitude faster than the estimated macroscopically-derived strain rate of 4.4 x 10^{-14} s^{-1}. Margirier et al. (2016) used thermochronometric and geobarometric inversion to determine an exhumation rate of ~0.2 km/Ma at 6 Ma to ~1 km/Ma at 2 Ma. Assuming the exhumation rate was constant along strike from Q. Rajururi to Q. Ishinca, given the 32° dipping detachment for Q. Rajururi, 22° detachment for Q. Gatay, and 30° detachment for Q. Ishinca (i.e. Fig. 2.2, Table S2), the slip rate at 6 Ma was 0.38 km/Ma at Q. Rajururi, 0.53 km/Ma at Q. Gatay, and 0.4 km/Ma at Q. Ishinca. At 2 Ma, the slip rates for each transect would have been 1.9 km/Ma, 2.67 km/Ma, 2 km/Ma at Q. Rajururi, Q. Gatay and Q. Ishinca, respectively. Following the assumption that strain rate = velocity (i.e. slip rate)/shear zone width (Behr and Platt, 2011), microstructurally-derived strain rates at ~6 Ma were 3.5 x 10^{-14} s^{-1} at Q. Rajururi, 4.4 x 10^{-14} s^{-1} at Q. Gatay, and 2.1 x 10^{-13} s^{-1} at Q. Ishinca. If instead the exhumation rate for 2 Ma (~1 km/Ma) is assumed, strain rates are roughly an order of magnitude higher. Temperature estimates from this study suggest that ductile deformation mainly occurred at temperatures above ~400 °C. The main leucogranodiorite facies of the batholith was emplaced at 720-800 °C (Margirier et al., 2016) between 6.3 ± 0.3 Ma and 8.2 ± 0.2 Ma (Mukasa, 1984; McNulty et al., 1998). The cooling rate after emplacement was 200 °C/Ma until ~4 Ma and 25 °C/Ma after 4 Ma (Margirier et al., 2015)(Fig. 2.9). Temperature estimates from quartz recrystallization microstructures, two-feldspar ASIM thermometry, and TitaniQ thermometry (this study, Hughes et al., 2019) suggest that ductile deformation in the CBSZ mainly occurred at temperatures above ~400 °C. Using the cooling rates above reported by Margirier et al. (2015) to derive approximate time-temperature relationships, the batholith was at ~300 °C at 5 Ma, 500 °C at 6 Ma, and 725 °C (lower limit of the emplacement temperature; Margirier et al., 2016) at

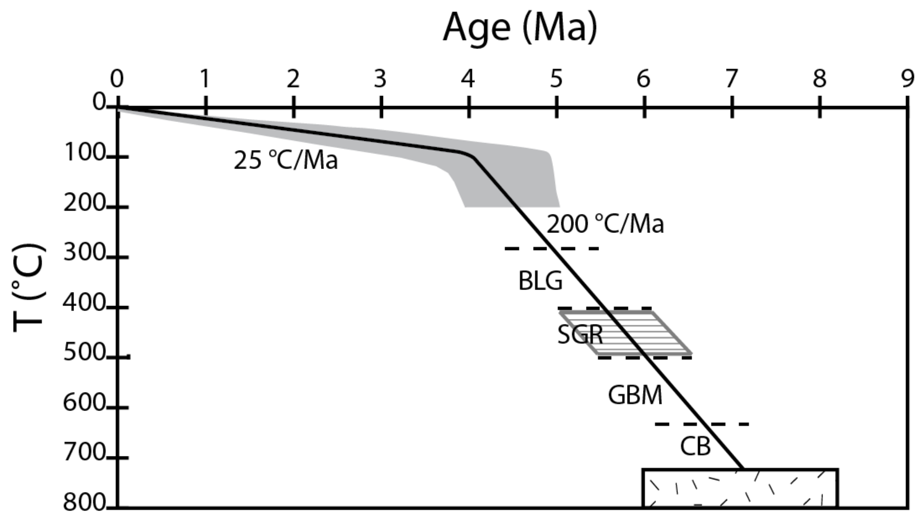

Fig. 2.9. Cooling profile for the Cordillera Blanca batholith modified from Margirier et al. (2015). From 0-5 Ma, black line denotes the published cooling rate with uncertainty (grey field) (Margirier et al. 2015). 200 °C/Ma cooling rate projected to the temperature range at which batholith emplacement occurred (hatched pattern; Margirier et al. 2016). Emplacement of the main leucogranodiorite facies of the batholith is between 6.3 ± 0.3 Ma and 8.2 ± 0.2 Ma (Mukasa, 1984; McNulty et al., 1998). Temperature ranges estimated from quartz recrystallization microstructures, assuming a strain rate of 10^{-12} s^{-1} (Stipp et al., 2002b) are depicted by dashed lines. BLG: bulging, SGR: subgrain rotation, GBM: grain boundary migration recrystallization; CB: chessboard extinction. Grey striped area denotes temperature range from ASIM and TitaniQ thermometry. Horizontal extents of quartz and TitaniQ/ASIM temperature ranges are arbitrary and for clarity are presented as the same length as the Margirier et al. (2015) uncertainty field at 200 °C.

7.3 Ma. Ductile deformation observed in this study thus likely occurred between ~ 6 and 5 Ma and we accordingly favor the use of the 6 Ma (~0.2 km/Ma) exhumation rate of Margirier et al. (2016) to derive strain rates.

Variation along Strike

Mylonite zone thickness varies by an order of magnitude along strike (Fig. 2.3, Fig. 2.8). Regardless of shear zone thickness, where mylonitization occurs and produces an undeformed granite → protomylonite → mylonite → ultramylonite → cataclasite progression towards the detachment fault, shear zone rocks also record similar temperatures. Notably, as supported by Titanium-in-quartz thermometry (Hughes et al. 2019), asymmetric strain-induced myrmekite, quartz crystallographic preferred orientations, and quartz recrystallization microstructures, ductile deformation occurs at temperatures predominantly above 400 °C along the geographically central part of the shear zone regardless of shear zone thickness (Fig. 2.5, Fig. 2.8).

Three explanations are provided here to explain the along-strike variability of shear zone thickness, and the discrepancy between calculated and slip-rate derived bulk strain rates in Q. Gatay. The discrepancy between calculated and bulk strain rates may arise from transient high strain-rate events (i.e. earthquakes) that could create instabilities that could either overprint or be overprinted by sustained ductile deformation. Another possibility is that shear zone thickness for the CBSZ is primarily due to variable amount of exhumation along strike, where the most exhumation occurs in the central segment, and thus the modern exposure preserves a record of deeper, more distributed ductile deformation (i.e. Behr and Platt, 2011). Lastly, the variability of mylonite thickness along strike, as well as the discrepancy between bulk and slip rates at Q. Gatay, may correspond to along-strike variation in exhumation rate or slip rates, where slower exhumation or slip rates correspond to overall slower strain rates, or decreased slip towards tips of fault segments. Variation in detachment geometry may also contribute to varying slip rates. If exhumation rate is constant, a more shallowly dipping fault will equate to a faster slip rate, and thus faster strain rate, than a more steeply dipping fault.

It can be difficult to discern between strain rate variability due to strain partitioning between rheological domains (i.e. Hughes et al., 2019*)* as opposed to strain rate variation along strike. Microfabrics do not follow a simple progression relative to structural position such as would be expected if the strain partitioning was related to the systematic nature of increasing strain rate towards the detachment. Local fluctuations in recorded strain rate may be possible such that strain rates calculated from differential stress measurements are representative of flow stress at a snapshot in time, whereas the time averaged strain rate over the duration of shear zone formation is variable along strike of the CBSZ.

Enhanced exhumation along the central segment of the CBSZ has been proposed by several authors (Wise and Noble, 2003; Margirier et al., 2016, 2018). Margirier et al. (2016) report the highest amount of exhumation in the highest relief areas, which occur in the central part of the Cordillera Blanca. The three transects quantified in this study record similar temperature ranges for deformation, primarily above ~400 °C (Fig. 2.5, Fig. 2.8, Table 2.2). BLG quartz recrystallization microstructures, without the presence of SGR or GBM microstructures, at shallow positions in Q. Ishinca may record a lower deformation temperature than Q. Rajururi or Q. Gatay. However, BLG microstructures may also result from relatively high strain rates, and GBM recrystallization microstructures indicative of deformation above ~500 °C occur at the deepest positions (~45-50 m) in Q. Ishinca. Although these GBM recrystallization microstructures in Q. Ishinca coincide with SGR microstructures, which could suggest slightly faster strain rates or lower temperatures than GBM alone, chessboard extinction at 43 ± 22 m, suggests that at least some deformation in Q. Ishinca occurred at temperatures above ~630 °C (Fig. 2.5, Fig. 2.8).

Complications in evaluating temperature estimates arise from the potential for juxtaposing high temperature and low temperature fabrics as strain localizes along the detachment (Behr and Platt, 2011). Even so, if the variation in thickness was related solely to the amount of exhumation assuming a constant exhumation rate, where the central part of the shear zone was exhuming a deeper record of ductile deformation, temperatures from less exhumed sections, should be lower than those of more exhumed sections. If enhanced exhumation along the geographically central part of the shear zone was related to faster exhumation rate over a constant period of time during ductile deformation, strain rates should be slower in Q. Ishinca than in Q. Rajururi. This is generally not supported by our data. Alternatively, if the exhumation rate was constant, this would likely correspond to a shorter duration of exhumation at Q. Ishinca relative to Q. Gatay and Q. Rajururi. Previous studies have proposed models for growth of the CBD by fault linkage of northern and southern faults, where San Cristobol effectively marks the relay zone between the two segments (Wise and Noble, 2003; Giovanni et al., 2010). Within this framework, Q. Ishinca would be near the southeastern tip of the northern fault, resulting in displacement potentially over a shorter period of time than in Q. Gatay or Q. Rajururi, in turn exhuming a shallower and narrower localized zone of ductile deformation (i.e. Behr and Platt, 2011b). This allows for the relatively higher bulk strain rate in Q. Ishinca, and is consistent with southeast-directed propagation of a fault towards Q. Ishinca and San Cristobal (Giovanni et al., 2010).

It is possible that strain could also localize at deeper positions than those observed and sampled. However, sampling was conducted similalrly across all transects between the detachment, mylonitic zone, and tranisition to the undeformed-weakly deformed granodioritic core. Because of this, while we recognize that strain may have localized at deeper structural positions in Q. Ishinca, strain also could have localized at deeper structural positions than those observed in any other transect. The interpretation here is thus limited primarily to variation in the shear zone that is continuous with and truncated by the detachment fault.

Variations in exhumation rate or slip rate along strike, are indirectly supported by our data. The discrepancy between the calculated and bulk strain rates at Q. Gatay, as opposed to the general agreement of these data at Q. Rajururi and Q. Gatay, can be resolved by an increased exhumation rate at Q. Gatay. Slip rates estimated by (Wise and Noble, 2003) for the central Cordillera Blanca from 8.2-6 Ma, derived using an initial age of intrusion at 8.2 Ma, initial intrusion depths of 3 and 5 km, timing of granitic exposure at the surface of 6 Ma, and a 40 degree dipping surface, were an order of magnitude greater at 2.1-3.5 km/Ma (Wise and Noble, 2003). Although there is considerable uncertainty in the depth of intrusion (Petford et al., 1996; Wise and Noble, 2003; Margirier et al., 2016), these rates are consistent with slip rates of 2.6 km/Ma derived from the faster exhumation rate (1 km/Ma) proposed by Margirier et al., (2016). The 2.6 km/Ma slip rate yields a bulk strain rate of 2.2 x 10^{-13} s^{-1}, which is similar to the deepest calculated strain rate in Q. Gatay (4.2 x 10^{-13}). The increase in strain rate from this position towards the detachment may then be related to narrowing of the active shear zone during exhumation down to a zone ~110 m wide at the transition from ductile to predominantly brittle deformation (Hughes et al., 2019).

Transient Elevated Geothermal Gradient in the CBSZ

Construction of regional crustal strength profiles relative to constraints on emplacement conditions and slip along the detachment illustrates the potential effect of an elevated transient geothermal gradient on shearing along the brittle-ductile transition within the CBSZ (Fig. 2.10). Margirier et al., (2018) calculated geothermal gradients of 25-35 °C/km within the CB region from 7-0 Ma using numerical landscape evolution modeling and AFT dates and (U-Th)/He mean dates in apatite and zircon (Margirier et al., 2018). Newell et al. (2015) assumed a gradient of 25 °C/km to estimate depth of fluid circulation, but also noted that data specifically for the Cordillera Blanca system are sparse, and a locally higher geothermal gradient may be possible. Indeed, a higher geothermal gradient of ca. 40-50 °C/km during the late Miocene was estimated for Cordillera Huayhuash, located ~100 km SSW of the CB, based on zircon (U-Th)/He and ZFT

Fig. 2.10. Strength profiles at 'normal' and elevated geothermal gradients for the Cordillera Blanca Shear Zone. Differential stresses for brittle failure envelope extrapolated from shear stress calculated using Byerlee's law (Byerlee, 1978) for the minimum and maximum measured fault dips (22° and 39°). Colored wedges denote different pore fluid factors (λ) with boundaries calculated at frictional coefficients (μ) of 0.85 (solid black lines) and 0.2 (black dashed lines). Frictional coefficient of 0.85 valid for most lithologies (Byerlee, 1978). Quartz creep curves are plotted at strain rates of 10^{-10} to 10^{-15} s^{-1} using the wet quartz flow law of Hirth et al. (2001). Light gray strain rate field shows range represented by quantitative data from CBSZ. Medium and dark gray fields denote the lower limit and upper limit, respectively, of temperature ranges for bulging (BLG), subgrain rotation (SGR), and grain boundary migration recrystallization (GBM) microstructures (Stipp et al., 2002b, 2002a) and chessboard extinction (CB; Kruhl., 1996). Key in panel c applies to all panels. [a]Minimum and maximum fault displacements based on offset derived from restored sedimentary contact (Giovanni, et al., 2010). [b]Emplacement depths calculated from Margirier et al. (2016) emplacement pressures of 90 MPa to 260 MPa and emplacement pressures between 200 MPa and 350 MPa (Petford and Atherton, 1992; Wise and Noble, 2003). [c]Asymmetric strain-induced myrmekite derived temperatures. [d]Titanium-in-quartz derived temperatures. Regional crustral strength profiles: a) 30 °C/km geothermal gradient and 39° fault dip. Arrow points towards average regional differential stress (Dalmayrac and Molnar, 1981) b) 30 °C/km geothermal gradient and 22° fault dip. c) 50 °C/km geothermal gradient and 39° fault dip. d) 50 °C/km geothermal gradient and 22° fault dip.

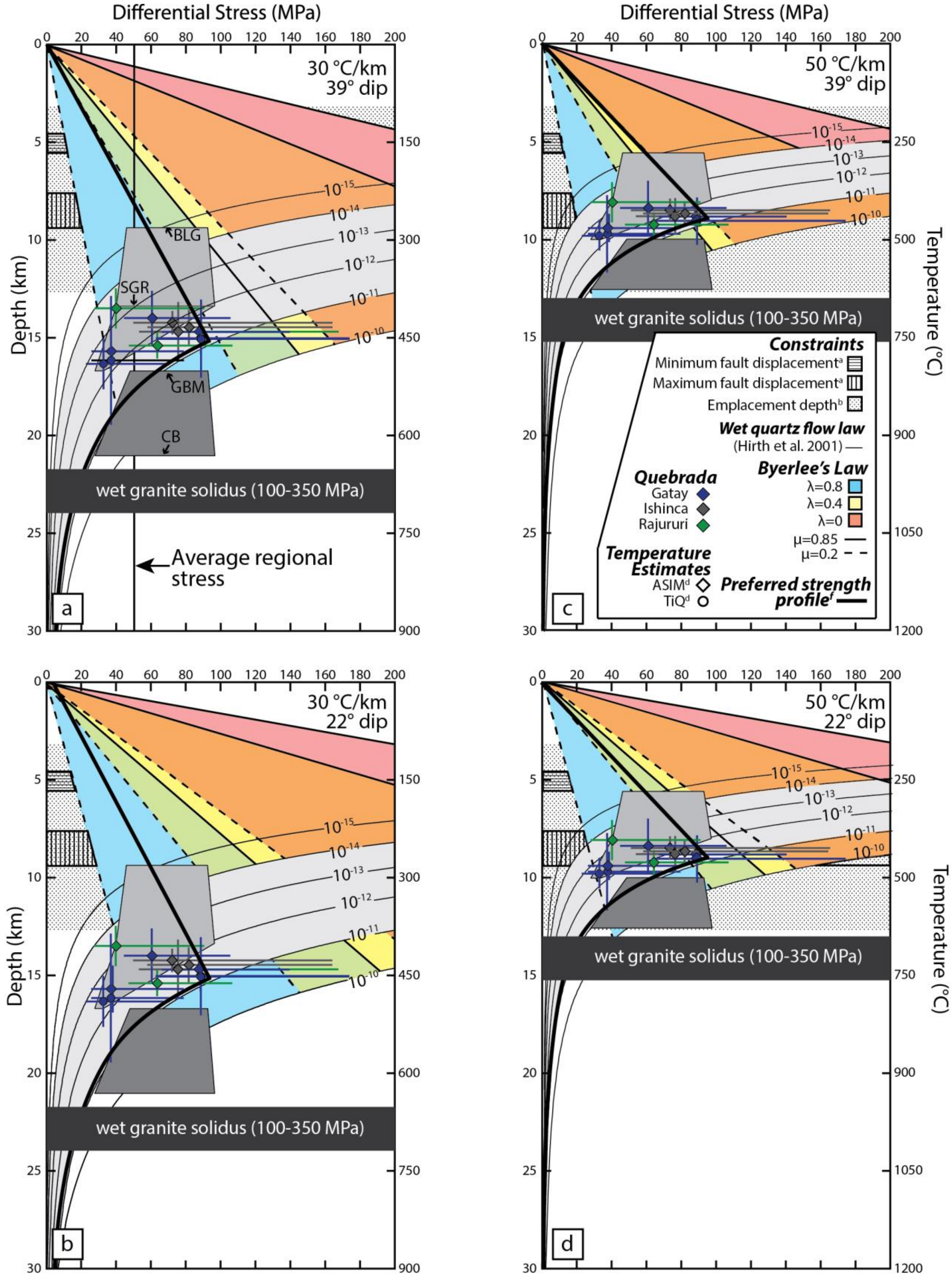

Differential Stress (MPa)
30 °C/km
39° dip
50 °C/km
39° dip
30 °C/km
22° dip
50 °C/km
22° dip
Depth (km)
Temperature (°C)
BLG
SGR
GBM
CB
wet granite solidus (100-350 MPa)
Average regional stress
Constraints
Minimum fault displacement[a]
Maximum fault displacement[a]
Emplacement depth[b]
Wet quartz flow law
(Hirth et al. 2001)
Byerlee's Law
λ=0.8
λ=0.4
λ=0
μ=0.85
μ=0.2
Quebrada
Gatay
Ishinca
Rajururi
Temperature Estimates
ASIM[d]
TiQ[d]
Preferred strength profile[f]
a
b
c
d

dates and attributed to Miocene granitoid plutonism (Garver, Reiners, et al., 2005). An estimatedgeothermal gradient of 30 °C/km is used for calculating a long-term average crustal strength profile for the CBSZ (Fig. 2.10a, 2.10b).

Strength profiles were constructed for the minimum and maximum measured fault dips, 22-39°, to demonstrate the possible range of brittle failure for the CBSZ. See Supplementary Text S3 for additional details regarding profile construction. The 30 °C/km strength profiles are compared to those for a 50 °C/km gradient, which is as an approximation of the gradient for the deepest estimates of emplacement depths (13.2 km; Petford and Atherton, 1992a) (Fig. 2.10c, 2.10d). CBSZ deformation began at submagmatic conditions (Petford and Atherton, 1992; Hughes et al., 2019). If deformation began at temperatures near the wet granite solidus, temperatures were likely between 650-720 °C (Holtz et al., 2001). Amphibole thermobarometry suggests emplacement occurred at 720-800 °C (Margirier et al., 2016), and although the thermobarometer used has been called into question (Margirier et al., 2016), the lower end of this range is consistent with expected temperatures for a hydrated granitoid at 100-350 MPa pressures (650-720 °C; Holtz et al., 2001). If we consider a ~720 °C batholith emplaced at 2 and 3.5 kbar, corresponding to depths of 7.6 and 13.3 km (Petford and Atherton, 1992; Wise and Noble, 2003), a transient elevated geothermal gradient becomes apparent. These estimates correspond to transient geothermal gradients upon emplacement of 96 °C/km to 54 °C/km, respectively.

The depths of emplacement calculated for our samples using a geothermal gradient of 30 °C/km, are deeper than the depth of emplacement predicted by Petford and Atherton (1992) or Margirier et al. (2016) (stippled pattern, 2.10a, 2.10b). Giovanni et al. (2010) estimated 12-15 km of offset along the detachment, corresponding to initial depths of 4.5-5.6 km for a 22°

dipping fault and 7.6-9.4 km for a 39° dipping fault (Fig. 2.10, minimum and maxmimum fault displacement). If deformation occurred in a 30 °C/km gradient, sample depths during deformation (i.e. paleodepths) would be ~13-16 km (Fig. 2.10a, 2.10b), requiring offset along the detachment of 21-27 km assuming a 39° fault. For a 22° dipping fault, required offset along the fault is 35-45 km. The preferred brittle strength profile projected from the highest differential stress estimate to the origin (Kidder et al., 2012) within a 30 °C/km suggests either a low friction coefficient (μ, of 0.2-0.3) at near hydrostatic pore fluid factors (λ, ~0.4) for a 39° dipping fault. For a 22° dipping fault at 30 °C/km, the preferred strength profile suggests either moderate friction coefficients (μ ~0.5-0.6) and pore fluid factors greater than hydrostatic. Although isolated instances of aligned fluid inclusion planes occur in some samples in Q. Gatay (Hughes et al., 2019), further support for significantly higher pore fluid factors, such as connected and/or abundant fluid-filled cracks (Healy, 2009), or low friction coefficients, such as the presence of > ~50% of a low-friction phase (e.g. wet chlorite or illite; Collettini, 2011) across the three observed transects is limited. Although the modern geotherm may be closer to 25-30 °C/km (i.e. (Newell et al., 2015; Margirier et al., 2018), our data support a 50 °C/km geothermal gradient during ductile deformation in the CBSZ.

The 50 °C/km strength profile is more consistent with existing data concerning the conditions and depths of batholith emplacement (Fig. 2.10c, 10d). Within a 50 °C/km geothermal gradient, samples analyzed with TitaniQ and ASIM thermometry plot at paleodepths of 8-10 km, which is within the range of emplacement depths proposed by (Petford and Atherton, 1992; Margirier et al., 2016). Calculated offset along the detachment based on these paleodepths is between 11 and 17 km for 22° and 39°, respectively. This is consistent with the 12-15 km offset proposed by Giovanni et al. (2010), lending additional support to the hypothesis that deformation within the CBSZ occurred within an elevated geothermal gradient. The preferred strength profiles at 50 °C/km and 39° dip (Fig. 2.10c) suggests a pore fluid factor closer to hydrostatic (μ ~0.4). A relatively high pore fluid factor (λ ~0.8) and friction coefficient (μ 0.6-0.85) or alternatively a low friction coefficient (μ 0.2-0.3) and near-hydrostatic pore fluid factor (λ ~0.4) are suggested by the preferred strength profile for a 22° dip at an elevated geothermal gradient (Fig. 2.10d). The former, a relatively high pore fluid factor and relatively high friction coefficient, is generally consistent with the available evidnce of abundant aligned fluid inclusion planes in a quartz-rich sample from Q. Gatay (22° dip). Overall, the preferred strength profiles along with the agreement between calculated sample depths, emplacement depths, and paleodepths derived from offset along the detachment, suggest that ductile deformation in the CBSZ occurred within an elevated transient geothermal gradient.

Conclusions

1. Where it is bounded by the Cordillera Blanca detachment fault, the mylonitic CBSZ varies in width by a factor of 6 along strike, from 60 ± 15 m at quebrada Ishinca to 393 ± 12 m at quebrada Gatay. The widest part of the CBSZ occurs within the central segments along strike between quebradas Paron and Gatay. Mylonitic shear zone widths decrease to 6 ± 2 m and do not grade into the detachment surface in the northernmost observed transects. Ductile deformation is limited in the southernmost observed transects, where deformation is instead characterized by cataclasis and brittle faulting truncating discontinuous mylonitic lenses and otherwise undeformed granodiorite.

2. Recrystallized quartz paleopiezometry suggests stresses in quartz in the CBSZ were between 28.0 +39/-9 MPa and 96.7 +60/-24 MPa. Quantitative temperature estimates are between 404 ± 31 and 470 ± 36 °C.

3. Strain rates calculated from recrystallized quartz paleopiezometry and quantitative temperature estimates are broadly consistent with bulk strain rates derived from a previously determined exhumation rates (~0.2 km/Ma). Paleopiezometry-derived strain rates range from 3.8 x 10^{-14} s^{-1} to 3.7 x 10^{-12} s^{-1} and bulk strain rates range from 4.4 x 10^{-14} s^{-1} to 2.1 x 10^{-13} s^{-1}. Locally in quebrada Gatay, calculated strain rates are an order of magnitude higher than bulk strain rates. Collectively these results suggest that variations in shear zone thickness along strike may be due to variation in exhumation rate, slip rate, and/or fault geometry along strike.

4. To be consistent with existing data for the Cordillera Blanca that suggest relatively shallow batholith emplacement (7.6-13.2 km) and offset along the detachment of 12-15 km, our results require that ductile deformation occurred within an elevated, presumably transient, geothermal gradient of ca. 50 °C/km.

Acknowledgements

We thank Laura Duncan and James Mauch for sampling and field support. Alberto Caffretta of Caraz, Peru and Julio and Tito Olaza of Huaraz, Peru were invaluable resources in accessing the length of the Cordillera Blanca range. We are grateful to Allan Patchen for continued analytical support for EPMA analysis at the University of Tennessee-Knoxville and Laura Kellerman for EBSD support in acquiring EBSD data at the Montana State University Imaging and Chemical Analysis Laboratory. Discussions with Tyler Grambling aided in refining methods for structural depth and shear zone thickness determinations. Lastly, we acknowledge the funding support from the U.S. National Science Foundation through grant EAR-122037 awarded to Micah Jessup and Colin Shaw, which made this work possible.

References

Allmendinger, R. W., Cardozo, N., and Fisher, D., 2012, Structural geology algorithms: Vectors and tensors in structural geology: Cambridge University Press, Cambridge, England.

Bachmann, F., Hielscher, R., and Schaeben, H., 2011, Grain detection from 2d and 3d EBSD data-Specification of the MTEX algorithm: Ultramicroscopy, v. 111, p. 1720–1733, doi: 10.1016/j.ultramic.2011.08.002.

Behr, W.M., and Platt, J.P., 2011, A naturally constrained stress profile through the middle crust in an extensional terrane: Earth and Planetary Science Letters, v. 303, p. 181–192, doi: 10.1016/j.epsl.2010.11.044.

Blacic, J.D., 1975, MECHANISMS IN QUARTZ : THE EFFECT OF In 1965 Griggs and Blacic reported the discovery of hydrolytic weakening of quartz crystals . This phenomenon consists of a large reduction in the com- pressive strength of quartz single crystals under appropriate cond: v. 27, p. 271–294.

Blumenfeld, P., Mainprice, D.H., and Bouchez, J.-L., 1986, C-slip in quartz from subsolidus deformed granite: Tectonophysics, v. 127, p. 97–115, doi: 10.1016/0040-1951(86)90081-8.

Bunge, H.J., and Esling, C., 1982, Reproducible Textures: Textures and Microstructures, v. 5, p. 87–94.

Byerlee, J.D., 1978, Friction of rocks: Pure and Applied Geophysics, v. 116, p. 615–626, doi: 10.1007/BF00876528.

Cobbing, E.J., Pitcher, W.S., Wilson, J.J., Baldock, J.W., Taylor, W.P., McCourt, W., and Snelling, N.J., 1981, The geology of the Western Cordillera of northern Peru: London, England, Institute of Geological Services, 144 p.

Collettini, C., 2011, The mechanical paradox of low-angle normal faults: Current understanding and open questions: Tectonophysics, v. 510, p. 253–268, doi: 10.1016/j.tecto.2011.07.015.

Couch, R., and Whitsett, R.M., 1981, Structures of the Nazca Ridge and the continental shelf and slope of southern Peru: , p. 569–586, doi: 10.1130/mem154-p569.

Cross, A.J., Prior, D.J., Stipp, M., and Kidder, S.B., 2017, The recrystallized grain size piezometer for quartz: An EBSD-based calibration: Geophysical Research Letters, v. 44, p. 6667–6674, doi: 10.1002/2017GL073836.

Dalmayrac, B., and Molnar, P., 1981, Parallel thrust and normal faulting in Peru and constraints on the state of stress: Earth and Planetary Science Letters, v. 55, p. 473–481, doi: 10.1016/0012-821X(81)90174-6.

Deverchere, J., Dorbath, C., and Dorbath, L., 1989, Extension related to a high topography: results from a microearthquake survey in the Andes of Peru and tectonic implications: Geophysical Journal International, v. 98, p. 281–292.

Gapais, D., and Barbarin, B., 1986, QUARTZ FABRIC TRANSITION IN A COOLING SYNTECTONIC GRANITE (HERMITAGE MASSIF , FRANCE) Berth4 et al . (1979a , b) have shown that this leads to C-S structures defined by the association of a schistosity (S surfaces) and of small-scale parallel ductil: v. 125, p. 357–370.

Garver, J.I., Montario, M., Perry, S.E., Reiners, P.W., and Ramage, J.R., 2005, Uplift and exhumation of the northern Peruvian Andes: Reviews in Mineralogy and Geochemistry, p. 305–307.

Garver, J.I., Reiners, P.W., Walker, L.J., Ramage, J.M., and Perry, S.E., 2005, Implications for Timing of Andean Uplift from Thermal Resetting of Radiation-Damaged Zircon in the

Cordillera Huayhuash, Northern Peru: The Journal of Geology, v. 113, p. 117–138, http://www.journals.uchicago.edu/doi/pdfplus/10.1086/427664 (accessed January 2018).

Giovanni, M.K., 2007, Tectonic and Thermal Evolution of the Cordillera Blanca Detachment System, Peruvian Andes: Implications for Normal Faulting in a Contractional Orogen: University of California Los Angeles, 237 p., https://search-proquest-com.proxy.lib.utk.edu:2050/pqdtglobal/docview/304872260/fulltextPDF/FA8BD4AAE1B8419DPQ/1?accountid=14766 (accessed May 2018).

Giovanni, M.K., Horton, B.K., Garzione, C.N., McNulty, B. a., and Grove, M., 2010, Extensional basin evolution in the Cordillera Blanca, Peru: Stratigraphic and isotopic records of detachment faulting and orogenic collapse in the Andean hinterland: Tectonics, v. 29, p. 1–21, doi: 10.1029/2010TC002666.

Healy, D., 2009, Anisotropy, pore fluid pressure and low angle normal faults: Journal of Structural Geology, v. 31, p. 561–574, doi: 10.1016/j.jsg.2009.03.001.

Hielscher, R., and Schaeben, H., 2008, A novel pole figure inversion method: Specification of the MTEX algorithm: Journal of Applied Crystallography, v. 41, p. 1024–1037, doi: 10.1107/S0021889808030112.

Hirth, G., Teyssier, C., Dunlap, J., Dunlap, W.J., and Dunlap, J., 2001, An evaluation of quartzite flow laws based on comparisons between experimentally and naturally deformed rocks: International Journal of Earth Sciences, v. 90, p. 77–87, doi: 10.1007/s005310000152.

Holtz, F., Johannes, W., Tamic, N., and Behrens, H., 2001, Maximum and minimum water contents of granitic melts generated in the crust: A reevaluation and implications: Lithos, v. 56, p. 1–14, doi: 10.1016/S0024-4937(00)00056-6.

Holyoke, C.W., and Kronenberg, A.K., 2010, Accurate differential stress measurement using the molten salt cell and solid salt assemblies in the Griggs apparatus with applications to strength, piezometers and rheology: Tectonophysics, v. 494, p. 17–31, doi: 10.1016/j.tecto.2010.08.001.

Hughes, C.A., Jessup, M.J., Shaw, C.A., and Newell, D.L., 2019, Deformation conditions during syn-convergent extension along the Cordillera Blanca shear zone (CBSZ), Peru: Geosphere, v. In press.

Kidder, S.B., Avouac, J.P., and Chan, Y.C., 2012, Constraints from rocks in the Taiwan orogen on crustal stress levels and rheology: Journal of Geophysical Research: Solid Earth, v. 117, p. 1–13, doi: 10.1029/2012JB009303.

Kirkpatrick, J.D., and Rowe, C.D., 2013, Disappearing ink: How pseudotachylytes are lost from the rock record: Journal of Structural Geology, v. 52, doi: 10.1016/j.jsg.2013.03.003.

Kirkpatrick, J.D., Shipton, Z.K., and Persano, C., 2009, Short Note Pseudotachylytes: Rarely Generated, Rarely Preserved, or Rarely Reported? 2Bulletin of the Seismological Society of America, v. 99, p. 382–388, doi: 10.1785/0120080114.

Kruhl, J.H., 1996, Prism- and basal-plane parallel subgrain boundaries in quartz: a microstructural geothermobaromether: Journal of Metamorphic Geology, v. 14, p. 581–589, doi: 10.1046/j.1525-1314.1996.00413.x.

Kruhl, J.H., 1998, Prism- and basal-plane parallel subgrain boundaries in quartz: a microstructural geothermobaromether: Journal of Metamorphic Geology, v. 14, p. 581–589, doi: 10.1046/j.1525-1314.1996.00413.x.

Langille, J.M., Jessup, M.J., Cottle, J.M., Newell, D.L., and Seward, G., 2010, Kinematic evolution of the Ama Drime detachment: Insights into orogen-parallel extension and exhumation of the Ama Drime Massif, Tibet-Nepal: Journal of Structural Geology, v. 32,

p. 900–919, doi: 10.1016/j.jsg.2010.04.005.

Lister, G.S., and Hobbs, B.. E., 1980, The simulation of fabric development during plastic deformation and its application to quartzite: the influence of deformation history: Journal of Structural Geology, v. 2, p. 355–370, doi: 10.1016/0191-8141(80)90023-1.

Margirier, A., Audin, L., Robert, X., Herman, F., Ganne, J., and Schwartz, S., 2016, Time and mode of exhumation of the Cordillera Blanca batholith (Peruvian Andes): Journal of Geophysical Research: Solid Earth, v. 121, p. 6235–6249, doi: 10.1002/2016JB013055.

Margirier, A., Audin, L., Robert, X., Pêcher, A., and Schwartz, S., 2017, Stress field evolution above the Peruvian flat-slab (Cordillera Blanca, northern Peru): Journal of South American Earth Sciences, v. 77, p. 58–69, doi: 10.1016/j.jsames.2017.04.015.

Margirier, A., Braun, J., Robert, X., and Audin, L., 2018, Role of erosion and isostasy in the Cordillera Blanca uplift: Insights from landscape evolution modeling (northern Peru, Andes): Tectonophysics, v. 728–729, p. 119–129, doi: 10.1016/j.tecto.2018.02.009.

Margirier, A., Robert, X., Audin, L., Gautheron, C., Bernet, M., Hall, S., and Simon-Labric, T., 2015, Slab flattening, magmatism, and surface uplift in the Cordillera Occidental (Northern Peru): Geology, v. 43, p. 1031–1034, doi: 10.1130/G37061.1.

McNulty, B. a., and Farber, D., 2002, Active detachment faulting above the Peruvian flat slab: Geology, v. 30, p. 567–570, doi: 10.1130/0091-7613(2002)030<0567:ADFATP>2.0.CO;2.

McNulty, B. a., Farber, D.L., Wallace, G.S., Lopez, R., and Palacios, O., 1998, Role of plate kinematics and plate-slip-vector partitioning in continental magmatic arcs: Evidence from the Cordillera Blanca, Peru: Geology, v. 26, p. 827–830, doi: 10.1130/0091-7613(1998)026<0827:ROPKAP>2.3.CO;2.

Mercier, J.L., Sebrier, M., Lavenu, A., Cabrera, J., Bellier, O., Dumont, J.-F., and Machare, J., 1992, Changes in the Tectonic Regime Above a Subduction Zone of Andean Type: The Andes of Peru and Bolivia During the Pliocene-Plesitocene: Journal of Geophysical Research, v. 97, p. 11945–11982.

Michalak, M., 2013, Exhumation of the Peruvian Andes; insights from mineral chronometers: , p. 166.

Montario, M.J., 2001, Exhumation of the Cordillera Blanca, Northern Peru, based on apatite fission track analysis: Unpublished Thesis, Department of Geology, Union College, Schenectady, New York, 55 p., p. 8, http://idol.union.edu/garverj/FT/Montario/Montario.html.

Mukasa, S.B., 1984, Comparative lead isotope systematics and zircon uranium-lead geochronology for the Coastal, San Nicolas, and Cordillera Blanca Batholiths, Peru: University of California, Santa Barbara, 148 p.

Newell, D.L., Jessup, M.J., Hilton, D.R., Shaw, C., and Hughes, C., 2015, Mantle-Derived Helium in Hot Springs of the Cordillera Blanca, Peru: Implications for Mantle-to- Crust Fluid Transfer in a Flat-Slab Subduction Setting: Chemical Geology Chemical Geology Chemical Geology, v. 417, p. 200–209, doi: 10.1016/j.chemgeo.2015.10.003.

Passchier, C.W., and Trouw, R. a J., 2005, Microtectonics: 366 p., doi: 10.1007/3-540-29359-0.

Petford, N., and Atherton, M.P., 1992, Granitoid emplacement and deformation along a major crustal lineament: The Cordillera Blanca, Peru: Tectonophysics, v. 205, p. 171–185, doi: 10.1016/0040-1951(92)90425-6.

Petford, N., and Atherton, M.P., 1996, Na-rich Partial Melts from Newly Underplated Basaltic Crust: the Cordillera Blanca Batholith, Peru: Journal of Petrology, v. 37, p. 1491–1521, doi: 10.1093/petrology/37.6.1491.

Petford, N., Atherton, M.P., and Halliday, A.N., 1996, Rapid magma production rates, underplating and remelting in the Andes: isotopic evidence from northern-central Peru (9–11 °S): Journal of South American Earth Sciences, v. 9, p. 69–78, doi: 10.1016/0895-9811(96)00028-4.

Schmid, S.M., and Casey, M., 1986, Complete Fabric Analysis of some Commonly Observed Quartz C-axis Patterns: Geophysical Monograph, v. 36, p. 263–286.

Schwartz, D.P., 1988a, Paleoseismicity and Neotectonics of the Cordillera Blanca Fault Zone, Northern Peruvian Andes: Journal of Geophysical Research, v. 93, p. 4712–4730.

Schwartz, D.P., 1988b, Paleoseismicty and Neotectonics of the Cordillera Blanca Fault Zone, Zorthern Peruvian Andes: Journal of Geophysical Research, v. 93, p. 4712–4730.

Sebrier, M., Mercier, J.L., Megard, F., Laubacher, G., and Carey-Cailhardis, C., 1985, Quaternary normal and reverse faulting and the state of stress in the central Andes of south Peru: Tectonics, v. 4, p. 739–780.

Skemer, P., Katayama, I., Jiang, Z., and Karato, S., 2005, The misorientation index: Development of a new method for calculating the strength of lattice-preferred orientation: Tectonophysics, v. 411, p. 157–167, doi: 10.1016/j.tecto.2005.08.023.

Stipp, M., Stünitz, H., Heilbronner, R.P., and Schmid, S.M., 2002a, Dynamic recrystallization of quartz: correlation between natural and experimental conditions: Geological Society, London, Special Publications, v. 200, p. 171–190, doi: 10.1144/GSL.SP.2001.200.01.11.

Stipp, M., Stünitz, H., Heilbronner, R.P., and Schmid, S.M., 2002b, The eastern Tonale fault zone: A “natural laboratory” for crystal plastic deformation of quartz over a temperature range from 250 to 700 °C: Journal of Structural Geology, v. 24, p. 1861–1884, doi:

10.1016/S0191-8141(02)00035-4.

Stipp, M., and Tullis, J., 2003, The recrystallized grain size piezometer for quartz: Geophysical Research Letters, v. 30, p. 1–5, doi: 10.1029/2003GL018444.

Stipp, M., Tullis, J., and Behrens, H., 2006, Effect of water on the dislocation creep microstructure and flow stress of quartz and implications for the recrystallized grain size piezometer: Journal of Geophysical Research: Solid Earth, v. 111, p. 1–19, doi: 10.1029/2005JB003852.

Suarez, G., Molnar, P., and Burchfiel, B.C., 1983, Seismicity, fault plane solutions, depth of faulting, and active tectonics of the Andes of Peru, Ecuador, and Southern Colombia: Journal of Geophysical Research, v. 88, p. 10,403-10,428, doi: 10.1029/JB088iB12p10403.

Toy, V.G., Prior, D.J., and Norris, R.J., 2008, Quartz fabrics in the Alpine Fault mylonites: Influence of pre-existing preferred orientations on fabric development during progressive uplift: Journal of Structural Geology, v. 30, p. 602–621, doi: 10.1016/j.jsg.2008.01.001.

Twiss, R.J., 1977, Theory And Applicability Of A Recrystallized Grain-Size Paleopiezometer: Pure And Applied Geophysics, v. 115, p. 227–244.

Uyeda, S., and Watanabe, T., 1970, Preliminary report of terrestrial heat flow study in the South American continent; distribution of geothermal gradients: Tectonophysics, v. 10, p. 235–242.

Wise, J.M., and Noble, D.C., 2003, Geomorphic Evolution of the Cordillera Blanca , Northern Peru: Boletin de la Sociedad geologica del Peru, v. 96, p. 65–85.

Zibra, I., Kruhl, J.H., Montanini, a., and Tribuzio, R., 2012, Shearing of magma along a high-grade shear zone: Evolution of microstructures during the transition from magmatic to solid-state flow: Journal of Structural Geology, v. 37, p. 150–160, doi: 10.1016/j.jsg.2012.01.011.

Appendix II.I. Supplemental Tables

TABLE S4. STRUCTURAL MEASUREMENTS AND STEREONET VALUES.

	DEM Detachment Mean Plane		Poles FMV							Field detachment Mean Plane		Poles FMV						
Quebrada	Strike	Dip	Trend	Plunge	N	a95	a99	kappa	mean length	Strike	Dip	Trend	Plunge	N	a95	a99	kappa	mean length
Corongo	169.3	32.3	79.3	57.7	918	0.6	0.7	64	0.984	NA	NA							
Honda	161.8	27.1	71.8	62.9	561	0.5	0.6	135.4	0.993									
Gatay	153.7	21.9	63.7	68.1	1473	0.4	0.5	88.6	0.989	NA	NA							
Ishinca	189.3	30	99.3	60	234	0.7	0.9	159.6	0.994	NA	NA							
Llaca	126.8	31	36.8	59	459	0.7	0.9	91.9	0.989	137.4	34.5	47.4	55.5	13	4.4	5.6	90	0.990
Llanganuco	149.1	31.8	59.1	58.2	1179	0.5	0.7	60.6	0.984	NA	NA	-	-	-	-	-	-	-
Mirasanta	180.2	37.8	90.2	52.2	6103	0.2	0.3	53.2	0.981	NA	NA	-	-	-	-	-	-	-
Paron	147.4	29.6	57.4	60.4	650	0.9	1.2	35.4	0.972	NA	NA	-	-	-	-	-	-	-
Pato	173.3	39.2	83.3	50.8	913	0.6	0.7	62.1	0.984	160.9	46.3			18	3.4	4.3	106.2	0.991
Rajururi	136.4	31.5	46.4	58.5	1004	0.5	0.6	90.2	0.989	139.2	36.7	49.2	53.3	57	2.3	2.9	65.6	0.985
Rajucolta	177.7	24.7	87.7	65.3	159	0.9	1.1	166.8	0.994	NA	NA	-	-	-	-	-	-	-
Santa Cruz	153.5	34.3	63.5	55.7	1751	0.4	0.5	73.2	0.986	154	50	64	40	8	10.5	13.9	28.6	0.969
San Cristobal	149.3	30.3	59.3	59.7	291	0.6	0.8	186.5	0.995	173	29.3	17.1	43.2	3	20	32.4	39.2	0.983
Ulta	146.3	31	56.3	59	831	0.5	0.6	0.3.3	0.990	118.2	37.9	28.2	52.1	5	6.9	9.7	122.9	0.994
Huascaran	149.5	29.3	59.5	60.7	605	0.7	0.9	67.8	0.985	140.1	35.3	50.1	54.7	6	8.8	11.9	59.5	0.986

Notes: FMV— fisher mean vector. a95,a99 are 95% and 99% confidence intervals on fisher mean vectors, and along with kappa and mean length, are descriptive statistics of fisher mean vectors calculated using Stereonet Version 10.1.1 (Allmendinger, 2013).

Table S4, continued.

	Field Normal Fault			Poles						Mean Foliation			Poles					
	Mean Plane			FMV														
Quebrada	Strike	Dip	N	Trend	Plunge	a95	a99	kappa	mean length	Strike	Dip	N	Trend	Plunge	a95	a99	kappa	Mean length
Corongo	206	56	1	116	36	100	100	0	1	150.5	42.8	2	60.5	47.2	114	100	7.3	0.931
Honda										115.5	27.3	10	25.5	62.7	8.9	11.5	30.6	0.971
Gatay																		
Ishinca																		
Llaca	127.3	56.7	19	37.3	33.3	5.6	7.1	37	0.974	125.7	28	34	35.7	62	4	5	39.4	0.975
Llanganuco	-	-	-	-	-	-	-	-	-	110.3	41.4	8	20.3	48.6	17.8	23.6	10.6	0.918
Mirasanta	-	-	-	-	-	-	-	-	-	182.3	35.5	6	92.3	54.7	9.6	13	50	0.983
Paron	-	-	-	-	-	-	-	-	-	106.5	31.4	10	16.5	58.6	12.6	16.4	15.7	0.943
Pato	164.3	40.6	17	72.6	43.7	4.7	6	59.1	0.984	127	30.5	16	37.1	59.5	11.5	14.7	11.2	0.917
Rajururi	-	-	-	-	-	-	-	-	-									
Rajucolta	-	-	-	-	-	-	-	-	-	158.2	32.7	16	68.2	57.3	8.5	10.9	19.7	0.952
Santa Cruz	-	-	-	-	-	-	-	-	-	117.7	29.4	13	27.7	60.6	16.3	21	7.4	0.876
San Cristobal	-	-	-	-	-	-	-	-	-	177.1	33.3	8	87.1	56.7	14.4	19.1	15.7	0.944
Ulta	-	-	-	-	-	-	-	-	-	160.4	26.2	6	70.4	63.8	23.6	32.2	9	0.908
Huascaran	-	-	-	-	-	-	-	-	-	115.1	36.2	4	25.1	35.8	4.4	6.3	446.7	0.998

Table S4, continued.

	Lineation						
Quebrada	N	Trend	Plunge	a95	a99	kappa	mean Length
Corongo	1	270	30	na	na	na	na
Honda	9	209	26.7	11.7	15.3	20.3	0.9563
Gatay							
Ishinca							
Llaca	15	237.1	25.8	8.6	11.1	20.5	0.9545
Llanganuco	7	216.7	41.7	21.6	28.9	8.8	0.9025
Mirasanta	4	239.1	34	19.2	28.1	23.9	0.9687
Paron	8	207.5	33.7	8.1	10.7	47.7	0.9817
Pato	14	220.8	38.1	10.6	13.6	15	0.9382
Rajururi							
Rajucolta	7	270	40.4	35.8	48.4	3.8	0.7746
Santa Cruz	10	217.5	36.3	5.1	6.6	90.7	0.9901
San Cristobal	4	236.2	24.6	18.7	27.5	25	0.97
Ulta	2	241	25.5	20.1	47	155.9	0.9968
Huascaran	4	224.6	31.2	12.9	18.9	51.5	0.9854

	Detachment Slickenlines						
	N	Trend	Plunge	a95	a99	kappa	mean Length
San Cristobal	29	224.7	29.6	6	7.5	21.2	0.9544
Huascaran	43	220.9	28.3	4.2	5.3	27.9	0.965

	SlickenSurfaces (in otherwise undeformed granite)								
San Cristobal	Strike	Dip	N	Trend	Plunge	a95	a99	kappa	mean length
Huascaran									
	116.8	30.7	44	26.8	59.3	3.2	4	47.2	0.9793

	Magmatic Foliation								
	Strike	Dip	N	Trend	Plunge	a95	a99	kapp	mean length
Huascaran	9.5	45	2	279.5	45	1.5	3.5	26262.9	1

TABLE S5. MACROSTRUCTURAL STRAIN RATE CALCULATIONS.

Quebrada	Dip	Slip Rate* (km/yr)	Strain Rate (s^{-1})
Rajururi	39	0.38	3.5×10^{-14}
Gatay	22	0.53	4.4×10^{-14}
Ishinca	30	0.4	2.1×10^{-13}

Note:
*assuming exhumation rate of 0.2 km/Ma (Margirier et al., 2016)

Appendix II.II. Supplemental Text

Supplemental Text S1. Shear Zone Thickness and Structural Depth Determinations

Shear zone thicknesses have been estimated based on field observations, including detachment orientation measurements and sample locations collected using a Garmin eTrex handheld GPS unit, and calculations of structural depth with reference to the detachment surface for a given transect. When possible, field measurements were used to constrain the orientation of the detachment surface. Field-derived detachment orientations were compared to the those determined using ArcGIS (Fig. 2.3, grey great circles). 30-meter (1 arcsecond) shuttle radar topography mission (SRTM) data was used to construct a digital elevation model (DEM) using 3DEM and imported into ArcMap 10.6, projected into the PSAD 1956 projected coordinate system (WGS 84 Geographic Coordinate System). Slope and aspect rasters were constructed from the DEM. Subsets of the slope and aspect rasters along the detachment surface were created for each transect, the locations of which were constrained based on sampling locations of breccias and field observations when possible, and otherwise constrained based on breaks in slope and aspect along with Airbus satellite imagery and 3D visualization using Google Earth. Caution was taken to exclude parts of detachment surfaces at relatively high elevations that likely experienced significant erosion, which are indicated by a notable decrease in slope is observed along with evidence of glacial scouring. Slope and aspect values, which correspond to dip and dip direction, for each transect were imported as planes into Stereonet 10.0 (Allmendinger et al., 2012). The mean detachment surface attitude was derived from the fisher mean vector to poles of imported planes for each transect. At least 1000 data points were used for most transects; specific number of data used for each transect, along with orientations derived from field-based, ArcGIS (i.e. DEM) -based, and Google Earth-based (Hughes et al., 2019) methods, are listed in Table S4.

Structural depths were projected along the dip direction of the average detachment surface orientation for each transect. The detachment orientation used for projection is averaged from orientations determined via field measurements, three-point problems solved using Google Earth with AirBus satellite imagery (i.e. Hughes et al., 2019), and DEM via ArcMap 10.6. For transects where samples were collected along the detachment surface, the datum of the average detachment surface orientation was hung at the location of the structurally highest sample from the detachment. ~10 m corrugations were observed along the detachment surface, such that for some samples nearer to the detachment, structural depths have error bars nearly equivalent to the calculated depth (i.e. quebrada Ishinca). This effect is exacerbated by differences in orientation derived from field measurements and DEM measurements. For the Mirasanta transect, samples were collected along a road oblique to strike of the detachment surface. Two shear zones were identified by projecting all Mirasanta samples to the same detachment surface in ArcGIS, hung on the structurally highest sample collected along the detachment in the transect.

Supplemental Text S2. EBSD Analytical Conditions and Raw Data Processing

Quartz crystallographic preferred orientations and recrystallized grain sizes were derived using EBSD on the field emission gun-scanning electron microscope at the Imaging and Chemical Analysis Laboratory (ICAL) at Montana State University. Operating conditions were 20 Pa variable pressure and 20-30 kV. 75 reflectors were used to index Kikuchi band patterns for quartz. Data was acquired using the Oxford Instruments HKL Channel 5 Flamenco software (version 5.5).

Raw data was initially processed in using Channel 5 Tango software (version 5.5). Wild spikes, individual pixels with an misorientation with all 8 surrounding neighbor grains greater than the critical misorientation (10°), were removed. Orientations of misindexed pixels were adjusted to based on 5 nearest neighbors. Rotations of 60° ± 5°about the c-axis {0001} were removed to adjust for quartz pseudosymmetry. Data was subsequently imported into the MTEX toolbox for MatLab using the script generated by the import wizard (Bachmann et al., 2010) and analyzed using scripts modified from Cross et al., (2017). Scripts used to finish processing the data, including removing pseudosymmetry that was not corrected for in the Channel 5 protocol, are provided at the end of this document.

Supplemental Text S3. Construction of Regional Crustal Strength Profiles

Deformation temperatures derived from asymmetric strain-induced myrmekite thermometry and titanium-in-quartz thermometry, along with differential stresses derived from recrystallized quartz paleopiezometry, serve as the basis for regional crustal strength profiles for the Cordillera Blanca shear zone (CBSZ). Sample depths were calculated from the deformation temperatures under geothermal gradients of 30 °C/km and 50 °C/km.

Brittle failure envelopes were plotted following Byerlee's law for initial friction of intact rock (Byerlee, 1978):

$$\tau = \mu\bar{\sigma}_v \qquad (1)$$

where τ is shear stress, μ is the friction coefficient (maximum of 0.85 for most lithologies (Byerlee, 1978); 0.6-0.85 for granite; ~0.7 for dry chlorite; 0.26-0.38 for wet chlorite (Collettini, 2011 and references therein), and $\bar{\sigma}_v$ is effective vertical stress. Equation (1) can thus be reformulated as:

$$\tau = \mu\rho g h(1-\lambda) \qquad (2)$$

where ρ is density, assumed to be 2700 kg/m^3, g is gravitational acceleration, h is depth, and λ is the pore fluid factor, which is the ratio of pore fluid pressure to total vertical stress (Brace & Kohlstedt, 1980). Shear stresses were calculated using equation (2) at a μ from 0.2 to 0.85 and λ of 0.8, 0.4 (hydrostatic), and 0 (dry). These shear stresses were used to calculate differential stress at the minimum and maximum measured dip angles along the Cordillera Blanca detachment, 22° and 39° by the following equation:

$$\tau = \frac{1}{2}\sin 2\theta\,(\sigma_1 - \sigma_3) \qquad (3)$$

where θ is the angle between σ_1 and the normal to the fault plane.

Ductile creep curves were calculated for strain rates from 10^{-10} to 10^{-15} s^{-1} following the flow law from Hirth et al., (2001):

$$\dot{\varepsilon} = A f_{H_2O}^{m} \sigma^{n} \exp\left(\frac{-Q}{RT}\right) \qquad (4)$$

where A is a material parameter, such that log (A)= -11.2 ± 0.6 MPa^{-n}/s, f_{H_2O} is water fugacity, determined using the fugacity calculator:

https://www.esci.umn.edu/people/researchers/withe012/fugacity.htm based on the equations in (Sterner & Pitzer, 1994), *m* is the fugacity exponent =1, σ is differential stress (MPa), *n* is the stress exponent = 4, Q is the activation energy =135 ± 15 kJ/mol, R is the ideal gas constant, and T is temperature (K).

Appendix II.III. Supplemental Figures

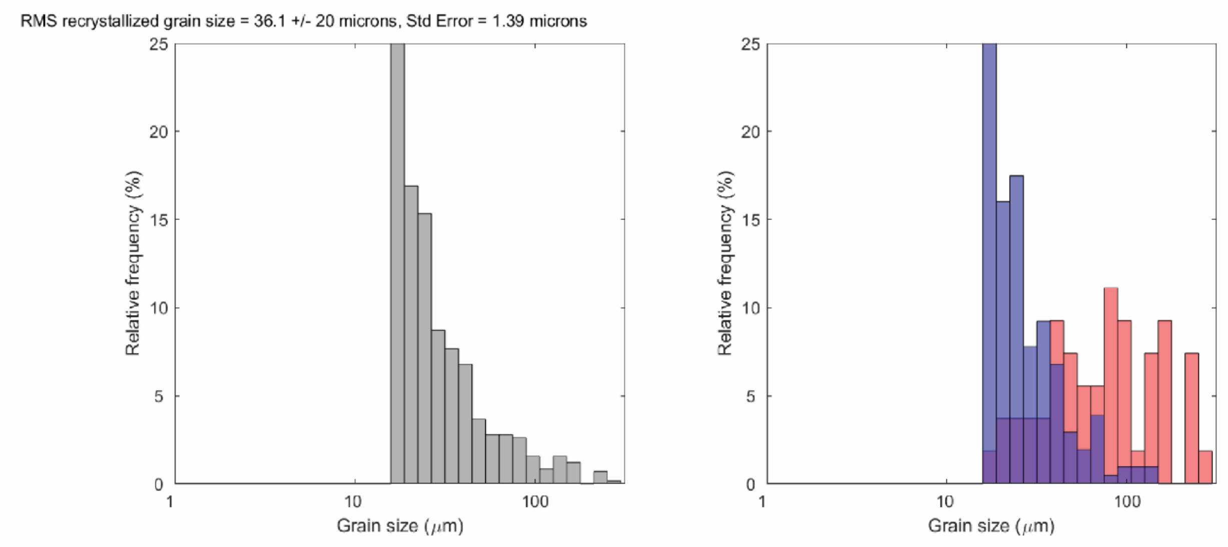

Fig. S3. Grain-size distribution for CB13-55a (Gatay). Grains are defined by 8 pixel cutoff, 10° critical misorientation. Left: grain-size distribution of recrystallized grains. Right: grain-size distributions of recrystallized grains (blue) and relict grains (red), showing overlap in grain-size between the two populations.

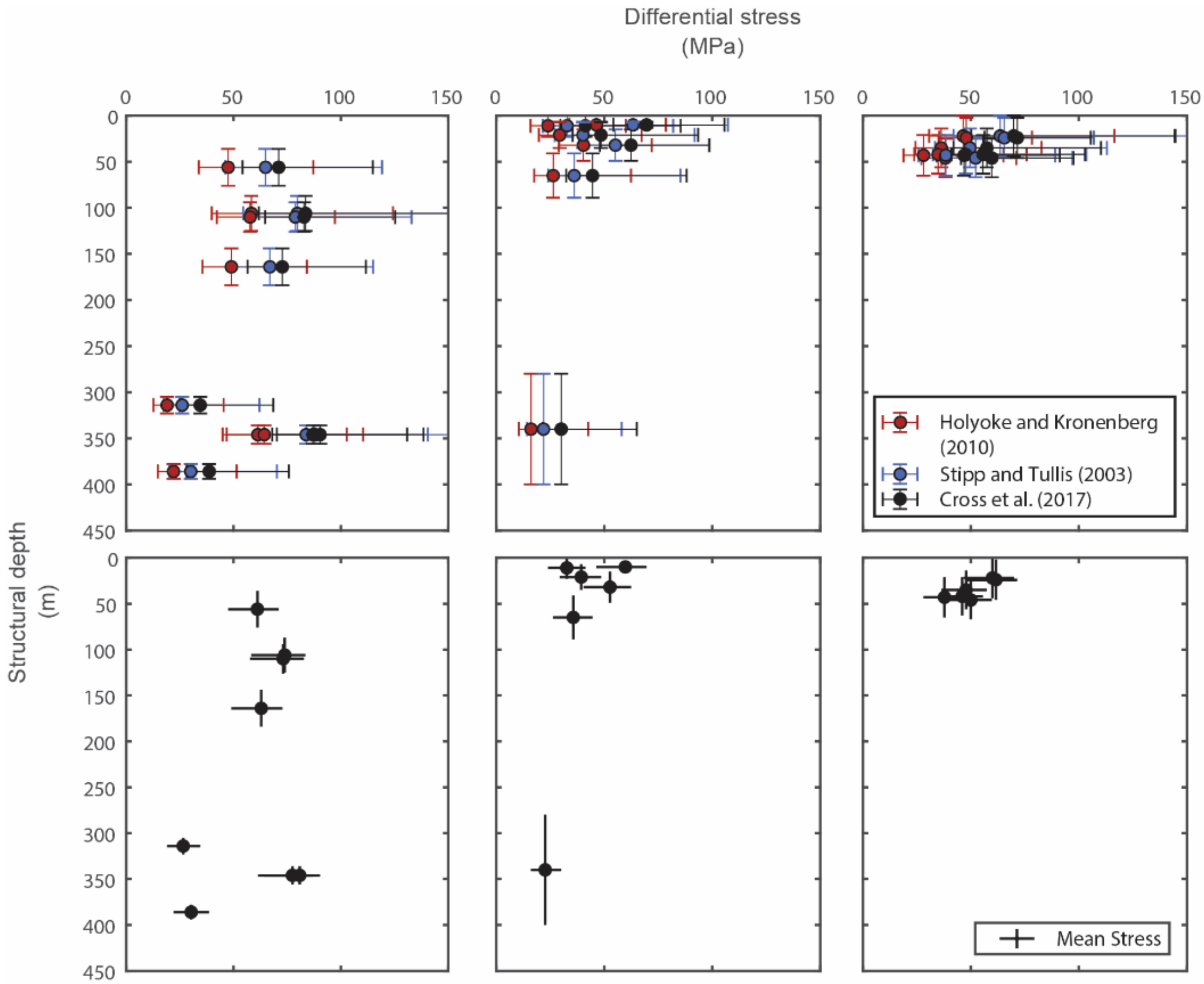

Fig. S4. Paleopiezometry results with respect to structural depth for quebradas Rajururi (left), Gatay (middle), and Ishinca (right). Upper plots show differences between three calibrations of the recrystallized quartz paleopiezometer. Lower plots show mean stress (average of three calibrations), with error bars denoting the range ofs tress estimates from different calibrations.

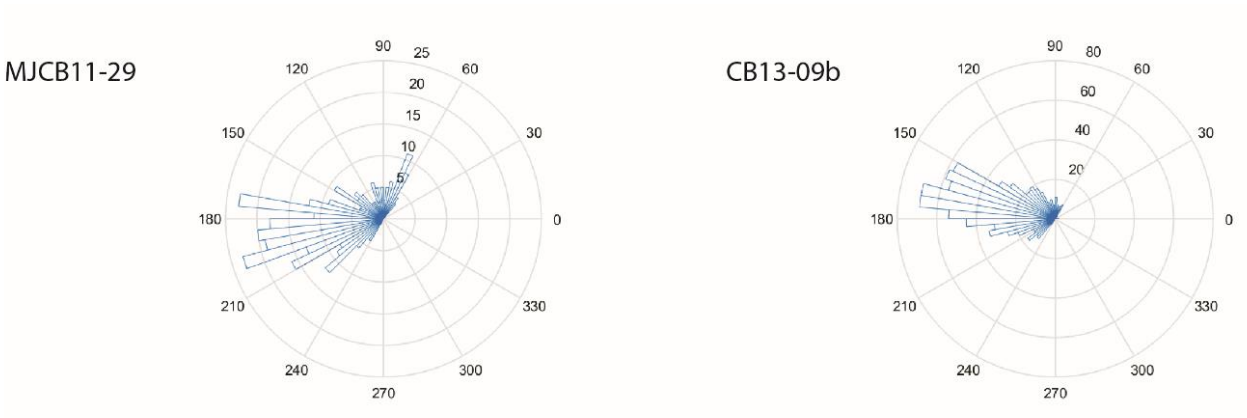

Fig. S5. Rose diagrams of shape preferred orientations for samples producing c- and a-axes pole figures indicative of prism [c] slip. Diagrams plotted using principle components via MTEX. Angles denote angle between x-axis and eigen-vector of grain long-axis with respect to aspect ratio of grain.

CHAPTER III

MASS TRANSFER IN HYDROTHERMAL FLUID SYSTEMS DURING EXTENSIONAL DEFORMATION IN THE CORDILLERA BLANCA SHEAR ZONE, PERU

Mass transfer in hydrothermal fluid systems during extensional deformation in the Cordillera Blanca Shear Zone, Peru

A version of this chapter by Cameron A. Hughes, Micah J. Jessup, Colin A. Shaw, Dennis A. Newell is currently in preparation for submission

Cameron A. Hughes, Micah J. Jessup, Colin A. Shaw, Dennis A. Newell: "Mass transfer during extensional deformation in hydrothermal systems: Insights from the Cordillera Blanca Shear Zone (CBSZ), Peru." *Journal of South American Earth Sciences, in preparation.*

My major contributions to this manuscript include: 1) field work to collect samples, 2) writing and receiving a Geological Society of America Graduate Student Research Grant for X-ray fluorescence (XRF) analysis 3) conducting petrographic analysis, 4) preparing samples for XRF analysis and interpreting XRF analysis, 5) writing the manuscript, and 6) drafting most figures for this manuscript. As corresponding author, I will be submitting this manuscript and will be responsible for manuscript revisions.

Abstract

The Cordillera Blanca shear zone (CBSZ), central Peru, preserves a gradient from ductile to brittle deformation across strike and variation in brittle and ductile behavior along strike of a ~200-km-long detachment fault. The hosts numerous hot springs, making it an excellent area to investigate the role of fluids in strain localization along the brittle-ductile transition (BDT). Fluids may promote deformation along the BDT through various mechanisms, including metasomatism, chemical weakening of the rock during ductile deformation, and increasing fluid pressure.

We evaluate element mobility and chemical mass transfer as potential indicators of fluid-assisted strain localization along the southern and central CBSZ. Mass-balance in whole-rock geochemistry demonstrates a correlation between degree of mylonitization and elemental gains or losses. In mylonites (50-90% dynamically recrystallized volume fraction) with <75 weight percent SiO_2, within range of the undeformed precursor, minimal volume gains of ≤ 13% accompany deformation. Mylonites with > 75 weight percent SiO_2 and ultramylonites (> 90% dynamically recrystallized volume fraction), which only have >75 weight percent SiO_2, show evidence of increasing degrees of mass transfer with progressive deformation with gains in siderophile elements, large-ion lithophile elements (LILE), Zr, and Zn and losses in Co and V. Mass gains of Ti and Zr in high-silica ultramylonites demonstrate that commonly assumed immobile elements TiO_2 and Zr mobilize with silicification and extensional quartz veining. Our results broadly demonstrate that element mobility is minimal in the production of mylonites with < ~70% recrystallized volume fraction, suggesting that relatively low-moderate finite strain ductile deformation is unlikely a result of fluid-induced chemical weakening or metasomatism within an open system. Conversely, increased element mobility (especially LILE) during

mylonitization at higher recrystallized volume fractions, brecciation, and cataclasis, alternatively suggests that high-finite-strain ductile deformation and the transition to brittle deformation were accompanied by fluid-rock interaction within an open system. Overall, our data suggest variability along strike of the CBSZ in the nature of mass transfer with increasing mylonitization between prominent silicification, relatively isochemical deformation, and K-metasomatism.

Introduction

Crustal deformation and fluid flow can strongly influence one another;, fluids moving through rocks can alter the nature of deformation and crustal deformation can affect the channelization of fluids (Sibson, 1994; Wintsch et al., 1995; Ring et al., 1999; Faulkner et al., 2010; Micklethwaite et al., 2010; Gottardi et al., 2015; Menegon et al., 2015). Fluid flow promotes transfer of chemical constituents through rocks during deformation that can result in metasomatism (Kerrich et al., 1980; Walther, 1994), ore mineralization (Sibson, 1987; Henian et al., 1997; Niroomand et al., 2018), chemical and/or textural weakening (Pryer and Robin, 1995; Wintsch et al., 1995; Wintsch and Yeh, 2013; Maggi et al., 2014), hydrolytic weakening (Mainprice and Paterson, 1984; Mancktelow and Pennacchioni, 2004; Kohlstedt, 2006; Stipp et al., 2006; Holyoke and Kronenberg, 2013), or rock strengthening through mineral precipitation (Micklethwaite et al., 2010; Maggi et al., 2014). Fluid movement through shear zones thus can significantly influence the amount of stress that can be accommodated before failure and the type of failure (Ring et al., 1999; Faulkner et al., 2010). Along the mid-crustal brittle-ductile-transition (BDT), fluids can act as weakening and/or strengthening agents, which can dictate whether rocks within mid-crustal shear zones deform ductilely or brittlely (Micklethwaite et al., 2010; Wintsch and Yeh, 2013; Maggi et al., 2014; Quilichini et al., 2016; Wehrens et al., 2016b), as well as how and where strain localizes (Newman and Mitra, 1993; Ring et al., 1999; Cox, 2002; Quilichini et al., 2016). Constraining the nature of possible shear zone fluids in terms of element mobility and chemical mass transfer can lend insight into what types of processes contribute to crustal rock strength and the transition between brittle and plastic deformation (Tobisch et al., 1991).

Extensional detachment fault zones are recognized as common pathways for fluids to move through the crust (Glazner and Bartley, 1991b; Rutter et al., 2001a; Collettini, 2011; Quilichini et al., 2015). Chemical and volumetric changes associated with deformation can be evaluated using whole-rock and mineral geochemistry of deformed and undeformed rocks (Kerrich et al., 1980; Rossi et al., 2005b; Rolland et al., 2008; Rolland and Rossi, 2016). Many such studies have inferred fluid-induced alteration, such as albitization, sericitization, silicification, or chloritization, in shear zones, while others have reported essentially isochemical deformation either without metasomatism or without notable fluid involvement (Kerrich et al., 1980; Tobisch et al., 1991). Thus, fluid flow during deformation cannot be assumed and individual shear zone case studies are required. Although many studies have investigated fluid-rock interactions during deformation with varying outcomes (Tobisch et al., 1991; McCaig, 1997), few of these have focused on shear zones within and directly related to active tectonic settings that can be directly related to a well-defined tectonic environment.

The Cordillera Blanca Shear Zone (CBSZ) in the central Peruvian Andes, is an ideal setting to investigate processes and spatial/lithological distribution of fluid-induced alteration as it relates to changes in rock strength in an active, syn-convergent extensional setting. Mineralogic and textural changes with increasing deformation intensity (Petford and Atherton, 1992) suggest fluids contribute at least locally to grain-size reduction and fabric development during shear zone deformation in the granodioritic footwall of the CBSZ (Hughes et al, 2019).

The CBSZ is still tectonically active (Schwartz, 1988b; Deverchere et al., 1989), has a relatively short and recent deformation history (Sebrier et al., 1985; Sébrier et al., 1988; Petford and Atherton, 1992), deforms a predominantly leucogranodioritic batholith of well-studied composition (Egeler and De Booy, 1956; Atherton and Sanderson, 1987; Atherton and Petford, 1993, 1996), and issues hot springs of known chemical composition along brittle fault surfaces (Newell et al., 2015). These facts allow us to establish the context of fluid-rock interactions during deformation in much greater detail than in ancient fault systems. Tectonic fabric gradients from undeformed leucogranodiorite through mylonite, ultramylonite, and cataclasite are exposed in glacially and fluvially incised valleys, providing a basis to evaluate changing geochemistry along a deformation gradient.

We use whole-rock major and trace-element geochemistry to evaluate the nature of fluids and the distribution of fluid-related alteration along a shear zone within an active, syn-convergent extensional setting. Metasomatism and thermal alteration within Cordillera Blanca batholith rocks near the contact with the intruded host rock and within the contact aureole have previously been described (Egeler and De Booy, 1956). Some commercial isotopic and whole-rock geochemical studies have been conducted on drill cores related to the Neuva California gold mine, located in a brecciated fault zone along the main detachment trace, (Park and Kalinaj, 2009; Focus Ventures Ltd., 2010). However, metasomatism related to deformation within the footwall CBSZ has not yet been studied. New data from deformed and undeformed rocks are compared to previously reported undeformed batholith rock geochemistry. These data are used to evaluate the spatial distribution of chemical and volumetric changes associated with various stages of finite strain along the ductile-brittle transition in the south-central CBSZ.

Geologic Background

The low-moderate angle, WSW-dipping Cordillera Blanca detachment fault extends for ~200 km along strike before breaking into smaller en-echelon segments at its southern end and forms the western boundary of the Cordillera Blanca batholith (Schwartz, 1988, Fig. 3.1). This detachment forms the upper boundary of the footwall Cordillera Blanca shear zone (CBSZ) (Petford and Atherton, 1992). Within the CBSZ, a gradient of generally increasing finite strain occurs from the core of the batholith westward through mylonites and ultramylonites, culminating in cataclasis and brecciation along the detachment surface (Petford and Atherton, 1992, Hughes et al., 2019). Leucogranodiorite with a trondhjemitic character makes up most of the CBB (Petford and Atherton, 1996). Less prominent petrologic facies include tonalite-quartz diorite located along the southwestern margin of the batholith (Fig. 3.2) and pegmatite-aplite

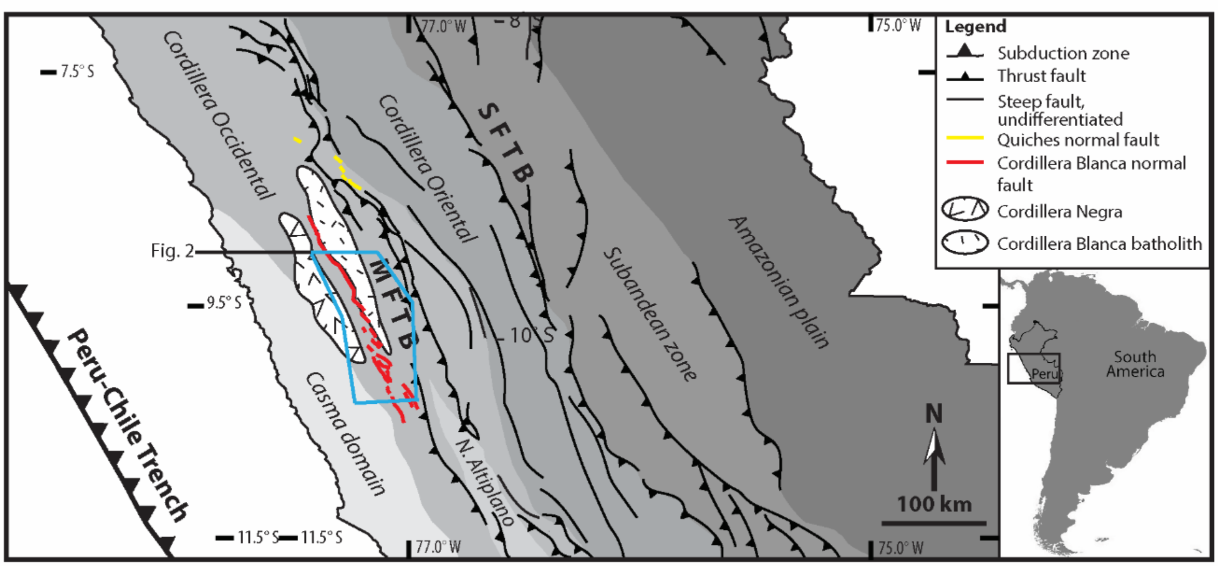

Fig. 3.1. Tectonophysiographic map of central Peru, originally after Pfiffner and Gonzalez (2013) (Hughes et al., in press), showing the relative position of the Cordillera Blanca (blue polygon). Inset shows location with respect to South American Continent. MFTB: Marañon fold and thrust belt SFTB: Subandean fold and thrust belt.

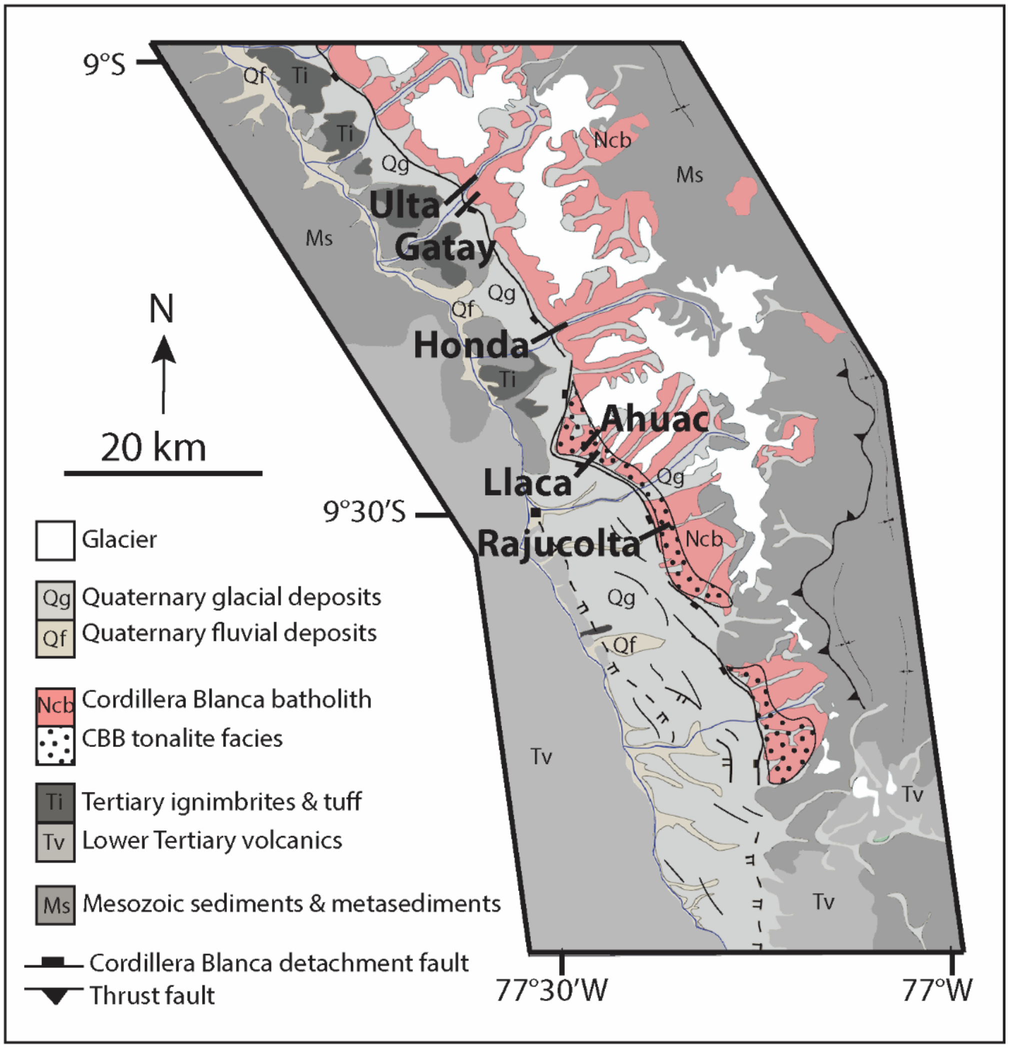

Fig. 3.2. Simplified geologic map of the Cordillera Blanca batholith and surrounding area. Quebradas (ravines) are labeled along the west side of the detachment fault. Map modified from Giovanni et al. (2010). Tonalite facies along western margin from (Petford and Atherton, 1996).

dikes that cut across the leucogranodiorite facies (Egeler and De Booy, 1956; Petford and Atherton, 1996) diorite located along the southwestern margin of the batholith (Fig. 3.2) and pegmatite-aplite dikes that cut across the leucogranodiorite facies (Egeler and De Booy, 1956; Petford and Atherton, 1996). The batholith was emplaced at 100-350 MPa pressure (Petford and Atherton, 1992; Wise and Noble, 2003; Margirier et al., 2016) between 14 and 5 Ma (U-Pb zircon; Giovanni, 2007; Margirier et al., 2016; McNulty et al., 1998; Mukasa, 1984).Youngest U-Pb zircon and $^{40}Ar/^{39}Ar$ biotite ages, 5.3 ± 0.3 Ma and 5.18 ± 0.05, respectively, are from leucogranodiorite in the central part of the batholith (Petford and Atherton, 1992; Giovanni, 2007). Early magmas (~14 Ma, 10-9 Ma) along the western and southern batholith margins are interpreted to derive from a basic source, whereas younger leucogranodiorites (6-5 Ma) were interpreted to derive from a Na-rich granitic source (Petford and Atherton, 1996).

Evidence exists for a relatively early role of fluids in the fractionation and crystallization of the Cordillera Blanca batholith (Petford and Atherton, 1996; Coldwell et al., 2011), as well as for the modern Cordillera Blanca, as seen by the issuing of thermal springs along the northern part of the detachment and faults within the hanging wall of the detachment (Newell et al., 2015). Isotopic signatures from pegmatite have ~1 ‰ higher $\delta^{18}O$ values relative to batholith rocks, suggesting fractionation in a hydrous setting (Petford and Atherton, 1996). 6 ‰ variation in $\delta^{18}O$ between the host Chicama shale and the Cordillera Blanca batholith suggest minimal interaction between the magma and country rock at the level of emplacement (Petford and Atherton, 1996). Alkaline-chloride to alkaline-carbonate hot springs with mantle-derived helium and relatively high trace metal concentrations issue along the detachment and along faults in the hanging wall within 5-10 km (Newell et al., 2015). Stable isotope, element, and cation geochemistry of these springs suggest that hot (200-260 °C) saline fluid mixes with cold meteoric waters along the detachment system. Gold, silver, copper, lead, zinc, and molybdenum deposits of the Nueva California mine, located within the brittle fault zone along the detachment at the base of Mt. Huascaran, are hosted within heavily altered hydrothermal breccias dated at ~ 4 Ma (Wise and Noble, 2003; Park and Kalinaj, 2009).

Sample Characterization

Petrographic and microstructural analysis was conducted to classify a suite of 37 rock samples from 6 transects across the CBSZ into groups by fault rock type. Groups were classified by deformation intensity, as follows: undeformed-weakly-deformed granodiorites (UWGs, i.e. precursor samples), mylonites, ultramylonites, and cataclasites using the fault rock classification scheme of Sibson (1977) modified by Scholz (2002) (Table 3.1). A notable change in deformation fabric occurs at ~9.5° S, south of Q. Llaca. Extensive mylonitization is observed at and to the north of Q. Llaca but is absent or discontinuous and localized to zones less than ~5 meters wide in the south. Sample locations and structural measurements are reported in Table S6. Chloritized and non-chloritized cataclasites were selected as well as quartz veins that are interpreted to be syn-kinematic based on their tabular nature and orientation parallel to macroscopic foliation in the field. Only one sample each from Qs. Ulta and Ahuac are included in this study as additional constraints on the undeformed precursor composition. Based on modal mineralogy, whole-rock geochemistry, and relative location, transects were placed into either northern: (Qs. Ulta, Gatay, Honda), or southern: (Qs. Ahuac, Llaca, Rajucolta) groups.

Rock samples were classified based on the volume percent of grain-size reduced (GSR) recrystallized matrix (Sibson, 1977; Scholz, 2002; Fig.3). Volume percent of GSR matrix, non-GSR recrystallized matrix, porphyroclasts, and igneous phenocrysts were determined by point counting on paired cross-polarized and plane-polarized light photomicrographs (Table 3.1,

TABLE 3.1. SAMPLE CLASSIFICATION

Sample	Fabric	Transect	Porphy-roclast (%)	GSR Matrix (%)	Non-GSR Matrix (%)	Igneous Phen. (%)	Classification[a]	Defor-mation[b]	N[c]
CB15-03	Ductile	Ahuac	1	26	0	73	protomylonite	u	720
CB13-54a	Ductile	Gatay	32	22	9	36	protomylonite	u	720
CB13-55a	Ductile	Gatay	49	42	9	0	protomylonite	d	720
CB13-55c	Ductile	Gatay	16	81	0	3	mylonite	d	720
CB13-56	Ductile	Gatay	8	93	0	0	ultramylonite	d	720
CB13-57a	Ductile	Gatay	31	67	1	1	mylonite	d	720
CB13-57b	Ductile	Gatay	1	99	0	0	ultramylonite	d	720
CB13-58	Ductile	Gatay	30	70	0	0	mylonite	d	720
CB13-71a	Brittle	Gatay	42	57	0	0	cataclasite	d	720
CB13-73a	Brittle	Gatay	16	84	0	0	cataclasite	d	720
CB13-74a	Brittle	Gatay	21	79	0	0	cataclasite	d	720
CB13-76	Ductile	Gatay	24	75	0	0	mylonite	d	720
CB13-77a	Ductile	Gatay	7	93	0	0	ultramylonite	d	720
CB13-77c	Ductile	Gatay	6	94	0	0	ultramylonite	d	720
CB13-84	Ductile	Gatay	35	65	0	0	mylonite	d	720
MJCB11-07	Brittle	Honda	41	59	0	0	cataclasite	d	720
MJCB11-08	Brittle	Honda	44	56	0	0	cataclasite	d	720
MJCB11-09	Ductile	Honda	38	52	2	8	mylonite	d	720
MJCB11-10	Ductile	Honda	35	59	1	6	mylonite	d	720
MJCB11-11	Ductile	Honda	26	74	0	0	mylonite	d	720
MJCB11-12	Ductile	Honda	25	75	0	0	mylonite	d	720
MJCB11-13	Ductile	Honda	37	54	2	7	mylonite	d	720
MJCB11-14	Ductile	Honda	38	48	8	5	protomylonite	d	720
MJCB11-15	Ductile	Honda	38	47	1	14	protomylonite	u	720
MJCB11-16	Ductile	Honda	43	38	5	15	protomylonite	u	720
CB15-04	Ductile	Llaca	8	92	0	0	ultramylonite	d	720
CB15-05a	Ductile	Llaca	35	64	0	0	mylonite	d	720
CB15-05b	Ductile	Llaca	35	64	1	1	mylonite	d	720
CB15-07	Ductile	Llaca	10	90	0	0	ultramylonite	d	360
CB15-09	Ductile	Llaca	16	4	25	55	undeformed-weakly deformed	u	720
CB15-16	Brittle	Llaca	69	31	0	0	protocataclasite	d	720
MJCB11-03	Ductile	Llaca	10	90	0	0	ultramylonite	d	720
MJCB11-04	Ductile	Llaca	33	66	0	1	mylonite	d	720
MJCB11-05	Ductile	Llaca	33	66	0	1	mylonite	d	720
CB13-24	Ductile	Rajucolta	0	6	0	94	undeformed-weakly deformed	u	720
CB13-28a	Brittle	Rajucolta	28	71	1	0	cataclasite	d	720
CB15-21b	Ductile	Ulta	32	22	9	36	protomylonite	u	720

Notes: GSR—grain-size reduced. Phen.— phenocryst

[a]Derived from GSR-matrix, based on classification scheme of Sibson (1977) and modification by Scholz (2002).

[b] d: deformed, u: undeformed

[c]Number of nodes analyzed for point counting

Supplemental Text S1, Fig. S6.). Undeformed granodiorites are distinguished as those containing less than 10% GSR matrix and over 10% igneous phenocrysts (n=2). Protomylonites (10-50% GSR matrix) that contain over 10% igneous phenocrysts are classified, along with the undeformed granodiorites, as the precursor undeformed-weakly deformed granodiorite (UWG) samples. Remaining ductilely deformed samples are classified as protomylonites (n=2), mylonites (n=14), and ultramylonites (n=7) for GSR matrix volume percentages of 10-50%, 50-90%, and >90%, respectively. These protomylonites have < 10% igneous phenocrysts and > 40% GSR matrix and are grouped with mylonites (total n=16). Brittlely deformed samples are classified as protocataclasites (n=1) and cataclasites (n=5) based on the volume percentages of fine-grained matrix of 10-50% and 50-90%, respectively (Sibson, 1977; Scholz, 2002) (Fig. 3.3). Additional sample descriptions are provided in Supplemental Text S2 and Fig. S7.

Methods

Whole-rock geochemistry was conducted using the Bruker Analytical SRS3000 Sequential X-ray Fluorescence Spectrometer (XRF) at the University of Wisconsin –Eau Claire. Fused glass beads and powdered pellets were analyzed for major and trace-elements, respectively (Taggert, 2002). See Supplemental Text S3 for details. Loss on ignition was determined by heating at 250 °C for 2 hours. Negative values for loss on ignition (i.e. gains on ignition) are attributed to oxidation of FeO in samples with exceedingly low amounts of volatiles (Lechler and Desilets, 1987).

Normative mineral abundances were calculated using the biotite and hornblende CIPW norm (Hutchison, 1974; Hutchison and Lumpur, 1975) in the *GCDkit* package for R (Janoušek et al., 2006). Point counting for one weakly deformed granite hand sample (CB15-21b, Q. Ulta)

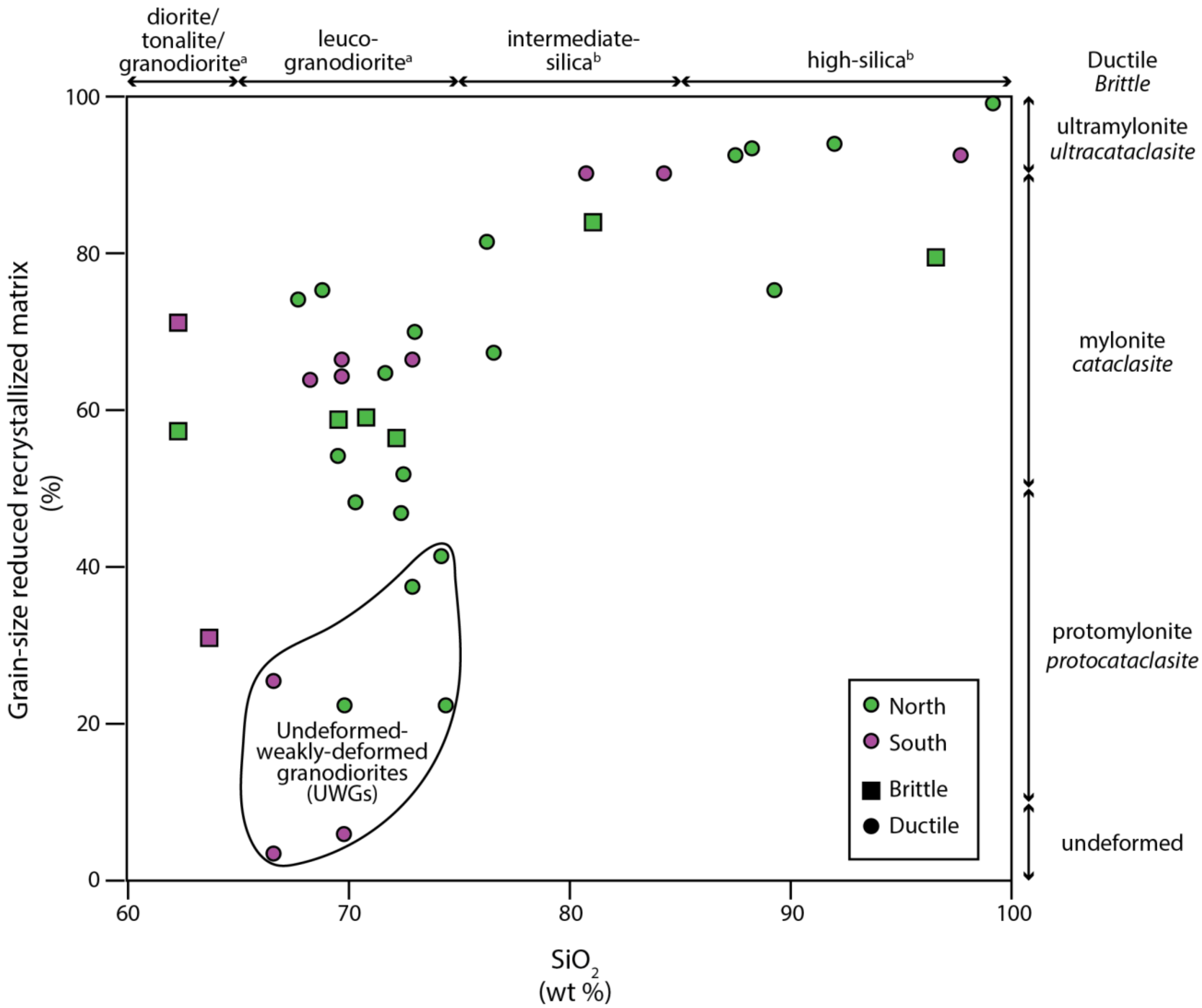

Fig. 3.3. Fault rock classification of Cordillera Blanca Shear Zone samples with respect to weight percent SiO_2 and volume percent grain-size reduced recrystallized matrix. [a]Diorite, tonalite, granodiorite, and leucogranodiorite fields from (Petford and Atherton, 1996). [b]Intermediate- and high-silica defined in this study as 75 to <85 weight percent SiO_2 and $\geq$ 85 weight percent SiO_2, respectively. Precursor samples meeting the criteria for UWGs shown in circled field. North: Qs. Gatay, Honda, and Ulta. South: Qs. Ahuac, Llaca, and Rajucolta.

was conducted to assess the validity of using CIPW norm abundances to estimate modal mineralogy. Point-counting for samples CB15-21b (n=399) and CB15-24 (n=158) was conducted using a 4 mm grid, where the spacing was slightly greater than the largest grain sizes (Van der Plas and Tobi, 1965; Neilson and Brockman, 1977). Modal abundance error was determined following the methods of (Van der Plas and Tobi, 1965) and is 5 wt % or less for all phases identified in CB15-21b (n=399) and < 8 wt % or less for those in CB13-24 (n=158) (Table 3.2).

Sample densities were calculated following the procedure in the CIPW norm Visual Basic Macro of Kurt Hollacher (https://minerva.union.edu/hollochk/c_petrology/other_files/norm_calculation.pdf), adjusted to include the biotite and hornblende modification of the CIPW norm (Hutchison and Lumpur, 1975). Sample densities were derived from normative mineral abundance using mineral densities (i.e. specific gravity) and calculated volume percent abundance. See Supplemental Text S4 for further discussion of deriving estimated volume proportions and densities.

Calculations of mass-balance and estimated volume loss were performed using the GCDkit package for R (Janousek et al., 2003; Janoušek et al., 2006, 2015). These methods solve Gresens equation (1967) to calculate volume and concentration changes during alteration:

$$X_i = \left[f_v \left(\frac{\rho^A}{\rho^O}\right) C_i^A - C_i^O\right] \times M^O \qquad (1)$$

where X_i is the amount of component *i* lost or gained, f_v is the volume factor, ρ is specific gravity, *O* and *A* denote the original and altered rock, respectively, *C* is the concentration (weight fraction) of element *i*, and M^O is the initial mass of the unaltered rock. The isocon method (Grant, 1986) reconfigures Gresens' equation (1967) as:

$$C_i^A = \frac{M^O}{M^A}\left(C_i^O - \Delta C_i\right) \qquad (2)$$

TABLE 3.2. HORNBLENDE—BIOTITE CIPW NORMATIVE ABUNDANCES

	Whole-rock Geochemistry (Volume percent)						Point Counting (Volume percent)					
	Petford and Atherton (1993)	This Study										
		Average UWG			CB15-21b	CB13-24	CB15-21b			CB13-24		
Mineral	*n=17*	*n=7*					*n=399*			*n=158*		
Quartz	29.1	33.2	±	3.4	29.2	32.1	25.6	±	4.3	32.2	±	7.3
Corundum	0.8	1.69	±	0.75	1.09	1.38		-			-	
Orthoclase	18.8	18.7	±	6.33	20.3	16.5	23.3	±	4.2	20.8	±	6.4
Albite	36.5	30.6	±	2.6	33.8	31.7	44.1	±	5.0	37.7	±	7.8
Anorthite	9.2	7.23	±	3.68	8.32	10.10		-			-	
Magnetite	0.84	0.11	±	0	0.00	0.00		-			-	
Ilmenite	0.51	2.73	±	0.07	0.04	0.06		-			-	
Hematite	0	0	±	2.82	1.28	2.02		-			-	
Apatite	0.19	0.17	±	0.09	0.17	0.17		-			-	
Biotite	2.97	1.95	±	1.2	1.45	1.98	7.0	±	2.4	9.3	±	4.9
Total	98.9	96.4	±	0.87	95.6	96	100			100		

where M^A is the mass of the altered sample and ΔC_i is the change in concentration relative to the initial reference concentration of i, such that a line of constant concentration (isocon) is derived at which $\Delta C_i = 0$ (Grant, 1986). TiO_2 and Al_2O_3 were initially assumed to be immobile (Bialek, 1999; Rolland et al., 2003b; Rossi et al., 2005a) in the construction of isocon wedge diagrams (Ague, 1994). Isocon wedge diagrams presented here are shown relative to Al_2O_3, as upon evaluation discussed below, TiO_2 was interpreted to be mobile. Volume changes were estimated in an immobile Al_2O_3 frame using densities calculated from normative mineral abundance and specific gravity. Isocon wedge plots (Bucholz and Ague, 2010), isocon volume diagrams (Grant, 1986) and variation, spider, classification, were constructed using the GCDkit package for R (Janousek et al., 2003; Janoušek et al., 2006, 2015).

Results

Whole-rock Geochemistry

Whole-rock major, minor, and trace-element geochemistry was obtained for 37 samples with representative lithologies of the study area. Average geochemistry of UWGs, granitic mylonite, ultramylonite, and cataclasite, as well as average geochemistry of quartz vein ultramylonites and catalcasites are reported in Table 3.3. Initial review of analyses led to further sub-grouping of mylonites into those with similar SiO_2 concentrations to those of UWGs (<75 wt %) and those with between 75 and 85 wt % SiO_2. Ultramylonites were subdivided into groups into those with 75 to < 85 wt % SiO_2 and those with 85 wt % SiO_2 or higher.

Consistency of Undeformed Granodiorite Composition

Undeformed-weakly deformed rocks from this study have similar lithology to undeformed batholith rocks reported by Petford and Atherton (1996) and Egeler and De Booy

TABLE 3.3. AVERAGE WHOLE-ROCK GEOCHEMISTRY OF REPRESENTATIVE LITHOLOGIES IN THE CORDILLERA BLANCA, PERU

Lithology	**Granite**	**s.d.**	**Granite**	**s.d.**	**Granite**	**s.d.**	**Granite**	**s.d.**	**Granite**	**s.d.**
Fabric	**UWG-North**	***4***	**UWG-South**	***3***	**UWG-All**	***7***	**PM and M-North**	***12***	**PM and M-South**	***4***
SiO2	72.4	1.91	67.7	1.86	70.4	3.04	73.4	5.72	70.1	1.96
TiO2	0.16	0.07	0.4	0.06	0.26	0.14	0.22	0.12	0.26	0.11
Al2O3	13.8	0.72	14.2	1.11	14	0.84	12.2	3.19	13.5	0.26
Fe2O3	1.29	0.2	4.64	3.77	2.73	2.82	3.82	1.67	3.89	1.78
MnO	0.03	0.01	0.07	0.05	0.05	0.03	0.06	0.03	0.07	0.04
MgO	0.33	0.08	0.92	0.29	0.59	0.36	0.39	0.1	0.54	0.2
CaO	1.07	0.52	2.19	0.57	1.55	0.78	0.88	0.24	1.36	0.39
Na2O	3.68	0.31	3.55	0.35	3.62	0.31	3.08	0.95	3.06	0.33
K2O	4.05	0.43	2.53	0.6	3.4	0.94	3.48	1.03	4.45	0.47
P2O5	0.05	0.03	0.1	0.03	0.07	0.04	0.04	0.02	0.06	0.03
LOI	0.49	0.33	0.43	0.45	0.47	0.35	0.13	0.42	0.3	0.2
Total	97.3	0.8	96.7	0.4	97.1	0.7	97.6	0.9	97.3	0.3
Ba	500	282	730	180	599	256	425	310	409	127
Ce	16	14	41	14	27	18	26	11	26	12
Cr	0	0	5	7.81	2.14	5.24	7.25	9.9	2.75	2.22
Co	106	51	121	47	113	46	89	55	54	8
Cu	5	3	15.67	11	9.57	9	11	6	33	10
Hf	6.25	2	6	2	6.14	2	6.08	2	5	1
La	9.25	4.5	21.7	9.29	14.6	9.11	12.5	5.09	13.5	8.54
Pb	23.9	7.19	22.7	3.21	23.4	5.45	21.5	8.62	23	3.83
Nd	12.5	4.5	18	8.2	14.9	6.4	15.4	5.2	13	2.7
Ni	3	0	4.67	3	3.71	2	5.67	2	4.5	1
Nb	9.88	3.17	12.3	5.13	11.0	3.94	15.4	4.34	12	3.92
Rb	166	41.6	130	10.5	150	35.6	179	48.5	248	44
Sc	1.5	0.58	4.67	2.08	2.86	2.12	2.67	1.3	3	1.15
Sr	299	185	378	177	333	171	205	133	274	70
Th	7.63	2.87	13.7	1.53	10.2	3.91	9	3.16	15.3	1.5
V	8.75	6.8	40	13.9	22.1	19.1	13.5	12.6	21	13.2
Y	16.9	2.95	13.7	4.62	15.5	3.8	16.3	6.89	9	1.41
Zr	129	85.5	153	49.4	139	68.1	147	81.6	110	27.7
Zn	33	20.1	73.3	9	50.3	26.3	45.4	17.2	120	51.1
Calculated density	2.66	0.01	2.73	0.07	2.69	0.06	2.7	0.03	2.7	0.04
% GSR recrystallized matrix	32	12	12	12	23	16	64	13	65	1
% Igneous phenocryst	25	13	74	20	46	30	3	3	1	0.4

Table 3.3, continued.

Lithology	Granite	s.d.	Granite	s.d.	Granite	s.d.	Granite	s.d.	Granite	s.d.
Fabric	PM and M-All	*16*	UM-All	*2*	CC-North	*4*	CC-South	*2*	CC-All	*6*
SiO2	72.6	5.18	84.5	5.35	71.3	7.72	63	0.95	68.5	7.38
TiO2	0.23	0.12	0.32	0.16	0.39	0.25	0.38	0.09	0.38	0.2
Al2O3	12.5	2.8	6.2	2.3	12.5	3.58	14.8	1.35	13.3	3.09
Fe2O3	3.84	1.63	3.6	1.39	5.6	1.26	8.63	0.79	6.61	1.88
MnO	0.06	0.03	0.03	0	0.06	0.02	0.09	0.04	0.07	0.03
MgO	0.42	0.14	0.41	0.07	0.87	0.66	0.83	0.23	0.85	0.52
CaO	1	0.35	0.89	0.52	1.65	1.76	1.73	0.35	1.68	1.37
Na2O	3.07	0.82	0.69	0.4	2.85	1.49	3.81	0.15	3.17	1.26
K2O	3.72	1.01	2.71	2.74	2.46	1.08	3.89	1.97	2.94	1.42
P2O5	0.04	0.02	0.03	0.01	0.08	0.05	0.12	0.01	0.09	0.04
LOI	0.17	0.38	0.4	1.14	0.54	0.77	-0.27	0.58	0.27	0.77
Total	97.6	0.8	99.8	0.5	98.3	0.9	97	0.1	97.8	1
Ba	421	271	202	55	332	146	642	299	435	237
Ce	26	11	20	12	24	12	31	4	26	11
Cr	6.13	8.77	11.5	14.85	12	6.68	10.5	4.95	11.5	5.68
Co	80	50	169	169	92	54	65	14	83	44
Cu	16.5	12	73.5	86	21	9	129	151	57	88
Hf	5.81	1	7	6	6.25	3	4.5	2	5.67	2
La	12.8	5.81	10	5.66	13	2.16	24	8.49	16.7	7.03
Pb	21.9	7.61	9	4.24	18	10.4	16.5	10.6	17.5	9.4
Nd	14.8	4.8	10.5	2.1	14.3	3.1	23	8.5	17.2	6.4
Ni	5.38	2	6	4	7.5	3	7	1	7.33	2
Nb	14.6	4.38	13	4.24	15	3.16	17.5	0.71	15.8	2.79
Rb	196	55.2	146	156	134	22.9	222	90.5	163	63.5
Sc	2.75	1.24	3	1.41	5.5	4.73	3.5	0.71	4.83	3.82
Sr	222	122	70	40	233	131	344	47	270	119
Th	10.6	3.95	26.5	34.7	7.5	1.29	15	1.41	10	4.05
V	15.4	12.7	29.5	10.6	45	39.6	41	22.6	43.7	32.4
Y	14.5	6.78	15	4.24	14	4.24	9.5	3.54	12.5	4.32
Zr	138	72.9	261	275	174	125	136	7.1	161	98.8
Zn	64	43	74.5	103	63	13.4	250	287	125	161
Calculated density	2.7	0.03	2.7	0.04	2.75	0.04	2.77	0.03	2.76	0.03
% GSR recrystallized matrix	64	11	92	2	64	13	51	28	60	18
% Igneous phenocryst	2	3	0	0	0	0	0	0		0

Table 3.3, continued

Lithology					Subgroups by SiO_2 (wt %)							
	QV	**s.d.**	**QV**	**s.d.**	**< 75 %**	**s.d.**	**< 85 %**	**s.d.**	**< 85 %**	**s.d.**	**≥ 85 %**	**s.d.**
Fabric	**UM-All**	***5***	**CC**	***1***	**M-All**	***14***	**M-All**	***2***	**UM-All**	***2***	**UM-All**	***5***
SiO2	92.1	6.4	96.6		70.4	1.87	76.4	0.2	82.5	2.5	92.9	5.33
TiO2	0.2	0.19	0.19		0.21	0.08	0.38	0.23	0.16	0.07	0.26	0.2
Al2O3	2.76	3.14	1.22		13.5	0.24	11.1	0.12	7.27	0.83	2.34	2.58
Fe2O3	3.3	2.14	2		3.98	1.62	3.11	0.9	2.06	0.79	3.91	1.92
MnO	0.02	0.01	0.01		0.06	0.03	0.06	0.01	0.02	0.01	0.02	0.01
MgO	0.29	0.12	0.2		0.43	0.14	0.44	0.13	0.39	0.11	0.3	0.13
CaO	0.3	0.37	0.15		1.11	0.32	0.86	0.05	1.11	0.22	0.22	0.18
Na2O	0.39	0.11	0.53		3.35	0.31	2.38	0.71	0.44	0.05	0.49	0.29
K2O	1.08	1.87	0.17		4.11	0.41	2.86	1.09	4.51	0.2	0.36	0.4
P2O5	0.01	0.02	0.01		0.05	0.02	0.03	0.03	0.03	0.01	0.01	0.02
LOI	-0.05	0.63	-0.11		0.17	0.33	0.47	0.63	0.89	0.45	-0.24	0.53
Total	100.5	0.9	100.9		97.3	0.5	98	0.2	99.3	0.2	100.6	0.6
Ba	57	50	21		519	237	114	29	184	81	64	63
Ce	10	14	1		28	10	25	0	6	8	16	15
Cr	8.8	12.2	2		2.91	2.17	19	18.38	0.5	0.71	13.2	12.2
Co	161	77	374		65	31	89	35	73	33	200	84
Cu	14.6	6	5		20.6	13	8.5	1	76	82	13.6	6
Hf	6	3	6		5.45	1	8.5	2	3.5	1	7.4	4
La	6	3.94	4		13.7	6.1	10	1.41	5	1.41	8	5.05
Pb	3.4	6.07	0		23.5	4.08	20.5	14.9	13	1.41	1.8	2.68
Nd	8.6	2.6	7		15.2	4.7	13.5	0.7	8	1.4	9.6	2.8
Ni	5.8	3	4		4.82	1	6.5	1	3.5	1	6.8	3
Nb	8.8	6.53	2		14.3	4.5	19.5	2.12	8	2.83	10.8	6.98
Rb	61	89.4	10		217	46.7	169	21.9	234	31.1	26	30.6
Sc	1.2	2.17	1		2.55	0.82	5	1.41	2.5	2.12	1.4	2.19
Sr	28	48	8		270	101	83	20	105	10	14	17
Th	0.8	1.1	0		11.8	3.4	11.5	2.12	26.5	34.7	0.8	1.1
V	11.6	16.0	7		13.4	9.55	31.5	26.2	23.5	19.1	14	16.7
Y	11.4	5.32	12		11.5	3.24	28.5	7.78	9.5	3.54	13.6	5.32
Zr	142	170	153		117	32.2	267	143	51	21.2	226	205
Zn	12.4	14	0		78.8	43.2	42.5	5	85	87.7	8.2	13.2
Calculated density	2.71	0.04	2.68		2.7	0.03	2.71	0.05	2.67	0	2.72	0.03
% GSR recrystallized matrix	94	3	79		65	7	74	10	90	0	94	3
% Igneous phenocryst	0	0	0		2	3	2	1	0	0	0	0

(1956) (Table 3.2). Previous work identified two different batholith facies: leucogranodiorites, defined by SiO_2 > 70% and comprising >85 % of the batholith, granodiorite, and tonalite-quartz monzodiorite (Petford & Atherton, 1996, Fig. 3.2). Chemically, the leucogranodiorites, which range in SiO_2 from 70-74 wt %, classify as granites (Petford and Atherton, 1996, Fig. 3.4). The average undeformed granite compositions used in this study as the protolith compositions for determining mass transfer (purple and green stars, Fig. 3.4) plot well within the range of modal mineralogy reported by Petford and Atherton (1996) and within ~5% difference of the average undeformed granodiorite batholith composition reported by Atherton and Petford (1993; Table 3.2).

For consistency with data from this study, modal abundances derived from the average composition reported by Atherton and Petford (1993) by calculating the hornblende-biotite CIPW-norms were plotted on the QAP and An-Or-Ab diagrams. Hornblende-biotite CIPW-norm mineralogy for previous and new data are in broad agreement, with 1σ standard deviation < 1 wt % for normative quartz, orthoclase, anorthite, corundum, ilmenite, and apatite, < 2 wt % for normative hypersthene and magnetite, and < 5 wt % normative albite (Table 3.2). Although the average composition across all transects agrees well with previous studies, it is important to note that the northern transects Q. Gatay and Honda have a more granitic character than the southern transects, Q. Llaca and Rajucolta, which have a more granodioritic character (Fig. 3.4b). Trace-element patterns for UWGs relative to primitive mantle are generally consistent with existing batholith chemistry (Fig. 3.5). UWGs from Qs. Gatay and Honda have compositions that tend slightly more towards previously defined leucogranodiorite facies, as indicated by higher K and Rb, lower P, and lower Ti contents (Fig. 3.5). Lower La and Ce contents are observed in Qs. Gatay and Honda relative to Qs. Llaca and Rajucolta and previously reported batholith

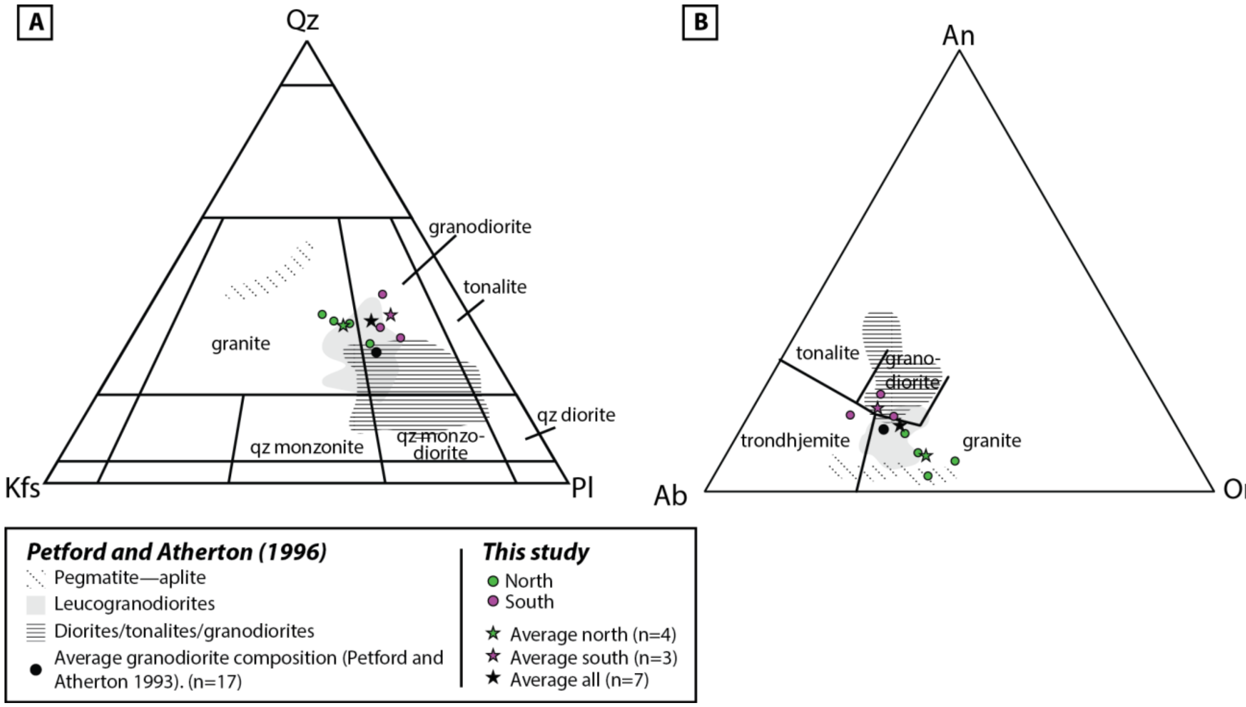

Fig. 3.4. Classification diagrams of CBSZ granitoid rocks. Position on diagrams for all points calculated from CIPW norm, modified for hornblende and biotite (Hutchison & Lumpur, 1975) abundances. A) QAP diagram (Le Maitre et al., 1989) showing the classification of the precursor composition (UWGs) relative to previously reported Cordillera Blanca batholith (undeformed) compositions, color coded by transect. ¬Average composition of all UWGs (black star) and those of the northern (green star) and southern (purple star) from this are consistent with the overlapping fields from Petford and Atherton (1996) and the average granodiorite composition reported by Atherton and Petford (1993). B) Ab-An-Or granitoid classification diagram (Barker, 1979) showing nature of UWGs relative to previously reported Cordillera Blanca batholith (undeformed compositions).

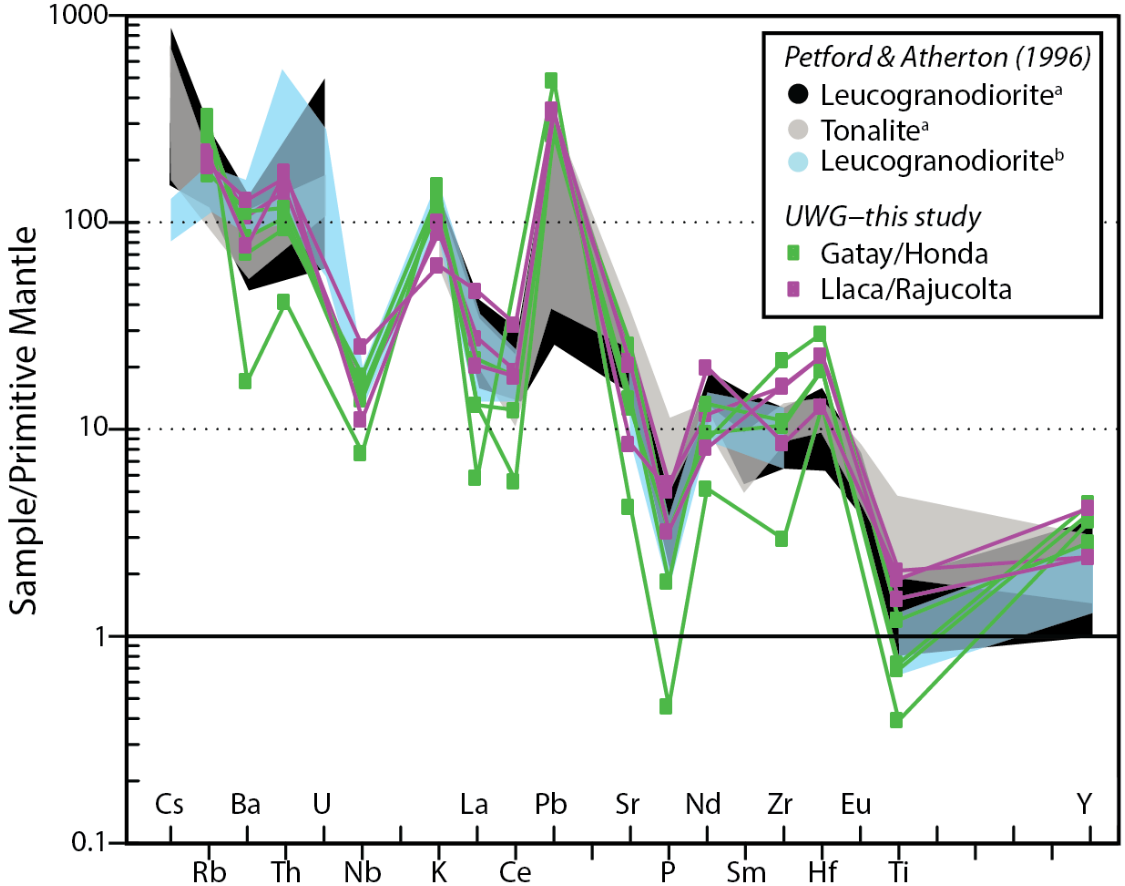

Fig. 3.5. Mantle-normalized trace-element diagram of northern (green) and southern (purple) UWGs. Samples are plotted against leucogranodiorites (black) and tonalites (gray) from a) Petford & Atherton (1996) and leucogranodiorites (blue) from b) Atherton & Sanderson (1987).

geochemistry. UWGs from this study have a wider range of Nb, Zr, and Sr concentrations and generally higher Hf concentrations than previously reported. UWGs tend slightly towards tonalite facies (Fig. 3.5). This distinction is consistent with the mapped distribution of petrologic facies and provides a basis for assigning transect-appropriate starting compositions to mass-balance calculations. For samples where SiO_2 < ~75 wt %, major-element oxides and trace-elements show similar concentrations to those reported by Petford & Atherton, (1996) for undeformed batholith rocks (Fig. 3.6). Deviations from these concentrations at increasing SiO_2 wt % concentrations are observed for most elements and will be discussed in greater detail below.

Alteration Indices

Major-element alteration indices offer insight into the representative destabilization of mineral phases during alteration by considering major-element variations in a system where the unaltered protolith is known (Mathieu 2018). These indices can elucidate processes such as muscovitization, albitization, sericitization, chloritization, and K-metasomatism. The muscovitization index: (Na+K)/Al(-), where Al(-) = Al-2*Ca, will be 1.0 for a pure feldspar rock and 0.33 for a pure muscovite rock (McCaig et al., 1990). Alteration of feldspar to muscovite can occur through a variety of metamorphic reactions, including:

3K-feldspar + $2H^+$ = muscovite + $6SiO_{2(aq)}$ $2K^+$ (3)

Plagioclase+ microcline + H_2O = zoisite + muscovite + quartz + albite (4)

(Phillips et al., 1972; Pryer and Robin, 1995; Wintsch and Yeh, 2013).

In the CB, K-feldspar and plagioclase break down in the production of mylonites from relatively undeformed granites (i.e. Hughes et al., 2019). Albite-forming reactions have also been observed, namely in the replacement of K-feldspar through myrmekite-forming reactions.

Fig. 3.6. Major-element oxide (weight percent) variation diagrams relative to weight percent SiO2¬. Colors denote transect localities, symbols denote fabric. Lines demarking boundary between tonalites/diorites and granodiorites as well as previously reported undeformed batholith chemistry shown in patterned and gray fields are from Petford & Atherton (1996).

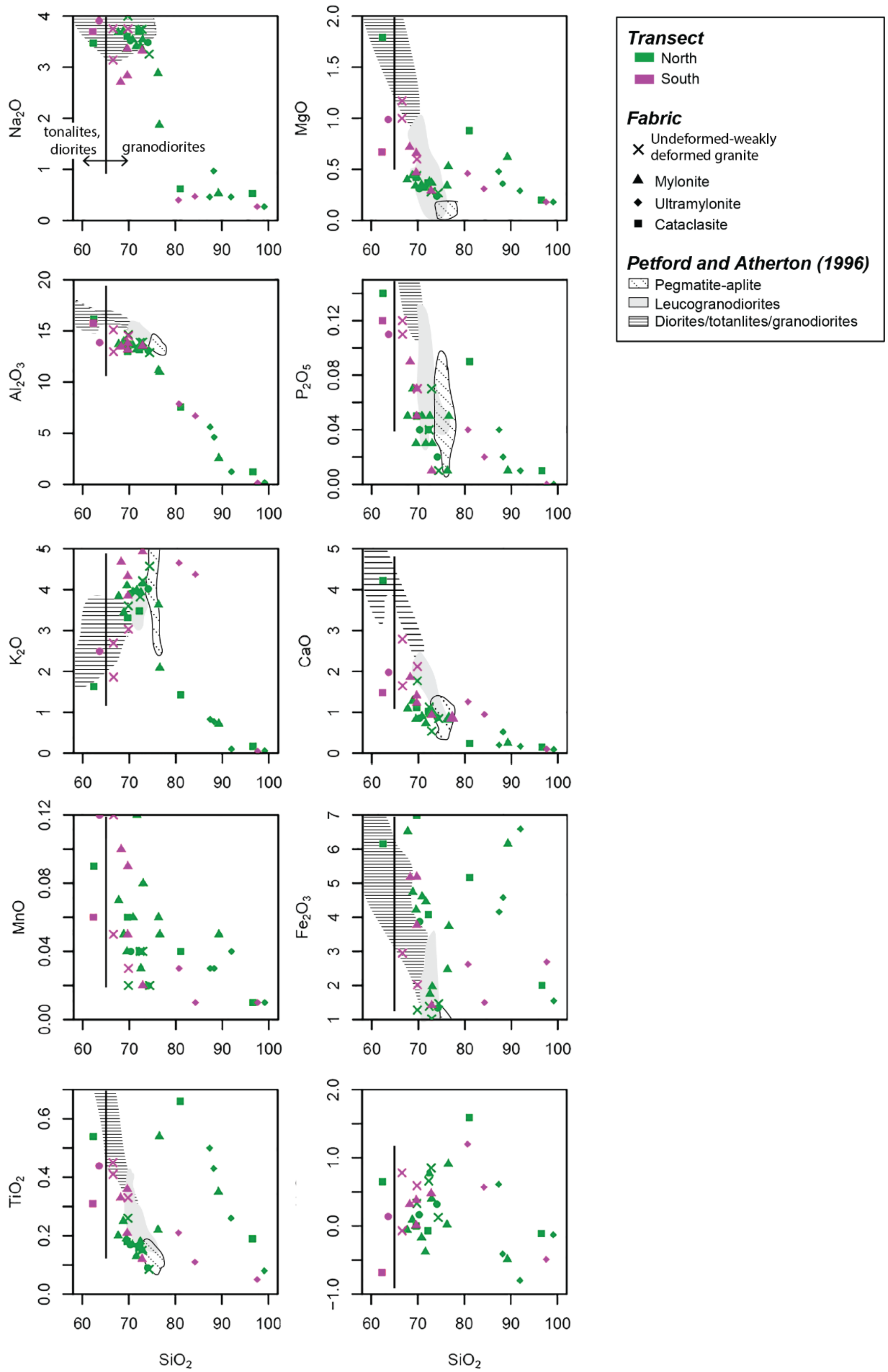

Transect
North
South
Fabric
Undeformed-weakly deformed granite
Mylonite
Ultramylonite
Cataclasite
Petford and Atherton (1996)
Pegmatite-aplite
Leucogranodiorites
Diorites/totanlites/granodiorites
tonalites, diorites
granodiorites
Na_2O
MgO
Al_2O_3
P_2O_5
K_2O
CaO
MnO
Fe_2O_3
TiO_2
SiO_2
SiO_2

The degree to which these alteration processes are reflected in the major-element alteration indices with respect to increasing deformation is shown in Fig. 3.7. UWGs have a fairly wide range of K/Al ratios (K-feldspar saturation index; Mathieu, 2018) from 1.5 and 3.9, with lower ratios in the southern transects relative to the northern transects (Fig. 3.7a). Increasing deformation, as reflected by increased percent of grain-size-reduced recrystallized matrix, corresponds to generally increasing K/Al ratios relative to UWGs in the southern transects. In the northern transects, K/Al ratios of increasingly deformed samples are mainly within the initial range defined by the UWGs. However, lower K/Al ratios are observed for some samples with over 55% grain-size reduced recrystallized matrix. UWG Na/Al ratios (albite saturation index; Mathieu, 2018) from the northern and southern transects are tightly clustered at 0.4 to 0.45 (Fig. 3.7b). Increasing deformation corresponds to decreasing Na/Al ratios in the southern transects and in some northern samples. However, some northern samples up to ~82% grain-size reduced recrystallized matrix have Na/Al ratios within the range of UWGs. UWGs have muscovitization index values between 0.72 and 0.96, with most above 0.8, reflecting that feldspars are the primary K- and Al-bearing phases (Fig. 3.7c). Similarly to the K/Al ratio, the muscovitization index increases with increasing deformation in the southern transects. In the northern transects, the muscovitization index is mostly within the range defined by UWGs for increasingly deformed samples through ~80% grain-size reduced recrystallized matrix. The most deformed samples in the northern transects show a wide range in muscovitization indices between 0.31 and 1.11.

Mass Balance Calculations

Isocon wedge diagrams plotted against immobile Al_2O_3 highlight mass gains and losses with deformation across the CBSZ. In northern Qs. Gatay and Honda (chemically granitic i.e.

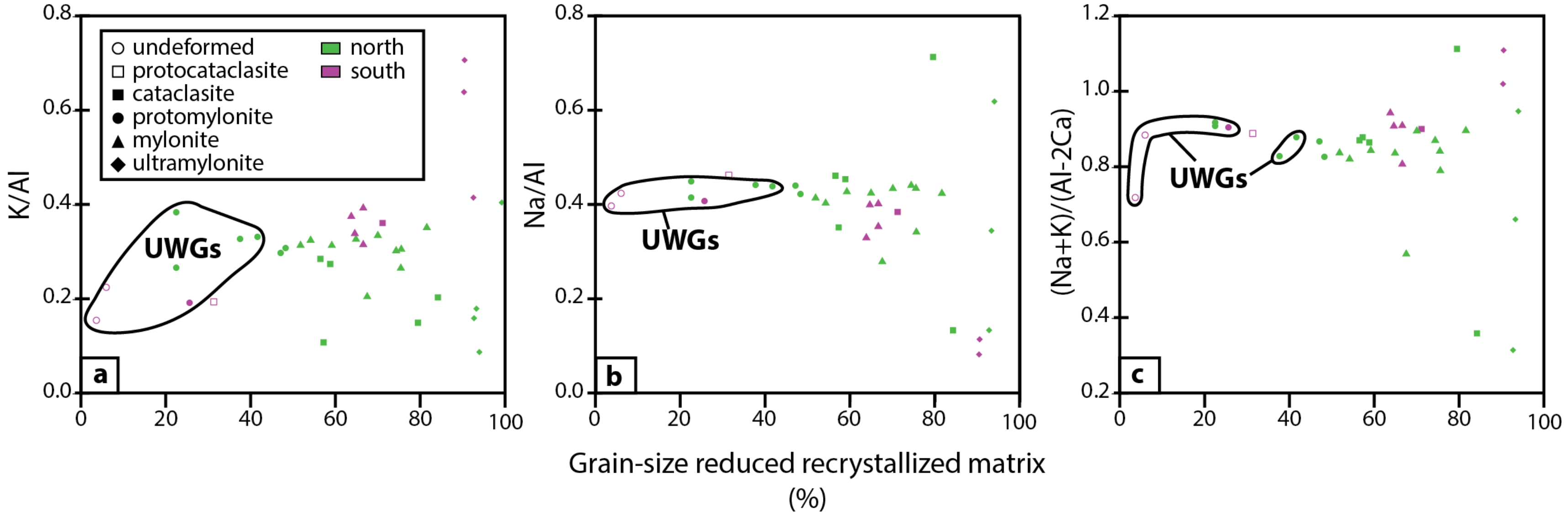

Fig. 3.7. Major-element ratios relative to volume percent grain-size reduced recrystallized matrix. a) K-feldspar saturation index, K/Al (molar), b) albite saturation index Na/Al (molar) c) muscovitization index ((Na+K)/(Al-2Ca)). Field defined by undeformed-weakly deformed granodiorites (UWGs) circled in black. Colors denote transect: north—Qs. Gatay, Ulta, and Honda; south: Qs. Ahuac, Llaca, and Rajucolta.

Fig. 3.4), mylonites with less than ~70% grain-size reduced matrix show minimal gains or losses relative to the undeformed granite (grey field) in all major-elements except MnO and Fe_2O_3, which show relative gains (Fig. 3.8a). Mylonites with more than ~70% grain-size reduced matrix and ultramylonites from Q. Gatay exhibit notable gains in SiO_2 and TiO_2 as well as gains in MgO, MnO, and FeO, and slight losses in Na_2O and K_2O. Intermediate-silica level mylonites and ultramylonites (75 to < 85 wt % SiO_2) and quartz veins show significant gains or losses for most elements other than MnO, MgO, and FeOt relative to TiO_2 (Fig. S8). However, these changes are less extreme or nonexistent when compared to Al_2O_3 (Fig. 3.8). In southern transects, highly recrystallized rocks from Q. Llaca exhibit relative gains in SiO_2 and relative losses in Na_2O (Fig. 3.8b). Mylonitic rocks from the southern transects (50-90% grain-size reduced matrix) exhibit notable gains in K_2O with slight losses in CaO and Na_2O. Mass gains in K_2O are observed across all deformation fabrics. Slight relative losses in P_2O_5 and TiO_2 are observed for some mylonitic to ultramylonitc samples.

Trace-element gains in Ce, Cr, Cu, La, Nd, Ni, Nb, Th, and Zn are observed in mylonites, ultramylonites, and cataclasites from Qs. Gatay and Honda (Fig. 3.9a). Additional mass gains in Co, Hf, Nb, Sc, Th, V, Y, and Zr, are observed for samples with over ~70 % grain-size reduced matrix in Q. Gatay. Samples from Q. Honda show minimal mass changes in these elements. In southern transects, Rb and Zn show notable mass gains regardless of deformation fabric (Fig. 3.9b). Unlike the northern transects, the southern transects show trace-element losses in Ce, and La, slight relative losses among mylonites and ultramylonites of Ba, Co, Sc, V, and Y, and minimal change in chalcophile or siderophile elements.

Mass gains and losses relative to immobile elements (i.e. Figs. 3.8, 3.9) are compared to constant mass assumptions (Fig. 3.10). Mass-balance calculations using the isocon method

Fig. 3.8. Isocon wedge diagrams depicting mass changes with deformation relative to assumed immobile Al_2O_3 for the northern transects, Qs.Gatay, Ulta and Honda (a) and southern transects, Qs. Llaca, Ahuac, and Rajucolta (b). Shaded gray area denotes compositional range of UWG precursors. Deformed samples that plot within the gray area have no significant material gains or loss. Samples plotting above the shaded area record mass gains whereas those plotting below the shaded area record mass losses. Symbols denote transect, colors denote deformation intensity (volume percent grain-size reduced matrix).

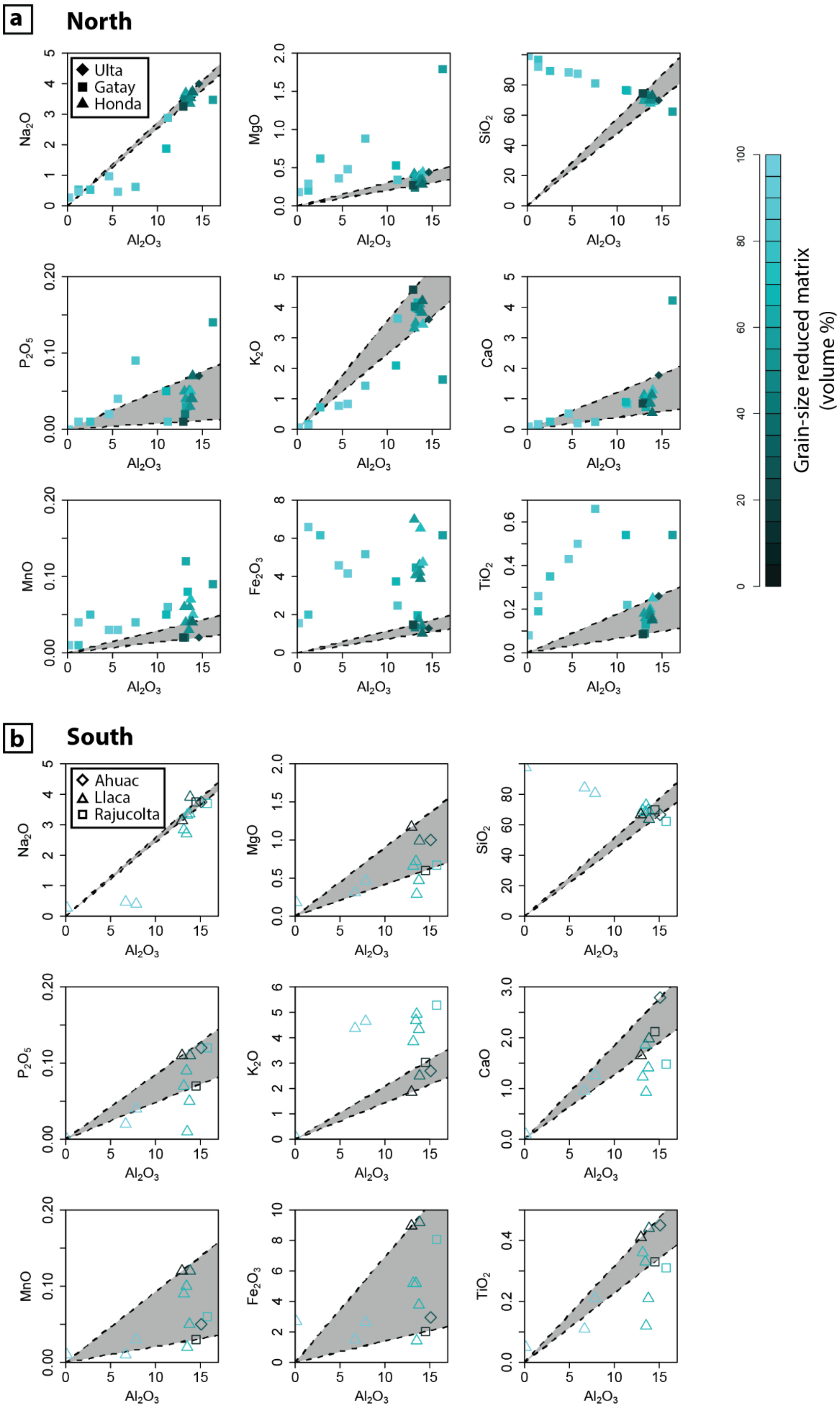
a
North
Ulta
Gatay
Honda
Na_2O
MgO
SiO_2
P_2O_5
K_2O
CaO
MnO
Fe_2O_3
TiO_2
Al_2O_3
Grain-size reduced matrix
(volume %)
b
South
Ahuac
Llaca
Rajucolta

Fig. 3.9. Isocon wedge diagrams depicting mass changes with deformation relative to assumed immobile Al_2O_3 for northern transects, Qs. Gatay, Ulta and Honda, (a) and southern transects, Qs. Ahuac, Llaca, and Rajucolta (b). Shaded gray area denotes compositional range of UWG precursor. Deformed samples that plot within the gray area have no significant material gains or loss. Samples plotting above the shaded area record mass gains whereas those plotting below the shaded area record mass losses. Symbols denote transect, colors denote deformation intensity (volume percent grain-size reduced matrix).

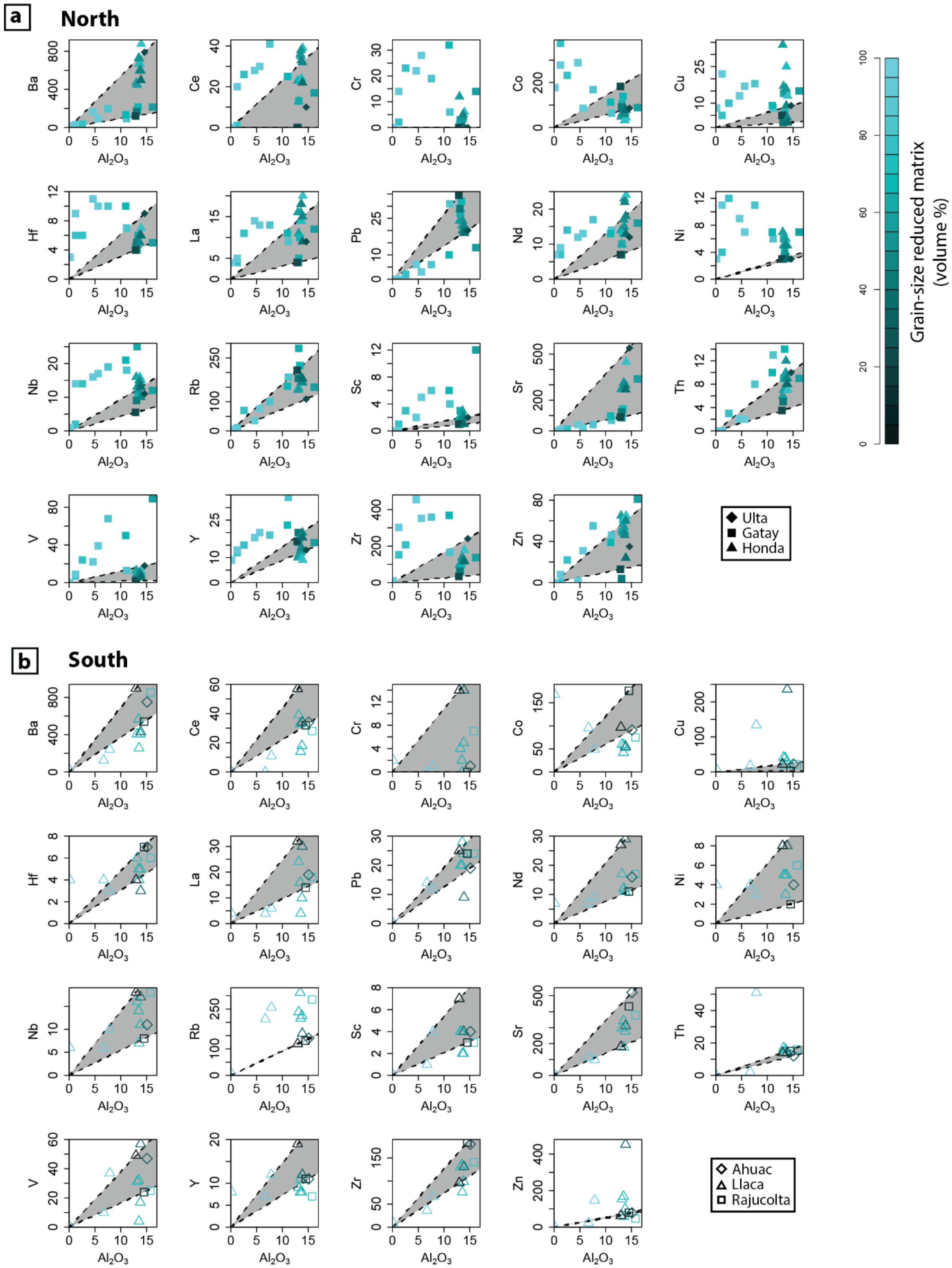
a
North
Ulta
Gatay
Honda
Grain-size reduced matrix (volume %)
b
South
Ahuac
Llaca
Rajucolta
Ba
Ce
Cr
Co
Cu
Hf
La
Pb
Nd
Ni
Nb
Rb
Sc
Sr
Th
V
Y
Zr
Zn
Al_2O_3

Fig. 3.10. Isocon diagrams (*C_0 vs. C_A*) for average compositions of deformation fabrics from the northern transects (left) and southern transects (right) assuming immobile Al_2O_3. Line of constant mass (1:1; blue line) compared to line assuming immobile Al_2O_3 (red dash). Elements that plot above the immobile element isocon represent mass gains, those below the isocon represent mass losses. Orange arrows denote volume change, with value at right, shown by constant mass vs. immobile element comparison. Volume changes and immobile Al_2O_3 isocon slopes from figure are reported in Table 3.4.

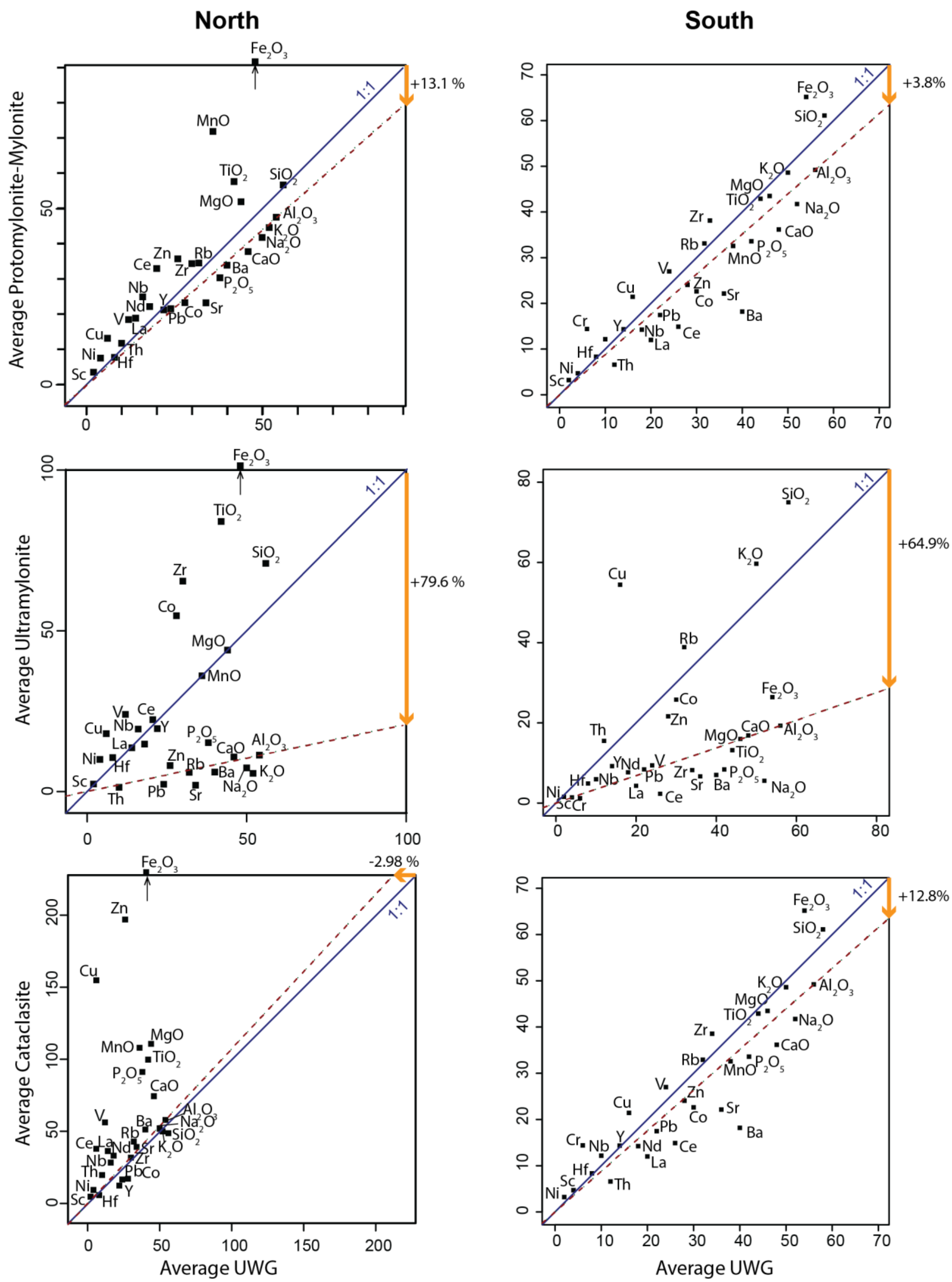
North
South
Average Protomylonite-Mylonite
Average Ultramylonite
Average Cataclasite
Average UWG
+13.1 %
+3.8%
+79.6 %
+64.9%
-2.98 %
+12.8%
1:1

TABLE 3.4. VOLUME CHANGES RELATIVE TO AVERAGE UNDEFORMED-WEAKLY DEFORMED GRANITE

Altered	Mass Change (%)	Volume Change (%)	Slope of Isocon
North			
Mylonite	13.4	13.1	0.878
Ultramylonite	377	79.6	0.204
Cataclasite	-6.75	-2.98	0.023
South			
Mylonite	5.19	3.88	0.961
Ultramylonite	190	64.9	0.351
Cataclasite	13.8	12.8	0.873
All-Granite			
Mylonite, < 75% SiO2	3.33	3.58	0.964
Mylonite, 75-85% SiO2	26.4	21.5	0.785
Ultramylonite, 75-85% SiO2	92.3	47.6	0.524
Cataclasite	5.51	7.63	0.924
All-Quartz Veins			
Ultramylonite	407	80.4	0.196
Cataclasite	1050	91.2	0.088

assuming immobile Al_2O_3 (Grant, 1986, 2005) and calculated densities for average compositions across fabric types (Table 3.3) suggests that minimal volume change (4-13 % increase) occurs during mylonitization with < 90% grain-size reduction (Table 3.4). Mylonitization where over 90% of the rock is comprised of a grain-size reduced recrystallized matrix is associated with a 65-80% volume increase associated with an increase in SiO_2. In the northern transects, this volume increase seen in ultramylonites is additionally associated with relative gains in TiO_2, and predominantly siderophile elements. In contrast, the volume increase in ultramylonites from the southern transects is associated primarily with relative gains in large-ion lithophile elements (LILE; K, Rb, Sr, Ba) and Cu. Cataclasites demonstrate a 3% volume loss in the northern transects that is accompanied by a slight loss in SiO_2 and gains in Ti and siderophile elements.

Southern cataclasites demonstrate a relatively low volume increase (13%) accompanied by slight gains in SiO_2 and Fe_2O_3.

Discussion

Immobile Elements

Al_2O_3, TiO_2, P_2O_5, and Zr are regularly assumed to be immobile elements during shear zone deformation (Grant, 1986, 2005; O'Hara and Blackburn, 1989; MacLean and Barrett, 1993; Bialek, 1999; Rolland et al., 2003c; Rossi et al., 2005b). Isocon wedge diagrams for the northern transects Q. Gatay and Honda reveal that TiO_2 is mobile in rocks with SiO_2 > ~75 wt % (Fig. 3.8 Fig. 3.9, Fig. S8). Side-by-side comparison of SiO_2, TiO_2 and Al_2O_3 shows that an increase in SiO_2 correlates to a decrease in Al_2O_3, as would be expected for major-elements based on closure to 100% (Whitbread and Moore, 2004). If TiO_2 was immobile across all deformation intensities, based on isocon wedge diagrams relative to TiO_2 (Fig. S8), mass losses for Al_2O_3, MgO, CaO, Na_2O, K_2O, and P_2O_5 as well as large ion lithophile elements (LILE: K, Rb, Sr, Ba) and Pb, Nd, Th, Y, and Zn could also be inferred. However, samples for which a mass loss of SiO_2 relative to TiO_2 is observed (Fig. S8) are the same as those that demonstrate a mass gain in TiO_2 and SiO_2 relative to immobile Al_2O_3 (Fig. 3.9a). These samples are ultramylonites or mylonites with > ~70% grain-size reduced matrix, which have SiO_2 concentrations above 75 weight percent (Fig. 3.3). The mass losses inferred from TiO_2 wedge plots for MgO, CaO, Na_2O, P_2O_5, and LILE for these samples are not observed when viewed against immobile Al_2O_3. Within most samples from Qs. Honda and Gatay with < ~70% grain-size reduced matrix, TiO_2 is immobile.

Strain Localization and Myrmekite Formation: Open or Closed System?

Myrmekite occurs regularly in UWG and granodioritic mylonite samples and occasionally in granodioritic UM samples. How myrmekite in different microstructural settings forms is debated (Shelley, 1964; Simpson and Wintsch, 1989; Castle and Lindsley, 1993; Menegon et al., 2006; Yuguchi and Nishiyama, 2008) such that myrmekite in UWGs may not form in the same manner as myrmekite in mylonites or ultramylonites. Hughes et al. (in press) recognized asymmetric strain-induced (ASIM) myrmekite (i.e. Simpson and Wintsch, 1989) as a likely contributor to grain-size reduction and development of layered mylonites with interlayered, fine-grained, recrystallized polyphase and quartz bands within the CBSZ. Evidence supporting the involvement of fluids in facilitating myrmekite growth, namely white mica growth at the inferred original interface between Kfs porphyroclast and surrounding matrix (Hughes et al., 2019; Fig. S7C), was observed in some, but not all, samples where ASIM was documented. Muscovite may form in association with myrmekite following the reaction (Phillips et al., 1972):

$$\underset{\substack{\text{alkali}\\\text{feldspar}}}{\left\{\begin{matrix}3KAlSi_3O_8\\NaAlSi_3O_8\end{matrix}\right\}} + \underset{\substack{\text{calcic}\\\text{plagioclase}}}{\left\{\begin{matrix}CaAl_2Si_2O_8\\NaAlSi_3O_8\end{matrix}\right\}} + \underset{\text{water}}{H_2O} \rightarrow \underset{\substack{\text{more sodic}\\\text{plagioclase}}}{\left\{\begin{matrix}CaAl_2Si_2O_8\\2NaAlSi_3O_8\end{matrix}\right\}} + \underset{\text{quartz}}{6SiO_2} + \underset{\text{muscovite}}{KAl_2(Al,Si_3)O_{10}(OH)_2} + K_2O \qquad (6).$$

Within Qs. Gatay and Honda mass changes of K, Na, Si, and Ca for samples with < ~70 % grain-size reduced matrix are within the range of variability defined by UWGs (Fig. 3.8a), suggesting that this reaction takes place in a predominantly closed system. This is further supported by the agreement between K-feldspar and albite saturation indices as well as muscovitization indices between these samples and UWGs (Fig. 3.7). Samples with greater amounts of grain-size reduced matrix, which exhibit more element mobility, typically contain little to no myrmekite.

Q. Llaca and Rajucolta record relative gains in K_2O for all mylonitic and ultramylonitic samples, and slight losses in Na_2O and CaO for a subset of samples, (Fig. 3.8b). This suggests myrmekite formation and mylonitization occurs within a more open system than in the northern transects, despite the southern transects and Q. Honda exhibiting less element mobility overall relative to Q. Gatay in the north. An open system is further suggested by the increasing K-feldspar- and decreasing albite-saturation indices as well as the increasing muscovitization index with increasing deformation in the southern transects (Fig. 3.7).

The UWG composition in the northern transects is more K-rich (~3.5-4.5 wt % K_2O) than the southern transects (~1.8-3 wt %K_2O). The contrast in element mobility and system openness may be explained by this difference in starting composition. If both the northern and southern transects were affected by the same composition fluid, if the fluid was relatively K-rich and in equilibrium with the more K-rich UWGs, it could still facilitate myrmekite formation in northern transects with minimal mass transfer (McCaig et al., 1990). This same composition fluid, in disequilibrium with the UWGs from southern transects, could then facilitate myrmekite formation and affect K-metasomatism suggested by mass gains in K_2O (Fig. 3.8b).

Silicification

The gradual increase in SiO_2 composition in Q. Gatay defines what could be considered a mixing line between the protolith composition and the quartz vein composition. Increasing deformation intensity coincides with a gradual increase in wt % SiO_2 (Fig. 3.3). One possibility to explain this relationship is that narrow (mm-thick) quartz veins increasingly intrude into deforming mylonites, which then become incorporated into S-C mylonitic and ultramylonitic fabrics. This may be consistent with rheological domains identified by Hughes et al. (2019), where the interconnected quartz domains observed in thin section were interpreted as deformed quartz veins, as opposed to original magmatic quartz that was subsequently recrystallized.

Our observations of increased overall element mobility with increased silicification relative to undeformed precursor compositions agrees with the trends observed in several geochemical studies of extensional shear zones. Kerrich et al. (1977) documented silica redistribution into extensional veins at the mm-m scale during deformation of metabasalts in the Campbell shear zone (Yellowknife greenstone belt, Northwest Territories, Canada), and proposed that extensional veins that form syn-tectonically with shear zone deformation act as "sinks" for mobile elements. Similar concentration of mobile elements, especially trace metals such as Au and Cu, within sheeted extensional quartz veins oriented subparallel to major faults was observed in the Baghu intrusion-related gold deposit in north-central Iran (Niroomand et al., 2018) and in Cu-Pb-Zn mineralization in the Tavsanli Area in NW Turkey (Kumral et al., 2016).

It is plausible that similar processes occurred within the CBSZ, at least in the central part of the shear zone (along strike-Q. Gatay), where silicification is observed essentially as a mixing line between almost pure (97-98 wt % SiO_2) quartz veins and UWGs. Ultramylonitic and cataclastic quartz veins in this study show mass gains in trace metals such as Cu, Cr, Zn, Zr, Co and Ni (Figs. 3.11 and 3.12) in Q. Gatay. Quartz veins in Q. Llaca variably record mass gains in Co, Cu, Ni, and Zn, but have relatively constant mass of Zr and Cr. Field and petrologic evidence, such as foliation-parallel quartz veins (Hughes et al., 2019) and quartz growth into a microcrack that is parallel to fluid inclusion planes in a quartz vein (Fig. S7), support the argument for syn-deformational quartz veining in the CBSZ. Mobilization of Ti and siderophile elements are further supported by the abundance of opaque oxides along shear bands and precipitation of titanite within a crack in a quartz vein (Fig. S7H).

At the thin-section scale and finer it is often difficult to distinguish which quartz-rich domains result from grain-size reduction and subsequent layering of quartz-rich and feldspar-mica rich domains as banded mylonites as opposed to those that result from syn-deformational veining. We recognize a potential bias towards more silicic bulk rock compositions in this study due to the amount of rock powdered for each sample, which ranged from 50-200 g and was limited due to a need to retain sample for additional analyses outside the scope of this paper. If the smaller sample includes foliation-parallel quartz-rich domains, this would naturally increase the overall Si content of the rock towards some intermediate value between a quartz vein and relatively undeformed granodiorite.

The trend of silicification in Q. Gatay likely suggests an importance of extensional veining in accommodating stresses (Cox et al., 1986). It may be argued that the prevalence of silicification in Q. Gatay would either be a result of late-stage silica-rich magmatic fluids filling up extensional fractures during submagmatic deformation, in which case the silicification would be related largely to the late influx of magma. Observations from Nevado Huascaran of discrete, narrow, ultramylonitic zones within otherwise undeformed granodiorite that exhibits magmatic fabrics such as schlieren and biotite layering (Fig. S9), support at least transient high-stress-events within a magmatic-submagmatic setting such as that which would favor extensional cracking at Q. Gatay. Such localization could also be related to channelization of fluids within a crystallizing magma.

Along Strike Variation

The most notable changes in geochemistry are recorded in Q. Gatay, where silicification accompanies a volume increase of up to 75% related to high-intensity deformation. Although relative gains in LILE are observed with increasing deformation in Qs. Llaca and Rajucolta, there appears to be less overall element mobility in the southern transects relative to Gatay. Q. Honda demonstrates mainly isochemical deformation. Although this may suggest lack of fluid-rock interaction during deformation in Q. Honda (i.e. Kerrich et al., 1980), McCaig (1984, 1997) cautioned that fluids may still be present, with the caveat that if they are they are in equilibrium with the rock. It is interesting to note that the shear zone width is reportedly narrower in Q. Honda than in both Qs. Gatay and Llaca. The anastamozing pattern of strain localization within shear zones at the regional scale has previously been attributed to fluid-influenced strain partitioning (Ring et al., 1999). Speculatively, the variation in shear zone width and strain localization observed in the Cordillera Blanca shear zone (Hughes et al. in prep) may be driven by channelization of fluids. If this were the case, the varying nature of mass transfer observed in the CBSZ could be explained by fluids being fairly distributed throughout Q. Gatay, such that most samples exhibit mass gains, and fluids being present at least locally in Q. Llaca but were in generally absent from Q. Honda, where deformed rocks have similar compositions to UWGs.

The nature of these fluids, whether they are meteoric, magmatic, or perhaps lower crustal, remains uncertain. If fluids moving through the shear zone also feed the hot springs issuing along the fault, at least some component must be deep-seated due to the mantle-derived He signature in the springs (Newell et al., 2015). Mass gains in Cu and Zn within silicified ultramylonites and cataclasites are consistent with the presence of Cu and Zn ore mineralization in hydrothermal breccias north along strike (Park and Kalinaj, 2009). Elevated concentrations of these chalcophile elements lends additional support to the idea proposed by Newell et al. (2015) of deep-seated (i.e. mantle-derived) fluids circulating along the Cordillera Blanca shear zone (Mungall, 2002).

The CBSZ is widest within the geographically central part of the shear zone Hughes et al. (in prep) (e.g. Q. Gatay). Previous authors have suggested a relatively young influx of magma to the central portion of the shear zone at 5-6 Ma (Petford and Atherton, 1996; Margirier et al., 2016). If this were the case, relatively high temperatures during submagmatic to subsolidus deformation (i.e. Hughes et al., 2019) would allow for more distributed deformation and facilitate (or possibly result from) a broader distribution of magmatic fluids. If this were the case, relatively high temperatures during submagmatic to subsolidus deformation (i.e. Hughes et al., 2019) would allow for more distributed deformation and facilitate (or possibly result from) a broader distribution of magmatic fluids. The shear zone at Q. Honda (north) and Q. Llaca (south), are up to ~6x narrower than Q. Gatay (Hughes et al., in preparation). A narrower shear zone would be consistent with generally cooler temperatures, faster strain rates, and/or more localized channelization of fluids. Q. Ishinca, in between Qs. Honda and Llaca, was found to have relatively fast strain rates (10^{-13} to 10^{-12} s^{-1}), based on recrystallized quartz grain size paleopiezometry as well as on slip rates derived from previously determined exhumation rates (Margirier et al., 2016). Without a recent magmatic pulse in this area, there may not be a mechanism by which to broadly distribute fluids or ductile deformation. Because the nature of the fluids is uncertain, there is a possibility that the geochemical signature of fluid-rock interaction in Q. Llaca is predominantly from later meteoric fluids. This seems reasonable considering the variable nature of geochemical changes in southern cataclasites.

Summary and Conclusions

New whole-rock geochemical data from the Cordillera Blanca shear zone suggests that mylonitization of granodioritic to granitic rocks of the Cordillera Blanca batholith with < 75 weight percent SiO_2 occurs nearly isochemically and isovolumetrically (volume gain ≤ 13%). Mylonitization of rocks with over ~70 volume percent grain-size reduced recrystallized matrix is accompanied by silicification. Silicification occurs mainly in the northern observed transects, and is associated with mobiliziation of TiO_2, mass gains in TiO_2, FeO, MgO, MnO, Cu, and Zn, and a volume increase of up to ~80%. Mass-balance calculations and major-element ratios from the southern transects demonstrate that there is less overall element mobility in the south relative to the north and that K-metasomatism likely occurred in the southern transects. Geochemical variation occurs along strike and broadly corresponds to variations in shear zone width, which suggests that fluid flow through the shear zone plays an important role in strain localization along the CBSZ.

Acknowledgements

This project was funded by a GSA graduate student research grant awarded to C. Hughes. Many thanks are owed to C. Fedo for guidance in sample preparation, J. B. Mahoney for XRF analysis. C. Mueller and A. Weist were invaluable mentors and assistants in preparing beads and pucks for XRF analysis. We thank J. Langille for assistance in drafting map modified from Giovanni et al. (2010).

References

Ague, J. J. (1994). Mass transfer during Barrovian metamorphism of pelites, south-central Connecticut. II: Channelized fluid flow and the growth of staurolite and kyanite.

Atherton, M. P., & Petford, N. (1993). Magmas From Newly Underplated Basaltic Crust. *Nature*, *362*(March), 1991–1993.

Atherton, M. P., & Petford, N. (1996). Plutonism and the growth of Andean Crust at 9 °S from 100 to 3 Ma. *Journal of South America Earth Sciences*, *9*, 1–9. https://doi.org/10.1016/0895-9811(96)00023-5

Atherton, M. P., & Sanderson, M. (1987). The Cordillera Blanca Batholith: a study of granite intrusion and the relation of crustal thickening to peraluminosity. *Geologisch Rundschau*, *76*(1), 213–232.

Barker, F. (1979). Trondhjemite: Definition, Environment and Hypotheses of Origin. *Developments in Petrology*, *6*, 1–12. https://doi.org/10.1016/B978-0-444-41765-7.50006-X

Bialek, D. (1999). Chemical changes associated with deformation of granites under greenschist facies conditions: The example of the Zawidow Granodiorite (SE Lusatian Granodiorite Complex, Poland). *Tectonophysics*, *303*(1–4), 251–261. https://doi.org/10.1016/S0040-1951(98)00248-0

Bucholz, C. E., & Ague, J. J. (2010). Fluid flow and Al transport during quartz-kyanite vein formation, Unst, Shetland Islands, Scotland. *Journal of Metamorphic Geology*, *28*(1), 19–39. https://doi.org/10.1111/j.1525-1314.2009.00851.x

Castle, R. O., & Lindsley, D. H. (1993). An exsolution silica-pump model for the origin of myrmekite. *Contributions to Mineralogy and Petrology*, *115*(1), 58–65. https://doi.org/10.1007/BF00712978

Coldwell, B., Clemens, J., & Petford, N. (2011). Deep crustal melting in the Peruvian Andes: Felsic magma generation during delamination and uplift. *Lithos*, *125*(1–2), 272–286.

https://doi.org/10.1016/j.lithos.2011.02.011

Collettini, C. (2011). The mechanical paradox of low-angle normal faults: Current understanding and open questions. *Tectonophysics*, *510*(3–4), 253–268. https://doi.org/10.1016/j.tecto.2011.07.015

Cox, S.F., Etheridge, M. A., & Wall, V. J. (1986). The role of fluids in syntectonic mass transport, and the localization of metamorphic vein-type ore deposists. *Ore Geology Reviews*, *2*(1–3), 65–86. https://doi.org/10.1016/0169-1368(87)90024-2

Cox, Stephen F. (2002). Fluid flow in mid- to deep crustal shear systems: Experimental constraints, observations on exhumed high fluid flux shear systems, and implications for seismogenic processes. *Earth, Planets and Space*, *54*(11), 1121–1125. https://doi.org/10.1186/BF03353312

Deverchere, J., Dorbath, C., & Dorbath, L. (1989). Extension related to a high topography: results from a microearthquake survey in the Andes of Peru and tectonic implications. *Geophysical Journal International*, *98*, 281–292.

Egeler, C. G., & De Booy, T. (1956). Geology and petrology of part of the southern Cordillera Blanca, Peru. *Treatises of the Royal Dutch Geological and Mining Society*, *Geology Series*, *17*, 1–86.

Faulkner, D. R., Jackson, C. A. L., Lunn, R. J., Schlische, R. W., Shipton, Z. K., Wibberley, C. A. J., & Withjack, M. O. (2010). A review of recent developments concerning the structure, mechanics and fluid flow properties of fault zones. *Journal of Structural Geology*, *32*(11), 1557–1575. https://doi.org/10.1016/j.jsg.2010.06.009

Focus Ventures Ltd. (2010). Focus cuts 46m @ 3.6 g/t Au equivalent at Nueva California; extends mineralized system to south and west of mine workings. Retrieved April 3, 2019, from https://www.prnewswire.com/news-releases/

Giovanni, M. K. (2007). *Tectonic and Thermal Evolution of the Cordillera Blanca Detachment System, Peruvian Andes: Implications for Normal Faulting in a Contractional Orogen*. University of California Los Angeles. Retrieved from https://search-proquest-com.proxy.lib.utk.edu:2050/pqdtglobal/docview/304872260/fulltextPDF/FA8BD4AAE1B8419DPQ/1?accountid=14766

Giovanni, M. K., Horton, B. K., Garzione, C. N., McNulty, B. a., & Grove, M. (2010). Extensional basin evolution in the Cordillera Blanca, Peru: Stratigraphic and isotopic records of detachment faulting and orogenic collapse in the Andean hinterland. *Tectonics*, *29*(6), 1–21. https://doi.org/10.1029/2010TC002666

Glazner, A. F., & Bartley, J. M. (1991). Volume loss, fluid flow and state of strain in extensional mylonites from the central Mojave Desert, California. *Journal of Structural Geology*, *13*(5), 587–594. https://doi.org/10.1016/0191-8141(91)90045-K

Gottardi, R., Teyssier, C., Mulch, A., Valley, J. W., Spicuzza, M. J., Vennemann, T. W., et al. (2015). Strain and permeability gradients traced by stable isotope exchange in the Raft River detachment shear zone, Utah. *Journal of Structural Geology*, *71*, 41–57. https://doi.org/10.1016/j.jsg.2014.10.005

Grant, J. A. (1986a). The isocon diagram; a simple solution to Gresens' equation for metasomatic alteration. *Economic Geology*, *81*(8), 1976–1982. https://doi.org/10.2113/gsecongeo.81.8.1976

Grant, J. A. (1986b). The Isocon Diagram - A Simple Solution to Gresens' Equation for Metasomatic Alteration. *Economic Geology*, *81*(8), 1976–1982. Retrieved from https://watermark.silverchair.com/1976.pdf?token=AQECAHi208BE49Ooan9kkhW_Erc

y7Dm3ZL_9Cf3qfKAc485ysgAAAj4wggI6BgkqhkiG9w0BBwagggIrMIICJwIBADCC
AiAGCSqGSIb3DQEHATAeBglghkgBZQMEAS4wEQQMChhMmGZ3EJLRuuFqAgE
QgIIB8bXA5v1B1CPK66AMVOK-jlUtXU7Pe3RhXMaQiHh-n43TrdMhkW

Grant, J. A. (2005). Isocon analysis: A brief review of the method and applications. *Physics and Chemistry of the Earth*, *30*(17-18 SPEC. ISS.), 997–1004. https://doi.org/10.1016/j.pce.2004.11.003

Gresens, R. L. (1967). Composition-volume relationships of metasomatism. *Chemical Geology*, *2*(C), 47–65. https://doi.org/10.1016/0009-2541(67)90004-6

Henian, W., Jun, C., Jun-Feng, J., & Xiao-Ming, Q. (1997). Geological and geochemical characteristics of the hetai gold deposit, south china: Gold mineralization in an auriferous shear zone. *International Geology Review*, *39*(2), 181–190. https://doi.org/10.1080/00206819709465266

Holyoke, C. W., & Kronenberg, A. K. (2013). Reversible water weakening of quartz. *Earth and Planetary Science Letters*, *374*, 185–190. https://doi.org/10.1016/j.epsl.2013.05.039

Hutchison, C. S. (1974). *Laboratory Handbook of Petrographic Techniques.* New York: John Wiley & Sons.

Hutchison, C. S., & Lumpur, K. (1975). The norm, its variations, their calculation and relationships. *Schweizerische Mineralogische Und Petrographische Mitteilungen*, *55*, 243–256.

Janousek, V., Farrow, C. M., Erban, V., Smid, J., & Survey, C. G. (2003). Geochemical Data Toolkit for Windows written in R language © 2000-2003. *Names*, 1–11.

Janoušek, V., Farrow, C. M., & Erban, V. (2006). Interpretation of whole-rock geochemical data in igneous geochemistry: Introducing Geochemical Data Toolkit (GCDkit). *Journal of*

Petrology, *47*(6), 1255–1259. https://doi.org/10.1093/petrology/egl013

Janoušek, V., Martin, H., Erban, V., Farrow, C., & Moyen, J.-F. (2015). Geochemical Modelling of Igneous Processes – Principles And Recipes in R Language. *Geochemical Modelling of Igneous Processes – Principles And Recipes in R Language*, 11–26. https://doi.org/10.1007/978-3-662-46792-3

Kerrich, R., Fyfe, W. S., German, B. E., & Allison, I. (1977). Local modification of rock chemistry by deformation. *Contributions to Mineralogy and Petrology*, *65*(2), 183–190. https://doi.org/10.1007/BF00371058

Kerrich, Robert, Allison, I., Barnett, R. L., Moss, S., & Starkey, J. (1980). Microstructural and Chemical Transformations Accompanying Deformation of Granite in a Shear Zone at Mieville, Switzerland; With Implications for Stress Corrosion Cracking and Superplastic Flow. *Contributions to Mineralogy and Petrology*, *73*, 221–242. Retrieved from https://link-springer-com.proxy.lib.utk.edu:2050/content/pdf/10.1007%2FBF00381442.pdf

Kohlstedt, D. L. (2006). The Role of Water in High-Temperature Rock Deformation. *Reviews in Mineralogy & Geochemistry*, *62*, 377–396. https://doi.org/10.2138/rmg.2006.62.16

Kumral, M., Abdelnasser, A., & Budakoglu, M. (2016). Geochemistry of Hydrothermal Alteration Associated with Cenozoic Intrusion-Hosted Cu-Pb-Zn Mineralization at Tavşanlı Area, Kütahya, NW Turkey. *Minerals*, *6*(1), 13. https://doi.org/10.3390/min6010013

Lechler, P. J., & Desilets, M. O. (1987). A review of the use of loss on ignition as a measurement of total volatiles in whole-rock analysis. *Chemical Geology*, *63*(3–4), 341–344. https://doi.org/10.1016/0009-2541(87)90171-9

MacLean, W. H., & Barrett, T. J. (1993). Lithogeochemical techniques using immobile elements. *Journal of Geochemical Exploration*, *48*(2), 109–133. https://doi.org/10.1016/0375-6742(93)90002-4

Maggi, M., Rossetti, F., Ranalli, G., & Theye, T. (2014). Feedback between fluid infiltration and rheology along a regional ductile-to-brittle shear zone: The East Tenda Shear Zone (Alpine Corsica). *Tectonics*, *33*(3), 253–280. https://doi.org/10.1002/2013TC003370

Mainprice, D. H., & Paterson, M. S. (1984). Experimental studies of the role of water in the plasticity of quartzites. *Journal of Geophysical Research*, *89*(B6), 4257–4269.

Le Maitre, R. W., Bateman, P., Dudek, A., & Keller, J. (1989). *A classification of igneous rocks and glossary of terms: Recommendations of the International Union of Geological Sciences Subcomission on the Systematics of Igneous Rocks.* (R. W. Le Maitre, Ed.). Oxford: Blackwell Scientific Publications.

Mancktelow, N. S., & Pennacchioni, G. (2004). The influence of grain boundary fluids on the microstructure of quartz-feldspar mylonites. *Journal of Structural Geology*, *26*(1), 47–69. https://doi.org/10.1016/S0191-8141(03)00081-6

Margirier, A., Audin, L., Robert, X., Herman, F., Ganne, J., & Schwartz, S. (2016). Time and mode of exhumation of the Cordillera Blanca batholith (Peruvian Andes). *Journal of Geophysical Research: Solid Earth*, *121*(8), 6235–6249. https://doi.org/10.1002/2016JB013055

Mathieu, L. (2018). Quantifying Hydrothermal Alteration: A Review of Methods. *Geosciences*, *8*(7), 245. https://doi.org/10.3390/geosciences8070245

McCaig, A. M. (1984). Fluid-rock interaction in some shear zones from the Pyrenees. *Journal of Metamorphic Geology*, *2*(2), 129–141. https://doi.org/10.1111/j.1525-

1314.1984.tb00292.x

McCaig, A. M. (1997). The geochemistry of volatile fluid flow in shear zones. In M. B. Holness (Ed.), *Deformation-enhanced fluid transport in the Earth's crust and mantle* (pp. 227–266). London, England: Chapman & Hall.

McCaig, A. M., Wickham, S. M., & Taylor, H. P. (1990). Deep fluid circulation in alpine shear zones, Pyrenees, France: field and oxygen isotope studies. *Contributions to Mineralogy and Petrology*, *106*(1), 41–60. https://doi.org/10.1007/BF00306407

McNulty, B. a., Farber, D. L., Wallace, G. S., Lopez, R., & Palacios, O. (1998). Role of plate kinematics and plate-slip-vector partitioning in continental magmatic arcs: Evidence from the Cordillera Blanca, Peru. *Geology*, *26*(9), 827–830. https://doi.org/10.1130/0091-7613(1998)026<0827:ROPKAP>2.3.CO;2

Menegon, L., Pennacchioni, G., & Stünitz, H. (2006). Nucleation and growth of myrmekite during ductile shear deformation in metagranites. *Journal of Metamorphic Geology*, *24*(7), 553–568. https://doi.org/10.1111/j.1525-1314.2006.00654.x

Menegon, L., Fusseis, F., Stünitz, H., & Xiao, X. (2015). Creep cavitation bands control porosity and fluid flow in lower crustal shear zones. *Geology*, *43*(3). https://doi.org/10.1130/G36307.1

Micklethwaite, S., Sheldon, H. A., & Baker, T. (2010). Active fault and shear processes and their implications for mineral deposit formation and discovery. *Journal of Structural Geology*, *32*(2), 151–165. https://doi.org/10.1016/j.jsg.2009.10.009

Mukasa, S. B. (1984). *Comparative lead isotope systematics and zircon uranium-lead geochronology for the Coastal, San Nicolas, and Cordillera Blanca Batholiths, Peru*. University of California, Santa Barbara.

Mungall, J. E. (2002). Roasting the mantle: Slab melting and the genesis of major Au and Au-rich Cu deposits. *Geology*, *30*(10), 915–918. https://doi.org/10.1130/0091-7613(2002)030<0915:RTMSMA>2.0.CO;2

Neilson, M. J., & Brockman, G. F. (1977). The error associated with point-counting. *American Mineralogist*, *62*, 1238–1244.

Newell, D. L., Jessup, M. J., Hilton, D. R., Shaw, C., & Hughes, C. (2015). Mantle-Derived Helium in Hot Springs of the Cordillera Blanca, Peru: Implications for Mantle-to- Crust Fluid Transfer in a Flat-Slab Subduction Setting. *Chemical Geology Chemical Geology Chemical Geology*, *417*, 200–209. https://doi.org/10.1016/j.chemgeo.2015.10.003

Newman, J., & Mitra, G. (1993). Lateral variations in mylonite zone thickness as influenced by fluid-rock interactions, Linville falls fault, North Carolina. *Journal of Structural Geology*, *15*(7), 849–863. https://doi.org/10.1016/0191-8141(93)90180-I

Niroomand, S., Hassanzadeh, J., Tajeddin, H. A., & Asadi, S. (2018). Hydrothermal evolution and isotope studies of the Baghu intrusion-related gold deposit, Semnan province, north-central Iran. *Ore Geology Reviews*, *95*(March 2017), 1028–1048. https://doi.org/10.1016/j.oregeorev.2018.01.015

O'Hara, K., & Blackburn, W. H. (1989). Volume-loss model for trace-element enrichments in mylonites. *Geology*, *17*(6), 524–527. https://doi.org/10.1130/0091-7613(1989)017<0524:VLMFTE>2.3.CO;2

Park, S. L. C., & Kalinaj, M. Rpg. (2009). *The Nueva California Property, Department of Ancash, Peru. NI 43-101 Technical Report*.

Petford, N., & Atherton, M. P. (1992). Granitoid emplacement and deformation along a major crustal lineament: The Cordillera Blanca, Peru. *Tectonophysics*, *205*(1–3), 171–185.

https://doi.org/10.1016/0040-1951(92)90425-6

Petford, N., & Atherton, M. P. (1996). Na-rich Partial Melts from Newly Underplated Basaltic Crust: the Cordillera Blanca Batholith, Peru. *Journal of Petrology*, *37*(6), 1491–1521. https://doi.org/10.1093/petrology/37.6.1491

Phillips, E. R., Ransom, D. M., & Vernon, R. H. (1972). Myrmekite and muscovite developed by retrograde metamorphism at Broken Hill, New South Wales. *Mineralogical Magazine*, *38*, 570–78.

Van der Plas, L., & Tobi, A. C. (1965). Reliability of point counting results; reply. *American Journal of Science*. https://doi.org/10.2475/ajs.263.8.722

Pryer, L. L., & Robin, P.-Y. F. (1995). Retrograde metamorphic reactions in deforming granites and the origin of flame perthite. *Journal of Metamorphic Geology*, *13*, 645–658.

Quilichini, A., Siebenaller, L., Nachlas, W. O., Teyssier, C., Vennemann, T. W., Heizler, M. T., & Mulch, A. (2015). Infiltration of meteoric fluids in an extensional detachment shear zone (Kettle dome, WA, USA): How quartz dynamic recrystallization relates to fluid-rock interaction. *Journal of Structural Geology*, *71*, 71–85. https://doi.org/10.1016/j.jsg.2014.11.008

Quilichini, A., Siebenaller, L., Teyssier, C., & Vennemann, T. W. (2016). Magmatic and meteoric fluid flow in the Bitterroot extensional detachment shear zone (MT, USA) from ductile to brittle conditions. *Journal of Geodynamics*, *101*, 109–128. https://doi.org/10.1016/j.jog.2016.05.006

Ring, U., Geowissenschaften, I., & Gutenberg-universität, J. (1999). Volume loss , fluid flow , and coaxial versus noncoaxial deformation in retrograde , amphibolite facies shear zones ,. *GSA Bulletin*, *l*(1), 123–142.

Rolland, Y., & Rossi, M. (2016). Two-stage fluid flow and element transfers in shear zones during collision burial-exhumation cycle: Insights from the Mont Blanc Crystalline Massif (Western Alps). *Journal of Geodynamics*, *101*, 88–108. https://doi.org/10.1016/j.jog.2016.03.016

Rolland, Y., Cox, S., Boullier, A.-M., Pennacchioni, G., & Mancktelow, N. S. (2003a). Rare earth and trace-element mobility in mid-crustal shear zones: insights from the Mont Blanc Massif (Western Alps). *Earth and Planetary Science Letters*, *214*, 203–219.

Rolland, Y., Cox, S., Boullier, A.-M., Pennacchioni, G., & Mancktelow, N. S. (2003b). Rare earth and trace-element mobility in mid-crustal shear zones: insights from the Mont Blanc Massif (Western Alps). *EPSL Cyaan Magenta Geel Zwart Earth and Planetary Science Letters*, *6753*(214), 18–8. https://doi.org/10.1016/S0012-821X(03)00372-8

Rolland, Y., Rossi, M., & Cox, S.F., Corsini, M., Mancktelow, N., Pennacchoni, G., Fornari, M., Boullier, A. M. (2008). 40Ar/39Ar dating of synkinematic white mica: insights from fluid-rock reaction in low-grade shear zones (Mont Blanc Massif) and constraints on timing of deformation in the NW external Alps. In C. A. J. Wibberley, J. Imber, R. E. Holdsworth, & C. Collettini (Eds.), *The Internal Structure of Fault Zones: Implications for Mechanical and Fluid-Flow Properties* (pp. 293–315). The Geological Society of London.

Rossi, M., Rolland, Y., Vidal, O., & Cox, S. F. (2005a). Geochemical variations and element transfer during shear-zone development and related episyenites at middle crust depths: insights from the Mont Blanc granite (French-Italian Alps). In D. Bruhn & L. Burlini (Eds.), *Geological Society, London, Special Publications* (Vol. 245, pp. 373–396). Retrieved from http://citeseerx.ist.psu.edu/viewdoc/download?doi=10.1.1.911.5189&rep=rep1&type=pdf

Rossi, M., Rolland, Y., Vidal, O., & Cox, S. F. (2005b). Geochemical variations and element transfer during shear-zone development and related episyenites at middle crust depths: insights from the Mont Blanc granite (French — Italian Alps). *Geological Society, London, Special Publications*, *245*(1), 373–396. https://doi.org/10.1144/GSL.SP.2005.245.01.18

Rutter, E. H., Holdsworth, R. E., & Knipe, R. J. (2001). The nature and tectonic significance of fault-zone weakening: an introduction. In R. E. HOldsowrth, R. A. Strachan, J. F. Magloughlin, & R. J. Knipe (Eds.), *The Nature and Tectonic Significance of Fault Zone Weakening. Geological Society, London, Special Publications, 186.* The Geological Society of London. Retrieved from http://sp.lyellcollection.org/content/specpubgsl/186/1/1.full.pdf

Scholz, C. H. (2002). *The Mechanics of Earthquakes and Faulting* (2nd ed.). Cambridge, United Kingdom: Cambridge University Press. https://doi.org/10.1785/gssrl.74.3.333

Schwartz, D. P. (1988). Paleoseismicty and Neotectonics of the Cordillera Blanca Fault Zone, Zorthern Peruvian Andes. *Journal of Geophysical Research*, *93*(B5), 4712–4730.

Sebrier, M., Mercier, J. L., Megard, F., Laubacher, G., & Carey-Cailhardis, C. (1985). Quaternary normal and reverse faulting and the state of stress in the central Andes of south Peru. *Tectonics*, *4*(7), 739–780.

Sébrier, M., Mercier, J. L., Machare, J., Bonnot, D., Cabrera, J., & Blanc, J. L. (1988). The state of stress in an overriding plate situated above a flat slab: The Andes of central Peru. *Tectonics*, *7*(4), 895–928.

Shelley, D. (1964). On Myrmekite. *The American Mineralogist*, *49*(January-February), 41–52.

Sibson, R. H. (1977). Fault rocks and fault mechanisms. *Journal of the Geological Society*, *133*(3), 191–213. https://doi.org/10.1144/gsjgs.133.3.0191

Sibson, R. H. (1987). Earthquake rupturing as a mineralizing agent in hydrothermal systems. *Geology*, *15*, 701–704.

Sibson, R. H. (1994). Crustal stress, faulting and fluid flow. *Geological Society, London, Special Publications*, *78*(1), 69–84. https://doi.org/10.1144/GSL.SP.1994.078.01.07

Simpson, C., & Wintsch, R. P. (1989). Evidence for deformation-induced K-feldspar replacement by myrmekite. *Journal of Metamorphic Geology*, *7*(2), 261–275. https://doi.org/10.1111/j.1525-1314.1989.tb00588.x

Stipp, M., Tullis, J., & Behrens, H. (2006). Effect of water on the dislocation creep microstructure and flow stress of quartz and implications for the recrystallized grain size piezometer. *Journal of Geophysical Research: Solid Earth*, *111*(4), 1–19. https://doi.org/10.1029/2005JB003852

Taggert, J. E. (2002). Analytical methods for chemical analysis of geologic and other materials. *U.S. Geological Survey Open-File Report 02-223*, 20.

Tobisch, O. T., Barton, M. D., Vernon, R. H., & Paterson, S. R. (1991). Fluid-enhanced deformation: transformation of granitoids to banded mylonites, western Sierra Nevada, California, and southeastern Australia. *Journal of Structural Geology*, *13*(10), 1137–1156. Retrieved from https://ac.els-cdn.com/019181419190074S/1-s2.0-019181419190074S-main.pdf?_tid=0f588c08-c527-4213-8b60-63d437a3c6b5&acdnat=1525482181_bc144f1287a3b13cf8f82e79ec65ec19

Walther, J. V. (1994). Fluid-Rock Reactions during Metamorphism at Mid-Crustal Conditions Fluid-Rock Reactions during Metamorphism at Mid-Crustal Conditions'. *The Journal of*

Geology, *102*(5), 559–570. Retrieved from http://www.jstor.org/stable/30068556

Wehrens, P., Berger, A., Peters, M., Spillmann, T., & Herwegh, M. (2016). Deformation at the frictional-viscous transition: Evidence for cycles of fluid-assisted embrittlement and ductile deformation in the granitoid crust. *Tectonophysics*, *693*, 66–84. https://doi.org/10.1016/j.tecto.2016.10.022

Whitbread, M., & Moore, C. (2004). Two lithogeochemical approaches to the identification of alteration patterns at the Elura Zn-Pb-Ag deposit, Cobar, New South Wales, Australia: Use of Pearce Element Radio analysis and Isocon analysis. *Geochemistry: Exploration, Environment, Analysis*, *4*(2), 129–141. https://doi.org/10.1144/1467-7873/03-031

Wintsch, R. P., & Yeh, M. W. (2013). Oscillating brittle and viscous behavior through the earthquake cycle in the Red River Shear Zone: Monitoring flips between reaction and textural softening and hardening. *Tectonophysics*, *587*, 46–62. https://doi.org/10.1016/j.tecto.2012.09.019

Wintsch, R. P., Christoffersen, R., & Kronenberg, a. K. (1995). Fluid-rock reaction weakening of fault zones. *Journal of Geophysical Research*, *100*(B7), 13021. https://doi.org/10.1029/94JB02622

Wise, J. M., & Noble, D. C. (2003). Geomorphic Evolution of the Cordillera Blanca , Northern Peru. *Boletin de La Sociedad Geologica Del Peru*, *96*(January 2003), 65–85.

Yuguchi, T., & Nishiyama, T. (2008). The mechanism of myrmekite formation deduced from steady-diffusion modeling based on petrography: Case study of the Okueyama granitic body, Kyushu, Japan. *Lithos*, *106*(3–4), 237–260. https://doi.org/10.1016/j.lithos.2008.07.017

Appendix III.I. Supplemental Tables

TABLE S6. SAMPLE LOCATIONS AND STRUCTURAL MEASUREMENTS.

Sample	Quebrada	Latitude	Longitude	Elevation	Strike	Dip	Trend	Plunge
CB15-03	Ahuac	-9.46325	-77.4898	4149	-*	-	-	-
CB13-54a	Gatay	-9.2029	-77.5709	3916	102	32	32	192
CB13-55a	Gatay	-9.20329	-77.57117	3902	141	24	24	231
CB13-55c	Gatay	-9.20305	-77.56789	4030	120	25	19	236
CB13-56	Gatay	-9.20385	-77.57175	3889	192	29	19	218
CB13-57a	Gatay	-9.2039	-77.57187	3878	172	36	36	247
CB13-57b	Gatay	-9.2039	-77.57187	3878	165	30	27	220
CB13-58	Gatay	-9.2041	-77.57257	3877	156	37	37	245
CB13-71a	Gatay	-9.20985	-77.56975	4226	166	30	30	256
CB13-73a	Gatay	-9.2059	-77.5709	4170	204	29	26	260
CB13-74a	Gatay	-9.20584	-77.57089	4164	145	10	5	241
CB13-76	Gatay	-9.2057	-77.57154	4155	155	19	18	245
CB13-77a	Gatay	-9.20673	-77.56929	4237	200	26	15	225
CB13-77c	Gatay	-9.20673	-77.56929	4237	196	31	15	231
CB13-84	Gatay	-9.20489	-77.57423	3911	112	20	17	230
MJCB11-07	Honda	-9.34555	-77.50502	3679	106	24	15	240
MJCB11-08	Honda	-9.3455	-77.50522	3673	165	34	15	305
MJCB11-09	Honda	-9.34528	-77.50503	3662	115	29	24	190
MJCB11-10	Honda	-9.34518	-77.50502	3658	105	30	24	235
MJCB11-11	Honda	-9.34505	-77.50497	3651	95	32	36	203
MJCB11-12	Honda	-9.34485	-77.50502	3669	85	40	32	195
MJCB11-13	Honda	-9.34447	-77.50468	3675	150	18	15	210
MJCB11-14	Honda	-9.34447	-77.50478	3651	97	31	28	190
MJCB11-15	Honda	-9.3443	-77.50468	3655	122	39	34	205
MJCB11-16	Honda	-9.34398	-77.50453	3649	-	-	-	-
CB15-04	Llaca	-9.47503	-77.46783	4042	113	39	29	256
CB15-05a	Llaca	-9.47503	-77.46783	4042	146	29	-	-
CB15-05b	Llaca	-9.47503	-77.46783	4042	-	-	-	-
CB15-07	Llaca	-9.47515	-77.46783	4042	123	30	29	238
CB15-09	Llaca	-9.47488	-77.46783	4059	100	31	19	242
CB15-16	Llaca	-9.47882	-77.46472	3990	163	26	-	-
MJCB11-03	Llaca	-9.47507	-77.46782	4043	105	46	40	223
MJCB11-04	Llaca	-9.47507	-77.46782	4043	90	34	31	226
MJCB11-05	Llaca	-9.47507	-77.46782	4043	90	17	11	198
CB13-24	Rajucolta	-9.5439	-77.40747	4197	-	-	-	-
CB13-28a	Rajucolta	-9.55105	-77.4028	4140	150	31	29	204
CB15-21b	Ulta	-9.12898	-77.51522	4789	-	-	-	-

*Notes: Elevation measured in field with Garmin eTrex. Strike and dip are of foliation plane; trend and plunge of stretching lineation. *- not applicable*

TABLE S7. XRF ANALYTICAL UNCERTAINTY

Standard Analyte	GSP-2 Analyzed	Recommended Value	+/-	BHV0-1 Analyzed	Recommended Value	+/-	QLO1A Analyzed	Recommended Value	+/-
WT %	n=6			n=6			n=4		
Na2O	3.4	2.8	0.1	2.5	2.26	0.07			
MgO	1.2	1.0	0.0	7.2	7.23	0.22			
Al2O3	14.7	14.9	0.2	13.7	13.8	0.21			
SiO2	0.3	66.6	0.8	49.2	49.9	0.53			
P2O5		0.3	0.0	0.3	n/a	n/a			
K2O	5.3	5.4	0.1	0.6	0.52	0.04			
CaO	2.1	2.1	0.1	11.4	11.4	0.17			
MnO	0.0			0.2	0.17	n/a			
Fe2O3	4.9	4.9	0.2	12.3	2.82	0.24			
TiO2	0.7	0.7		2.7	2.7	0.06			
Sum	98.4	0.0		99.9					
PPM									
Ba	1311	1340	44	130	139	14	1441	1370	80
Ce	402	410	30	38	39	4	52	54	6
Cr	18.5	20	6	271	289	22	0	3.2	1.7
Co	5.5	7	1	43	45	2	7	7.2	0.5
Cu	45	43	4	138	136	6	36	29	3
Hf	12	14	1	3	4.38	0.22	7	n/a	n/a
La	173.5	180	12	16	16	1.3	28	27	2
Pb	40.5	42	3	3	n/a	n/a	15	20	0.8

Table S7, continued.

Standard Analyte *WT %*	GSP-2 Analyzed n=6	Recommended Value	+/-	BHV0-1 Analyzed n=6	Recommended Value	+/-	QLO1A Analyzed n=4	Recommended Value	+/-
Nd	193	200	12	25	25	2	29	26	n/a
Ni	17.5	17	2	117	121	2	3	n/a	n/a
Nb	25	27	2	20	19	2	13	10	1.3
Rb	246.5	245	7	11	11	2	74	74	3
Sc	7	6	1	32	32	1.3	10	n/a	n/a
Sr	240	240	10	392	403	25	343	340	12
Th	103.5	105	8	1	1.08	0.15	6	4.5	0.5
V	58	52	4	306	317	12	54	54	6
Y	24	28	2	19	27.6	1.7	25	24	3
Zr	521	550	30	142	179	21	218	185	16
Zn	136	120	10	83	105	5	75	61	3

Appendix III.II. Supplemental Text

Supplemental Text S1. Point Counting Procedure

Standard X-Z thin sections, parallel to lineation and perpendicular to foliation, were used for point counting analysis. A set of 9 cross-polarized light images, and 9 plane-polarized light photomicrographs were collected from the same position on the thin section when needed for clarification, were collected for each sample. The relative positioning of the photomicrographs for all samples was standardized to avoid selection bias (Figure S1). A 500 µm-spaced grid was overlain on photomicrographs using ImageJ software, resulting in 720 data points for each sample. Each node within the grid was circular with a 25 µm area.

Components evaluated were grain-size-reduced (GSR) recrystallized matrix, non-GSR recrystallized matrix, porphyroclasts, and igneous phenocrysts. Whichever of these components constituted the majority of the node gridpoint was assigned to that node. Igneous feldspar phenocrysts were identified based on the presence of oscillatory or concentric zoning, inclusion of euhedral granitic phases such as plagioclase, quartz, biotite, or K-feldspar within coarse (> 1 mm) plagioclase or feldspar grains. Igneous quartz was identified as that which was relatively coarse-grained, interstitial between coarse feldspar grains, and exhibited relative straight crystal faces and/or exhibited chess-board extinction. If quartz was still coarse-grained and interstitial, but exhibited undulatory extinction or amoeboid grain boundaries, it was assigned to be non-GSR matrix. Igneous biotite was identified as that which was interstitial, subhedral-euhedral, relatively coarse grained, and exhibited minimal to no internal deformation such as kinking or undulatory extinction.

Porphyroclasts were identified as relatively large grains that were surrounded by a finer-grained, recrystallized (either GSR or non-GSR) matrix, where the foliation within the matrix wrapped around the porphyroclasts (Passchier & Trouw, 2005). Phases that exhibited characteristic microstructures of dynamic recrystallization such as irregular grain boundaries, undulatory extinction, grain boundary bulges, or subgrain formation (i.e. (Tullis & Yund, 1985; Stipp et al., 2002; Rosenberg & Stünitz, 2003; Passchier & Trouw, 2005) but were still coarse grained relative to a finer-grained matrix, were considered non-GSR recrystallized. Phases exhibiting dynamic recrystallization microstructures that were within the finer-grained matrix were thus classified as the GSR matrix.

Supplemental Text S2. Sample Descriptions

Undeformed to weakly-deformed granodiorites (UWGs) are texturally variable but are typically defined by large euhedral-to-subhedral plagioclase and K-feldspar phenocrysts up to 2-5 mm in length with anhedral quartz and anhedral ~2-10 mm interstitial biotite (Fig. S7A). In the southernmost transect (Q. Rajucolta), micrographic textures are observed primarily with coarse (>1 cm) perthitic K-feldspar phenocrysts and to a lesser extent with plagioclase. Micrographic textures were not identified in any observed samples north of Q. Rajucolta. In Qs. Llaca, Honda, and Gatay transects, coarse (2-3 mm) K-feldspar phenocrysts regularly include smaller (euhedral 200-1000 μm) plagioclase grains. Interstitial quartz regularly exhibits grain boundary migration recrystallization microstructures (Stipp et al., 2002) and/or chessboard extinction (Kruhl, 1996). Biotite is the primary mica phase and is often kinked and associated with oxides along cleavages. Some minor amounts of white mica, interpreted to be secondary (i.e. Petford and Atherton, 1992), occur between feldspar porphyroclasts, and sericitization sometimes occurs within some plagioclase cores. Trace amounts of chlorite are also observed, predominantly within feldspar fractures. High-temperature to sub-magmatic fractures occur within feldspar phenocrysts, some of which are filled with quartz (Hughes et al., 2019). Overall, UWGs are distinguished by their coarse grain size, weakly to undeformed biotite, primary igneous feldspar textures, and interstitial quartz. S-C fabrics are only weakly developed, if present, and would classify as proto-mylonites (< 50% recrystallization), where the recrystallization is predominantly observed as grain-boundary migration recrystallization or chessboard extinction in quartz (i.e. Stipp et al., 2002; Kruhl, 1996).

Mylonites exhibit grain-size reduction is observed in quartz and feldspar. Coarse (0.5-2 mm) K-feldspar and plagioclase grains are porphyroclastic within a relatively finer grained matrix and regularly tails or core-and-mantle structures (Fig. S7B, S7C). Mylonites contain discernable S-C or S-C-C' fabrics where the S-plane is commonly defined by quartz oblique grain-shape fabrics.

Ultramylonites thus are samples where extensive grain-size reduction occurs such that more than 90% of the sample is recrystallized. Remaining porphyroclasts are reduced to relatively small (< ~50 μm), rounded grains without tails or core-and-mantle structures (Fig. S7D, S7E). S-C(-C') fabrics are well developed and often have dominant C-surfaces parallel to macroscopically observed foliation.

Cataclasites are distinguished from other samples by through-going fractures at the hand-sample scale. Small-slip faults regularly offset mylonitic foliation (Fig. S7F) and mylonitic quartz clasts are sometimes included within a cataclastic matrix. However, not all cataclasite samples contain mylonitic quartz clasts. All cataclasite samples do contain fine-grained matrices with quartz and feldspar clasts that truncate undeformed-weakly-deformed, mylonitic, and/or ultramylonitic fabrics (Fig. S7G).

Quartz Veins

Observed quartz veins classify as ultramylonites or cataclasites. Ultramylonitic fabrics are distinguished by pervasive oblique grain-shape fabrics in quartz that exhibits characteristic bulging and/or subgrain rotation recrystallization microstructures (i.e. Stipp et al., 2002). In some instances, abundant fluid inclusion planes truncate oblique grain-shape fabrics. These fluid inclusion planes are subparallel to discontinuous fractures into which quartz crystals grow (Fig. S7H). Like granodioritic cataclasites, quartz vein cataclasites possess evidence of through-going brittle deformation, including cataclasite injection veins and variably rotated mylonitic clasts (Fig. S7I).

Supplemental Text S3. Sample Preparation for XRF Analysis and XRF Protocols

Fused glass beads and powdered pellets were created from rock powders for major and trace elements, respectively. 6.0 g lithium tetraborate (Spectromelt) was mixed with 0.75 g rock powder and fused into glass beads using a Siemens Autofluxer. 1.2 g SpectroBlend® powder was mixed with 8.0 g rock powder and pressed into pellets.

The XRF spectrometer was calibrated using standards GSP-2, BHV0-1, and QLO1A. See Table S7 for analytical uncertainties.

Supplemental Text S4. Derivation of Volume Proportions and Densities

Densities were estimated by calculating volume % norm (i.e. mode) following procedures of Hutchison 1976, where biotite was assumed to be annite and hornblende assumed to be Mg-edenite. Three calculation schemes of the CIPW norm (Kelsey, 1965; Hutchison & Lumpur, 1975; Holocher, 2014) and the mesonorm (Janoušek et al., 2006) were compared along with the derived mineral volume proportion and density for each method. Difference between the normative mineral abundances and volume percentages from any of the different methods are <1%. density calculations, regardless of whether feldspar was calculated as anorthite and albite or simply as albite and regardless of whether biotite was included in the norm (i.e Hutchison & Lumpur, 1975; Janoušek et al., 2006), densities are consistent to within 0.01 g/cm^3.

Appendix III.III. Supplemental Figures

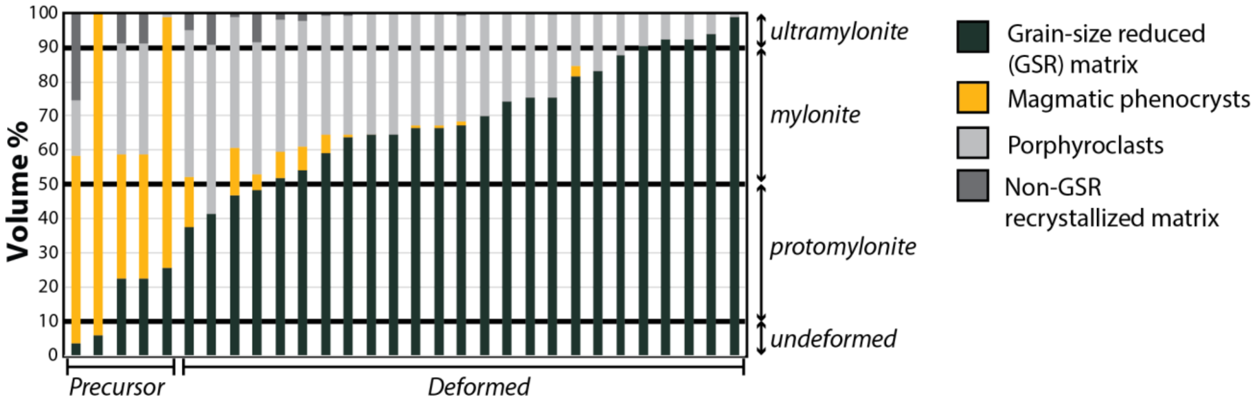

Fig. S6. Volume distribution of fabric and textural components quantified for classification of ductile fault rocks. Magmatic phenocrysts taken as those with no recrystallized tails in addition to original magmatic textures, such as concentric or oscillatory zoning, in-tact albite, Carlsbad, or simple twinning, and inclusions (typically in concentric configuration) of quartz or euhedral biotite or feldspar.

Fig. S7. Photomicrographs of representative deformation fabrics across the CBSZ. All images are cross-polarized light (XPL) unless otherwise noted. Arrows in labels situated between lineation plunge measurement (left) and trend measurement (right) and point down plunge of lineation. A) Undeformed granite from Q. Rajucolta. Kfs includes smaller Pl grains. Qz fills interstices between feldspar phenocrysts and exhibits chessboard extinction (T > 630 °C; Kruhl, 1996). B) Granodioritic mylonite from Q. Gatay. Myrmekite grows into Kfs porphyroclasts asymmetrically, signifying strain-induced replacement of Kfs by quartz and albite (Simpson & Wintsch, 1989). Pl is partly altered to sericite. Mylonitic fabric is layered between coarse feldspar-rich domains, qz-rich domains exhibiting dynamic recrystallization microstructures, and fine-grained qz+fsp+wm domains. Recrystallized tails along feldspar porphyroclasts indicate top-to-the-southwest shear sense (yellow arrows). C) Granodioritic mylonite from Q. Honda. Myrmekite grows asymmetrically along Kfs porphyroclast. WM occurs along the outer edge of myrmekite lobes. WM fish and tails along delta Kfs clast signify top-to-the-south shear. D) Granodioritic ultramylonite from Q. Llaca. Abundant WM fish are kinked and recrystallized. Qz occurs primarily as elongate ribbons that exhibit bulging and subgrain-rotation dynamic recrystallization mechanisms (Stipp et al., 2002). Pl porphyroclasts are fine grained. Tails on Kfs porphyroclasts deflect into WM-rich shear bands (yellow arrow). E) Grandioritic mylonite from Q. Gatay. Pl porphyroclasts are fine grained (< ~200 µm) and rounded. Dynamically recrystallized Qz-domains are interlayered with fine-grained recrystallized Bt+Kfs+Pl+Qz to more Bt-rich domains and exhibit asymmetric folding. F) Granodioritic cataclasite from Q. Gatay. Chl rim surrounds Bt fish. Ilmenite, rutile, and other opaque oxides primarily along cleavage. G) Granodioritic cataclasite from Q. Rajucolta. Mylonitic foliation with dynamically recrystallized Qz domains are cross-cut by cataclastic fabric (yellow arrows) and offset by micro-faults (red arrows). Fine-grained layers of Qz+fsp+chl±wm form discontinuous layers with Qz-rich domains. H). Quartz vein ultramylonite from Q. Gatay. Gypsum-plate photomicrograph of dynamically recrystallized Qz exhibiting subgrain rotation recrystallization microstructures (Stipp et al., 2002). Fluid inclusion planes (black arrows) are abundant and are subparallel to a partially open fracture (center). Qz crystals grow into fracture opening (white arrows) and have orientations that are mostly continuous with dynamically recrystallized Qz orientations. Titanite forms within fracture. I) Quartz vein cataclasite from Q. Gatay. Clasts of dynamically recrystallized Qz (e.g. black dashed lines) included within fine grained Qz matrix. Sparse Pl grains are relatively fine grained (~200 µm), rounded, and are found primarily within dynamically recrystallized qz clasts.Abbreviations: Qz: quartz, Kfs: K-feldspar, Pl: plagioclase, Bt: biotite, Chl: chlorite, M: myrmekite, Ser: sericite, Fsp: feldspar (undifferentiated), WM: white mica, Ttn: titanite, Ap: apatite, Rt: rutile, Ilm: ilmenite.

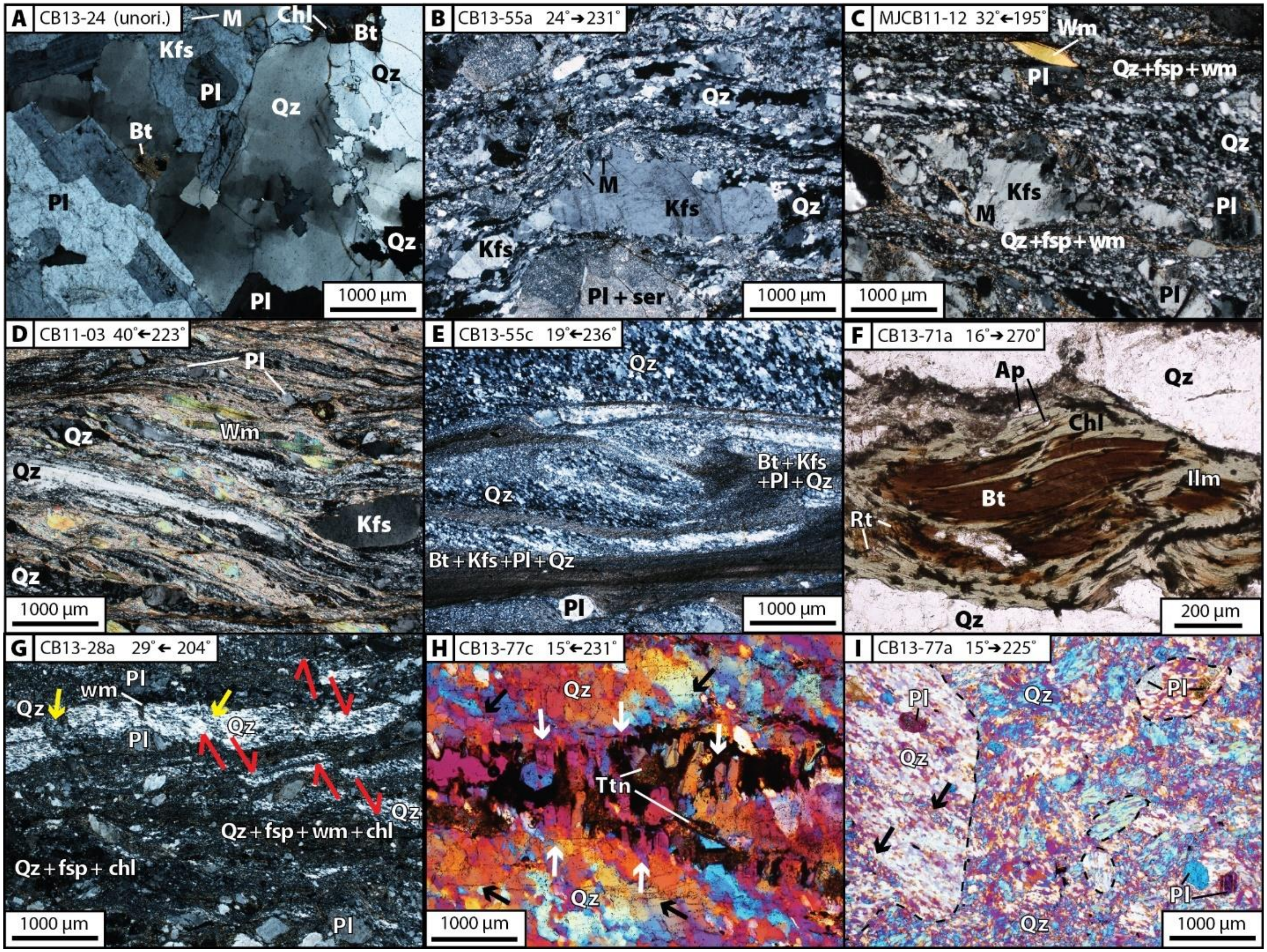
A CB13-24 (unori.)
M
Chl
Bt
Kfs
Pl
Qz
Qz
Bt
Pl
Qz
Pl
1000 μm
B CB13-55a 24°➔231°
Qz
M
Kfs
Qz
Kfs
Pl + ser
1000 μm
C MJCB11-12 32°←195°
Wm
Pl
Qz + fsp + wm
Qz
Kfs
M
Pl
Qz + fsp + wm
Pl
1000 μm
D CB11-03 40°←223°
Pl
Wm
Qz
Qz
Kfs
Qz
1000 μm
E CB13-55c 19°←236°
Qz
Bt + Kfs
+Pl + Qz
Qz
Bt + Kfs + Pl + Qz
Pl
1000 μm
F CB13-71a 16°➔270°
Ap
Qz
Chl
Ilm
Bt
Rt
Qz
200 μm
G CB13-28a 29° ← 204°
Pl
wm
Qz
Qz
Pl
Qz
Qz + fsp + wm + chl
Qz + fsp + chl
Pl
1000 μm
H CB13-77c 15°←231°
Qz
Ttn
Qz
1000 μm
I CB13-77a 15°➔225°
Pl
Qz
Pl
Qz
Qz
Pl
1000 μm

Fig. S8. Isocon wedge diagrams relative to TiO2. a) Major elements for northern transects. b) Trace elements for northern transects. c) Major elements for southern transects. d) Trace elements for southern transects. Bright colors correspond to higher deformation intensity, darker colors to lower deformation intensity. Symbols denote transect-filled square: Gatay, filled triangle: Honda, filled diamond: Ulta, open triangle: Llaca, open square: Rajucolta, open diamond: Ahuac.

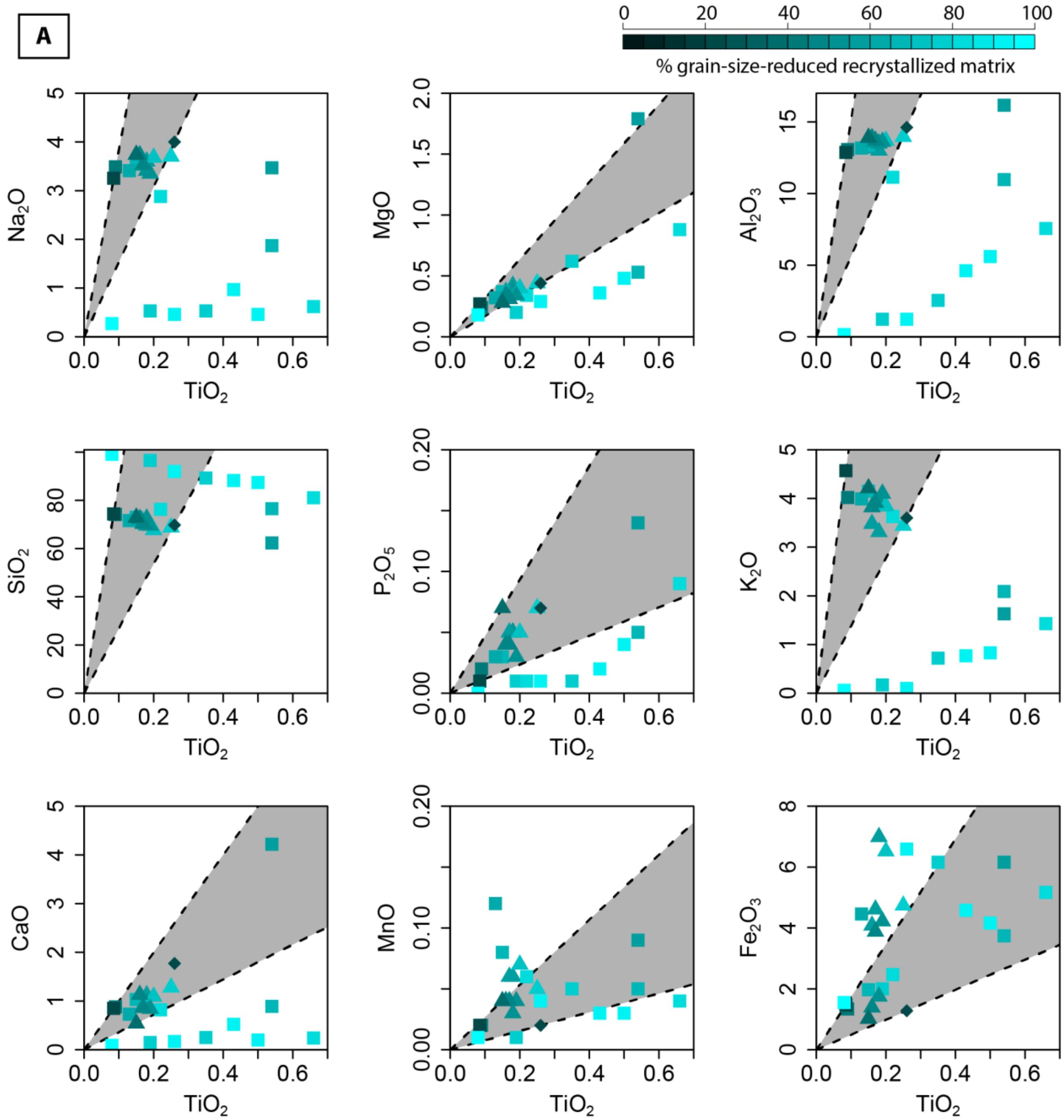
A
0
20
40
60
80
100
% grain-size-reduced recrystallized matrix
Na2O
MgO
Al2O3
SiO2
P2O5
K2O
CaO
MnO
Fe2O3
TiO2

Fig. S8.

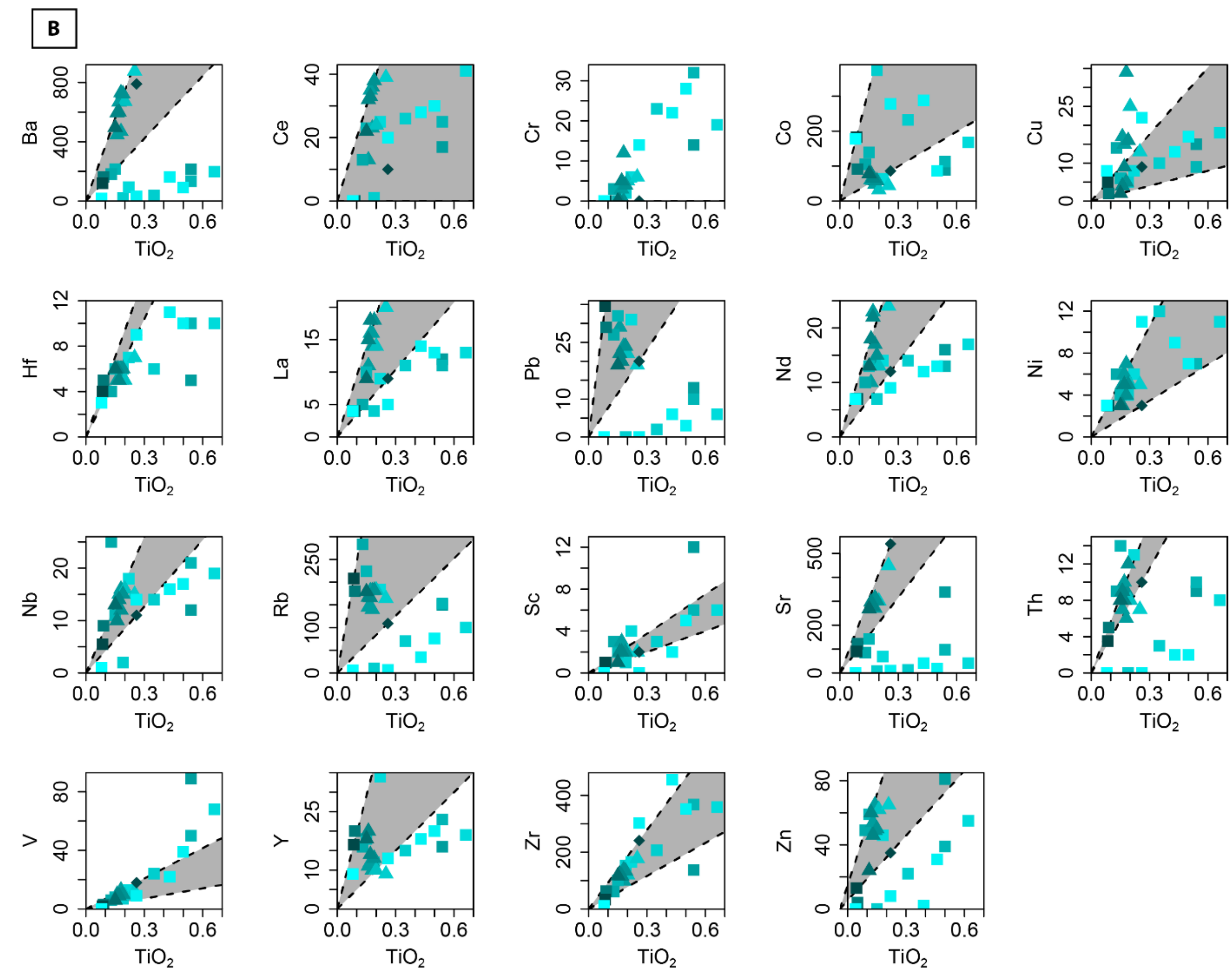

Fig. S8, continued.

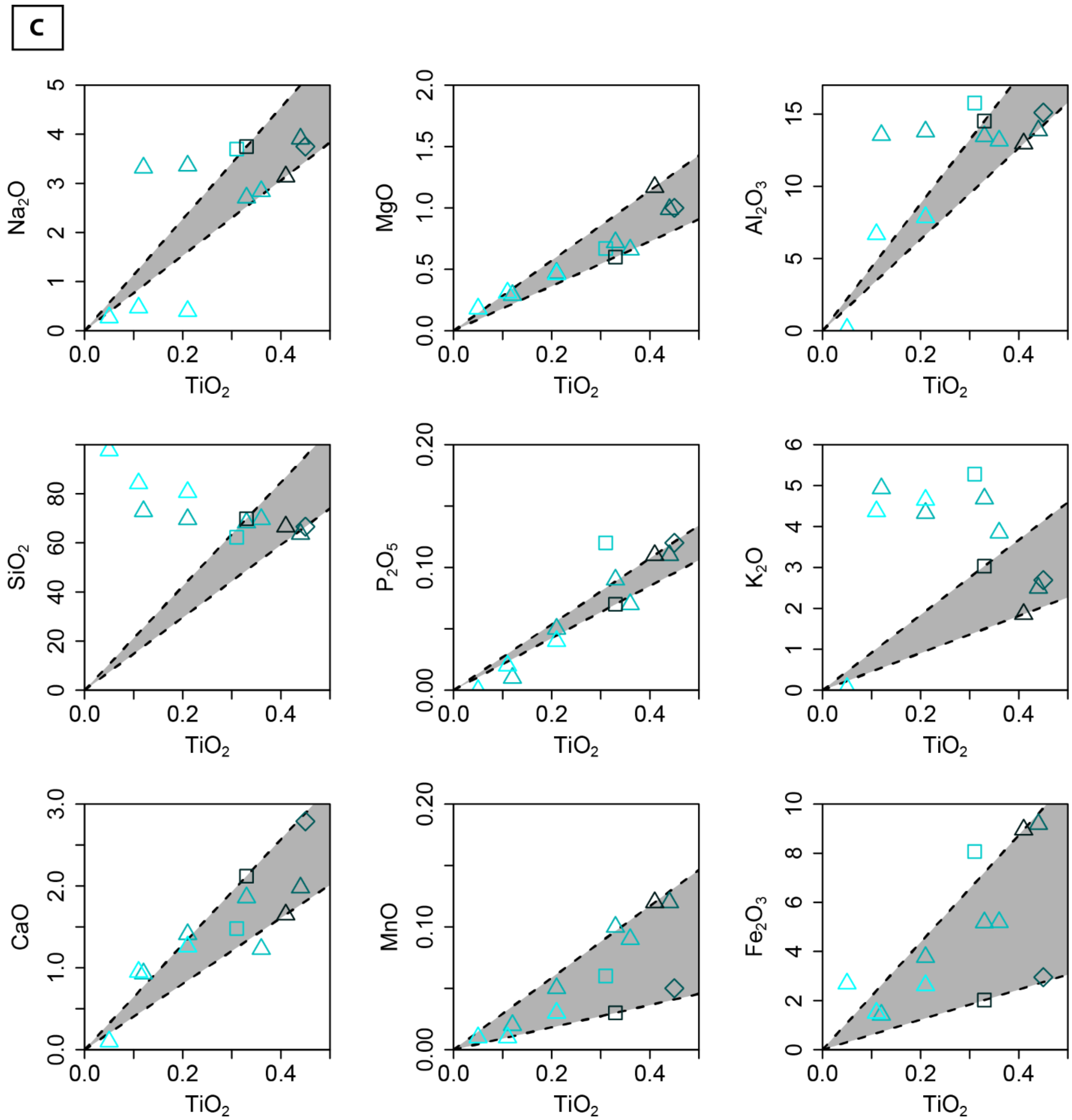

Fig. S8, continued.

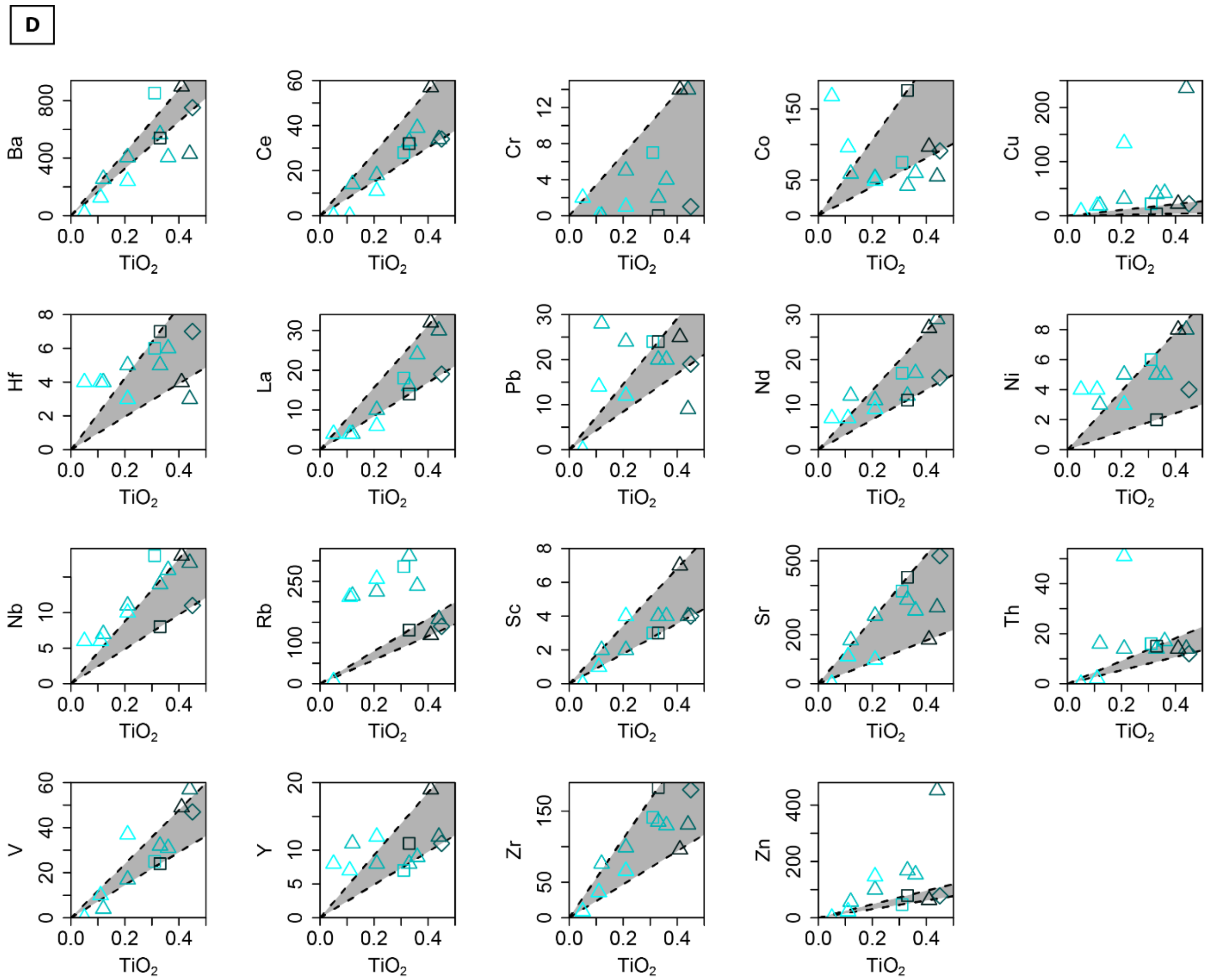

Fig. S8, continued.

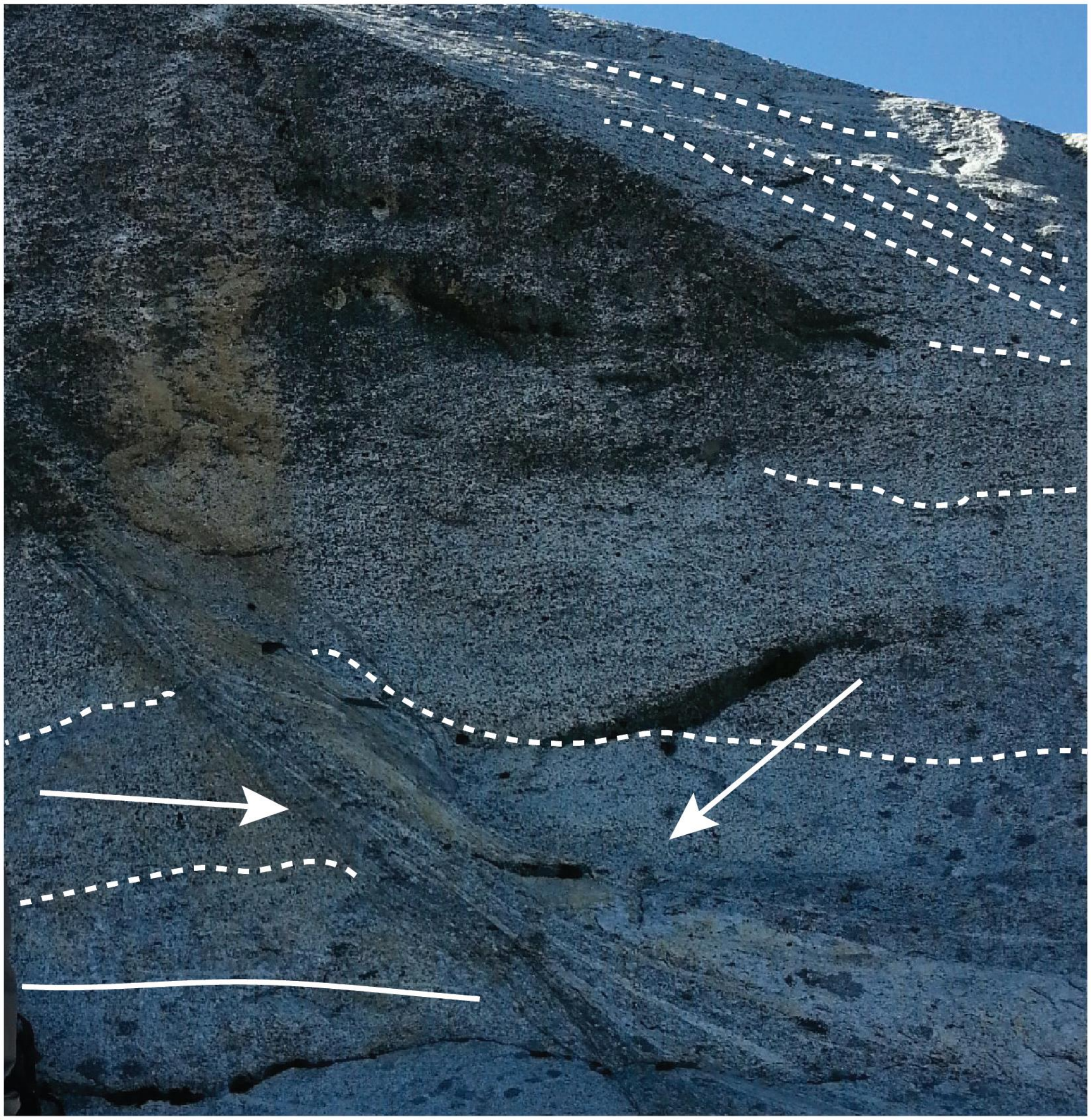

Fig. S9. Localized shear zone (white arrows) within otherwise weakly deformed granodiorite that exhibits minor layering (white dashed lines).

CONCLUSION

Deformation conditions during the progression of relatively undeformed granodiorite to mylonite, ultramylonite, and cataclasite in the CBSZ were determined using microstructural analysis, quartz crystallographic preferred orientation analysis, recrystallized quartz paleopiezometry, two-feldspar thermometry, and TitaniQ thermometry. Early high-temperature deformation was accommodated by fracturing of feldspar phenocrysts within interconnected feldspar networks. The transition between these networks and interconnection of quartz domains occurred via dislocation creep in feldspar and quartz and myrmekite-forming reactions. In both layered and S-C mylonites, quartz deformed predominantly via dislocation creep at temperatures between 400 and 500 °C. Layered mylonites also show evidence for at least local deformation by dissolution and precipitation creep along with grain-boundary sliding, suggesting a role of fluids in strain localization. Overall, deformation began at temperatures above ~630 °C and continued at temperatures above ~400 °C. Differential stresses during deformation ranged from 30 to 90 MPa. Collectively, these data suggest that, although deformation temperatures decrease slightly from structurally deep positions to structurally shallow positions along the detachment, strain localization in the CBSZ is promoted largely by variation in strain rate across the CBSZ.

Strain rate variability also is observed along strike of the CBSZ, as supported by the 6-fold variation in width of the mylonitic parts of the CBSZ that are continuous with, and truncated by, the detachment. Mylonitic shear zone width is greatest (~400 m), in the geographically central part of the CBSZ. Strain rates derived from shear zone widths at different locations along strike are broadly consistent with those calculated from differential stress and deformation temperature estimates from the same locations. Deformation within the CBSZ occurred at strain rates on the order of 10^{-14} to 10^{-12} s^{-1}. A regional crustal strength profile was derived from differential stresses and deformation temperatures from three transects across the CBSZ. Within the context of existing constraints on emplacement depth, this strength profile indicate that ductile deformation occurred within an elevated, likely transient, ~50 °C/km geothermal gradient.

Whole-rock geochemistry lends additional insight into the nature of fluid-rock interaction during deformation as well as shear zone variability along strike. Mass-balance calculations derived from whole-rock geochemistry indicate that mylonitization of rocks with less than 70% grain-size-reduced recrystallized matrix (i.e. protomylonites and mylonites) occurs isochemically and nearly isovolumetrically. Deformation of rocks with over 70% grain-size-reduced recrystallized matrix (i.e. high-strain mylonites and ultramylonites) is accompanied by volume increases of up to ~80%, silicification, and mobiliziation of TiO_2 and other siderophile elements. The nature of fluid-rock interaction along the geographically central CBSZ differs from that of the geographically southern CBSZ. Silicification occurs primarily in the geographically central CBSZ where the shear zone is wider, whereas the narrower southern CBSZ likely experienced K-metasomatism. The broad correlation between geochemical variation and shear zone width along strike may suggest that fluid flow plays an important role along with strain rate variation in localizing strain along the CBSZ.

VITA

Cameron was born in Lancaster, PA to parents Steve and Mary Hughes. She is the youngest of three siblings, including her older sister, Melanie Winters and older brother, Hayden Hughes. As an infant her family moved to Excelsior, MN, where she later attended Minnewashta Elementary School, Minnetonka Middle School West, and Minnetonka High School. At age 5 she began playing piano after becoming enthralled with music and theater in high school, Cameron pursued a degree in Music Education with a piano concentration at the University of North Texas. She picked up the geology 'bug' in a geology course taken to 'knock-out' a science requirement. Shortly after, Cameron transferred to the University of Wisconsin-Eau Claire and switched majors to Geology after taking another geology course with Dr. Geoff Pignotta. At UWEC, she grew to love field geology and got the itch to continue research through work with Dr. Phil Ihinger. During her junior year, Cameron spent a semester at the University of Alaska Anchorage through the National Student Exchange program. While there, she ventured to Wrangell St. Elias National Park with the Outdoor Recreation Program, which led to an interest in high relief areas and flat-slab subduction zones. After graduating with her Bachelor of Science in Geology from UWEC, Cameron worked as a geologist at the Alaska Division of Geological and Geophysical Survey. Soon after, she kicked off her PhD via a month-long field season with Dr. Micah Jessup. While pursuing her Doctor of Philosophy, Cameron was lucky to have the opportunity to intern at ExxonMobil and at the U.S. Geological Survey in Menlo Park. She got engaged to Tim Diedesch at the summit of Huapi Pass in the Cordillera Blanca during the final summer of her PhD.